Phenomenological Phase-Fluctuation Model for the Underdoped Cuprates

Dissertation zur Erlangung des
naturwissenschaftlichen Doktorgrades
der Bayerischen Julius-Maximilians-Universität
Würzburg

vorgelegt von

THOMAS ECKL

aus

Bad Mergentheim

Würzburg 2004

Eingereicht am 23. Juni 2004

bei der Fakultät für Physik und Astronomie

1. Gutachter: Prof. Dr. Werner Hanke

2. Gutachter: Prof. Dr. Enrico Arrigoni

3. Gutachter: . . . .

der Dissertation

1. Prüfer: Prof. Dr. Werner Hanke

2. Prüfer: Prof. Dr. Jean Geurts

der mündlichen Prüfung

Tag der mündlichen Prüfung: 19. Juli 2004

Doktorurkunde ausgehändigt am: . . . .

Contents

Introduction **1**

1 Phase-fluctuation scenario **3**

2 Model and techniques **8**

2.1 Hamiltonian 9
2.2 Derivation of effective phase-action 11
2.2.1 Mixed phase-field and fermionic action 11
2.2.2 Coarse-grained phase-only action 21
2.3 Self-consistent vs. non-self-consistent phase-action 23
2.4 The XY action 26
2.4.1 Quantum and classical XY model 26
2.4.2 The Kosterlitz-Thouless transition 29
2.4.3 The XY universality class 31
2.5 Numerical implementation and choice of parameters 32
2.6 Reducing finite-size effects — Assaad's method 36
2.6.1 Alternative methods 37
2.6.2 Peierls-Factors, Part I — static magnetic field 38
2.6.3 Gauge-invariant vs. non-gauge-invariant implementation 40
2.7 Optimization of algorithms for high-performance computing 43
2.7.1 Wolff's cluster algorithm vs. local Metropolis algorithm 43
2.7.2 Different Monte-Carlo error-estimators 44
2.7.3 Vectorization and the avoidance of cache-trashing 46

3 Single-particle properties **48**

3.1 Tunneling conductance 48
3.1.1 Experimental results 49
3.1.2 The d-wave case 51
3.1.3 The s-wave case — implications for electron-doped cuprates 52

3.2 Spectral weight $A(\boldsymbol{k},\omega)$ 59
  3.2.1 Quasiparticle dispersion 59
  3.2.2 Superconducting gap and pseudogap 63
  3.2.3 $(\pi,0)$-peak 64
3.3 The CPA as a high-temperature approximation? 77

4 Optical properties 81
4.1 The current-current correlation function 81
  4.1.1 Continuum model 81
  4.1.2 Linear response theory — Kubo formula 82
  4.1.3 Lattice model — Peierls-Factors, Part II 84
  4.1.4 General properties of $D_c(\boldsymbol{q},\omega)$ and $\sigma(\omega)$ 88
4.2 Optical sum-rule and kinetic energy 91
4.3 Optical conductivity 98
  4.3.1 General properties 98
  4.3.2 Paraconductivity 108

5 Magnetic properties 112
5.1 Diamagnetic susceptibility 112
5.2 Spin susceptibility 125

6 Conclusion 130

Summary 133

Bibliography 137

Zusammenfassung 149

Lebenslauf 153

Publikationen 155

Danksagung 157

Introduction

The study of quantum many-particle physics has lead to the discovery of many new states of matter over the past decades. Experimental discoveries like superfluidity, the Meissner effect, the Kondo effect, and the fractional quantum Hall effect, have puzzled physicists for a long time and did not fit into the earlier physical picture. However, they finally all lead to important new concepts in many-particle physics.

Landau has shown that phase transitions can be understood in the framework of broken symmetries, which can be described in terms of order parameters. Furthermore, he has shown in his theory of Fermi liquids, that the single-particle concept is still valid for interacting many-particle systems close to the Fermi surface, if the electrons are replaced by quasiparticles, which are adiabatically connected to the free non-interacting electronic states.

In a metal, the kinetic energy dominates the physical properties and the quasiparticle states can be described by delocalized plane waves. On the other hand, if the potential energy dominates, the quasiparticles become localized for a filling of one electron per lattice site. Many ferromagnets can be perfectly described by localized magnetic moments. In cases, where the kinetic energy is of the same order of magnitude as the potential energy, or in cases where delocalized electrons interact with local magnetic moments, like in heavy fermion systems, it is difficult to find an appropriate starting point.

Instead, collective behavior and emergent properties of matter start to play an important role [1]. Emergent properties are well known in biology and mean, that at each level of complexity, entirely new properties of the quantum many-particle system appear. For the fractional quantum Hall effect, this lead to the concept of fractional statistics and composite fermions.

Recently, the possibility to create Bose-Einstein condensates (BEC's) with a macroscopic number of atoms or molecules [2–6] has renewed the interest in the mesoscopic physics, where the quantum world comes into touch with our everyday world. Many of the new concepts of quantum many-particle physics have also lead to new developments in other fields of physics, like cosmology [1]. Furthermore, they also triggered many new possible technical applications in the field of quantum computing, quantum encryption, sensor devices, and energy technology.

In the following, we concentrate on the phenomenon of superconductivity. For about 100 years, it is known that some metals become superconducting at very low temperatures. These metals completely loose their resistance for an electric current and expel any applied magnetic field (Meissner effect). The phenomenology of Ginzburg and Landau, and later the microscopic theory of Bardeen, Cooper and Schrieffer (BCS), were able to provide a satisfactory explanation of these conventional low-temperature superconductors in terms of gauge-symmetry breaking and the macroscopic occupation of an electron-pair (Cooper-pair) wave function, where the pairing-interaction is mediated by lattice distortions (phonons) [7].

About 20 years ago, high-temperature superconductors were discovered. The common property of all high-temperature superconductors are Copper-oxide (CuO_2) planes, which are responsible for their superconducting properties. All high-temperature-superconducting cuprates are doped Mott insulators with numerous competing orders in their ground state [8–12]. Mott insulators differ from conventional band insulators in that the strong on-site Coulomb repulsion makes a double occupancy of two electrons per lattice-site energetically unfavorable. As a result, the electronic system behaves like an insulator rather than a good conductor at half-filling. An important signature of doped Mott insulators is the strong correlation among the charge carriers and the high sensitivity of their ground state to the doping level. In cuprates, the ground state of the undoped (half-filled) perovskite oxide is an antiferromagnetic Mott insulator.

More than fifteen years after their discovery, the high-temperature superconductors (HTSC) and the microscopic mechanism leading to superconductivity is still a central and unsolved problem in solid-state research, as can be seen from the large amount of controversial papers, appearing every week on this subject [13–17]. One reason is the not yet achieved connection of the microscopic interactions at the level of electrons and ions at high energy and high temperature, with the "emerging phenomena" at lower temperatures, i. e. competing and nearly degenerate order, like antiferromagnetism, d-wave superconductivity, d-density-wave order, charge order, etc.

What one needs to do is to correctly bridge high to low energies and eventually solve the ground-state problem. Up to now, it is not obvious how one can systematically apply the renormalization-group idea to integrate out the irrelevant degrees of freedom, due to the different competing orders, which are not separated by distinct energy scales, and which might be a sign for an unstable fixpoint controlling the phase diagram of the cuprates.

Instead of trying this seemingly impossible task, one could alternatively assume a certain low-energy order to be realized in the cuprates and explore the consequences of this order. A detailed comparison between theory and experiment then allows to confirm or rule out this order in the cuprates. In this thesis, we proceed along this line and use a phenomenological BCS-like model to discuss the possibility of a phase fluctuation regime in the underdoped cuprates, which is characterized by local Cooper-pairs without global phase coherence. The fluctuations of the phase were treated by means of a Monte Carlo simulation of a classical XY action.

1

Phase-fluctuation scenario

A number of different experiments indicate a suppression of low-frequency spectral weight in the underdoped cuprates below a characteristic temperature T^*, that is higher than the superconducting (SC) transition temperature T_c [18–27]. This striking behavior — termed pseudogap — initiated a variety of proposals as to its origin [28–36], since the answer to this question may be a key ingredient for the understanding of high-T_c superconductivity. One of these proposals is that the pseudogap arises from phase fluctuations of the superconducting gap [32].

Experimental findings

The phase-fluctuation scenario of the pseudogap is motivated by two experimental observations. Firstly, the pseudogap has the same size as the SC gap and continously evolves out of the SC gap above T_c [24, 26]. Secondly, in the underdoped cuprates, the SC transition temperature T_c does not scale with the SC gap size $\Delta_{sc}(T = 0)$, as expected from the conventional BCS theory, but rather scales with the zero-temperature superfluid density $\rho_s(0)$ [37]. On the other hand, the onset temperature of the pseudogap T^* scales with the SC gap size $\Delta_{sc}(T = 0)$.

However, the pseudogap temperature T^* is not a sharp transition line. Different experiments yield different results for T^*. Therefore, it is rather a smooth crossover line where fluctuations of different kinds are getting large enough to become experimentally detectable. In fact, there exist at least two pseudogaps in the underdoped cuprates. Besides the low-energy pseudogap of size Δ_{sc}, also a high-energy pseudogap was observed in photoemission experiments, which is of the order of the magnetic exchange energy J and associated with local antiferromagnetic fluctuations [38].

Phase-fluctuation model of Emery and Kivelson

Many pseudogap phenomena can be understood by the assumption that the low-energy pseudogap is of superconducting origin. Emery and Kivelson [32] pointed out that two ingredients are necessary for superconductivity: pairing of the electrons into Cooper-pairs *and* global phase coherence among the pairs (see Fig. 1.1). The pair-binding temperature can be obtained

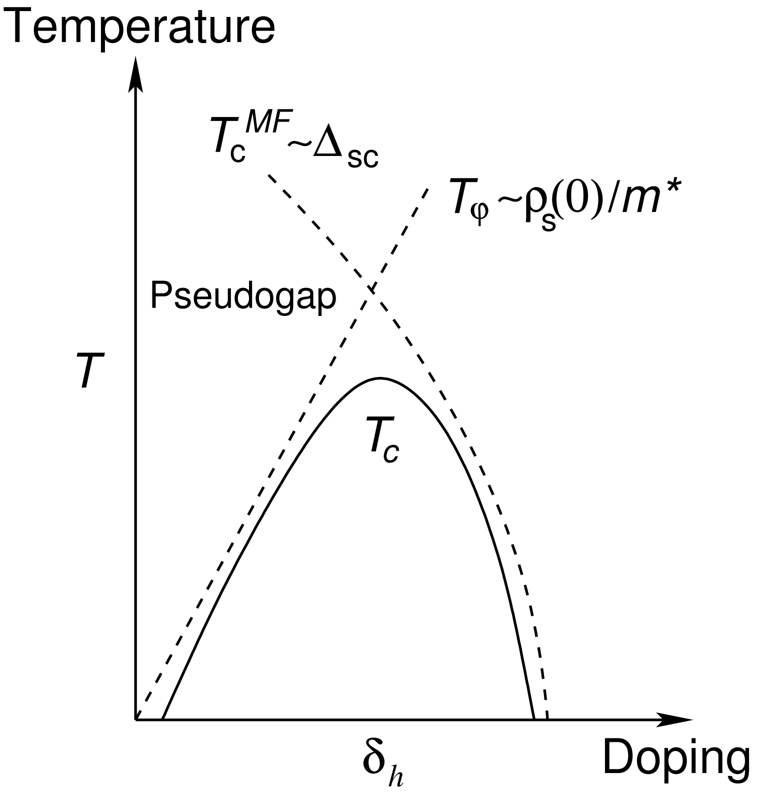

Figure 1.1: Sketch of the cuprate phase diagram. The superconducting dome is a result of two temperature scales. The pairing temperature $T_c^{MF} \sim \Delta_{sc}$, below which local pairs form, and the phase ordering temperature $T_\varphi \sim \rho_s(0)/m^*$, below which global phase coherence among the pairs is established. The pairing strength and accordingly Δ_{sc} decrease with increasing doping, whereas the superfluid density $\rho_s(0)$ increases with number of doped charge carriers. In the doping regime, where $T_\varphi \lesssim T_c^{MF}$, phase fluctuations give rise to pseudogap phenomena above T_c.

from the standard BCS mean-field theory and is proportional to the SC gap size: $T_c^{MF} \sim \Delta_{sc}$. On the other hand, the phase ordering temperature T_φ, below which global phase coherence among the pairs is established, is determined by the zero temperature superfluid density $\rho_s(0)$: $T_\varphi \sim \rho_s(0)/m^*$.

In conventional metallic superconductors and in the overdoped cuprates, the density of superconducting electrons is large. There, one has $T_c^{MF} \ll T_\varphi$ and consequently with pairing one immediately obtains phase coherence among the pairs (see Fig. 1.1). Therefore, the transition temperature T_c to the superconducting state is solely determined by the BCS mean-field pairing-temperature ($T_c \simeq T_c^{MF}$).

On the other hand, the underdoped cuprates are in close proximity to the Mott insulating state. Accordingly they have a very small charge carrier density. Hence $T_\varphi \lesssim T_c^{MF}$ and the SC transition temperature T_c is determined by the phase ordering temperature T_φ. Thus, starting from high temperatures, local pairs form at a temperature $T^* \simeq T_c^{MF}$, well above the actual SC transition temperature $T_c \simeq T_\varphi$, where phase coherence among these pairs finally sets in (see Fig. 1.1). In the intermediate temperature regime between $T_c^{MF} \equiv T^*$ and $T_\varphi \equiv T_c$, phase fluctuations give rise to pseudogap phenomena.

BCS, BEC, and phase fluctuations

The phase fluctuation scenario differs from the conventional BCS scenario as well as from the scenario of a Bose-Einstein condensation (BEC) of tightly bound pairs. In metals, the Cooper-pair radius ξ_0 is much larger than the distance d between the pairs ($\xi_0 \gg d$). Due to the strong overlap of a vast number of pairs, pair fluctuations are unimportant and the transition to the SC state can be described by the BCS mean-field theory.

In cases, where the pairing potential is very large, the Cooper pairs are tightly bound and can approximately be considered as bosons.[1] Hence the term Bose-Einstein condensation for the SC transition. Since in the strong coupling limit, the pair size ξ_0 is much smaller than the distance d between the pairs ($\xi_0 \ll d$), pair fluctuations start to become very important.

The pair fluctuations are usually treated in a perturbative way by taking into account diagrams beyond the BCS mean-field approximation. These are the famous Aslamazov-Larkin diagrams, describing short-time Cooper-pair fluctuations above T_c, the Maki-Thompson diagrams, describing the Andreev reflection of single-particle excitations by SC fluctuations, and finally the density of states diagrams, describing the suppression of the density of states of the normal charge carriers due to Cooper-pair fluctuations.

In the phase fluctuation scenario for the underdoped cuprates, we are in the intermediate coupling regime with $\xi_0 \sim d$, in between the BCS and BEC limits. Furthermore, due to the proximity to the Mott insulating state, the superfluid density is strongly suppressed. Hence, the dominating fluctuation channel is that of the phase of the Cooper pairs. In fact, it is assumed, that phase fluctuations are the only fluctuations channel up to T^*. This anomalously large phase-fluctuation regime cannot be understood within a simple strong-coupling Ansatz. It is believed (see Sec. 2.3), that bad screening of the charge carriers and competing orders are a possible reason to stabilize local pairs with fluctuating phases up to highest temperatures. The justification and consequences of this assumption will be discussed in great detail in Chap. 2.

Analogy to magnetism — local moments

The phase fluctuation scenario has an analogy in the theory of itinerant electron ferromagnetism [39]. Within the Stoner mean-field description, the ferromagnetic state appears below the Curie temperature T_C. The magnetic moments leading to the uniform homogeneous magnetism are absent above T_C and form exactly at T_C, concomitant with the macroscopic ferromagnetic phase.

However, in band-ferromagnets like Fe, Co and Ni, there is evidence for rather strong local magnetic moments already in the paramagnetic phase above T_C. These materials rather resemble a picture, where at a temperature $T > T_C$, disordered local magnetic moments are formed, with $\langle \boldsymbol{s}_i^2 \rangle \neq 0$ and $\langle \boldsymbol{s}_i \rangle = 0$. The Curie temperature T_C is then given by the temperature, where the local magnetic moments align co-linear and $\langle \boldsymbol{s}_i \rangle \neq 0$.

---

[1] This analogy is not exact, since Cooper pairs do not satisfy the commutation relation for bosons.

The formation of local magnetic moments above T_C is completely analogous to the formation of local pairs in the phase-fluctuation picture above T_c. The phase transition to the ferromagnetic state at T_C, where all local moments are getting aligned along the same direction and which is associated with the spontaneous breaking of spin rotation symmetry, is completely analog to the transition into the superconducting state at T_c within the phase-fluctuation model, where global phase coherence among the pairs sets in and which is associated with the spontaneous breaking of gauge symmetry.

Note that the formation of local magnetic moments or the formation of a local pairs with fluctuating phases is no phase transition, since it is not accompanied by a spontaneous symmetry breaking. It is rather a crossover temperature, below which the different fluctuations are getting important. There exist other theories of the pseudogap (see below), which assume a phase transition.

Further experimental support for phase fluctuations

Besides the already mentioned observation of a pseudogap in the excitation spectrum above T_c, which has the same size as the SC gap, and the fact that T_c scales with the superfluid density, there are various other findings strongly supporting a phase-fluctuation scenario for the pseudogap in the underdoped cuprates. For example, high-frequency conductivity experiments have indicated a SC scaling behavior of the optical conductivity already above T_c in underdoped $Bi_2Sr_2CaCu_2O_{8+\delta}$ (Bi2212) [40] and photoemission experiments revealed a close connection between the SC $(\pi, 0)$-photoemission peak and the superfluid density [41]. The SC $(\pi, 0)$-photoemission peak was observed even slightly above T_c in underdoped Bi2212. These experiments will be discussed in greater detail in Sec. 4.3 and Sec. 3.2.

Furthermore, a strongly enhanced Nernst signal was measured above T_c in underdoped samples of $La_{2-x}Sr_xCuO_4$ (LSCO), which is usually associated with the presence of vortices in the superconducting state and therefore implies that T_c corresponds to a loss of phase rigidity rather than a vanishing of the pairing amplitude [27]. The evolution of T_c with electron irradiation in underdoped $YBa_2Cu_3O_{7-\delta}$ (YBCO) also emphasizes the importance of phase fluctuations [42].

Finally, detailed measurements of the doping dependence of the low-temperature heat conductivity in LSCO and YBCO clearly show that the quasiparticle excitation gap has a pure d-wave form throughout the cuprate phase diagram [43]. Moreover, no sign was found of a possible (quantum) phase transition or a different order parameter being responsible for the pseudogap [43].

Alternative scenarios

As already said, the pseudogap temperature T^* is not a sharp transition line, but rather a smooth crossover line where fluctuations of different kinds are getting large enough to become detectable. Alternatively, it could also be a phase transition line, which is strongly broadened by disorder. A possible order compatible with the experimental observations is a d-density wave (DDW) order [28]. However, until now, no clear evidence for a quantum critical point or a phase transition was found [43].

On the other hand, if the pseudogap is only caused by fluctuations, no clear experimental identification of the type of fluctuations might be possible due to the near degeneracy of the various competing orders. Depending on the temperature, doping and material, contributions from spin fluctuations, SC phase fluctuations, dynamic spin/charge-stripes, DDW fluctuations, etc., might be observed.

Different theoretical models

On the theoretical side, the phase fluctuation scenario was explored by various different approaches. Franz and Millis calculated the single-particle spectral weight by a semi-classical coupling of the supercurrent to the quasiparticles, which leads to a Doppler-shifted excitation spectrum [34]. A similar perturbative approach was used by Kwon and Dorsey to calculate several single-particle properties [35].

Franz and Tešanović exploited a connection between the phase action of a phase fluctuation model for the cuprates and quantum electrodynamics in $(2+1)$ dimensions (QED$_3$) to obtain the single particle excitation spectrum and quantum critical behavior of their model [44]. Herbut has shown, using the same approach, that the topological vortex defects in a phase fluctuation model can lead to an incommensurate spin-density wave [45].

In this thesis, we introduce a phenomenological phase fluctuation model, which allows the exact calculation of the single-particle excitation spectrum, *as well as* the calculation of optical and magnetic properties. The advantage of using a *single* model with a *fixed* set of parameters is that it gives a more coherent picture of the role of phase fluctuations in the pseudogap regime of the cuprates.

2

Model and techniques

In this chapter we introduce a BCS-like Hamiltonian that accounts for phase fluctuations of the superconducting order parameter. The fluctuations of the phase have eventually been treated by means of a Monte Carlo simulation, where the statistical weight of each phase configuration is given by a classical XY action. Results of this simulation are shown in chapters 3 to 5. Before discussing this approach, we first address the more general case and demonstrate, how one can obtain a *microscopic* phase action from the BCS-like Hamiltonian, which includes the full quantum dynamics of the phase and under which conditions this more general *microscopic* action reduces to a XY-like action.

Furthermore, we discuss, how one can — in principle — obtain a quantum XY action for the phase by coarse graining the microscopic action on the scale of the Cooper-pair coherence length ξ_0. This *coarse-grained* quantum XY action no longer depends on the microscopic details of the system and the only parameter left is the superfluid density or phase stiffness. After a discussion of the general properties of the XY model, we show how to fix the parameters of our phenomenological phase fluctuation model. Finally, it is explained, how the model is implemented and solved numerically.

Our general goal is to derive a simple model, that contains only two free parameters (T_c and T^*, in units of the energy scale t), but nevertheless captures all the essential physics of the phase-fluctuation scenario. In particular, we are interested in the coupling between phase fluctuations and the electronic degrees of freedom. The model will be solved exactly, without any further approximations or readjustments of parameters. Our idea is to compare the results of this model with a variety of experiments in the pseudogap region of the underdoped cuprates, in order to explore the notion, that the pseudogap and related phenomena observed in this region of the phase diagram, have their origin in phase fluctuations of the superconducting order parameter.

In the following sections we use units such that $\hbar = c = k_B = 1$ and measure all energies in units of t, unless otherwise specified.

2.1 Hamiltonian

The Hamiltonian, we want to consider, can be separated into two parts

$$H = H_0 + H_1, \tag{2.1}$$

where the first part H_0 is the Hamiltonian of tightly-bound non-interacting electrons on a two-dimensional (2D) square lattice

$$H_0 = -t \sum_{\langle \boldsymbol{ij} \rangle,\sigma} (c^\dagger_{\boldsymbol{i}\sigma} c_{\boldsymbol{j}\sigma} + c^\dagger_{\boldsymbol{j}\sigma} c_{\boldsymbol{i}\sigma}) - t' \sum_{\langle\langle \boldsymbol{ij} \rangle\rangle,\sigma} (c^\dagger_{\boldsymbol{i}\sigma} c_{\boldsymbol{j}\sigma} + c^\dagger_{\boldsymbol{j}\sigma} c_{\boldsymbol{i}\sigma}) - \mu \sum_{\boldsymbol{i},\sigma} n_{\boldsymbol{i}\sigma}. \tag{2.2}$$

Here, $c^\dagger_{\boldsymbol{i}\sigma}$ ($c_{\boldsymbol{i}\sigma}$) creates (annihilates) an electron of spin σ on the $\boldsymbol{i}^{th}$ site of the 2D square lattice and $n_{\boldsymbol{i}\sigma} = c^\dagger_{\boldsymbol{i}\sigma} c_{\boldsymbol{i}\sigma}$ is the number operator. t and t' denote effective nearest-neighbor and next-nearest-neighbor hopping-terms and μ is the chemical potential. The angles $\langle \cdots \rangle$ and $\langle\langle \cdots \rangle\rangle$ indicate sums over nearest-neighbor and next-nearest-neighbor sites of the 2D square lattice, respectively. In what follows, we set in most cases $t' = 0$.

The second part of the Hamiltonian H_1 contains a BCS-like interaction, which for the d-wave case is given by

$$H_1 = -g \sum_{\boldsymbol{i}\delta} (\Delta_{\boldsymbol{i}\delta} \langle \Delta^\dagger_{\boldsymbol{i}\delta} \rangle + \Delta^\dagger_{\boldsymbol{i}\delta} \langle \Delta_{\boldsymbol{i}\delta} \rangle), \tag{2.3}$$

with

$$\Delta^\dagger_{\boldsymbol{i}\delta} = \frac{1}{\sqrt{2}} (c^\dagger_{\boldsymbol{i}\uparrow} c^\dagger_{\boldsymbol{i}+\delta\downarrow} - c^\dagger_{\boldsymbol{i}\downarrow} c^\dagger_{\boldsymbol{i}+\delta\uparrow}) \tag{2.4}$$

and δ connecting nearest-neighbor sites. The coupling constant g stands for the strength of the effective next-neighbor $d_{x^2-y^2}$-wave pairing-interaction. The origin of this pairing interaction is unimportant for the further calculation. It can be either of pure electronic origin, like spin fluctuations, or phonon mediated. The only important thing is, that there exists an effective pairing interaction, that produces a finite local $d_{x^2-y^2}$-wave gap as one goes below a certain temperature T^*. In contrast to conventional BCS theory, we consider the pairing-field amplitude not as a constant real number, but rather as a complex number

$$\langle \Delta^\dagger_{\boldsymbol{i}\delta} \rangle = \frac{1}{\sqrt{2}} \langle c^\dagger_{\boldsymbol{i}\uparrow} c^\dagger_{\boldsymbol{i}+\delta\downarrow} - c^\dagger_{\boldsymbol{i}\downarrow} c^\dagger_{\boldsymbol{i}+\delta\uparrow} \rangle = \Delta e^{i\Phi_{\boldsymbol{i}\delta}}, \tag{2.5}$$

with a constant magnitude Δ and a fluctuating bond-phase field $\Phi_{\boldsymbol{i}\delta}$. In order to get a description, where the *center of mass* phases of the Cooper pairs are the only relevant degrees of freedom, we write the $d_{x^2-y^2}$-wave bond-phase field in the following way

$$\Phi_{\boldsymbol{i}\delta} = \begin{cases} (\varphi_{\boldsymbol{i}} + \varphi_{\boldsymbol{i}+\delta})/2 & \text{for} \quad \delta \text{ in } x\text{-direction} \\ (\varphi_{\boldsymbol{i}} + \varphi_{\boldsymbol{i}+\delta})/2 + \pi & \text{for} \quad \delta \text{ in } y\text{-direction,} \end{cases} \tag{2.6}$$

where $\varphi_{\boldsymbol{i}}$ is the *center of mass* phase of a Cooper pair localized at lattice site $\boldsymbol{i}$.

As already said at the beginning, this model has been solved by means of a Monte Carlo simulation, where the phase configurations are constructed from a classical XY action (see

Secs. 2.4 and 2.5). The validity of this approach will be discussed in great detail in Secs. 2.2 and 2.3. There, we derive a *microscopic* quantum phase action for our Hamiltonian and discuss, how a *coarse-grained* quantum XY phase action can be obtained, which only depends on the superfluid density. So far, this means that we consider all high-energy degrees of freedom, including those responsible for the magnitude of the local pairing gap and internal $d_{x^2-y^2}$-wave structure of the Cooper pairs, as effectively being integrated out.

Since it is still not clear, whether the electron doped cuprates are s-wave or d-wave superconductors and because phase fluctuations might also be important for these materials, due to the proximity to the Mott insulating phase, we consider in addition to the d-wave form of the superconducting gap, also an s-wave on-site pairing interaction of the form

$$H_1 = U \sum_{\boldsymbol{i}} (c_{\boldsymbol{i}\downarrow} c_{\boldsymbol{i}\uparrow} \, \Delta \, e^{i\varphi_{\boldsymbol{i}}} + c^{\dagger}_{\boldsymbol{i}\uparrow} c^{\dagger}_{\boldsymbol{i}\downarrow} \, \Delta \, e^{-i\varphi_{\boldsymbol{i}}}). \tag{2.7}$$

This pairing interaction can be viewed as being derived from a negative U ($U < 0$) attractive Hubbard model. Additionally, comparing our d-wave results with those obtained for the s-wave gap, allows for a deeper understanding of the general phase fluctuation problem.

All the interaction terms (Eqs. (2.3) and (2.7)) can formally be obtained from a general many-body Hamiltonian, with the help of a Hubbard-Stratonovich transformation in the pairing field [46]. After the Hubbard-Stratonovich transformation, one makes a saddle-point (BCS) approximation for the magnitude of the pairing field, but then takes into account phase fluctuations around this mean-field saddle-point. The magnitude of the superconducting (SC) mean-field pairing-gap Δ_{sc} can be determined by the usual BCS gap-equation. The single-particle excitation gap at the Fermi surface has the maximum value $E_{\text{gap}}^{\text{max}} = 2\Delta_{sc}$. For the d-wave case it is related to the pairing amplitude, defined in Eq. (2.5), by $\Delta_{sc} = 2\sqrt{2}\, g\Delta$ and for the s-wave case by $\Delta_{sc} = U\Delta$, with Δ defined in Eq. (2.7). The size of the quasi-particle excitation gap Δ_{sc}, again determines the mean-field transition temperature T_c^{MF}, which we take as pseudogap temperature T^*.

Thus, our Hamiltonian has all ingredients necessary for the phase fluctuation scenario: below a temperature T^*, a finite local SC gap develops, however due to phase fluctuation of the SC order parameter, the true SC transition is suppressed to a much lower temperature $T_c < T^*$, where phase coherence finally develops. This model Hamiltonian contains, in principle, only one tunable parameter, i. e. the size of the SC gap Δ_{sc} in units of t and therefore T^*. The hopping parameter t only defines the overall energy scale of the Hamiltonian. The partition function Z is then given by

$$Z = \mathrm{Tr}\, e^{-\beta H}. \tag{2.8}$$

Here one has to take the trace over all fermionic states *and* the phase variables $\varphi_{\boldsymbol{i}}$. In the following section we illustrate different ways to carry out this procedure. Eventually, we will make a quenched average over the phase degrees of freedom, which is done by means of a Monte Carlo importance sampling procedure of a classical XY phase action.

2.2 Derivation of effective phase-action

In this section, we discuss different methods to calculate the partition function (Eq. (2.8)). We first start with a mixed representation, that explicitly contains the fermionic and phase degrees of freedom in the partition function and show how the trace over the phase-field could be performed, in principle, with the help of a (quantum) Monte Carlo (MC) simulation. We then introduce an effective scheme, to construct an approximative *microscopic* phase-only action from our Hamiltonian, which is based on a cumulant expansion of the partition function. This effective *microscopic* action can be expressed in terms of pair-correlation functions. Then we go one step further and discuss, how a *coarse-grained* XY phase-only action can be obtained, which only depends on the superfluid density.

2.2.1 Mixed phase-field and fermionic action

In section 2.1 we have neglected the time dependence of the phase field to get a Hamiltonian description. In general, one however has to take this time dependence into account, which has its origin in the Hubbard-Stratonovich transformation on the discrete imaginary time slices [46]. Here one writes the partition function as

$$Z = \mathrm{Tr} \prod_{l=1}^{L} e^{-\Delta\tau H}, \tag{2.9}$$

with $\beta = L\Delta\tau$. Now one can write

$$e^{-\Delta\tau H} = e^{-\Delta\tau(H_0+H_V)} \simeq e^{-\Delta\tau H_0}\, e^{-\Delta\tau H_V} + O(\Delta\tau^2), \tag{2.10}$$

where H_V is the *full* interaction term, which in case of the d-wave Hamiltonian is given by

$$H_V = -g \sum_{\boldsymbol{i}\delta} (\Delta_{\boldsymbol{i}\delta} \Delta^{\dagger}_{\boldsymbol{i}\delta} + \Delta^{\dagger}_{\boldsymbol{i}\delta} \Delta_{\boldsymbol{i}\delta}), \tag{2.11}$$

and H_0 contains only single-particle operators. The error in doing this is of order $\Delta\tau^2$ and negligible in the limit $\Delta\tau \to 0$ ($L \to \infty$). In the next step one uses the Hubbard-Stratonovich transformation, which is nothing but an operator version of the familiar Gaussian integral, to bring the interaction term in $e^{-\Delta\tau H_V}$ into a form that is bilinear in the fermion operators and where the fermions now “interact” with a complex pairing field $\Delta_{\boldsymbol{ij}}$ [46]. This yields integrals over $\Delta_{\boldsymbol{ij}}$ and its complex conjugate $\Delta^*_{\boldsymbol{ij}}$.

So far everything is exact. Now, since we are interested in fluctuations of the SC phase around the BCS mean-field solution, one can write the integration variable $\Delta_{\boldsymbol{ij}}$ as $\Delta_{\boldsymbol{ij}} = |\Delta_{\boldsymbol{ij}}|\, e^{i\Phi_{\boldsymbol{ij}}}$ and fix the magnitude of $|\Delta_{\boldsymbol{ij}}|$ at the mean-field saddle-point value. In case of the next-neighbor d-wave interaction, introduced in Sec. 2.1 this means, that one approximates the full interaction in $e^{-\Delta\tau H_V}$ by

$$\frac{1}{N_{\Delta\tau}} \int_0^{2\pi} \prod_{\langle \boldsymbol{ij} \rangle} d\Phi_{\boldsymbol{ij}}(\tau_l)\, e^{-\Delta\tau H_1(\tau_l)}, \tag{2.12}$$

where $H_1(\tau_l)$ is the interaction term defined in Eqs. (2.3) and (2.5) with $\Phi_{\boldsymbol{ij}} \to \Phi_{\boldsymbol{ij}}(\tau_l)$ and $N_{\Delta\tau}$ is a normalization constant. The discrete imaginary time index $\tau_l = l\,\Delta\tau$ has been introduced to emphasize, that this transformation has to be performed at each time step. In the exponent of Eq. (2.12) we have omitted the term $\sim |\Delta_{\boldsymbol{ij}}|^2$, that only contributes, when the magnitude of the gap fluctuates and that has already been used to obtain the magnitude of the BCS mean-field gap.

By introducing the new creation (annihilation) operators $\psi_m^\dagger$ (ψ_m), with

$$\psi_m^\dagger = (\cdots c_{\boldsymbol{i}\uparrow}^\dagger \cdots, \cdots c_{\boldsymbol{j}\downarrow} \cdots), \tag{2.13}$$

one can simplify the notation and define

$$D_l = e^{-\Delta\tau H_0}\, e^{-\Delta\tau H_1(\tau_l)} = e^{-\Delta\tau\, \psi_m^\dagger T_{mn} \psi_n}\, e^{-\Delta\tau\, \psi_m^\dagger V_{mn}(\tau_l) \psi_n} \tag{2.14}$$

and

$$B_l = e^{-\Delta\tau T} e^{-\Delta\tau V(\tau_l)}, \tag{2.15}$$

where T and $V(\tau_l)$ are the matrices defined in Eq. (2.14). After putting everything together, one finally gets

$$Z = \frac{1}{N} \int \mathrm{Tr} \prod_{l=1}^{L} \prod_{\langle \boldsymbol{ij} \rangle} d\Phi_{\boldsymbol{ij}}(\tau_l)\, D_l, \tag{2.16}$$

with $N = L\,N_{\Delta\tau}$. This is the standard auxiliary field quantum Monte Carlo (QMC) problem [47–49]. The trace over fermions can be taken explicitly, since there are only bilinear forms of fermion operators [48, 50, 51]

$$\mathrm{Tr} \prod_{l=1}^{L} D_l = \det[1 + B_L B_{L-1} \cdots B_1] \equiv \det O_{\{\Phi_{\boldsymbol{ij}}(\tau_l)\}} \tag{2.17}$$

and one obtains

$$Z = \frac{1}{N} \int \prod_{l=1}^{L} \prod_{\langle \boldsymbol{ij} \rangle} d\Phi_{\boldsymbol{ij}}(\tau_l)\, \det O_{\{\Phi_{\boldsymbol{ij}}(\tau_l)\}} \equiv \mathrm{Tr}_\Phi \det O_\Phi. \tag{2.18}$$

The trace over the phase field can be calculated with standard MC techniques. The determinant is in general not positive and one has to define

$$P(\Phi) = |\det O_\Phi| \tag{2.19}$$

as Boltzmann weight for the MC simulation. This is the so called "sign problem", which can cause severe problems at low temperatures, where it produces large MC errors that increase the computing time dramatically [52, 53].

The Green's function $\widetilde{G}_{mn}(\tau_1, \tau_2) \equiv G[\Phi]$ for a *fixed* phase-field configuration can be obtained by [48]

$$\widetilde{G}_{mn}(\tau_1, \tau_2) = \langle \psi_m(\tau_{l_1}) \psi_n^\dagger(\tau_{l_2}) \rangle = (B_{l_1} B_{l_1 - 1} \cdots B_{l_2+1} \frac{1}{1 + B_{l_2} \cdots B_1 B_L \cdots B_{l_2+1}})_{mn} \tag{2.20}$$

and the *full* Green's function $G_{mn}(\tau_1, \tau_2)$ by

$$G_{mn}(\tau_1, \tau_2) = \langle\langle \psi_m(\tau_{l_1}) \psi_n^\dagger(\tau_{l_2}) \rangle\rangle = \frac{\mathrm{Tr}_\Phi \, G[\Phi] \, \det O_\Phi}{Z}. \tag{2.21}$$

On the other hand, if we treat the phase as a classical field-variable, things look much simpler. The partition function (Eq. (2.8)) can be written as

$$Z = \mathrm{Tr}_\varphi \, \mathrm{Tr}_F \, e^{-\beta H(\{\varphi_i\})}, \tag{2.22}$$

where Tr_φ and Tr_F are traces over the classical phase degrees of freedom denoted by $\{\varphi_i\}$ and the fermion degrees of freedom, respectively, and $H(\{\varphi_i\})$ is the Hamiltonian defined in section 2.1. The trace over the fermion degrees of freedom is easily calculated by diagonalizing the Hamiltonian matrix for a fixed set of phases $\{\varphi_i\}$

$$\mathrm{Tr}_F \, e^{-\beta H(\{\varphi_i\})} = \prod_{\nu=1}^{N_{\mathrm{dim}}} [1 + e^{-\beta E_\nu(\{\varphi_i\})}], \tag{2.23}$$

where $E_\nu(\{\varphi_i\})$ are the eigenvalues of the Hamiltonian $H(\{\varphi_i\})$ and N_{dim} is the dimension of the single-particle Hilbert space. After this, the problem can be considered as a classical one, in which the partition function is given by

$$Z = \mathrm{Tr}_\varphi \, e^{-S_{\mathrm{eff}}(\{\varphi_i\})}, \tag{2.24}$$

with the effective phase action

$$S_{\mathrm{eff}}(\{\varphi_i\}) = -\sum_{\nu=1}^{N_{dim}} \log[1 + e^{-\beta E_\nu(\{\varphi_i\})}]. \tag{2.25}$$

The trace over the phase is effectively calculated by a MC importance sampling with Boltzmann weight $e^{-S_{\mathrm{eff}}(\{\varphi_i\})}$ for a given configuration of phases $\{\varphi_i\}$. This procedure is less computing time intensive then the determinantal QMC algorithm. Furthermore no sign problem occurs, since the Boltzmann weight is *always* positive, so that one can run the MC simulation, in principle, at arbitrarily low temperatures.

Moreo, Dagotto and others have applied this method successfully to fermions interacting with classical spin degrees of freedom [54–56]. However, the disadvantage is that one neglects the quantum dynamics of the phase-field which is getting more and more important as on reduces the temperature. Therefore, one question naturally arises: can one take into account the quantum dynamics of the phase-field without running into the computing-time intensive sign problem of the determinantal QMC algorithm, an obstacle that could even defeat the whole QMC simulation at low temperatures?

Bickers and Scalapino [57] have proposed a general scheme to construct an effective τ-dependent action for fermions coupling to a Hubbard-Stratonovich field. Their method was first implemented by Monthoux and Scalapino for the Holstein model [58]. There however, they eventually made a static Ising-like approximation for the effective action. In this work, we want to follow the original ideas of Bickers and Scalapino and construct an effective phase action for our BCS-like Hamiltonian which takes the quantum character of the phase into account.

Bickers' and Scalapino's general scheme allows to create the phase configurations much faster, in a less computing-time consuming way, than the methods introduced above. It also allows for a deeper insight into the physics of the phase-fluctuation problem and gives us some control over the sign problem.

We start again with equation (2.16). In an explicit form, it can be written as

$$\begin{aligned} Z &= \frac{1}{N}\int \mathrm{Tr}\prod_{l=1}^{L}\prod_{\langle \boldsymbol{ij}\rangle} d\Phi_{\boldsymbol{ij}}(\tau_l)\, e^{-\Delta\tau H_0}\, e^{-\Delta\tau H_1(\tau_l)} \\ &= \frac{1}{N}\int \mathrm{Tr}\prod_{\langle \boldsymbol{ij}\rangle} d\Phi_{\boldsymbol{ij}}(\tau_L)\cdots\prod_{\langle \boldsymbol{ij}\rangle} d\Phi_{\boldsymbol{ij}}(\tau_1)\; e^{-\Delta\tau H_1(\tau_L)}\, e^{-\Delta\tau H_0}\,\dots\, e^{-\Delta\tau H_1(\tau_1)}\, e^{-\Delta\tau H_0}, \end{aligned} \tag{2.26}$$

where we have formally labeled the indices in the second line such that we start with the largest τ_l from the left. Please note, that we have also interchanged the interacting with the non-interacting part of the Hamiltonian in the exponents of the second line, which is always allowed for $\Delta\tau \to 0$. Now, we introduce a unity operator of the form $e^{-\tau_l H_0}\cdot e^{\tau_l H_0}$ between each time slice $l+1$ and l.

$$\begin{aligned} Z &= \frac{1}{N}\int \mathrm{Tr}\prod_{\langle \boldsymbol{ij}\rangle} d\Phi_{\boldsymbol{ij}}(\tau_L)\cdots\,(e^{-\tau_L H_0}e^{\tau_L H_0})\, e^{-\Delta\tau H_1(\tau_L)}\, e^{-\Delta\tau H_0}\,(e^{-\tau_{L-1}H_0}e^{\tau_{L-1}H_0})\, e^{-\Delta\tau H_1(\tau_{L-1})}\dots \\ &= \frac{1}{N}\int \mathrm{Tr}\prod_{\langle \boldsymbol{ij}\rangle} d\Phi_{\boldsymbol{ij}}(\tau_L)\cdots\, e^{-\tau_L H_0}\,(e^{\tau_L H_0}e^{-\Delta\tau H_1(\tau_L)}e^{-\tau_L H_0})\,(e^{\tau_{L-1}H_0}e^{-\Delta\tau H_1(\tau_{L-1})}e^{-\tau_{L-1}H_0})\cdots \\ &= \frac{1}{N}\int \mathrm{Tr}\, e^{-\beta H_0}\,\mathrm{T}_l[\prod_{l=1}^{L}\prod_{\langle \boldsymbol{ij}\rangle} d\Phi_{\boldsymbol{ij}}(\tau_l)\,(e^{\tau_l H_0}e^{-\Delta\tau H_1(\tau_l)}e^{-\tau_l H_0})], \end{aligned} \tag{2.27}$$

where in the second line we have used that $e^{-\Delta\tau H_0}\, e^{-\tau_{l-1}H_0} = e^{-\tau_l H_0}$ and recalling in the third line that $\tau_L = \beta$. At this point, we are no longer allowed to change the τ_l-order. Therefore, we had to introduce the l-ordering operator T_l in the third line, which should indicate that the product over l inside the brackets $[\cdots]$ starts with the largest l to the left.

Equation (2.27) can now be brought into a more compact form by using the path integral notation

$$Z = \int \prod_{\langle \boldsymbol{ij}\rangle} \mathcal{D}[\Phi_{\boldsymbol{ij}}(\tau)]\,\mathrm{Tr}\{e^{\beta H_0}\,\mathrm{T}_\tau[e^{-\frac{1}{\hbar}\int_0^{\beta\hbar} H_1^I(\tau)\,d\tau}]\}. \tag{2.28}$$

Here, T_τ is the (imaginary) time-ordering operator which puts the operator at the latest time farthest to the left and $H_1^I(\tau)$ is the interaction picture form of $H_1(\tau)$, defined as

$$H_1^I(\tau) = e^{\tau H_0}\, H_1(\tau)\, e^{-\tau H_0}. \tag{2.29}$$

Next we expand $\mathrm{T}_\tau[e^{-\frac{1}{\hbar}\int_0^{\beta\hbar} H_1^I(\tau)\,d\tau}]$ in powers of the coupling g to the phase field. Up to second order we get

$$\begin{aligned}
&\mathbf{1}+\frac{1}{\hbar}\,g\Delta\int_0^{\beta\hbar}d\tau\sum_{\boldsymbol{i}\delta}[\Delta_{\boldsymbol{i}\delta}(\tau)\,e^{i\Phi_{\boldsymbol{i}\delta}(\tau)}+\Delta^\dagger_{\boldsymbol{i}\delta}(\tau)\,e^{-i\Phi_{\boldsymbol{i}\delta}(\tau)}]\\
&+\frac{1}{2\hbar^2}\,g^2\Delta^2\int_0^{\beta\hbar}d\tau_1\int_0^{\beta\hbar}d\tau_2\sum_{\boldsymbol{i}\delta,\boldsymbol{j}\delta'}\mathrm{T}_\tau[(\Delta_{\boldsymbol{i}\delta}(\tau_1)\,e^{i\Phi_{\boldsymbol{i}\delta}(\tau_1)}+\Delta^\dagger_{\boldsymbol{i}\delta}(\tau_1)\,e^{-i\Phi_{\boldsymbol{i}\delta}(\tau_1)})\\
&\qquad\cdot(\Delta_{\boldsymbol{j}\delta'}(\tau_2)\,e^{i\Phi_{\boldsymbol{j}\delta'}(\tau_2)}+\Delta^\dagger_{\boldsymbol{j}\delta'}(\tau_2)\,e^{-i\Phi_{\boldsymbol{j}\delta'}(\tau_2)})]+\mathcal{O}(g^3),
\end{aligned}\tag{2.30}$$

where $\Delta_{\boldsymbol{i}\delta}(\tau)=e^{\tau H_0}\,\Delta_{\boldsymbol{i}\delta}\,e^{-\tau H_0}$. Taking the trace over fermions then yields

$$\begin{aligned}
Z\approx Z_0\int\prod_{\langle\boldsymbol{ij}\rangle}\mathcal{D}[\Phi_{\boldsymbol{ij}}(\tau)]\,\Bigg[&\mathbf{1}+\frac{1}{\hbar}\,g\Delta\int_0^{\beta\hbar}d\tau\sum_{\boldsymbol{i}\delta}(\langle\Delta_{\boldsymbol{i}\delta}(\tau)\rangle_0\,e^{i\Phi_{\boldsymbol{i}\delta}(\tau)}+\langle\Delta^\dagger_{\boldsymbol{i}\delta}(\tau)\rangle_0\,e^{-i\Phi_{\boldsymbol{i}\delta}(\tau)})\\
&+\frac{1}{2\hbar^2}\,g^2\Delta^2\int_0^{\beta\hbar}d\tau_1\int_0^{\beta\hbar}d\tau_2\sum_{\boldsymbol{i}\delta,\boldsymbol{j}\delta'}\\
&\cdot\{\langle\mathrm{T}[\Delta_{\boldsymbol{i}\delta}(\tau_1)\Delta_{\boldsymbol{j}\delta'}(\tau_2)]\rangle_0\,e^{i\Phi_{\boldsymbol{i}\delta}(\tau_1)}\,e^{i\Phi_{\boldsymbol{j}\delta'}(\tau_2)}\\
&+\langle\mathrm{T}[\Delta_{\boldsymbol{i}\delta}(\tau_1)\Delta^\dagger_{\boldsymbol{j}\delta'}(\tau_2)]\rangle_0\,e^{i\Phi_{\boldsymbol{i}\delta}(\tau_1)}\,e^{-i\Phi_{\boldsymbol{j}\delta'}(\tau_2)}\\
&+\langle\mathrm{T}[\Delta^\dagger_{\boldsymbol{i}\delta}(\tau_1)\Delta_{\boldsymbol{j}\delta'}(\tau_2)]\rangle_0\,e^{-i\Phi_{\boldsymbol{i}\delta}(\tau_1)}\,e^{i\Phi_{\boldsymbol{j}\delta'}(\tau_2)}\\
&+\langle\mathrm{T}[\Delta^\dagger_{\boldsymbol{i}\delta}(\tau_1)\Delta^\dagger_{\boldsymbol{j}\delta'}(\tau_2)]\rangle_0\,e^{-i\Phi_{\boldsymbol{i}\delta}(\tau_1)}\,e^{-i\Phi_{\boldsymbol{j}\delta'}(\tau_2)}\}\Bigg],
\end{aligned}\tag{2.31}$$

with the partition function of the free Hamiltonian $Z_0=\mathrm{Tr}\,e^{\beta H_0}$. Here, $\langle\cdots\rangle_0$ indicate normal expectation values and $\langle\mathrm{T}[\cdots]\rangle_0$ expectation values of the time-ordered operator product with respect to the free Hamiltonian H_0.

Next, we want to bring the approximate partition function back into an exponential form by using the following cumulant expansion

$$1+gA+\frac{1}{2}g^2B=e^{\ln(1+gA+\frac{1}{2}g^2B)}\approx e^{gA+\frac{1}{2}g^2B-\frac{1}{2}g^2A^2},\tag{2.32}$$

where we have used in the final step $\ln(1+x)\approx x-\frac{x^2}{2}$ which is correct to $\mathcal{O}(g^3)$. We therefore obtain

$$Z\approx Z_0\int\prod_{\langle\boldsymbol{ij}\rangle}\mathcal{D}[\Phi_{\boldsymbol{ij}}(\tau)]\,e^{-S_{\mathrm{eff}}[\Phi_{\boldsymbol{ij}}(\tau)]}\tag{2.33}$$

with the *effective action*

$$\begin{aligned}
S_{\text{eff}}[\Phi_{\boldsymbol{ij}}(\tau)] = &-\frac{1}{\hbar}\, g\Delta \int_0^{\beta\hbar} d\tau \sum_{\boldsymbol{i}\delta} \left(\langle \Delta_{\boldsymbol{i}\delta}(\tau)\rangle_0 \, e^{i\Phi_{\boldsymbol{i}\delta}(\tau)} + \langle \Delta^{\dagger}_{\boldsymbol{i}\delta}(\tau)\rangle_0 \, e^{-i\Phi_{\boldsymbol{i}\delta}(\tau)}\right) \\
&-\frac{1}{2\hbar^2}\, g^2\Delta^2 \int_0^{\beta\hbar} d\tau_1 \int_0^{\beta\hbar} d\tau_2 \sum_{\boldsymbol{i}\delta,\boldsymbol{j}\delta'} \\
&\qquad \cdot\{\langle \mathrm{T}[\Delta_{\boldsymbol{i}\delta}(\tau_1)\Delta_{\boldsymbol{j}\delta'}(\tau_2)]\rangle_0 \, e^{i\Phi_{\boldsymbol{i}\delta}(\tau_1)}\, e^{i\Phi_{\boldsymbol{j}\delta'}(\tau_2)} \\
&\qquad +\langle \mathrm{T}[\Delta_{\boldsymbol{i}\delta}(\tau_1)\Delta^{\dagger}_{\boldsymbol{j}\delta'}(\tau_2)]\rangle_0 \, e^{i\Phi_{\boldsymbol{i}\delta}(\tau_1)}\, e^{-i\Phi_{\boldsymbol{j}\delta'}(\tau_2)} \\
&\qquad +\langle \mathrm{T}[\Delta^{\dagger}_{\boldsymbol{i}\delta}(\tau_1)\Delta_{\boldsymbol{j}\delta'}(\tau_2)]\rangle_0 \, e^{-i\Phi_{\boldsymbol{i}\delta}(\tau_1)}\, e^{i\Phi_{\boldsymbol{j}\delta'}(\tau_2)} \\
&\qquad +\langle \mathrm{T}[\Delta^{\dagger}_{\boldsymbol{i}\delta}(\tau_1)\Delta^{\dagger}_{\boldsymbol{j}\delta'}(\tau_2)]\rangle_0 \, e^{-i\Phi_{\boldsymbol{i}\delta}(\tau_1)}\, e^{-i\Phi_{\boldsymbol{j}\delta'}(\tau_2)}\} \\
&+\frac{1}{2\hbar^2}\, g^2\Delta^2 \int_0^{\beta\hbar} d\tau_1 \int_0^{\beta\hbar} d\tau_2 \sum_{\boldsymbol{i}\delta,\boldsymbol{j}\delta'} \\
&\qquad \left(\langle \Delta_{\boldsymbol{i}\delta}(\tau_1)\rangle_0 \, e^{i\Phi_{\boldsymbol{i}\delta}(\tau_1)} + \langle \Delta^{\dagger}_{\boldsymbol{i}\delta}(\tau_1)\rangle_0 \, e^{-i\Phi_{\boldsymbol{i}\delta}(\tau_1)}\right) \\
&\qquad \cdot\left(\langle \Delta_{\boldsymbol{j}\delta'}(\tau_2)\rangle_0 \, e^{i\Phi_{\boldsymbol{j}\delta'}(\tau_2)} + \langle \Delta^{\dagger}_{\boldsymbol{j}\delta'}(\tau_2)\rangle_0 \, e^{-i\Phi_{\boldsymbol{j}\delta'}(\tau_2)}\right).
\end{aligned} \tag{2.34}$$

At this point one can see that the additional third term, which is a result of the cumulant expansion, exactly cancels the *disconnected* contributions from the second term. Therefore one can write

$$\begin{aligned}
S_{\text{eff}}[\Phi_{\boldsymbol{ij}}(\tau)] = &-\frac{1}{\hbar}\, g\Delta \int_0^{\beta\hbar} d\tau \sum_{\boldsymbol{i}\delta} \left(\langle \Delta_{\boldsymbol{i}\delta}(\tau)\rangle_0 \, e^{i\Phi_{\boldsymbol{i}\delta}(\tau)} + \langle \Delta^{\dagger}_{\boldsymbol{i}\delta}(\tau)\rangle_0 \, e^{-i\Phi_{\boldsymbol{i}\delta}(\tau)}\right) \\
&-\frac{1}{2\hbar^2}\, g^2\Delta^2 \int_0^{\beta\hbar} d\tau_1 \int_0^{\beta\hbar} d\tau_2 \sum_{\boldsymbol{i}\delta,\boldsymbol{j}\delta'} \\
&\qquad \cdot\{\langle \mathrm{T}[\Delta_{\boldsymbol{i}\delta}(\tau_1)\Delta_{\boldsymbol{j}\delta'}(\tau_2)]\rangle_0^{\text{conn}} \, e^{i\Phi_{\boldsymbol{i}\delta}(\tau_1)}\, e^{i\Phi_{\boldsymbol{j}\delta'}(\tau_2)} \\
&\qquad +\langle \mathrm{T}[\Delta_{\boldsymbol{i}\delta}(\tau_1)\Delta^{\dagger}_{\boldsymbol{j}\delta'}(\tau_2)]\rangle_0^{\text{conn}} \, e^{i\Phi_{\boldsymbol{i}\delta}(\tau_1)}\, e^{-i\Phi_{\boldsymbol{j}\delta'}(\tau_2)} \\
&\qquad +\langle \mathrm{T}[\Delta^{\dagger}_{\boldsymbol{i}\delta}(\tau_1)\Delta_{\boldsymbol{j}\delta'}(\tau_2)]\rangle_0^{\text{conn}} \, e^{-i\Phi_{\boldsymbol{i}\delta}(\tau_1)}\, e^{i\Phi_{\boldsymbol{j}\delta'}(\tau_2)} \\
&\qquad +\langle \mathrm{T}[\Delta^{\dagger}_{\boldsymbol{i}\delta}(\tau_1)\Delta^{\dagger}_{\boldsymbol{j}\delta'}(\tau_2)]\rangle_0^{\text{conn}} \, e^{-i\Phi_{\boldsymbol{i}\delta}(\tau_1)}\, e^{-i\Phi_{\boldsymbol{j}\delta'}(\tau_2)}\},
\end{aligned} \tag{2.35}$$

where $\langle\cdots\rangle_0^{\text{conn}}$ means, that only diagrams connecting $\boldsymbol{i}$ with $\boldsymbol{j}$ and τ_1 with τ_2 contribute to the effective action if one uses Wick's theorem to write the expectation value of the time ordered product in terms of Green's functions. This is the so-called linked cluster theorem [46, 59].

By introducing the two-component field operator

$$\widehat{\Psi}(\boldsymbol{i},\tau) \equiv \begin{bmatrix} c_{\boldsymbol{i}\uparrow}(\tau) \\ c^{\dagger}_{\boldsymbol{i}\downarrow}(\tau) \end{bmatrix} \tag{2.36}$$

one can define the 2 × 2 superconducting (Nambu) Green's function matrix

$$\begin{aligned}
\mathbf{G}(\boldsymbol{i},\tau;\boldsymbol{i}',\tau') &= -\langle \mathrm{T}_{\tau}[\widehat{\Psi}(\boldsymbol{i},\tau)\,\widehat{\Psi}^{\dagger}(\boldsymbol{i}',\tau')]\rangle \\
&= \begin{bmatrix} G(\boldsymbol{i},\tau;\boldsymbol{i}',\tau') & F(\boldsymbol{i},\tau;\boldsymbol{i}',\tau') \\ F^{\dagger}(\boldsymbol{i},\tau;\boldsymbol{i}',\tau') & \widetilde{G}(\boldsymbol{i},\tau;\boldsymbol{i}',\tau') \end{bmatrix}
\end{aligned} \tag{2.37}$$

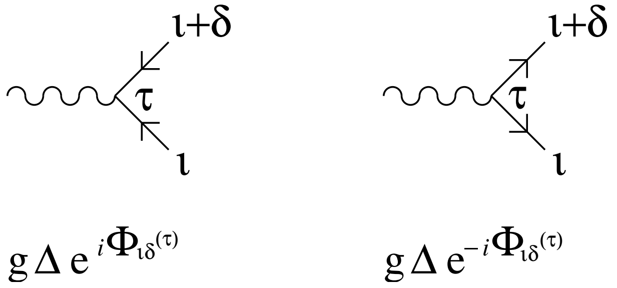

Figure 2.1: Elementary vertices of the cumulant expansion for S_{eff}.

with

$$\begin{aligned}
G(\boldsymbol{i},\tau;\boldsymbol{i}',\tau') &= -\langle \mathrm{T}_\tau[c_{\boldsymbol{i}\uparrow}(\tau)\, c^\dagger_{\boldsymbol{i}'\uparrow}(\tau')]\rangle \\
F(\boldsymbol{i},\tau;\boldsymbol{i}',\tau') &= -\langle \mathrm{T}_\tau[c_{\boldsymbol{i}\uparrow}(\tau)\, c_{\boldsymbol{i}'\downarrow}(\tau')]\rangle \\
F^\dagger(\boldsymbol{i},\tau;\boldsymbol{i}',\tau') &= -\langle \mathrm{T}_\tau[c^\dagger_{\boldsymbol{i}\downarrow}(\tau)\, c^\dagger_{\boldsymbol{i}'\uparrow}(\tau')]\rangle \\
\widetilde{G}(\boldsymbol{i},\tau;\boldsymbol{i}',\tau') &= -\langle \mathrm{T}_\tau[c^\dagger_{\boldsymbol{i}\downarrow}(\tau)\, c_{\boldsymbol{i}'\downarrow}(\tau')]\rangle
\end{aligned} \tag{2.38}$$

and we finally obtain the effective action in terms of Green's functions

$$\begin{aligned}
S_{\text{eff}}[\Phi_{\boldsymbol{ij}}(\tau)] = &-\frac{1}{\hbar}g\Delta\int_0^{\beta\hbar}d\tau\sum_{\boldsymbol{i}\delta}\sqrt{2}(F_0(\boldsymbol{i},\tau;\boldsymbol{i}+\delta,\tau)\,e^{i\Phi_{\boldsymbol{i}\delta}(\tau)}+F_0^\dagger(\boldsymbol{i},\tau;\boldsymbol{i}+\delta,\tau)\,e^{-i\Phi_{\boldsymbol{i}\delta}(\tau)}) \\
&-\frac{1}{2\hbar^2}g^2\Delta^2\int_0^{\beta\hbar}d\tau_1\int_0^{\beta\hbar}d\tau_2\sum_{\boldsymbol{i}\delta,\boldsymbol{j}\delta'} \\
&\quad\cdot\{-[F_0(\boldsymbol{i},\tau_1;\boldsymbol{j},\tau_2)\,F_0(\boldsymbol{i}+\delta,\tau_1;\boldsymbol{j}+\delta',\tau_2) \\
&\qquad+F_0(\boldsymbol{i},\tau_1;\boldsymbol{j}+\delta',\tau_2)\,F_0(\boldsymbol{i}+\delta,\tau_1;\boldsymbol{j},\tau_2)]\,e^{i\Phi_{\boldsymbol{i}\delta}(\tau_1)}\,e^{i\Phi_{\boldsymbol{j}\delta'}(\tau_2)} \\
&\quad+[G_0(\boldsymbol{i},\tau_1;\boldsymbol{j},\tau_2)\,G_0(\boldsymbol{i}+\delta,\tau_1;\boldsymbol{j}+\delta',\tau_2) \\
&\qquad+G_0(\boldsymbol{i},\tau_1;\boldsymbol{j}+\delta',\tau_2)\,G_0(\boldsymbol{i}+\delta,\tau_1;\boldsymbol{j},\tau_2)]\,e^{i\Phi_{\boldsymbol{i}\delta}(\tau_1)}\,e^{-i\Phi_{\boldsymbol{j}\delta'}(\tau_2)} \\
&\quad+[G_0(\boldsymbol{j},\tau_2;\boldsymbol{i},\tau_1)\,G_0(\boldsymbol{j}+\delta',\tau_2;\boldsymbol{i}+\delta,\tau_1) \\
&\qquad+G_0(\boldsymbol{j},\tau_2;\boldsymbol{i}+\delta,\tau_1)\,G_0(\boldsymbol{j}+\delta',\tau_2;\boldsymbol{i},\tau_1)]\,e^{-i\Phi_{\boldsymbol{i}\delta}(\tau_1)}\,e^{i\Phi_{\boldsymbol{j}\delta'}(\tau_2)} \\
&\quad-[F_0^\dagger(\boldsymbol{i},\tau_1;\boldsymbol{j},\tau_2)\,F_0^\dagger(\boldsymbol{i}+\delta,\tau_1;\boldsymbol{j}+\delta',\tau_2) \\
&\qquad+F_0^\dagger(\boldsymbol{i},\tau_1;\boldsymbol{j}+\delta',\tau_2)\,F_0^\dagger(\boldsymbol{i}+\delta,\tau_1;\boldsymbol{j},\tau_2)]\,e^{-i\Phi_{\boldsymbol{i}\delta}(\tau_1)}\,e^{-i\Phi_{\boldsymbol{j}\delta'}(\tau_2)}\}.
\end{aligned} \tag{2.39}$$

Fig. 2.1 shows the elementary vertices of this cumulant expansion and Fig. 2.2 the diagrams for the second order contribution to S_{eff}. All Green's functions appearing in Eq. (2.39) are free Green's functions. However, one can improve the approximation, as in the usual perturbation theory, by using Hartree-Fock Green's functions or starting directly from the symmetry broken BCS state. Which starting point (Green's function) one chooses depends on the physics of the problem. If one wants to consider small deviations from the BCS solution that are caused by phase fluctuations at low temperatures then one uses BCS-Nambu Green's functions

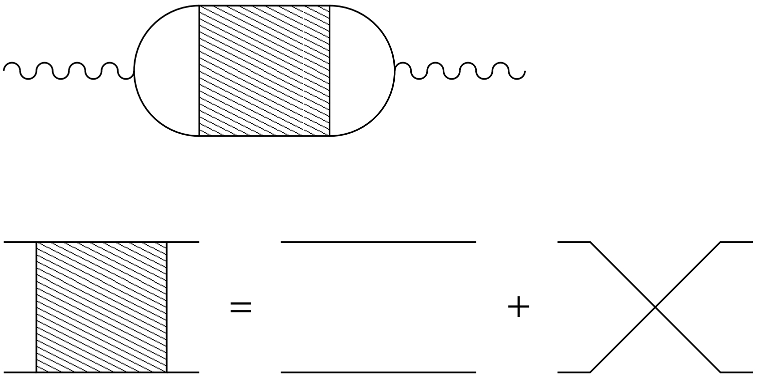

Figure 2.2: Diagrammatic representation of the second-order contribution to S_{eff}. This term contains the dynamic coupling of the quasi-particles to phase fluctuations. The wavy lines represent phase fluctuations and the straight lines stand for all allowed combinations of Nambu-Green's functions.

in Eq. (2.39). On the other hand, if one wants to study the onset of phase coherence at high temperatures caused by superconducting phase fluctuations then one rather uses free Green's functions.

It is very instructive to consider Eq. (2.39) term by term and discuss the contributions of the different terms depending on which Ansatz for the Green's functions one chooses. We start with the first term containing only single anomalous Green's functions. For free Green's functions this term identically disappears. For BCS-Green's functions one can show by using the cyclic property of the trace, that the fermionic contribution is static. Moreover, one can show that this term is real and couples to the phase field in the form $\sim \cos(\Phi_{\boldsymbol{i}\delta}(\tau))$. This is the simplest term invariant under the transformation $\Phi_{\boldsymbol{i}\delta}(\tau) \longrightarrow \Phi_{\boldsymbol{i}\delta}(\tau) + 2\pi$, however, it breaks gauge symmetry. This is an artefact of simple BCS-theory which always chooses one fixed phase and therefore one obtains a term that tries to push the phase back into the BCS gauge-symmetry-broken state. Also for the most general anomalous Green's function this term is real, and the fermionic contribution static, as in the well-known Hartree tadpole-diagram.

Next, we consider the term containing the product of two anomalous Green's functions. This term obviously also disappears if one uses only free Green's functions in the effective action. If one, however, uses anomalous Green's functions and if they are symmetric under the interchange of coordinates $\boldsymbol{i} \leftrightarrow \boldsymbol{j}$, which for a translational invariant system means symmetric under space-inversion, then one can show that this term is real by using again the cyclic property of the trace. Furthermore, in the BCS-case it is proportional to $\cos(\Phi_{\boldsymbol{i}\delta}(\tau_1) + \Phi_{\boldsymbol{j}\delta'}(\tau_2))$. Thus, this term is a higher harmonic contribution to the BCS gauge-symmetry-breaking term $\sim \cos(\Phi_{\boldsymbol{i}\delta}(\tau))$.

Finally, we come to the term containing two normal Green's functions. This is the most interesting term since it also contributes in the case of free Green's functions and in addition it is gauge invariant in all cases. However, it is only real if the system is particle-hole symmetric and if the normal Green's functions are symmetric under the interchange of coordinates $\boldsymbol{i} \leftrightarrow \boldsymbol{j}$, which again implies space-inversion symmetry for a translational invariant system. In fact, particle-hole symmetry is sufficient to show that the phases couple in an XY-like form $\sim \cos(\Phi_{\boldsymbol{i}\delta}(\tau_1) -$

$\Phi_{\boldsymbol{j}\delta'}(\tau_2))$ to the fermions.

The inclusion of a magnetic field produces additional phase factors that change the explicit form of this term. In the following, we want to give an approximate analytical expression for this case. To simplify the notation, we only consider on-site s-wave pairing, i. e. we neglect for the moment the δ's in the effective action. We also assume that the phases are static objects, that can be treated by a classical ensemble average, i. e. $\Phi_{\boldsymbol{i}}(\tau) = \Phi_{\boldsymbol{i}}$.

To get an idea of the effect of a static magnetic field on the effective phase action it is useful to recall that the Green's function $G(\boldsymbol{i},\tau_1;\boldsymbol{j},\tau_2)$ can be interpreted as the propagator of a system that contains an additional particle. This additional particle is created at position $\boldsymbol{j}$ at time τ_2 and then propagates to position $\boldsymbol{i}$ at time $\tau_1 > \tau_2$. If we treat the trajectory *quasi-classical,* taking only the direct path into account and neglect all other effects of the magnetic field on the many-particle state then the electron propagator acquires a phase factor $\sim e^{2\pi i \frac{e}{hc}\int_{\boldsymbol{j}}^{\boldsymbol{i}} \boldsymbol{A}(\boldsymbol{l})\, d\boldsymbol{l}}$, where e is the electron charge and $\boldsymbol{A}(\boldsymbol{l})$ the vector potential. Therefore, one could write the Green's function in the presence of a static magnetic field $G^A(\boldsymbol{i},\tau_1;\boldsymbol{j},\tau_2)$ in terms of the Green's function without magnetic field approximately as[1]

$$G^A(\boldsymbol{i},\tau_1;\boldsymbol{j},\tau_2) \approx e^{2\pi i \frac{e}{hc}\int_{\boldsymbol{j}}^{\boldsymbol{i}} \boldsymbol{A}(\boldsymbol{l})\, d\boldsymbol{l}} G(\boldsymbol{i},\tau_1;\boldsymbol{j},\tau_2). \tag{2.40}$$

Using this expression in Eq. (2.39), we can shift the magnetic field dependence of the effective action from the Green's functions to the cosine factor and finally obtain

$$S_{\text{eff}} \approx -\beta \sum_{\boldsymbol{ij}} \tilde{J}_{\boldsymbol{ij}} \cos\left(\Phi_{\boldsymbol{i}} - \Phi_{\boldsymbol{j}} + 2\pi \frac{2e}{hc} \int_{\boldsymbol{j}}^{\boldsymbol{i}} \boldsymbol{A}(\boldsymbol{l})\, d\boldsymbol{l}\right), \tag{2.41}$$

where $\tilde{J}_{\boldsymbol{ij}}$ is a short hand notation for the prefactor in Eq. (2.39). This prefactor is no longer τ-dependent if we assume the phases to be classical static variables. Please note that we get a factor of $\frac{hc}{2e}$ for the flux quantum in the cosine instead of a factor $\frac{hc}{e}$ in the Green's functions. This is due to the fact that we have a product of Green's functions in the effective action and exactly corresponds to the phase acquired by a Cooper-pair of charge $2e$ moving in a magnetic field from position $\boldsymbol{j}$ to $\boldsymbol{i}$.

In the preceding discussion, we made the "ad hoc" assumption, that the phases are static objects, in order to obtain a simple expression for the phase action in the presence of a magnetic field (Eq. (2.41)). Any dynamic phase fluctuations will surely increase the total energy of the system. Therefore, in order to take the time-dependence of the effective action (Eq. (2.39)) to a first approximation into account, one can make a Gaussian approximation and add a term $\sim (\dot{\Phi}_{\boldsymbol{i}}(\tau))^2$ to Eq. (2.41) and write

$$S_{\text{eff}} \approx \frac{1}{\hbar}\int_0^{\beta\hbar} d\tau \left[\widetilde{C}\sum_{\boldsymbol{i}} (\dot{\Phi}_{\boldsymbol{i}}(\tau))^2 - \sum_{\boldsymbol{ij}} \tilde{J}_{\boldsymbol{ij}} \cos\left(\Phi_{\boldsymbol{i}}(\tau) - \Phi_{\boldsymbol{j}}(\tau) + 2\pi \frac{2e}{hc} \int_{\boldsymbol{j}}^{\boldsymbol{i}} \boldsymbol{A}(\boldsymbol{l})\, d\boldsymbol{l}\right)\right]. \tag{2.42}$$

The parameter $\widetilde{C}$ can, in principle, be obtained from Eq. (2.39) and controls the strength of the dynamic fluctuations. This is just a very rough picture which should sketch the physics included

---

[1] Please note that in a realistic calculation one has to take into account all paths, exchange terms, and also the effects of the magnetic field on the many-particle wave-function like the breaking of translational invariance. Hence, this is at best a heuristic way to motivate the physics included in this term.

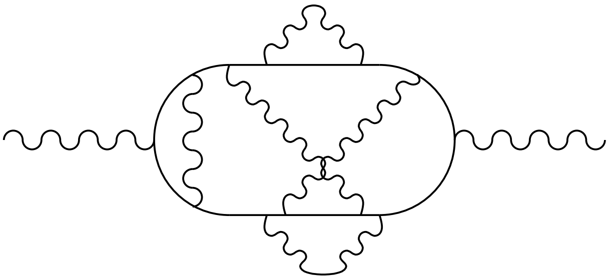

Figure 2.3: A typical diagram showing vertex corrections for the effective phase action S_{eff} which can be obtained by calculating S_{eff} selfconsistently.

in Eq. (2.39). In general the microscopic phase action (Eq. (2.39)) is not only non-local in space but also non-local in imaginary time. The interesting thing is that also for a pure local on-site s-wave interaction in the original Hamiltonian we obtain a longe-range phase interaction in the effective action. Exactly the same happens if one derives an effective Hamiltonian by integrating out the short-range and high-energy degrees of freedom in a renormalization group study.

We have seen above that whether a sign problem occurs or not depends on the underlying symmetries of the system (Green's functions) and can differ from term to term. The advantage of the procedure introduced above lies in the fact that one obtains some control over the sign problem. One can check for each term in the effective action if it causes a sign problem and make appropriate approximations, if necessary, since one knows the physical meaning of each term. Furthermore the dynamical phase configurations are created much faster than with the determinantal expression (Eq. (2.17)) and the explicit analytical form also allows for other techniques [60] to circumvent the sign problem.

Up to now we have only discussed different possible choices for the Green's functions in the effective action S_{eff}. We also have the possibility to improve the approximation by calculating S_{eff} selfconsistently. That means, we start with a certain choice for the Green's functions in S_{eff}. In an intermediate step we calculate the pair correlation functions occurring in S_{eff} directly in the Monte Carlo simulation. Then these correlation functions can be used to construct the new phase action. The scheme can now be repeated an arbitrary number of times, until convergence. This selfconsistency procedure introduces vertex corrections and a typical diagram containing these vertex corrections is shown in Fig. 2.3. Finally, we want to mention that in the following calculations we only use the gauge invariant term $\sim \cos(\Phi_{\boldsymbol{i}} - \Phi_{\boldsymbol{j}})$. This is motivated by the fact that we are interested in the pseudogap regime above T_c and also by the fact that we perform our calculations on a finite lattice where no spontaneous symmetry-breaking is possible. Therefore, all our results are gauge invariant.

So far, we have used a *microscopic* description of the phase action in terms of pair-correlation functions. In the next section, we discuss how a *coarse-grained* phase action on the scale of the superconducting coherence length ξ_0 can be derived. This action has the form of a quantum XY model and contains only the superfluid density (or phase stiffness D_s) of the Cooper-pairs.

2.2.2 Coarse-grained phase-only action

The general idea for deriving a coarse-grained phase-only action is motivated by the assumption that all phase fluctuations on the scale $l < \xi_0$ represent internal degrees of freedom of the Cooper-pair. Thus, they can be considered as high-energy degrees of freedom which can effectively be integrated out, exactly like the fluctuations of the magnitude of the local pairing gap Δ, as long as we are not too close to T_c^{MF}. In the end one obtains a quantum XY action, which is defined on the length scale of the superconducting coherence length ξ_0 and which contains only two parameters: one that controls the strength of the Coulomb interaction between Cooper pairs and the other determining the phase stiffness D_s.

In general, there exists no exact mapping between the microscopic phase action and the coarse-grained quantum XY action. Only for the case of an attractive Hubbard model at $T = 0$ and for $\frac{t}{|U|} \ll 1$ this mapping is consistently possible [61]. However, in addition, one needs the characteristic time over which the phases fluctuate to be much larger than the inverse quasi-particle gap in order to get a cosine term that is local in time. In the following, we want to briefly outline the derivation of the coarse-grained phase-only action and discuss some important points, especially those that are relevant for d-wave superconductors. For more details we refer to [62] and [63] for the d-wave case and [61] for the s-wave case.

The first problem specific to a d-wave superconductor is that the SC gap has nodes with zero excitation energy. Therefore already the assumption that we have a fixed magnitude of the local pairing field is not obvious. In fact it was shown [62] that the spectral weight for fluctuations of the amplitude of the local pairing field is not gaped for a d-wave superconductor but rather exhibits a power law down to zero energy. However, the spectral weight associated with these fluctuations is very small and negligible at small temperatures $T \ll T_c^{MF}$. Note, that we are talking about thermal fluctuations of the gap parameter Δ and not excitations of nodal quasi-particles which are important and taken into account in our Hamiltonian (Sec. 2.1).

The second problem is that the d-wave order parameter is defined on the bonds of the 2D lattice. Thus we have two degrees of freedom for the phase at each lattice site. One is associated with the internal symmetry of the Cooper-pair and thus describes fluctuations from the d-wave to the extended s-wave symmetry. This phase mode shows a power law spectral weight like the amplitude fluctuations and is also less important than quasi-particles at low temperatures $T \ll T_c^{MF}$ [62]. The other mode is the usual *center of mass* Goldstone-mode that couples to the vector-potential. By fixing the internal phase mode at the d-wave saddle point, one can write the bond phase $\Phi_{\boldsymbol{i}\delta}$ in terms of the *center of mass* phase $\varphi_{\boldsymbol{i}}$ as in Eq. (2.6)

$$\Phi_{\boldsymbol{i}\delta} = \begin{cases} (\varphi_{\boldsymbol{i}} + \varphi_{\boldsymbol{i}+\delta})/2 & \text{for} \quad \delta \text{ in } x\text{-direction} \\ (\varphi_{\boldsymbol{i}} + \varphi_{\boldsymbol{i}+\delta})/2 + \pi & \text{for} \quad \delta \text{ in } y\text{-direction.} \end{cases}$$

In going to the *center of mass* phase description one looses the invariance of the phase action under the transformation $\varphi_{\boldsymbol{i}} \rightarrow \varphi_{\boldsymbol{i}} + 2\pi$ in the coupling of the phase to the Hamiltonian. This causes no problem if the phase difference between neighboring sites is small $\Delta\varphi \ll 2\pi$ and the worst thing that could happen is a vortex singularity in the middle of a square plaquette. However, also in this case the phase difference between neighboring sites is only $\Delta\varphi = \frac{\pi}{2}$ and by defining all phases modulo 2π this causes no serious problem in terms of the bond phase variables.

Coarse-grained phase-only action with Coulomb interaction

Up to now, we have completely neglected the Coulomb interaction between the electrons or Cooper pairs in our effective lattice Hamiltonian. For the phase action, this means that we describe a neutral superfluid. Now, the question, whether the phase fluctuations in superconductors (charged superfluids) are of quantum nature (dynamic) or whether they can be treated classically (static), depends on the strength of the screened Coulomb interaction between the Cooper pairs. Hence, in order to discuss this topic, one needs to add

$$H_{\text{coulomb}} = \frac{1}{2N} \sum_{\boldsymbol{q}} V_{\boldsymbol{q}} \, \rho_{\boldsymbol{q}} \, \rho_{-\boldsymbol{q}} \tag{2.43}$$

to the pairing Hamiltonian, where $V_{\boldsymbol{q}}$ is the Fourier transformed Coulomb interaction for a anisotropic layered system [62] and $\rho_{\boldsymbol{q}}$ is the Fourier transformed electron density operator.

The derivation of the coarse-grained phase action now proceeds as follows [61, 62]: first one performs the usual Hubbard-Stratonovich transformation in the pairing-channel, then one makes a gauge transformation that shifts the phase-dependence from the pairing-amplitude to the fermionic variables. As a result of this gauge transformation, the pairing interaction contains no more phase variables. Finally, by considering only slow spatial fluctuations of the phase (small $\boldsymbol{q}$ expansion of the kinetic energy term with respect to phase gradients), one obtains an effective microscopic Gaussian phase-action after integrating out the fermions.

On the other hand, one can write down the most general quantum XY action on a coarse grained lattice with lattice parameter ξ_0 that is invariant under the transformation $\varphi_{\boldsymbol{i}} \to \varphi_{\boldsymbol{i}} + 2\pi$. Due to the cosine term in the quantum XY action there are no constraints on the spatial gradient of the phase which is important to get vortices on the scale ξ_0. In order to compare the coefficients of the quantum XY action with those of the microscopic Gaussian phase action, one has to go to the limit of small spatial variations on the scale ξ_0. In this way, one arrives at the effective quantum XY action in the form [62]

$$S_{\text{eff}} = \frac{1}{8T} \sum_{\boldsymbol{Q},\omega_n}{}' \frac{\omega_n^2 \xi_0^2 d_c}{V(\boldsymbol{Q})} \varphi(\boldsymbol{Q}, \omega_n) \varphi(-\boldsymbol{Q}, -\omega_n) + \frac{D_s^0 d_c}{4} \int_0^{\frac{1}{T}} d\tau \sum_{\langle \boldsymbol{R}, \boldsymbol{R}' \rangle} \{1 - \cos[\varphi(\boldsymbol{R}, \tau) - \varphi(\boldsymbol{R}', \tau)]\}, \tag{2.44}$$

where $V(\boldsymbol{Q})$ is the Fourier transform of the two-dimensional (2D) Coulomb interaction, D_s^0 the bare in-plane phase stiffness and d_c the distance between two 2D planes. Note that the interplane distance d_c appears in Eq. (2.44), since it describes a three-dimensional system of layered 2D planes. The prime in the sum denotes a cut-off in the Matsubara sum over ω_n analogous to the momentum cut-off.

In principle, in a d-wave superconductor already the bare phase stiffness D_s^0 shows a temperature dependence due to the presence of nodal quasi-particles and therefore cannot be taken as constant in more sophisticated calculations at higher temperatures. We stress again that no direct derivation of the XY action is possible as a result of the small gradient expansion needed to obtain the microscopic Gaussian phase action. It is however a well known fact that one needs to replace the quadratic term in the Gaussian phase action by a cosine term, in order to impose the 2π periodicity of the phase action. This 2π periodicity is required to get vortices, which are essential for the Kosterlitz-Thouless transition at higher temperatures (see Sec. 2.4.2).

It is important to note that the momentum cut-off is implicitly taken into account in going to the coarse-grained lattice. This should be stressed by using $\boldsymbol{R}$ and $\boldsymbol{Q}$ in Eq. (2.44) to denote position and momentum in order to indicate that all phase variables and spatial fluctuations are defined on a scale ξ_0. Therefore, the small phase gradient used in the derivation of the Gaussian phase action causes no problem since Eq. (2.44) automatically fulfills the condition $\boldsymbol{Q} < \frac{\pi}{\xi_0}$. Thus, there is no need for any constraint on the phase-difference between neighboring $\boldsymbol{R}$-sites.

For an on-site s-wave superconductor the effective phase action can be derived in an alternative way, without the need to make the approximation of small phase-gradients to obtain an effective XY phase action [61]. This is done by means of a strong-coupling expansion in $\frac{t}{U}$. This strong-coupling expansion is only possible for on-site s-wave pairing, since $\xi_0 \to 0$ for $U \to \infty$. Hence, the Cooper pairs become *highly* localized at a *single* lattice site, whereas for next-neighbor d-wave pairing, the Cooper pair size has always a lower bound, which is given by the lattice spacing a. In any case one has to assume that the time scale of phase fluctuations is larger than the characteristic time scale of quasi-particle processes to finally obtain an expression that is local in time.

The above-described procedure of first performing a gauge transformation to shift the phase-dependence from the interaction to the kinetic energy part of the Hamiltonian and then expanding in small gradients of the phase is necessary in order to derive a coarse-grained phase action that is local in space, i. e. contains only next-nearest-neighbor couplings. Without this procedure one obtains also further distant coupling terms, as can be seen in our cumulant expansion for the effective *microscopic* phase action in Sec. 2.2.1, where we made an expansion in powers of the coupling g, *without* any restriction on the spatial behavior of the phase.

In order to take into account dissipation effects, which are not included in the BCS-like approach and which arise from the experimentally observed unexpected large low-frequency conductivity of the high-T_c cuprates below T_c [63], one can add an additional term linear in the time-derivative and proportional to the conductivity σ to the effective phase action [64].[2] This additional quasi-particle damping-term can reduce the crossover temperature between quantum and thermal fluctuations of the phase drastically [63]. Finally we want to mention that for a neutral superfluid one simply has to replace the Coulomb interaction $\frac{1}{V(\boldsymbol{Q})}$ in Eq. (2.44) by the density-density correlation function [62].

2.3 Self-consistent vs. non-self-consistent phase-action

The effective phase-only action in Sec. 2.2.2 was derived for low temperatures ($T \ll T_c^{MF}$) where *center of mass* phase fluctuations and nodal quasi-particles dominate the physics. Thus, the phase-only action is an effective theory for a minimal description of the low energy properties of a superconductor that only takes into account the leading momentum and frequency dependencies. The long-wavelength phase fluctuations correspond to the kinetic energy of the superfluid at low temperatures and are spin-wave-like excitations which vary slowly in space and time. At higher temperatures the couplings of the effective phase-only action renormalize and additional fluctuation channels open. In case of our BCS-like model these are — besides vortex excitations of the phase field — amplitude fluctuations of the pairing-field and *internal* phase fluctuations of the Cooper-pairs. In more general models charge and spin fluctuations start to play an important role.

---

[2] A heuristic way to see that the dissipation is proportional to the conductivity σ is by realizing that the dissipative power of an electrical current I across a potential difference U is given by $P = UI$, which can be either written as $P = I^2/\sigma$ or $P = \sigma U^2$, where the last equation corresponds to our case, since the time derivative of the phase in the XY action corresponds to the electrostatic energy, whereas the spatial gradient of the phase corresponds to the supercurrent.

Within the phase-fluctuation scenario one however assumes that the phase-only action also holds for finite temperatures even above the phase ordering temperature T_φ and up to T_c^{MF}. For this to hold true one needs the vortex energy to be very cheap, so that phase fluctuations remain the dominating fluctuation channel of the system. In the XY phase action, the vortex energy is of the order T_φ. This is contrary to the well-known BCS mean-field theory, where the vortex energy is of the order T_c^{MF} [7]. If we would perform a self-consistent calculation within the BCS-like model introduced in Sec. 2.1 for a fixed size of the superconducting gap,[3] then the phase fluctuations would immediately freeze out due to the large phase stiffness of the BCS-like model, unless for very high temperatures close to T_c^{MF}, or for a very small electron density. For phase fluctuations to become important over a large temperature region, one needs the phase stiffness and vortex energy to become very small. In the BCS-like model of Sec. 2.1 this can only be done by going to very small fillings (electron numbers) or very high temperatures. However, then also amplitude fluctuations become very cheap due to the small gap size and we obtain strong phase *and* amplitude fluctuations.[4]

Therefore, additional ingredients are needed which are not included in the BCS-like approach. Nevertheless, the BCS viewpoint is useful in order to derive an effective phase action and its dependency on the electronic properties of the many-particle system. Then, however, one needs to include information about the Mott insulating state and strong electron correlations by hand. Since it was found in many experiments that the low-lying excitations of the superconducting state of the cuprates are perfectly BCS-like, i. e. can be described by Bogoliubov quasiparticles, this indicates that strong electron correlations may change the coefficients (energy scales) but *not* the qualitative form of the phase action. Therefore, we can still work with the BCS phase action and only have to adjust the parameters to the underdoped cuprates. However, we always have to keep in mind that the phase-fluctuation scenario of the underdoped cuprates cannot be understood in terms of a simple BCS-like theory since the vortex core energy must be small compared to the BCS case. It also cannot be understood in terms of the condensation of real-space Cooper-pairs as in BEC models, since tightly bound real-space pairs cannot originate from pure repulsive interactions. For example, if we consider Hubbard-like models as an appropriate starting point for the high-energy description of the cuprates, then electrons would avoid to come too close together, due to the Hubbard U repulsion. Hence, no tightly bound pairs can form.

---

[3] Selfconsistent means, that by fixing the size of the superconducting gap, we automatically also fix the superfluid density, i. e. the phase stiffness is no longer treated as an independent parameter of the model.

[4] One could consider a limit, where the electron density goes to zero and at the same time the pairing strength becomes infinite, but this exactly yields to the BEC scenario of tightly bound pairs, which was discussed in Cap. 1.

Up to now, it is still not clear, whether a small phase stiffness necessarily implies a small vortex core energy or if these two quantities are independently tuneable. In all known cases the small vortex core energy directly follows from the small phase stiffness [65]. The mechanisms leading to the small vortex core energy are, however, quite different and there is still a large discussion going on as to which of them could be realized in the cuprates. Proposals range from the more conventional picture of a granular superconductor, where the vortices arrange themselves to live in the normal conducting (metallic) or insulating regions between the SC grains, up to the proposal of a competing order that exists inside the magnetic vortex cores. This competing order, which could be some antiferromagnetic (AF) fluctuations or a d-density wave (DDW) order parameter, is supposed to be nearly degenerate with the superconducting state. As soon as the superconducting order parameter is suppressed inside the magnetic vortex core, the system develops the competing order instead of going into a normal conducting paramagnetic state and thus has a much smaller vortex energy compared to a conventional BCS superconductor. Recently, it was shown [66], that vortices with staggered-flux core can provide a way to understand the low vortex energy over a wide temperature range above T_c.

As a matter of fact, neutron scattering, nuclear magnetic resonance (NMR) and muon spin rotation (μSR) measurements show an enhancement of AF correlations and the presence of local antiferromagnetism in the vortex core region of different optimally and underdoped cuprates in an applied magnetic field [67–71]. Furthermore, scanning tunneling microscopy (STM) revealed a “checkerboard pattern”-like modulation of the local density of states around vortices in Bi2212 [72]. On the theoretical side, the negative U Hubbard model near half-filling also shows a pseudogap regime above T_c [36] for weak to intermediate coupling strengths. There, the competing order to the s-wave superconductivity is a charge density wave (CDW) [73, 74]. This CDW suppresses on the one hand the superfluid density as one approaches half-filling but produces on the other hand cheap vortices due to its presence inside the cores[5]. The scenario of cheap vortices is analog to Josephson junctions or coupled Josephson junction arrays. There, the magnetic field penetrates the insulating regions between the superconducting circuits. Therfore one can assume that the magnitude of the mesoscopic superconducting wave function $|\Psi| \sim \sqrt{\rho_s}$ inside the SC circuits remains unchanged and a phase-only description is possible.

On a more general ground one can show [75] that a transition from a well formed mean field regime with a spontaneous broken O(N) symmetry is always initiated by directional O(N) fluctuations at a temperature well below T_c^{MF} and also below the famous Ginzburg temperature where size fluctuations are getting important. Close to T_c^{MF}, where the density of thermally excited vortices becomes very large, one can no longer distinguish between amplitude and phase fluctuations. The extremely large temperature regime where phase fluctuations are supposed to be important in the underdoped cuprates can then directly be related to the low stiffness of this phase mode close to the Mott insulating state [75]. In addition, poorly screened Coulomb interactions are able to further enhance the role of (quantum) fluctuations of the phase (see Sec. 2.4.1). The Coulomb interaction is not included in the simple BCS-like approach and has to be introduced ad hoc in the XY phase action (Eq. 2.44).

---

[5] Exactly at half-filling, the repulsive U Hubbard model can be directly mapped onto the attractive U Hubbard model by means of a particle-hole transformation. The z-spin component maps onto the charge-operator and the transverse spin components onto the pair creation and annihilation operators. As a result of this mapping the CDW and s-wave BCS ground states are degenerate at half-filling.

To summarize the preceding discussion: in contrast to the common BCS scenario where the vortex core energy is of the order of the mean-field condensation energy $E_{\text{cond}} \sim T_c^{MF}$, one assumes that thermally excited vortices in the underdoped cuprates are cheap and their cost in energy of order $T_\varphi \ll T_c^{MF}$. Nevertheless, the qualitative form of the BCS phase action is still valid, however, with adjusted parameters which account for the proximity to the Mott insulating state and strong electron correlations. Thus, within our BCS-like phase fluctuation model for the underdoped cuprates, we have to perform a *quenched average* over the different phase configurations. This means that we have a *phenomenological model* for a strongly correlated "Mott superconductor" and not a selfconsistent microscopic theory. In addition, also the BCS temperature dependence of the magnitude of the local superconducting pairing gap is not clear. In fact, the experimentally observed gap size is rather constant up to highest temperatures. Therefore, in most calculations we use a constant gap parameter in our Hamiltonian (Sec. 2.1). In cases where the results of our calculations are very sensitive to the gap size, we contrast the results for a constant gap parameter with those for a BCS temperature dependent gap parameter. From the above is it also obvious that our phenomenological theory must break down close to T_c^{MF}.

2.4 The XY action

As described in section 2.2.2, after integrating out all high-energy degrees of freedom, including those responsible for the local pair-formation and pair symmetry, we finally obtain an effective XY action for the phase of the superconducting order-parameter. The effective XY action is defined on a coarse-grained lattice of length-scale ξ_0 — the superconducting coherence length. In this section, we want to briefly discuss the properties of the quantum and classical XY model, the nature of the Kosterlitz-Thouless transition and the applicability of the XY model to other phenomena besides superconductivity.

2.4.1 Quantum and classical XY model

The most general starting point is the quantum XY model, however, as we will see below, it is in many cases sufficient to treat the phase $\varphi_{\boldsymbol{i}}$ as a classical static field variable and to neglect the quantum dynamics completely.

Quantum XY model

The quantum XY action is given by

$$S_{XY} = \frac{1}{\hbar}\int_0^{\beta\hbar} d\tau \left[\frac{1}{2}\, C \sum_{\boldsymbol{i}} (\dot{\varphi}_{\boldsymbol{i}}(\tau))^2 - J \sum_{\langle \boldsymbol{ij} \rangle} \cos\left(\varphi_{\boldsymbol{i}}(\tau) - \varphi_{\boldsymbol{j}}(\tau)\right) \right]. \tag{2.45}$$

In our case, the coordinates $\boldsymbol{i}$ and $\boldsymbol{j}$ run over the sites of a 2D square lattice with lattice constant ξ_0. The angles $\langle \cdots \rangle$ indicate, as in the fermionic Hamiltonian (Eq. (2.2)), sums over nearest neighbor sites. The model can also be used to describe granular superconductors. In this case the coordinates $\boldsymbol{i}$ and $\boldsymbol{j}$ denote the different superconducting grains.

The second term in Eq. (2.45) represents the Josephson coupling energy $\sim J$ between two neighboring regions (superconducting grains) with phase $\varphi_{\boldsymbol{i}}$ and $\varphi_{\boldsymbol{j}}$ and the first term $\sim C$ contains the quantum dynamics and is due to the Coulomb repulsion between Cooper pairs occupying the same region (superconducting grain). Without Coulomb interaction, $C \to \infty$, and the phases will become static. The properties of the quantum XY model were studied extensively in literature [64, 76–79]. The model can also be used to simulate capacitively coupled Josephson junction arrays [80–82]. The origin of the first term in Eq. (2.45) and its consequences are more clearly seen in a Hamiltonian form.

Hamiltonian form

After a Legendre transformation we obtain the effective XY Hamiltonian [46, 64, 76, 81]

$$H_{XY} = \frac{1}{2C} \sum_{\boldsymbol{i}} \hat{\rho}_{\boldsymbol{i}}^2 - J \sum_{\langle \boldsymbol{ij} \rangle} \cos\left(\hat{\varphi}_{\boldsymbol{i}} - \hat{\varphi}_{\boldsymbol{j}}\right), \tag{2.46}$$

where $\hat{\rho}_{\boldsymbol{i}} = -i\frac{\partial}{\partial \varphi_{\boldsymbol{i}}}$ is the operator of the number of Cooper pairs in a region of size ξ_0^2 (or on a superconducting grain) and $\hat{\varphi}_{\boldsymbol{i}}$ is the operator of the corresponding phase. Here one can clearly see, that the first term describes the Coulomb interaction between Cooper pairs occupying the same region on the XY lattice. The Coulomb interaction is however assumed to be renormalized to a pure on-site interaction as a result of the screening by normal electrons.

The XY Hamiltonian (Eq. (2.46)) is completely equivalent to the Hamiltonian of particles interacting via a periodic potential:

$$H = \frac{1}{2m} \sum_{\boldsymbol{i}} \hat{p}_{\boldsymbol{i}}^2 + \sum_{\langle \boldsymbol{ij} \rangle} V\left(\hat{x}_{\boldsymbol{i}} - \hat{x}_{\boldsymbol{j}}\right), \tag{2.47}$$

where $V\left(\hat{x}_{\boldsymbol{i}} - \hat{x}_{\boldsymbol{j}}\right) \sim \cos\left(\hat{x}_{\boldsymbol{i}} - \hat{x}_{\boldsymbol{j}}\right)$. One simply has to make the substitutions

$$\hat{p} = -i\hbar\frac{\partial}{\partial x} \quad \longleftrightarrow \quad \hat{\rho} = -i\frac{\partial}{\partial \varphi}, \tag{2.48}$$

$$\hat{x} \quad \longleftrightarrow \quad \hat{\varphi}, \tag{2.49}$$

$$m \quad \longleftrightarrow \quad C. \tag{2.50}$$

This analogy can, for example, be used to describe phase-slip experiments in Josephson junctions by solving the Hamiltonian of a particle moving in a “tilted-washboard” potential [7]. Furthermore, we see that, like position and momentum are conjugate variables, also the phase and the number of Cooper pairs are conjugate variables. This immediately implies an uncertainty relation between the relative phase φ of neighboring regions and the total number of electrons N in a region [7, 32, 64]:

$$\Delta N \Delta\varphi \gtrsim 1. \tag{2.51}$$

According to this uncertainty relation, phase coherence between neighboring regions implies a large relative number fluctuation and correspondingly large Coulomb energies, unless there is sufficient screening.

In taking a closer look to Eqs. (2.46) and (2.47), one can see a remarkable property of the phase-only XY Hamiltonian. The dynamical part, corresponding to the kinetic energy in Eq. (2.47), stems from the electrostatic Coulomb repulsion of the Cooper pairs, whereas the static part, that is represented by the Josephson coupling term and which has the form of a potential energy, describes the superflow, and thus, kinetic energy of the Cooper pairs. This means that somehow the roles of potential and kinetic energy have been interchanged.

Classical XY model

At high temperatures, all fluctuations are classical. This can be seen by the fact, that the integral running over the imaginary time axis τ in the quantum XY action (Eq. (2.45)) extends from 0 to β. When we go to very high temperatures $T \sim \frac{1}{\beta}$, $\beta \to 0$ and any quantum fluctuation must develop on a very small τ-interval, so that any variation of the phase along the τ-axis must either be very small or will have a very high cost of energy and therefore the quantum dynamics plays no role. In contrast, at very low temperatures, $\beta \to \infty$ and quantum fluctuations dominate the physics, since also for a large parameter C in the quantum XY action (Eq. (2.45)), there is always enough “space” on the τ-axis for many quantum fluctuations to develop. The exact crossover temperature between quantum and classical behavior is determined by the strength of the screening, i. e. by C. For a strongly screened Coulomb interaction, the parameter C in the XY Hamiltonian (Eq. (2.46)) will be very large, which implies a high cost of energy for any dynamic fluctuation in the quantum XY action (Eq. (2.45)) and therefore classical static thermal fluctuations down to very low temperatures.

There have been various discussions regarding the regime over which a classical phase-action is appropriate for the cuprates [62–64]. It turns out, that quantum phase fluctuations are dominant in the underdoped cuprates for $T \ll T_c$. At higher temperature $T \gtrsim T_c$ and with sufficiently strong screening, the phase fluctuations are predominantly classical [32, 83]. The exact crossover temperature is however still not clear. Since we are only interested in the temperature region between T_c and T^* (pseudogap regime), we will neglect in the following the quantum fluctuations, which leads us to the effective classical XY free energy

$$F_{XY}\left[\varphi_{\boldsymbol{i}}\right] = -J \sum_{\langle \boldsymbol{ij} \rangle} \cos\left(\varphi_{\boldsymbol{i}} - \varphi_{\boldsymbol{j}}\right) . \tag{2.52}$$

We call Eq. (2.52) free energy since, as discussed in section 2.2.2, we obtained it by integrating out all high-energy degrees of freedom, i. e. after the Hubbard-Stratonovich transformation, all fermions and the magnitude of the pairing field. Thus, equation (2.52) has the form of a free energy. In order to calculate the partition function from (2.52), we only have to integrate over the classical field-variables $\varphi_{\boldsymbol{i}}$ from 0 to 2π, instead of formally calculating quantum-mechanical path-integrals over the dynamical field-variables $\varphi_{\boldsymbol{i}}(\tau)$ from $-\infty$ to $+\infty$. We do this by performing a Monte Carlo (MC) importance-sampling procedure, which will be discussed below.

The 2D classical XY model is, like the Ising model, a standard model of statistical physics and its properties have been studied numerically in various publications [83–90]. One of its major characteristics is a Kosterlitz-Thouless transition to a quasi phase-ordered state below a critical temperature T_{KT}, which will be discussed in the next section.

2.4.2 The Kosterlitz-Thouless transition

In high dimensions D ($D \to \infty$), phase transitions in many-particle systems are correctly described by a set of mean-field equations. When the dimensionality of space is reduced, fluctuations around the mean-field behavior are getting more and more important. Finally these fluctuations can even prevent the system from developing any long-range order. The dimension where this first happens is called *lower critical dimension* D_c. In 1966[6] Hohenberg [92] pointed out, that a rigorous inequality, first proofed by Bogoliubov, can be used to rule out any conventional superfluid or superconducting ordering in one and two dimensions at finite temperatures. Shortly after, Mermin and Wagner showed in a seminal paper [91] the absence of any magnetic ordering in one- and two-dimensional isotropic Heisenberg models. Their method of proof is also capable of excluding other types of ordering in one and two dimensions. The generalization of the Hohenberg-Mermin-Wagner theorem states, that in systems with discrete symmetries, like the Ising model, no long range order can develop in one dimension ($D_c = 1$). In systems with continuous symmetry, like the XY model, fluctuations are even more severe and increase the lower critical dimension to $D_c = 2$. This means, that there cannot be a spontaneous breaking of a continuous symmetry in $D \leq 2$ dimensions at any finite temperature.

Berezinskiĭ [93, 94] was the first to realize, that these systems however show a remarkable change in the long-distance asymptotic behavior of the correlation functions at low temperatures. Kosterlitz and Thouless [95] proposed a new kind of order, called topological order, for two-dimensional systems in which no long-range order of the conventional mean-field type exists. This topological order can cause the system to go through a phase transition at low temperatures, visible in a change of the long-distance behavior of the correlation functions.

For the 2D classical XY model, this means the following: At low temperatures, the long-range behavior of the system is dominated by spin-wave physics. The phase correlations show a power-law decay, which can be explained by a harmonic spin-wave theory that is modified by the presence of pairs of tightly bound topological defects of opposite sign (vortices) at small distances. At high temperatures, these pairs start to “melt” and single vortices can now move freely throughout the lattice (see Fig. 2.4). This proliferation of free topological defects (vortices) causes the phase correlations to decay exponentially in space. The temperature where this first happens is called the Kosterlitz-Thouless transition temperature T_{KT}.

In the following, we want to summerize some properties of the 2D classical XY model [96–98]. At high temperatures $T \gg T_{KT}$ the phase correlations decay like

$$\left\langle e^{i\varphi_{i+\ell}} e^{-i\varphi_i} \right\rangle \sim e^{-\frac{r}{\xi}}, \tag{2.53}$$

---

[6] The paper was actually published in 1967 after the appearance of Mermin and Wagner’s article, but the work was done earlier, which was also stated by Mermin and Wagner [91].

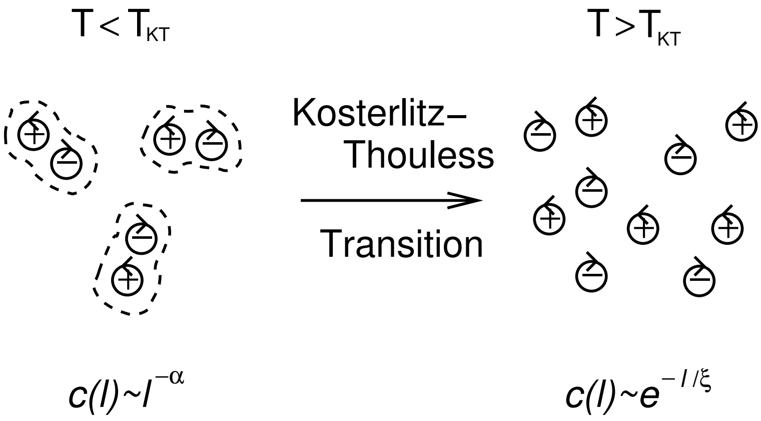

Figure 2.4: Below the Kosterlitz-Thouless transition temperature T_{KT}, vortices are closely bound into pairs of zero total vorticity which exist in a background of spin-wave excitations. The phase correlations $C(\ell) = \left\langle e^{i\varphi_{i+\ell}} e^{-i\varphi_i} \right\rangle$ show a power-law decay. Above the Kosterlitz-Thouless transition temperature T_{KT}, one gets a fluid of freely moving unbound vortices which cause the phase correlations to decay exponentially.

with phase correlation length

$$\xi \approx \frac{a}{\ln(\frac{T}{J})} \tag{2.54}$$

and lattice constant a. The low temperature spin-wave approximation yields for the long-distance behavior ($\frac{r}{a} \gg 1$):

$$\left\langle e^{i\varphi_{i+\ell}} e^{-i\varphi_i} \right\rangle \sim \left(\frac{a}{r}\right)^{\frac{T}{2\pi J}}. \tag{2.55}$$

To a first order approximation, the Kosterlitz-Thouless transition temperature T_{KT} is given by

$$T_{KT} \approx \frac{\pi}{2} J, \tag{2.56}$$

where in our case

$$J \sim \rho_s(0), \tag{2.57}$$

with the zero temperature 2D superfluid density $\rho_s(0)$. If one defines a renormalized coupling

$$\tilde{J} \sim \rho_s(T_{KT}), \tag{2.58}$$

one can show exactly

$$T_{KT} = \frac{\pi}{2} \tilde{J}, \tag{2.59}$$

or

$$T_{KT} = \frac{\pi \hbar^2 \rho_s(T_{KT})}{2 m^* k_B}, \tag{2.60}$$

where m^* is the effective mass of the superfluid particles (Cooper pairs). Equation (2.60) directly implies, that there must be a jump in the superfluid density at T_{KT} from some finite value to zero.[7] The quantity $D_s(0) = \frac{\hbar^2 \rho_s(0)}{2m^*}$ is also called *bare phase-stiffness* and $D_s(T) = \frac{\hbar^2 \rho_s(T)}{2m^*}$

---

[7] Since $\rho_s(T > T_{KT}) \equiv 0$, T_{KT} only has a finite value, if $\rho_s(T_{KT}) > 0$.

renormalized phase-stiffness or *helicity modulus* Υ.

Numerically it is found that [84–86]

$$T_{KT} \approx 0.89 J. \tag{2.61}$$

Also the jump in the helicity modulus has very recently been confirmed numerically [90]. For the 2D quantum XY model there is also numerical evidence for a Kosterlitz-Thouless transition[77–79], however at lower temperatures due to the additional quantum fluctuations. These dynamic quantum fluctuations can even inhibit any phase ordering if the Coulomb interaction is strong enough [64, 81], since a strong Coulomb repulsion (weak screening ↔ small C) means very cheap quantum fluctuations, as can be seen from Eqs. (2.45) and (2.46). This can also be seen from the uncertainty relation (Eq. (2.51)): a strong Coulomb repulsion suppresses any charge (particle-number) fluctuations, which are necessary for phase ordering.

2.4.3 The XY universality class

As already mentioned, the XY model is a standard model of statistical physics, that not only serves to describe superconductors with low superfluid density and Josephson junction arrays but can also account for many other physical phenomena. In the following, we briefly want to provide some other examples of the XY universality class.

Superfluid helium

In superfluid helium, a fraction of the atoms condense into a macroscopic quantum state with a complex wave-function $\Psi(\boldsymbol{r})$. For most purposes it is sufficient to assume that the magnitude of $\Psi(\boldsymbol{r})$ is fixed, thus

$$\Psi(\boldsymbol{r}) = \Psi_0 \, e^{i\theta(\boldsymbol{r})}. \tag{2.62}$$

The kinetic energy of the superfluid is then given by [7]

$$H = \frac{\hbar^2}{2m^*} |\Psi_0|^2 \int dr \, [\nabla\theta(\boldsymbol{r})]^2, \tag{2.63}$$

where $|\Psi_0|^2$ is associated with the superfluid density ρ_s and $v_s = \frac{\hbar}{m^*}\nabla\theta(\boldsymbol{r})$ is the superfluid velocity. Moreover, the short range repulsion of the helium atoms can be modeled by localizing the coordinates of the phase-field on a discrete lattice $\theta(\boldsymbol{r}) \to \theta_{\boldsymbol{i}}$. After taking the discrete derivative and changing the integral into a sum we finally obtain

$$H = \frac{\hbar^2}{2m^*} \rho_s \sum_{\langle \boldsymbol{ij} \rangle} [\theta_{\boldsymbol{i}} - \theta_{\boldsymbol{j}}]^2. \tag{2.64}$$

In this form the Hamiltonian can be mapped to the classical XY model (Eq. (2.52)), by requiring periodicity of the phase and replacing the discrete squared derivative by the cosine ($\frac{1}{2}[\theta_{\boldsymbol{i}} - \theta_{\boldsymbol{j}}]^2 \to \cos(\theta_{\boldsymbol{i}} - \theta_{\boldsymbol{j}})$). Alternatively, we can map coefficients by expanding the XY free energy (Eq. (2.52)) in powers of the phase difference. Here we assume, that configurations with small phase difference between neighboring sites $|\varphi_{\boldsymbol{i}} - \varphi_{\boldsymbol{j}}| \ll 1$ are the most relevant for the thermodynamic properties, since they can most easily be excited:

$$F_{XY} \approx -J \sum_{\langle \boldsymbol{ij} \rangle} \left[1 - \frac{(\varphi_{\boldsymbol{i}} - \varphi_{\boldsymbol{j}})^2}{2} \right]. \tag{2.65}$$

The constant term can be absorbed into the ground state energy and we get

$$J = \frac{\hbar^2}{m^*} \rho_s, \tag{2.66}$$

which we have already used in our discussion of the Kosterlitz-Thouless transition in section 2.4.2.

Anisotropic magnets

The simplest way of modeling magnets is to consider spins $\boldsymbol{S_i}$ localized on a lattice with sites $\boldsymbol{i}$. The model Hamiltonian describing these spins is the quantum Heisenberg model:

$$H = -J \sum_{\langle \boldsymbol{ij} \rangle} \boldsymbol{S_i} \cdot \boldsymbol{S_j}. \tag{2.67}$$

The Hamiltonian has full rotational symmetry. At high temperatures, one can treat the spins classically. Furthermore, in real materials, crystalline fields act on the spins and make them prefer to lie along certain axis. If the spins are confined along the z-axis, one obtains the Ising model with $s_z = \pm 1$. Alternatively, the spins may prefer to lie in the xy-plane, so that one has to consider only two spin components satisfying $s_x^2 + s_y^2 = 1$. This leads to the XY or $O(2)$ (planar) rotor model.

2D Coulomb gas

The two-dimensional Coulomb gas model of statistical physics describes particles with equal or opposite charge, interacting through a Coulomb interaction [99]. In 2D, the Coulomb potential has a logarithmic form exactly like the short distance interaction between vortices in a superconductor [7]. In fact, there is a direct mapping between 2D superfluids and a 2D Coulomb gas if one replaces vortices by charges [99]. The Kosterlitz-Thouless unbinding transition of vortices then corresponds to the unbinding of charges with opposite sign. Above T_{KT} one gets a 2D plasma of freely moving positive and negative charges. This analogy also indicates the connection of the QED$_3$ theory (quantum electrodynamics in (2+1) dimensions) to phase fluctuations.

2.5 Numerical implementation and choice of parameters

In this section, we conclude the preceding discussion, elucidate the appropriate parameters for our model Hamiltonian and explain its numerical evaluation. In all our calculations we use the fermionic Hamiltonian introduced in Sec. 2.1 and then perform a *quenched average* over the

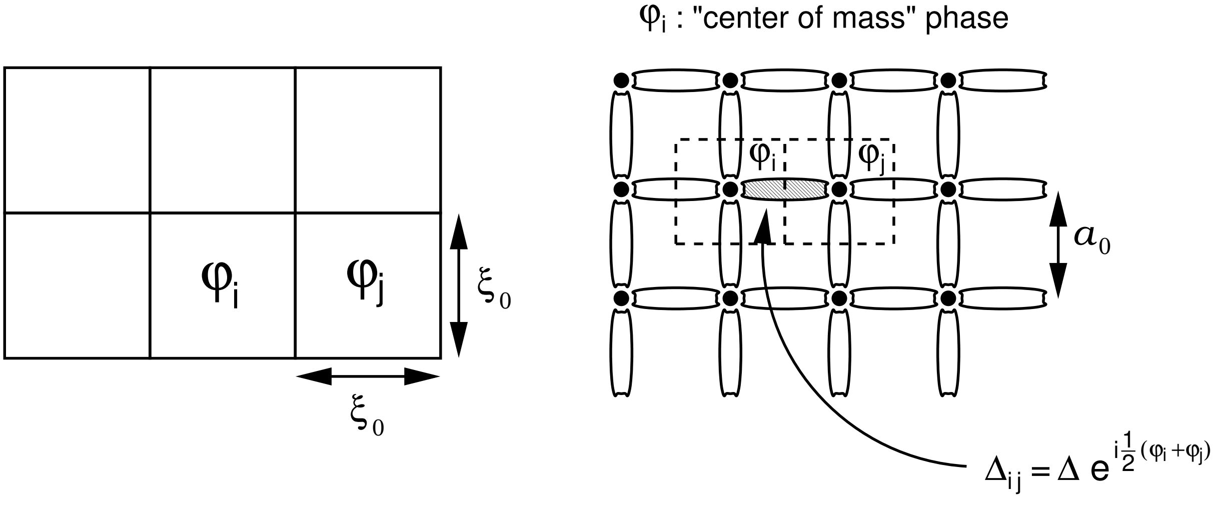

Figure 2.5: The XY lattice (left) is defined on the scale of the BCS pair coherence length ξ_0 whereas the fermionic Hamiltonian (right) has a lattice constant a_0 given by the distance of neighboring copper atoms. With $\Delta_{sc} = 1.0t$ we obtain $\xi_0 \approx a_0$, which allows us to directly couple the XY phases $\varphi_{\boldsymbol{i}}$ (dashed squares in the right figure) to the local pairing amplitude $\Delta_{\boldsymbol{ij}}$ (grey shaded area) via $\Delta_{\boldsymbol{ij}} = \Delta e^{i\frac{1}{2}(\varphi_{\boldsymbol{i}}+\varphi_{\boldsymbol{j}})}$.

different phase configurations with the help of the classical XY free energy given in Eq. (2.52). This is done by means of a Monte Carlo importance sampling procedure and will be discussed in greater detail below, but first we want to determine the model parameters.

LDA calculations and photoemission studies indicate [100] that the total bandwidth of the energy band crossing E_F in the cuprates is about $2\,eV$. For our 2D tight-binding dispersion this means that the next-neighbor hopping-parameter t has a value of $t \approx 250\,meV$. On the other hand, the maximum size of the superconducting gap Δ_{sc} in underdoped Bi2212 is about $40\,meV$ [14, 101], which would mean $\Delta_{sc} \approx \frac{1}{5}t$. Now, the superconducting coherence length ξ_0 in the cuprates is about 15 – 20 Å [7] and with a copper-copper distance a_0 of about 4 – 5 Å [100] we obtain $\xi_0 \approx$ 3 – 4 a_0. The exact values of these parameters clearly vary between the different compounds but we just want to make reasonable assumptions. Thus, the XY lattice has to be defined on a length scale that is about 4 times larger than the fermionic lattice defined by the Hamiltonian Eq. (2.1). For a typical 32×32 fermionic lattice, which is numerical feasible, we would only have a 8×8 phase lattice on top of it. This wouldn't allow for any proper temperature scaling of the phase correlation length $\xi(T)$ and obscure the Kosterlitz-Thouless transition.

In order to overcome this difficulty, we have chosen to take a larger value of the gap, i. e. $\Delta_{sc} = 1.0t$. This yields a pair size coherence length $\xi_0 \sim \frac{v_F}{\Delta_{sc}}$ (v_F is the Fermi velocity) of $\xi_0 \lesssim a_0$ and allows the Monte Carlo phase simulation to be carried out on the same $L \times L$ lattice that is used for the diagonalization of the fermionic Hamiltonian. Therefore, we can couple the XY phases $\varphi_{\boldsymbol{i}}$ (Eq. (2.52)) directly to the local fermionic pairing field via Eqs. (2.5) to (2.7). For the d-wave case this is illustrated in Fig. 2.5. In addition, the choice of $\Delta_{sc} = 1.0t$ automatically introduces the important short distance cut-off for the phase fluctuations that is discussed in Sec. 2.2.2.

With Δ_{sc} fixed, we have also fixed the pseudogap temperature $T^* \equiv T_c^{MF}$ and the coupling constants (g and U) in the BCS-like pairing-interaction terms of our Hamiltonian. In case of the d-wave order parameter (Eq. (2.3)) we obtain $T_c^{MF} = 0.42t$ ($g = 1.03t$) and for the s-wave case (Eq. (2.7)) we obtain $T_c^{MF} = 0.54t$ ($U = -3.3t$) at half-filling, and a slightly reduced temperature for 10% doping. Thus, we have effectively only one free parameter left. This is the phase stiffness J in the classical XY free energy (Eq. (2.52)). The phase stiffness J determines the Kosterlitz-Thouless transition temperature T_{KT} of the classical XY model as we have seen in Sec. 2.4.2. Below T_{KT} the phases are effectively ordered on the finite lattice and we therefore take T_{KT} as phase ordering temperature T_φ which in the phase fluctuation model determines the transition temperature to the ideal superconducting state T_c.

Typically, one gets a ratio of $T^*/T_c = 4$ – 5 in the underdoped cuprates (see e. g. the scanning tunneling results for Bi2201 [26]). Therefore we have set $T_{KT} = 0.1t$ ($J = 0.112t$) which for the d-wave case yields $T^* = 4.2T_c$ and for the s-wave case $T^* = 5.4T_c$. As we have already mentioned, the transition to the superconducting state in the cuprates is not a real 2D Kosterlitz-Thouless transition but rather a 3D XY transition [83] with true long-range order due to the coupling between the superconducting copper oxide planes. When the phase correlation length $\xi(T)$ diverges close to T_c, Josephson coupling terms between the planes cause the phase to "lock-in". Away from this (2D→3D) crossover regime, a 2D model is however certainly suitable.

In addition, on the finite size lattice that we will study, the system becomes effectively ordered as T approaches T_{KT} and the correlation length $\xi(T)$ exceeds the lattice size L. This means that we do not obtain a true Kosterlitz-Thouless transition in our MC simulation, which is very hard to obtain numerically. Also in experiments, the jump in the superfluid density $\rho_s(T)$ at T_{KT}, which was discussed in Sec. 2.4.2, was not observed. There the superfluid density $\rho_s(T)$ continously disappears at T_c [83].

The range of validity of our model starts at about $T_c \equiv T_{KT}$, since close to a finite temperature phase transition all fluctuations are (renormalized) classical and reaches up to $T^* \equiv T_c^{MF}$. However, our model cannot describe the region close to T^* since it neglects amplitude fluctuations and it is also not appropriate for low temperatures close to $T = 0$, where the quantum dynamics of the phase has to be taken into account.

The evaluation of our phase fluctuation model now proceeds as follows. For a given phase configuration one can write the Hamiltonian (Eq. (2.1)) in matrix form as

$$H = \begin{pmatrix} \cdots & c^\dagger_{\boldsymbol{i}\uparrow} & \cdots, \cdots & c_{\boldsymbol{i}\downarrow} & \cdots \end{pmatrix} \begin{pmatrix} t_{\boldsymbol{ij}} & \Delta^*_{\boldsymbol{ij}} \\ \\ \Delta_{\boldsymbol{ij}} & -t_{\boldsymbol{ij}} \end{pmatrix} \begin{pmatrix} \cdot \\ c_{\boldsymbol{j}\uparrow} \\ \cdot \\ c^\dagger_{\boldsymbol{j}\downarrow} \\ \cdot \end{pmatrix} - \mu N, \tag{2.68}$$

with $N = L \times L$ the number of lattice points. For the d-wave superconductor with next-neighbor hopping the matrix elements take the values

$$t_{\boldsymbol{ij}} = \begin{cases} -t & \text{for} \quad \boldsymbol{i} = \boldsymbol{j} + \delta, \\ -\mu & \text{for} \quad \boldsymbol{i} = \boldsymbol{j}, \\ 0 & \text{else} \end{cases} \tag{2.69}$$

and

$$\Delta_{\boldsymbol{ij}} = \begin{cases} -g\sqrt{2}\Delta e^{i\Phi_{\boldsymbol{i}\delta}} & \text{for} \quad \boldsymbol{i} = \boldsymbol{j} + \delta, \\ 0 & \text{else}, \end{cases} \tag{2.70}$$

with δ connecting next-neighbor lattice sites. By using the operators $\psi_m^\dagger$ (ψ_m) defined in Eq. (2.13) this can be written in a more compact form as

$$H = \psi_m^\dagger A_{mn} \psi_n \, [-\mu N] \tag{2.71}$$

with A_{mn} a complex hermitian matrix. Here, we can neglect the last term which is just a constant number. Next, the matrix A_{mn} is diagonalized using a standard LAPACK[8] routine which gives us all eigenvectors and eigenvalues. Thus, the Hamiltonian now has the form

$$H = \phi_m^\dagger B_{mm} \phi_m \tag{2.72}$$

with

$$\psi_m = U_{mn} \phi_n, \tag{2.73}$$

$$B_{mm'} = U_{nm}^* A_{nn'} U_{n'm'} \tag{2.74}$$

and

$$U_{mn}^\dagger = U_{nm}^* \tag{2.75}$$

a unitary transformation matrix. The Nambu Green's functions can now be written in terms of these eigenvectors and eigenvalues as

$$\begin{aligned} G_{\boldsymbol{ij}}(i\omega_n) &= \langle\langle c_{\boldsymbol{i}\uparrow} c_{\boldsymbol{j}\uparrow}^\dagger \rangle\rangle \\ &= \langle\langle \psi_m \psi_n^\dagger \rangle\rangle \\ &= U_{mm'} U_{nn'}^* \langle\langle \phi_{m'} \phi_{n'}^\dagger \rangle\rangle \\ &= \frac{U_{ml} U_{nl}^*}{i\omega_n - B_{ll}}. \end{aligned} \tag{2.76}$$

With these Green's functions one can calculate all expectation values and correlation functions by applying Wick's theorem for a given phase configuration. After the calculation of the expectation value of an observable A for a given phase configuration $A(T, \{\varphi_i\}) = \langle \hat{A} \rangle_{\{\varphi_i\}}$, further phase configurations are generated using a Monte Carlo importance sampling procedure and the average value of the observable $A(T) = \langle \hat{A} \rangle$ at a given temperature is determined.

We have used two different algorithms for the importance sampling procedure, a cluster and a local updating scheme, depending on the temperature, which is detailed in Sec. 2.7. The Monte Carlo program is written in Fortran90 and almost all the calculations have been performed on the Hitachi SR8000-F1 at the Leibniz-Rechenzentrum München (LRZ) and on the Cray T3E at the High Performance Computing Center Stuttgart (HLRS). In order to get reliable results, we had to typically average over about 2500 independent phase configurations.

---

[8] The LAPACK – Linear Algebra PACKage can, for example, be found on http://www.netlib.org/ (6/15/2004).

2.6 Reducing finite-size effects — Assaad's method

We have already talked about finite-size effects in the preceding section concerning the critical properties of the XY model and the coupling of the XY phases to the fermionic Hamiltonian. However, despite the large SC gap of $\Delta_{sc} \sim t$, we still suffer from the discreteness of the energy eigenvalues of the fermionic Hamiltonian. The MC simulations for the calculation of expectation values and single-particle response functions are typically carried out on a 32×32 or a 36×36 lattice. The two-particle correlation functions can only be calculated on a 16×16 lattice due to the limited available computing power. The number of eigenvalues obtained by diagonalizing the Hamiltonian (Eq. (2.68)) is $2N = 2L^2$ for a $L \times L$ lattice. Due to spin inversion and spatial symmetries these eigenvalues are highly degenerate in the BCS ground state. The degeneracy is somewhat reduced at higher temperatures by phase fluctuations but there are still many nearly degenerate energy-levels which cause difficulties in the calculation of the response functions and expectation values.

The idea of Assaad [102] was to introduce a static magnetic field B that couples to the hopping term of the Hamiltonian. The strength of the magnetic field is given by

$$B = \frac{\Phi_0}{L^2}, \tag{2.77}$$

with $\Phi_0 = \frac{hc}{|e|}$. This means that exactly one quantum of flux is running through the whole lattice. The magnetic field disappears in the thermodynamic limit ($L \to \infty$), where we approach the original Hamiltonian. The advantage of this method is that it completely lifts the degeneracy of the energy eigenvalues due to spatial symmetries[9] and that the calculated quantities approach the exact results much faster for $L \to \infty$ than without magnetic field. The disadvantage of this method is, however, that it breaks translation invariance. Therefore one has to be careful with $\boldsymbol{k}$-dependent quantities like the spectral weight $A(\boldsymbol{k}, \omega)$, where the magnetic field produces nasty artifacts. Furthermore, Assaad's method of reducing finite-size effects could suppress phases that act very sensitively to an applied magnetic field, like weak superconducting correlations. Nevertheless, for $\boldsymbol{k}$-independent quantities Assaad's method works amazingly well.

Before we show how to implement this method we first briefly discuss alternative procedures to reduce finite-size effects in expectation values and response functions. However, one always has to keep in mind that all these procedures just act to smooth the "spiky" features in the calculated functions. Away from phase transitions this yields results that are very close to those of the infinite system. But we still do not see real critical behavior close to a phase transition, i. e. the divergence of the corresponding correlation function as one approaches the critical point. Instead, these correlation functions still show a maximum rather than a true singularity, due to the finite lattice size, which is moreover shifted slightly away from the true critical temperature.[10]

---

[9] The spin inversion symmetry is still intact since the magnetic field does not couple to the spin degrees of freedom.

[10] For a finite system with periodic boundary conditions, this maximum is shifted to temperatures $T_{\max} > T_c$, whereas for systems with open boundary conditions one obtains $T_{\max} < T_c$ due to the enhanced fluctuations [96].

2.6.1 Alternative methods

From Eq. (2.76) it is obvious that, after the analytic continuation, the physical response functions have a pole structure of the form

$$\frac{1}{\omega+i\eta-E_n} \equiv \frac{\omega-E_n}{(\omega-E_n)^2+\eta^2} - i\frac{\eta}{(\omega-E_n)^2+\eta^2}, \tag{2.78}$$

with $\eta \to 0$. This yields a first order pole $\sim \frac{1}{\omega-E_n}$ in the real part and a δ-function $\sim \pi\,\delta(\omega-E_n)$ in the imaginary part. In addition, one has to perform the sum over all energy eigenvalues E_n. In an actual numerical calculation η is always finite, which produces a zero in the real part at $\omega=E_n$ and a Lorentzian peak-function in the imaginary part centered at $\omega=E_n$. It is thus clear that for a limited number of energy eigenstates one always obtains very "spiky" response functions. One way to reduce finite size effects is to make η sufficiently large.[11] This washes out the sharp pole structure, broadens the peak-function and therefore produces smooth response functions. However, the disadvantage of this method is that it also washes out physically relevant sharp features, like coherence peaks, which makes it only of limited use.[12]

A more sophisticated method to reduce finite size effects is the so-called tetrahedron method for Brillouin-zone integrations [103–105]. Its general idea is to turn the sum over the finite number of energy eigenvalues into a continuous integral. One prerequisite of this method is a well defined mesh, say in $\boldsymbol{k}$-space, on which the energy eigenvalues $E(\boldsymbol{k})$ are given. Instead of performing the sum over all discrete $\boldsymbol{k}$-points, one divides the (three dimensional) Brillouin-zone into tetrahedrons with the corners given by the actually calculated eigenvalues $E(\boldsymbol{k})$ on the mesh. The eigenvalues $E(\boldsymbol{k})$ and matrix elements are then interpolated linearly in each tetrahedron which allows the integral over these micro-zones to be calculated analytically. As a result, one obtains an infinite number of approximated energy levels which contribute to the response functions. In our case, this method is only applicable in the BCS and free-electron limit where the states are characterized by momentum $\boldsymbol{k}$. For an arbitrary phase configuration, $\boldsymbol{k}$ is no longer a good quantum number due to the destroyed lattice translational symmetry. Thus, there exists no well defined mesh in $\boldsymbol{k}$-space on which the energy eigenvalues and matrix elements can be defined.[13] Therefore, the proper weighting and interpolation of energy levels and matrix elements is no longer possible.

The twisted boundary condition integration technique [106] is a method to reduce finite size effects which is also applicable to interacting and non-translational invariant systems. The method is exact for a non-interacting or mean-field Hamiltonian.[14] To see how it works, consider a large cluster of $\tilde{N}=\tilde{L}\times\tilde{L}$ lattice points in 2D. Now divide the cluster into smaller clusters of size $N=L\times L$. Each coordinate can now be written as $\boldsymbol{r}=\boldsymbol{i}+L\boldsymbol{R}$, where $\boldsymbol{i}$ indicates the position inside the smaller cluster and $\boldsymbol{R}$ marks the position of the smaller cluster. Similarly, after a Fourier transformation, the momentum can be decomposed into $\boldsymbol{K}=\boldsymbol{k}+\boldsymbol{Q}$, with $N=L\times L$ wave vectors $\boldsymbol{k}$ of the smaller cluster with spacing $\Delta k=\frac{2\pi}{L}$ and $\frac{\tilde{N}}{N}=\frac{\tilde{L}}{L}\times\frac{\tilde{L}}{L}$ supercell wave-vectors $\boldsymbol{Q}$ with spacing $\Delta Q=\frac{2\pi}{\tilde{L}}$. With the help of a partial Fourier transformation in the cluster vectors $\boldsymbol{R}$ one can very easily show that the Hamiltonian is block-diagonal in the super-cell wave-vectors $\boldsymbol{Q}$. This means that instead of solving the large $\tilde{L} \times \tilde{L}$ cluster, one can solve a smaller $L \times L$ cluster for each $\boldsymbol{Q}$. However, the smaller N-site cluster now has twisted boundary conditions, with the twist given by $c_{\boldsymbol{i}+L\Delta\boldsymbol{R},\sigma} \to e^{-i\boldsymbol{Q}L\Delta\boldsymbol{R}} c_{\boldsymbol{i},\sigma}$. The twisted boundary conditions can be absorbed into a redefinition of the canonical momentum with the help of a gauge transformation.[15] The energies $E_{\boldsymbol{Q}}(\boldsymbol{k})$ of the cluster with twisted boundary conditions are then given in terms of the energies $E(\boldsymbol{k})$ of the cluster with periodic boundary conditions as $E_{\boldsymbol{Q}}(\boldsymbol{k}) = E(\boldsymbol{k}+\boldsymbol{Q})$. Thus, we can see that the twist introduces a shift in the $\boldsymbol{k}$-mesh of the N-site cluster by an amount $\boldsymbol{Q}$. By summing over all values of $\boldsymbol{Q}$ one recovers all the energies and eigenvectors of the original $\tilde{N}$-site cluster exactly. The advantage of this method is that also for interacting systems, one obtains a set of approximated energies for a larger $\tilde{N}$-site cluster out of a smaller N-site cluster with a cost of computing time that increases linearly with the number of sites ($\sim \tilde{N}/N$). However, the disadvantage of this method of reducing finite size effects is, that one has to run the MC simulation for each $\boldsymbol{Q}$ independently. In addition, if one averages only over a few values of $\boldsymbol{Q}$, the response functions show artificial oscillation effects which are related to $\boldsymbol{Q}$.

---

[11] This actually means $\eta \gtrsim |E_{n+1}-E_n|$

[12] In fact this method is always used in combination with one of the other methods discussed in this section.

[13] Please note that translational invariance is restored *after* the averaging over all phase configurations.

[14] Mean-field always includes BCS.

As we will see below, the twisted boundary condition integration technique is related to Assaad's method of introducing a magnetic field. In fact, whereas the magnetic field in Assaad's method is applied perpendicular to the 2D plane, the twist in the boundary condition corresponds to a magnetic flux Φ threaded through the center of the torus which is formed out of the 2D plane [73, 107]. The magnitude of the flux Φ is given by $\Phi/\Phi_0 = Q_x L/2\pi$.[16] The twisted boundary condition method was used in [108], however, it is much less effective than Assaad's method and even more computing time consuming. In Assaad's method one just has to apply a flux of strength $\Phi = \Phi_0$ for a given lattice size, whereas for the twisted boundary technique, one formally would have to integrate the flux over $0 \leq \Phi < \Phi_0$.

2.6.2 Peierls-Factors, Part I — static magnetic field

The standard way of introducing a magnetic field into a second quantized tight-binding lattice Hamiltonian is by means of the so-called Peierls-Factors [109]. In the following we want to motivate the Peierls-Factors for a non-interacting electron system. The generalization to an interacting many-particle system is straightforward.

The single particle propagator $\mathcal{U}(\boldsymbol{i},t;\boldsymbol{j},t_0) \equiv \langle \boldsymbol{i},t|\boldsymbol{j},t_0\rangle$ of an electron can be written as Feynman path integral [46, 110]:

$$\mathcal{U}(\boldsymbol{i},t;\boldsymbol{j},t_0) = \int_{\boldsymbol{j}}^{\boldsymbol{i}} \mathcal{D}[\boldsymbol{l}(t)]\, e^{\frac{i}{\hbar}\int_{t_0}^{t} L_0(\boldsymbol{l}(t),\dot{\boldsymbol{l}}(t))\,dt}, \tag{2.79}$$

where L_0 is the corresponding single-particle Lagrangian without magnetic field. In the presence of a static magnetic field one has to make the substitution

$$L_0 \to L_0 + \frac{e}{c}\,\dot{\boldsymbol{l}}(t)\boldsymbol{A}(\boldsymbol{l}), \tag{2.80}$$

---

[15] The gauge transformation is given by $c_{\boldsymbol{i}\sigma} \to e^{-i\boldsymbol{Q}\boldsymbol{i}} c_{\boldsymbol{i}\sigma}$.

[16] Similarly $\Phi/\Phi_0 = Q_y L/2\pi$, since there are two "centers" through which the flux can be threaded.

with $e < 0$ the charge of the electron and $\boldsymbol{A}(\boldsymbol{l})$ the vector potential. Thus, the single-particle propagator now has the form

$$\mathcal{U}(\boldsymbol{i},t;\boldsymbol{j},t_0) = \int_{\boldsymbol{j}}^{\boldsymbol{i}} \mathcal{D}[\boldsymbol{l}(t)]\, e^{\frac{i}{\hbar}\int_{t_0}^{t} L_0(\boldsymbol{l}(t),\dot{\boldsymbol{l}}(t))\,dt} \cdot e^{\frac{i}{\hbar}\int_{t_0}^{t} \frac{e}{c}\,\dot{\boldsymbol{l}}(t)\boldsymbol{A}(\boldsymbol{l})\,dt}, \tag{2.81}$$

which means that the electron picks up an additional phase $\sim e^{\frac{i}{\hbar}\int_{t_0}^{t} \frac{e}{c}\,\dot{\boldsymbol{l}}(t)\boldsymbol{A}(\boldsymbol{l})\,dt}$ for each path contributing to the propagator in Eq. (2.81). On the other hand, the matrix elements of the time evolution operator in coordinate space for a tight-binding Hamiltonian H_0 are given by ($\boldsymbol{i} \neq \boldsymbol{j}$)

$$\begin{aligned}\mathcal{U}(\boldsymbol{i},t;\boldsymbol{j},t_0) &= \langle \boldsymbol{i}|e^{-\frac{i}{\hbar}H_0(t-t_0)}|\boldsymbol{j}\rangle \\ &\approx \left(-\frac{i}{\hbar}\right) t_{\boldsymbol{ij}}\,(t-t_0) + \frac{1}{2}\sum_{\boldsymbol{k}}\left(-\frac{i}{\hbar}\right)^2 t_{\boldsymbol{ik}}\,t_{\boldsymbol{kj}}\,(t-t_0)^2 + \dots\ .\end{aligned} \tag{2.82}$$

Here, the first term can be interpreted as the contribution from the direct path from $\boldsymbol{j}$ to $\boldsymbol{i}$, whereas the second term is the contribution from a path where the electron first moves from $\boldsymbol{j}$ to $\boldsymbol{k}$ and then from $\boldsymbol{k}$ to $\boldsymbol{i}$ and so on. Therefore, it is obvious from comparing Eq. (2.82) with Eq. (2.81) that the hopping-matrix element $t_{\boldsymbol{ij}}$ in the presence of a static magnetic field has to acquire an additional phase factor $\sim e^{i\frac{e}{\hbar c}\int_{t_0}^{t} \dot{\boldsymbol{l}}(t)\boldsymbol{A}(\boldsymbol{l})\,dt}$. Thus, one has to make the substitution

$$t_{\boldsymbol{ij}} \longrightarrow t_{\boldsymbol{ij}}\, e^{i\frac{e}{\hbar c}\int_{\boldsymbol{j}}^{\boldsymbol{i}} \boldsymbol{A}(\boldsymbol{l})\,d\boldsymbol{l}}, \tag{2.83}$$

where the integral has to be evaluated by taking only the direct path (straight line) from $\boldsymbol{j}$ to $\boldsymbol{i}$ into account.[17]

The vector potential of a static magnetic field $\boldsymbol{B}$ in z-direction is given by $\boldsymbol{A}(\boldsymbol{l}) = (-\frac{1}{2}By,\, \frac{1}{2}Bx,\, 0)$ ($\boldsymbol{A}(\boldsymbol{l}) = (0,\, Bx,\, 0)$) for symmetric (asymmetric) gauge. However, the torus geometry imposes some additional restrictions on $\boldsymbol{A}(\boldsymbol{l})$ [102]. Firstly, the Hamiltonian has to look the same after a translation of the amount $L\boldsymbol{e}_x$ ($L\boldsymbol{e}_y$). In order to fulfill this constraint, the translation of the argument of the vector potential has to be absorbed in a gauge transformation [110]

$$\begin{aligned}\boldsymbol{A}(\boldsymbol{l} + L\boldsymbol{e}_x) &= \boldsymbol{A}(\boldsymbol{l}) + \nabla\chi_x(\boldsymbol{l}), \\ \boldsymbol{A}(\boldsymbol{l} + L\boldsymbol{e}_y) &= \boldsymbol{A}(\boldsymbol{l}) + \nabla\chi_y(\boldsymbol{l}),\end{aligned} \tag{2.84}$$

which is compensated by choosing the boundary conditions

$$\begin{aligned}c^{\dagger}_{\boldsymbol{i}+L\boldsymbol{e}_x} &= e^{i\frac{2\pi}{\Phi_0}\chi_x(\boldsymbol{i})}\, c^{\dagger}_{\boldsymbol{i}}, \\ c^{\dagger}_{\boldsymbol{i}+L\boldsymbol{e}_y} &= e^{i\frac{2\pi}{\Phi_0}\chi_y(\boldsymbol{i})}\, c^{\dagger}_{\boldsymbol{i}}.\end{aligned} \tag{2.85}$$

Secondly, the translation operators $T_{L\boldsymbol{e}_x}$ ($T_{L\boldsymbol{e}_y}$) in the presence of a magnetic field belong to the magnetic translation group [111]. In order for them to mutually commute, one needs in addition the requirement of flux quantization

$$BL^2 = n\,\Phi_0, \tag{2.86}$$

---

[17] On the tight-binding lattice, one has to limit the paths contributing to the phase factor to straight lines connecting $\boldsymbol{j}$ with $\boldsymbol{i}$. The consequences of this approach for transport properties like the optical conductivity will be discussed in Sect. 4.3.

where n is an integer.

For Assaad's method one uses $B = \Phi_0/L^2$. Hence, the next-neighbor hopping matrix elements take the form

$$\begin{aligned} t_{\boldsymbol{ij}} &= -t\, e^{-i\frac{\pi}{L^2} i_y} && \text{for} \quad \boldsymbol{j} = \boldsymbol{i} + \boldsymbol{e}_x, \\ t_{\boldsymbol{ij}} &= -t\, e^{i\frac{\pi}{L^2} i_x} && \text{for} \quad \boldsymbol{j} = \boldsymbol{i} + \boldsymbol{e}_y, \end{aligned} \tag{2.87}$$

for symmetric gauge and

$$\begin{aligned} t_{\boldsymbol{ij}} &= -t && \text{for} \quad \boldsymbol{j} = \boldsymbol{i} + \boldsymbol{e}_x, \\ t_{\boldsymbol{ij}} &= -t\, e^{i\frac{2\pi}{L^2} i_x} && \text{for} \quad \boldsymbol{j} = \boldsymbol{i} + \boldsymbol{e}_y, \end{aligned} \tag{2.88}$$

for asymmetric gauge. The boundary conditions are given by

$$\begin{aligned} c^{\dagger}_{\boldsymbol{i}+L\boldsymbol{e}_x} &= e^{i\frac{\pi}{L} i_y} c^{\dagger}_{\boldsymbol{i}}, \\ c^{\dagger}_{\boldsymbol{i}+L\boldsymbol{e}_y} &= e^{-i\frac{\pi}{L} i_x} c^{\dagger}_{\boldsymbol{i}}, \end{aligned} \tag{2.89}$$

for symmetric gauge and

$$\begin{aligned} c^{\dagger}_{\boldsymbol{i}+L\boldsymbol{e}_x} &= e^{i\frac{2\pi}{L} i_y} c^{\dagger}_{\boldsymbol{i}}, \\ c^{\dagger}_{\boldsymbol{i}+L\boldsymbol{e}_y} &= c^{\dagger}_{\boldsymbol{i}}, \end{aligned} \tag{2.90}$$

for asymmetric gauge. Using two different gauges (symmetric vs. asymmetric) is a very useful test for the correctness of the calculations, since the results should not depend on the gauge for a gauge invariant Hamiltonian. As one can see from Eqs. (2.89) and (2.90), Assaad's method of reducing finite size effects introduces many different boundary conditions, all at the same time, in addition to generating a complex hopping parameter.

2.6.3 Gauge-invariant vs. non-gauge-invariant implementation

The implementation of Assaad's method for a gauge-invariant Hamiltonian is straight forward. For a non-gauge-invariant BCS Hamiltonian there are, however, two possible ways to introduce the magnetic field. The physically correct way would be to first introduce the magnetic field and then make the BCS mean-field approximation. In that way, the magnetic field couples only to the hopping terms in H_0 (Eq. (2.2)) so that after the BCS approximation, the Hamiltonian is no longer gauge-invariant due to the pair creation operators $\sim c^{\dagger}_{\boldsymbol{i}\uparrow} c^{\dagger}_{\boldsymbol{i}+\delta\downarrow}$ occurring in the interaction term (Eq. (2.3)).

On the other hand, we can start with the BCS Hamiltonian and perform the particle-hole transformation defined in Eq. (2.13). After the particle-hole transformation, which only effects the spin-down operators, the pairing term transforms into a next-neighbor spin-flip hopping term

$$c^{\dagger}_{\boldsymbol{i}\uparrow} c^{\dagger}_{\boldsymbol{i}+\delta\downarrow} \rightarrow \psi^{\dagger}_{\boldsymbol{i}\uparrow} \psi_{\boldsymbol{i}+\delta\downarrow}. \tag{2.91}$$

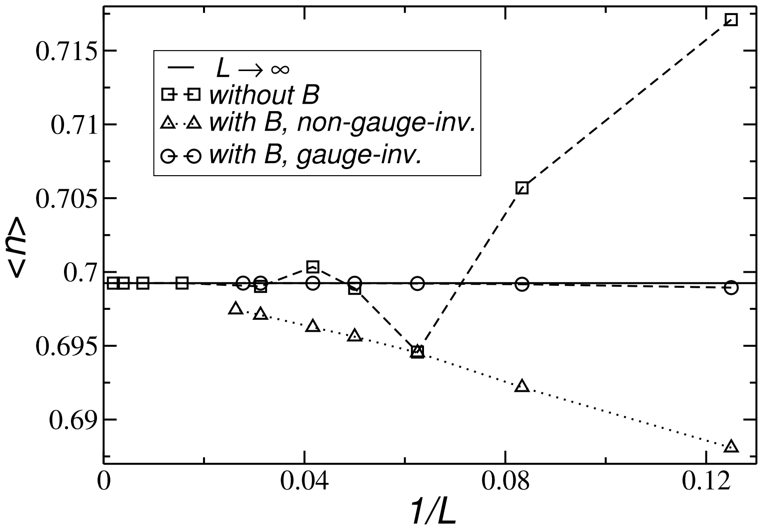

Figure 2.6: Mean particle number per lattice site $\langle n \rangle$ as a function of the inverse lattice size $1/L$ for fixed chemical potential μ. The results have been obtained from the BCS d-wave Hamiltonian using different methods to reduce finite-size effects. The straight line is the result for $L \longrightarrow \infty$.

If we consider this particle-hole transformed Hamiltonian as the original electronic Hamiltonian[18], then the magnetic field also couples to the terms $\sim \psi^\dagger_{\boldsymbol{i}\uparrow}\psi_{\boldsymbol{i}+\delta\downarrow}$. These spin-flip hopping-terms correspond to the pairing terms of the original Hamiltonian H_1 (Eq. (2.3)). In this way, the pairing amplitude $\Delta_{\boldsymbol{ij}}$ in H_1 acquires a phase factor similarly to the hopping-matrix elements $t_{\boldsymbol{ij}}$ in H_0 (see Eqs. (2.68) – (2.71)). As a result, the coupling to the vector potential is now implemented in a gauge-invariant manner.[19] Since the magnetic field is only a means to reduce finite size effects which disappears in the thermodynamic limit ($L \longrightarrow \infty$), it has no physical relevance and therefore we are free to choose the version that works better in reducing finite-size effects.

Fig. 2.6 shows the mean occupation number $\langle n \rangle$ for the BCS d-wave Hamiltonian ($\Delta_{sc} = 1.0t$) as a function of lattice size L for fixed chemical potential μ. Without magnetic field, strong finite-size oscillations are visible as function of $1/L$. The inclusion of a *physical* magnetic field into the BCS Hamiltonian strongly attenuates the oscillations, however, the convergence towards the exact result for $L \longrightarrow \infty$ is still fairly slow. Since the results are not gauge-invariant, one might increase the convergence by choosing a different gauge. However, this would require an optimization procedure with respect to the gauge field. Finally, the gauge-invariant implementation of Assaad's method yields extremely good results already for an 8×8-lattice. Consequently, in all calculations where it is possible to use Assaad's method, we have chosen the gauge-invariant implementation. We stress again, that this magnetic field has no physical meaning and is just needed to reduce finite size effects.[20]

---

[18] In fact, this treatment corresponds to reversing the charge of the spin-down electrons ($e \longrightarrow -e$).

[19] For s-wave pairing (Eq. 2.7), the on-site pair-creation operator $c^\dagger_{\boldsymbol{i}\uparrow}c^\dagger_{\boldsymbol{i}\downarrow}$ transforms into an on-site spin-flip operator $\psi^\dagger_{\boldsymbol{i}\uparrow}\psi_{\boldsymbol{i}\downarrow}$ and thus acquires no phase factor. However, also there the charge of the spin down electrons has to be reversed in order to obtain a gauge-invariant description due to $c_{\boldsymbol{i}\downarrow}c^\dagger_{\boldsymbol{j}\downarrow} \longrightarrow \psi^\dagger_{\boldsymbol{i}\downarrow}\psi_{\boldsymbol{j}\downarrow}$.

[20] A physical magnetic field also has to be included in the effective phase action of our phase-fluctuation model

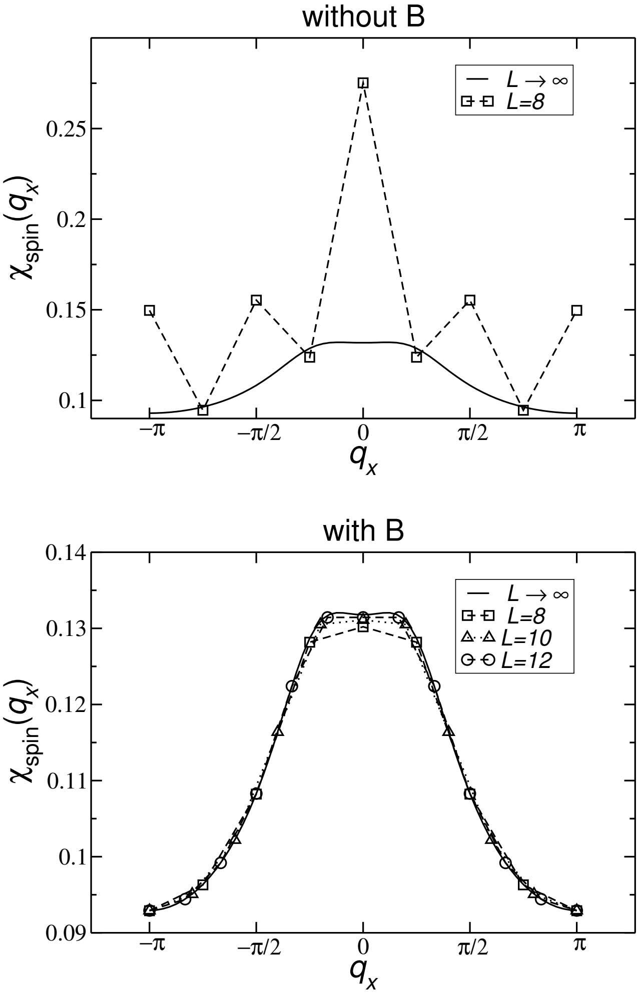

Figure 2.7: Static spin susceptibility $\chi_{spin}(q_x, q_y = 0, \omega = 0)$ calculated from the tight-binding Hamiltonian H_0 at half-filling for different lattice sizes L. The full line is the result for $L \longrightarrow \infty$. Top: $\chi_{spin}(q_x)$ calculated without magnetic field. Bottom: $\chi_{spin}(q_x)$ calculated using Assaad's method of including a static magnetic field $B = \frac{\Phi_0}{L^2}$. Please note the much smaller scale of the lower figure.

As was pointed out before, the magnetic field destroys the lattice translation symmetry. Therefore, Assaad's method is only useful for correlation functions in the limit of $\boldsymbol{q} \longrightarrow 0$, where one effectively averages over all lattice points. The only exception is the static spin susceptibility $\chi_{\mathrm{spin}}(\boldsymbol{q})$ which is shown in Fig. 2.7 for different lattice sizes as a function of q_x, with $q_y = 0$. It is a further example of how efficiently this method works in reducing finite-size effects. The reason as to why we obtain these amazingly good results despite the destruction of translation symmetry is due to the fact that the charge degrees of freedom directly couple to the vector potential whereas the spin degrees of freedom couple to the magnetic field.

(see Eq. (2.41)).

2.7 Optimization of algorithms for high-performance computing

Many-particle physics tries to link the microscopic quantum-mechanical world to our macroscopic everyday world. The bridge between these two worlds is the number of particles. In order to obtain macroscopic quantities, one needs to describe many-particle systems containing about 10^{23} particles. Thus, it is obvious that the limited number of lattice points, or number of quantum-mechanical states which are taken into account, is the main obstacle in all calculations. Besides the physical side of this problem, which was discussed before, one also needs deep insight into the computational side. For a numerical simulation, advanced knowledge of computer hardware and software is required in order to apply the most appropriate numerical algorithms and optimization techniques. This side of the problem is called "high performance computing" and it is still necessary to spend quite some time on the numerics despite the yearly growing computer power.

In this section we will briefly discuss some aspects of numerical optimization. To "speed up" our Monte Carlo (MC) simulation one has to mainly concentrate on three issues. Firstly, to reduce the number of different phase configurations which are effectively needed to obtain reliable results. Secondly, to use a fast diagonalization procedure. Thirdly, to implement the calculation of the correlation functions in a fast and effective way. Concerning the second and third point: an increase in speed always has to be paid with larger memory requirements. In all cases, the first step must always be to find the most effective numerical algorithm and the last step to optimize the program code for a given compiler or computer architecture.

2.7.1 Wolff's cluster algorithm vs. local Metropolis algorithm

It would take a much too long time to create the different phase configurations $\{\varphi\}$ in the MC simulation in a random way and then weight each configuration with the Boltzmann factor $e^{-\beta F_{XY}[\{\varphi\}]}$ until one obtains reliable results. Instead, we use the technique of importance sampling [112]. There, one starts from a phase configuration $\{\varphi\}$ and then constructs a new configuration $\{\varphi'\}$. Each change $\{\varphi\} \to \{\varphi'\}$ is associated with a certain transition probability $P(\{\varphi\} \to \{\varphi'\})$. That means, one draws a uniformly distributed random number r with $0 < r < 1$. If $r < P(\{\varphi\} \to \{\varphi'\})$, then the new configuration $\{\varphi'\}$ is accepted, else, the old configuration $\{\varphi\}$ is taken into account for a second time. The transition probabilities $P(\{\varphi\} \to \{\varphi'\})$ have to be constructed in such a way that they generate the stationary distribution $e^{-\beta F_{XY}[\{\varphi\}]}$. This requirement of *detailed balance* can be written as

$$e^{-\beta F_{XY}[\{\varphi\}]}\, P(\{\varphi\} \to \{\varphi'\}) = e^{-\beta F_{XY}[\{\varphi'\}]}\, P(\{\varphi'\} \to \{\varphi\}). \tag{2.92}$$

Eq. (2.92) gives us some freedom to define $P(\{\varphi\} \to \{\varphi'\})$ such that it generates the relevant phase configurations in a very effective and computing time saving way.

One way to define $P(\{\varphi\} \to \{\varphi'\})$ is the so-called Metropolis algorithm. There, a new configuration is always accepted if it is energetically favorable ($\Delta F_{XY} < 0$).[21] If $\Delta F_{XY} > 0$, the acceptance rate is given by $P(\{\varphi\} \to \{\varphi'\}) = e^{-\Delta F_{XY}}$. The updating scheme is purely local. That is, one starts with a lattice site $\boldsymbol{i}$ and proposes a change $\varphi_{\boldsymbol{i}} \to \varphi'_{\boldsymbol{i}}$.[22] Then, one continues with the neighboring site, moving along a well defined path through the whole lattice. One complete pass through of the lattice is called sweep. It is clear that if some form of long-range order starts to develop, the local updating rate goes to zero, since all the neighboring spins (phases) tend to be aligned along the same direction. Hence, every change of one single spin (phase) always increases the energy and is thus very unlikely. Therefore, a system close to a phase transition gets trapped for a very long time in one statistical configuration. This is the problem of *critical slowing down*, where the number of sweeps needed to obtain a statistical independent configuration increases dramatically due to the domains that start to develop. These domains tend to oscillate and a complete flip of one domain is rather unlikely.

---

[21] $\Delta F_{XY} = F_{XY}[\{\varphi'\}] - F_{XY}[\{\varphi\}]$.

Swendsen and Wang (SW) [113] proposed an algorithm to overcome the problem of critical slowing down for Potts spin models, like the Ising model, where the spins take on certain discrete values. Their idea was to replace the single spin as elementary unit by a cluster of spins. The clusters are constructed in such a way as to ensure detailed balance. Instead of a single spin, the whole cluster is flipped in the updating procedure. Wolff [114] proposed an extension of the SW method to continuous spin models like the XY model. He was able to show [115] that his algorithm completely eliminates critical slowing down for the XY model. In Wolff's method, one starts with a random lattice site $\boldsymbol{i}$ and then starts growing a cluster around this site. In addition, one generates a random vector defining a hyperplane. The spin on each site added to the cluster is reflected with respect to the hyperplane. As in the SW algorithm, detailed balance is ensured through the way the cluster is constructed [114].

The cluster updating schemes work at arbitrary temperatures. However, for practical purposes it turned out, that the local Metropolis algorithm performs more efficiently on the Hitachi SR8000-F1 at high temperatures than Wolff's cluster algorithm. This is due to the recursive book-keeping procedure needed for the cluster construction. Therefore, we used the local Metropolis algorithm at high temperatures $T > 1.5T_{KT}$ where the phase correlation length is of order unity ($\xi \approx 1$). At lower temperatures $T \lesssim 1.5T_{KT}$, Wolff's cluster algorithm was used with no sign of any critical slowing down at the Kosterlitz-Thouless transition $T = T_{KT}$.

2.7.2 Different Monte-Carlo error-estimators

The most important point of the MC simulation is the sampling of uncorrelated phase configurations. A measure for the number of MC updating steps t_n (Metropolis sweeps or cluster updates) needed to obtain a statistically independent phase configuration is the auto-correlation time τ [116]. After τ updating steps, the new phase configuration should be completely uncorrelated to the old one. The auto-correlation time τ can be obtained from the time correlation function [116]

$$c(t_n) = \left\langle e^{i\varphi_{\boldsymbol{i}}(t_0)}\, e^{-i\varphi_{\boldsymbol{i}}(t_n)} \right\rangle, \tag{2.93}$$

where $\langle \cdots \rangle$ is the average over phase configurations and lattice sites $\boldsymbol{i}$.

---

[22] This is implemented numerically by drawing a random number $d\varphi$ between $-\frac{\pi}{2}$ and $\frac{\pi}{2}$, and adding $d\varphi$ to the old phase.

The so-called binning analysis is another method to check the statistical independence of the $n = 1 \cdots N$ different quantum-mechanical expectation values $A(t_n)$ which were calculated from N different phase configurations. In this method, M expectation values at a time are combined into one bin, so that for example the first bin contains $\{A(t_1), \cdots, A(t_M)\}$. For each of the N/M bins, the standard deviation σ_{bin} is calculated. Then, the mean standard deviation $\bar{\sigma}_{\text{bin}}$ averaged over all bins is computed for different values of M. As long as the expectation values contained in each bin are correlated, $\bar{\sigma}_{\text{bin}}$ increases as a function of M. Finally, $\bar{\sigma}_{\text{bin}}$ starts to converge once $t_M - t_1 \gg \tau$, which is another estimate for the auto-correlation time τ.

Alternatively, one can calculate the higher statistical moments of the sample $\{A(t_1), \cdots, A(t_N)\}$. These are the skewness and the kurtosis [117]. The skewness is a measure for the asymmetry of the distribution around its mean. The kurtosis measures the relative peakedness or flatness of the sample distribution relative to a normal (Gaussian) distribution. Thus, they both indicate a possible correlation of the sample values. However, also for an ideal Gaussian distribution, skewness and kurtosis fluctuate quite strongly for a finite sample, which makes them only of limited use.

In our MC simulation, we first calculated the auto-correlation time τ from the time correlation function (Eq. (2.93)) for a given temperature and lattice size and then used $t_{n+1} - t_n \gtrsim \tau$. This is most convenient, since τ can be obtained solely from the XY model without the computing time intensive diagonalization of the fermionic Hamiltonian. After the MC simulation of the complete phase fluctuation Hamiltonian, we re-checked the statistical independence of the calculated expectation values with the help of a binning analysis and the calculation of the higher statistical moments. Furthermore, as we always start the MC simulation from a random phase configuration, we performed $O(\tau)$ warm-up sweeps, in order to ensure, that thermal equilibrium is reached before the measurement of the expectation values $\{A(t_1), \cdots, A(t_N)\}$ starts.

After the statistical independence of the sample of expectation values for different phase configurations $\{A(t_1), \cdots, A(t_N)\}$ is guaranteed, one next needs to estimate the statistical MC error of the mean expectation value $\bar{A} = \frac{1}{N} \sum_{n=1}^{N} A(t_n)$. Since we are interested in the statistical MC error of the mean expectation value and not the fluctuation of expectation values around the mean, which are solely a function of temperature for classical phase fluctuations, we group as before respectively M expectation values $A(t_n)$ into $N_{\text{bin}} = N/M$ bins. Then, for each bin the mean expectation value $\bar{A}_{\text{bin}}(m)$, with $m = 1, \cdots, N/M$ is calculated.

Next, one needs a measure for the statistical Monte Carlo error which can be estimated from the statistical fluctuations of $\bar{A}_{\text{bin}}(m)$ around $\bar{A} = \frac{M}{N} \sum_{n=1}^{N/M} \bar{A}_{\text{bin}}(m)$ for $N, M \gg 1$. The standard procedure would be to calculate the standard error

$$\sigma_s = \left[\frac{1}{N_{\text{bin}}(N_{\text{bin}} - 1)} \sum_{m=1}^{N_{\text{bin}}} (\bar{A}_{\text{bin}}(m) - \bar{A})^2 \right]^{\frac{1}{2}} . \tag{2.94}$$

However, it turns out that for the uncorrelated but small number of data points $\bar{A}_{\text{bin}}(m)$, this yields a much too large error. Due to the limited number of bins, one therefore needs a more robust error estimator. The jackknife and bootstrap estimators are the methods of choice, if one needs to estimate the standard error of a statistic of independent and identically distributed variables from a small sample [118].

The jackknife estimate of the standard error is

$$\sigma_J = \left[\frac{N_{\text{bin}}-1}{N_{\text{bin}}} \sum_{i=1}^{N_{\text{bin}}} (\overline{A}_{(i)} - \overline{A}_{(\cdot)})^2 \right]^{\frac{1}{2}} , \tag{2.95}$$

where $\overline{A}_{(i)} = \frac{1}{N_{\text{bin}}-1} \sum_{m \neq i} \overline{A}_{\text{bin}}(m)$ is the sample average with the ith bin deleted and $\overline{A}_{(\cdot)} = \frac{1}{N_{\text{bin}}} \sum_{i=1}^{N_{\text{bin}}} \overline{A}_{(i)}$ the average of the deleted averages.

The bootstrap works as follows [118]: (i) draw from the original sample $\{\overline{A}_{\text{bin}}(1), \cdots, \overline{A}_{\text{bin}}(N_{\text{bin}})\}$ a bootstrap sample $\{\overline{A}^{*}_{\text{bin}}(1), \cdots, \overline{A}^{*}_{\text{bin}}(N_{\text{bin}})\}$ by N_{bin} random draws with replacement. (ii) compute the bootstrap replication $\overline{A}^{*b} = \sum_{m=1}^{N_{\text{bin}}} \overline{A}^{*}_{\text{bin}}(m)$. Repeat step (i) and (ii) a large number B of times. The bootstrap estimate for the standard error is then given by

$$\sigma_B = \left[\frac{1}{B-1} \sum_{b=1}^{B} (\overline{A}^{*b} - \overline{A}^{*\cdot})^2 \right]^{\frac{1}{2}} , \tag{2.96}$$

where $\overline{A}^{*\cdot} = \frac{1}{B} \sum_{b=1}^{B} \overline{A}^{*b}$.

In general, the bootstrap is the best method to obtain a reliable standard error of a statistical distribution from a small random sample. We carefully compared all error estimators by repeated MC runs. In our case, jackknife and bootstrap yield nearly identical results. Therefore, we have chosen the less computing time intensive jackknife method as MC error estimate.[23]

2.7.3 Vectorization and the avoidance of cache-trashing

Having optimized the computational algorithms and number of MC steps needed to obtain reliable results, one finally needs to optimize the program code for a given computer architecture to "speed up" the MC simulation. Generally, one can always reduce the number of calculations at the expense of memory. Examples for computing time intensive functions are the sine, cosine and exponentional function or the determination of neighboring lattice sites, where modulo calculations are necessary. Since we are performing our calculations on a lattice, we only need the function values for a set of $N = L \times L$ discrete points.[24] Consequently, we can calculate all function values at the beginning of the program and save them in a table (vector or matrix). Instead of calculating the exponential any time it is needed, one only needs to calculate it once and thereafter only look it up in the table, which increases the program performance tremendously.

Furthermore, everything has to be removed from the inner loops which does not necessarily have to be calculated there. Large nested loops should only contain vectors or matrices and no functions or conditional statements like if-clauses. This procedure is called vectorization and is facilitated by a special processor architecture with special vector registers for a fast (pseudo) parallel addition and multiplication of vectors [119].

By replacing all functions by vectors and making the vector sizes larger and larger, one finally reaches a point where the memory access time sets a limit to a further increase of performance. All vectors have to be loaded from the main memory into the vector-processor registers which becomes the bottleneck of the whole calculation. A memory with a fast access time is expensive and therefore all computers have two kinds of memory. A large but slow main memory and a fast but small memory which is called cache. To make sure that the processor does not have to wait for many cycles until a vector is loaded into the registers, one has to take care that the vectors which are needed next are already in the fast cache memory.

---

[23] In fact, one can show [118] that the jackknife is almost a bootstrap estimate itself.

[24] An exception is the cosine in the XY free energy, which we have to calculate for continuous values of phases.

The cache is divided into different cache lines, where in a direct mapped cache, each cache line loads data only from a well-defined successive region of main memory [119]. Since the main memory is much larger than the cache, different regions of main memory map to the same cache line. For very large vectors with a size s of large powers of 2 ($s = 2^l$, $l \gg 1$), it can happen that two vectors (A, B) which, for example, should be added, are mapped to the same cache line. In this case, first vector A is loaded into the cache but then it is replaced by vector B, so that only one vector at a time is in the cache. Therefore, for each vector entry the whole vector has to be reloaded from main memory into the cache and the memory performance suddenly completely breaks down.

This effect is called cache-trashing and was a serious problem on the Hitachi SR8000-F1 for large lattice sizes ($N \gtrsim 30 \times 30$). It can be circumvented by avoiding large powers of 2, which practically means to make the vectors slightly larger (for example: $s = 2^l + 19, l \gg 1$). This ensures that the vectors are now loaded into different cache lines [119]. Finally, the repeated throw of one dice can be done in parallel by many dices, as long as the dices are not manipulated.[25] Thus, the MC simulation can most easily be parallelized on a massively parallel system by using MPI (Message Passing Interface[26]).

---

[25] This, one has to make sure by initializing the “random number” generators properly.

[26] See, for example: http://www.lam-mpi.org/ and http://www.mpi-forum.org/ (6/15/2004).

3

Single-particle properties

In this chapter we calculate as a first application of our phase-fluctuation model several single-particle properties and compare them with experiment. We start with the simplest quantity, which is the tunneling conductance. The tunneling conductance is determined by the density of states $N(\omega)$ of the many-electron system. Then, we apply our model to angle resolved photoemission spectroscopy (ARPES) experiments, which measure the single-particle spectral weight $A(\boldsymbol{k},\omega)$. In this way we want to further confirm the principle consistency of our phenomenological approach and its usefulness in explaining experimental results. Finally, we discuss to what extent a possible alternative high-temperature approach based on the coherent potential approximation (CPA) can serve as a useful tool in analyzing the experimental results in the pseudogap phase of the cuprates.

3.1 Tunneling conductance

The general idea of tunneling experiments is that there is a nonzero probability for electrons to quantum-mechanically tunnel between two conductors separated by an insulating region. The tunneling probability falls exponentially with the distance between the two conductors. In a typical experimental setup, the tunneling current $I(V)$ is measured as a function of the applied potential difference V across the tunneling junction. The differential conductance $G = \frac{dI}{dV}$ is then directly related to the density of states of the two conductors on both sites of the insulating barrier.

In a scanning tunneling microscopy (STM) experiment, a metallic tip is scanning over the superconducting copper-oxide plane. Therefore, one has a superconductor-normal tunneling and the differential conductance G_{sn} is given by [7]

$$G_{sn}(V,T) \equiv \frac{dI_{sn}(V,T)}{dV} \sim \int_{-\infty}^{+\infty} N(\omega)\, \frac{\partial f(\omega - V)}{\partial V}\, d\omega, \tag{3.1}$$

with $N(\omega)$ the density of states of the superconductor and $f(\omega) = [\exp(\omega/T) + 1]^{-1}$ the Fermi function. Here, one assumes that the density of states of the metal is constant over the relevant energy range of order of the superconducting gap Δ_{sc}. Thus, the tunneling conductance in STM experiments is proportional to the temperature broadened local density of states of the superconductor.

On the experimental side, numerous controversial papers on the tunneling conductance in the cuprates were published in recent years. This is a general problem of high-T_c superconductivity, where many different experiments were carried out on different samples (with varying chemical composition, doping and sample preparation) using different experimental techniques and yielding different results. In fact, this could be a sign for the unstable fixpoint discussed in the introduction. Therefore, we first summarize and clarify the experimental situation and try to elaborate the universal and intrinsic properties of the CuO_2 planes.

3.1.1 Experimental results

In analyzing the experimental tunneling spectra, one always has to keep in mind, that tunneling and photoemission are surface sensitive probes, where the detected electrons stem — at most — from the first few CuO_2 layers. Thus, one always has to face the general problem as to what are surface effects and what are true bulk properties. A similar question arises in case of local inhomogeneities, namely whether they are due to a true phase separation of the electronic system or just impurity caused.

local inhomogeneities

Various STM experiments on $Bi_2Sr_2CaCu_2O_{8+\delta}$ (Bi2212) show a spatial variation of the local density of states (DOS) and the SC gap [120, 121]. Superconducting domains of size $\sim 3\,$nm, with a well-defined SC gap and coherence peaks, seem to live in underdoped Bi2212 on an electronically distinct background with a broader pseudogapped-like structure [120, 122]. These structures first were considered as a consequence of doping a Mott insulator, where the doped holes concentrate in certain hole-rich superconducting domains [121, 122].

However, after Fourier transforming the spatial STM modulations and comparing their dispersion with ARPES experiments, it turned out that the characteristic modulation wavevectors can be related to elastic quasiparticle scattering vectors between different regions of the Fermi surface close to the nodal points [123, 124]. On the theoretical side, it was verified, that quantum interference due to weak impurity scattering potentials has a non-neglectable effect on the observed STM spectra for experimentally relevant impurity concentrations [125, 126]. Thus, the DOS modulations are predominantly a quasiparticle interference pattern due to elastic scattering from impurity potentials with no other order parameter or competing electronic phase required.

On the other hand, experiments on thin films of Bi2212 indicate that crystal disorder can indeed produce electronic inhomogeneities with small superconducting regions coexisting with dominating semiconducting areas [127]. This is further confirmed by experiments on heavily Pb-doped Bi2212, where no correlations between the distribution of Pb impurities and the STM local DOS variations was found [128], but a clear correlation between the excess oxygen introduced crystal disorder and pseudogap-like STM spectra.

Thus, without impurity quantum-interference-scattering and (surface) crystal disorder, one would expect the electronic phase to be truly homogenous. This is further supported by the analysis of specific heat and NMR data on Bi2212, where no indication for phase segregation or gross inhomogeneity of bulk Bi2212 was found [129].

peak-dip-hump feature

STM experiments on $Bi_2Sr_2CuO_{6+\delta}$ (Bi2201) and Bi2212 clearly show, that the pseudogap continously develops out of the SC gap as a function of temperature [24, 26]. The characteristic SC coherence peaks dissappear above T_c but the SC gap shows now BCS temperature dependence and does not close at T_c. Instead the SC gap continously evolves into a pseudogap with the same magnitude. This pseudogap "fills in" with increasing temperature but its size remains constant. It is visible in STM spectra up to a temperature T^*, which can be as high as room temperature in underdoped Bi2212 samples.

On the other hand, intrinsic tunneling spectroscopy in Bi2212 and La-doped Bi2201 samples rather indicates a coexistence of SC gap and a larger pseudogap below T_c with the superconducting gap seemingly disappearing at T_c [130–132]. This is the so-called peak-dip-hump structure of intrinsic tunneling spectra, where the hump is supposed to be due to the larger pseudogap and which was also observed in trilayer $Bi_2Sr_2Ca_2Cu_3O_{10+\delta}$ (Bi2223) [133]. The general idea of intrinsic or interlayer tunneling is that each pair of CuO_2 planes, respectively, acts as a Josephson tunneling junction for a short current pulse applied along the c-direction, perpendicular to the planes. Therfore, it is a bulk sensitive probe, which is often claimed to show the true bulk properties of the density of states in contrast to the rather surface sensitive STM experiments.

Recently, it was however shown [134, 135], that the tunneling characteristics of intrinsic tunneling experiments can be reproduced qualitatively *and* quantitatively by assuming that the hump feature is simply due to Joule heating of the sample. This was done by using the experimental normal state out-of-plane resistance $R_c(T)$ and applying *Newton's Law of Cooling* from 1701. It is now experimentally confirmed [136, 137] that local overheating due to the poor thermal conductivity of the cuprates is a sever problem of intrinsic and perhaps even some break junction tunneling experiments. Thus, indeed, the hump features of [132] are an artefact of Joule heating. Unfortunately, no comment on this from other intrinsic tunneling groups is up to now available.

Nevertheless, STM measurements using Bi2212/vacuum/Bi2212 tunneling junctions, exhibit two kinds of pseudogap [138]. A small pseudogap comparable to the SC gap appears below T^* and continously evolves into the SC gap at T_c; and a large pseudogap of size 3–4 times the SC gap which remains open also above T^* and is possibly of spin fluctuation origin. Furthermore, there are some indications from tunneling spectra acquired for a-axis $YBa_2Cu_3O_{7-\delta}$ (YBCO) films, that one needs to take into account $\boldsymbol{k}$-dependent tunneling matrix elements in order to explain the variation of the tunneling characteristics with the surface roughness of the sample [139].

3.1.2 The d-wave case

To summarize again, the STM spectra of Ref. [24, 26] are supposed to reflect the true homogenous bulk properties of the cuprates. They show that a pseudogap with the same magnitude as the SC gap develops below a characteristic temperature T^* and evolves continously into the SC gap at T_c, where finally the characteristic SC coherence peaks appear.

In Fig. 3.1, we show the density of states $N(\omega)$ as a function of temperature, calculated from our phase fluctuation model with $d_{x^2-y^2}$-wave gap. For $T > T_c^{MF}$, the gap amplitude vanishes and the density of states exhibits the usual Van Hove peak at $\omega = 0$. For $T < T_c^{MF}$, the presence of a finite gap amplitude gives rise to a pseudogap whose size is set by $2\Delta_{sc}$. Then, as T approaches T_{KT} and the XY phase correlation length $\xi(T)$ rapidly increases, coherence peaks evolve, the separation of which is determined by $2\Delta_{sc}$. An important point is that the temperature scale over which the evolution of the coherence peaks occurs, is set by some fraction of T_{KT} ($1 < T/T_{KT} \lesssim 1.5$) which means that it appears fast on a scale set by $T_c^{MF} \gg T_{KT}$. Furthermore, the gap fills in above T_{KT} instead of closing, which is however masked by the van Hove peak at higher temperatures.

An *effective* correlation length $\xi(T)$, extracted by fitting an exponential form to the phase correlation function

$$C(\ell) = \left\langle e^{-i\varphi_{i+\ell}} e^{i\varphi_i} \right\rangle \tag{3.2}$$

is plotted versus T in Fig. 3.2 for our 32×32 lattice. The rapid onset of $\xi(T)$ as T_{KT} is approached is clearly seen. It is this sudden increase of $\xi(T)$ that is responsible for the appearance of the coherence peaks as T approaches T_{KT}. This effect is further enhanced by the 2D to 3D crossover that occurs in the actual materials.

In order to compare these results for $N(\omega)$ with scanning tunneling spectra, we have calculated $dI(V)/dV$ using the standard quasi-particle expression for the tunneling current given in Eq. (3.1). Results for $dI(V)/dV$ are displayed in Fig. 3.3. The effect of the Fermi factors in Eq. (3.1) is to provide a thermal smoothing of the quasi-particle density of states over a region of order $2T$. This becomes significant at the higher temperatures, where the prominent pseudogap dependence of $N(\omega)$ seen in Fig. 3.1 is smoothed out in $dI(V)/dV$.

One sees that the size of the pseudogap scales with the spacing between the coherence peaks and evolves continuously out of the superconducting state. Above $T \simeq 1.5T_{KT}$, coherence peaks are no longer visible in $dI(V)/dV$ but the pseudogap persists over a large temperature range measured in units of T_{KT}, becoming smoothed out by the thermal effects as T approaches T_c^{MF} and vanishing above T_c^{MF}.

Finally, in order to sort out band-structure effects, we have plotted in Fig. 3.4 in accordance with the experiment [26], the tunneling conductance $dI/dV_{\text{norm}} = \frac{dI/dV|_T}{dI/dV|_{T_c^{MF}}}$, normalized to its ($V$-dependent) value at $T = T_c^{MF}$. Fig. 3.4 most clearly shows, that our numerical results for the tunneling conductance $dI(V)/dV$ are very similar to the scanning tunneling measurements on Bi2212 and Bi2201 [24, 26], where the superconducting gap for $T < T_c (\equiv T_{KT})$ evolves continuously into the pseudogap regime extending up to $T = T^* (\equiv T_c^{MF})$. Exactly as in the STM experiments, the coherence peaks suddenly appear as $T_c (\equiv T_{KT})$ is approached and at higher temperatures, the pseudogap fills in rather than closing. Furthermore, the temperature range associated with the pseudogap regime can be large compared with the size of the superconducting regime. All this gives strong support for the phase-fluctuation scenario of the pseudogap.

A final remark on inhomogeneities is in place here. The study of the local density of states variations caused by impurities is a very important second tool in exploring the quasi-particle states besides ARPES. In fact, quasi-particle interference due to impurity scattering can help to distinguish and rule out various alternative scenarios for the pseudogap [140]. Impurities can very easily be included in our Hamiltonian.

Unfortunately, including an impurity no longer allows us to use Assaad's method of reducing finite-size effects (see Sec. 2.6). As was pointed out before, the magnetic field destroys translation invariance. This was no problem without impurities, where local DOS and global DOS are the same. In averaging the local DOS with magnetic field over all lattice sites, we obtained amazingly good DOS curves displayed in Fig. 3.1. Including impurities no longer allows for this averaging. Without magnetic field, the finite size effects for our 32×32 lattice are of the same order of magnitude as the expected impurity-induced local DOS modulations which makes it very difficult to obtain reliable results.

3.1.3 The s-wave case — implications for electron-doped cuprates

While there is strong evidence that the hole-doped high-T_c cuprates have a $d_{x^2-y^2}$-symmetry of the SC gap, the experimental situation for the electron-doped cuprates is not as clear. The in-plane penetration depth $\lambda_{ab}(T)$ of the electron-doped cuprate superconductor $Nd_{1.85}Ce_{0.15}CuO_{4-y}$ has an exponential temperature dependence [141] which is typical for an isotropic s-wave SC gap. Furthermore, there is increasing experimental evidence for a change of the SC order parameter as a function of electron doping from a d-wave gap in the underdoped samples to a s-wave gap in overdoped samples. Tunneling experiments in $Pr_{2-x}Ce_xCuO_4$ show a zero-bias conductance peak, which is typical for Andreev bound states appearing in d-wave SC tunneling junctions, only in underdoped samples [142]. In addition, a detailed doping and temperature analysis of the penetration depth in $La_{2-x}Ce_xCuO_{4-y}$ and $Pr_{2-x}Ce_xCuO_{4-y}$ [143] further supports the picture of a transition from d- to s-wave pairing near optimal doping. Whereas quasi-particle tunneling spectra of optimally doped $Sr_{0.9}La_{0.1}CuO_2$ [144] show no zero-bias conductance peak and deviations from a pure d-wave gap. These experiments rather support an anisotropic s-wave gap in the underdoped samples. Only in strong magnetic fields, which destroy superconductivity, a pseudogap is visible in the electron doped cuprates [145]. It is not clear whether this pseudogap is caused by a competing order parameter or by the suppression of phase coherence in the magnetic field.

In view of these experiments, we consider the phase-fluctuation Hamiltonian with s-wave gap as a possible prototype Hamiltonian for the electron doped cuprates. Fig. 3.5 shows the density of states $N(\omega)$ as a function of temperature, calculated from our phase-fluctuation model with s-wave gap. The density of states exhibits the same features as in the d-wave case. The SC coherence peaks completely dissappear above $T \simeq 1.5 T_{KT}$, whereas the gap is visible up to T_c^{MF} and gradually fills in, instead of closing. These features and the smooth evolution of the pseudogap are more clearly visible in the tunneling conductivity $dI(V)/dV$ shown in Fig. 3.6.

However, there is one important additional aspect for the s-wave case: the shape of the gap changes. Below $T \simeq T_{KT}$, the gap has the characteristic form of a BCS s-wave gap. But as soon as the temperature is raised above $T \simeq 1.25T_{KT}$, the shape of the gap in the density of states (Fig. 3.5) looks very similar to the d-wave gap in Fig. 3.1. This is exemplified in Fig. 3.7 where the tunneling conductance $dI(V)/dV$ for the $d_{x^2-y^2}$-gap at $T = T_{KT}$ is compared with the tunneling conductance for the s-wave gap at $T = 1.25T_{KT}$. Both tunneling spectra have a nearly identical shape. The reason for this similarity is that the s-wave gap starts to close anisotropically above T_{KT}, which will be discussed in great detail in Sec. 3.2.

Thus, a possible alternative scenario to a quantum-critical point close to optimal doping, where the SC order parameter changes from $d_{x^2-y^2}$-wave (underdoped) to s-wave (overdoped) could be, that phase fluctuations (possibly of quantum nature) also play an important role in the electron doped cuprates and make the s-wave gap resemble a $d_{x^2-y^2}$-wave one. With this hypothesis, the experimental results can be described consistently by the assumption that the SC order parameter has s-wave symmetry *in the whole doping range*. However, in the underdoped region, close to the AF Mott insulator, (quantum) phase fluctuations start to become relevant due to the small superfluid density. These (quantum) phase fluctuations than lead to an anisotropic s-wave gap which looks very similar to a d-wave gap in tunneling experiments as shown in Fig. 3.7.

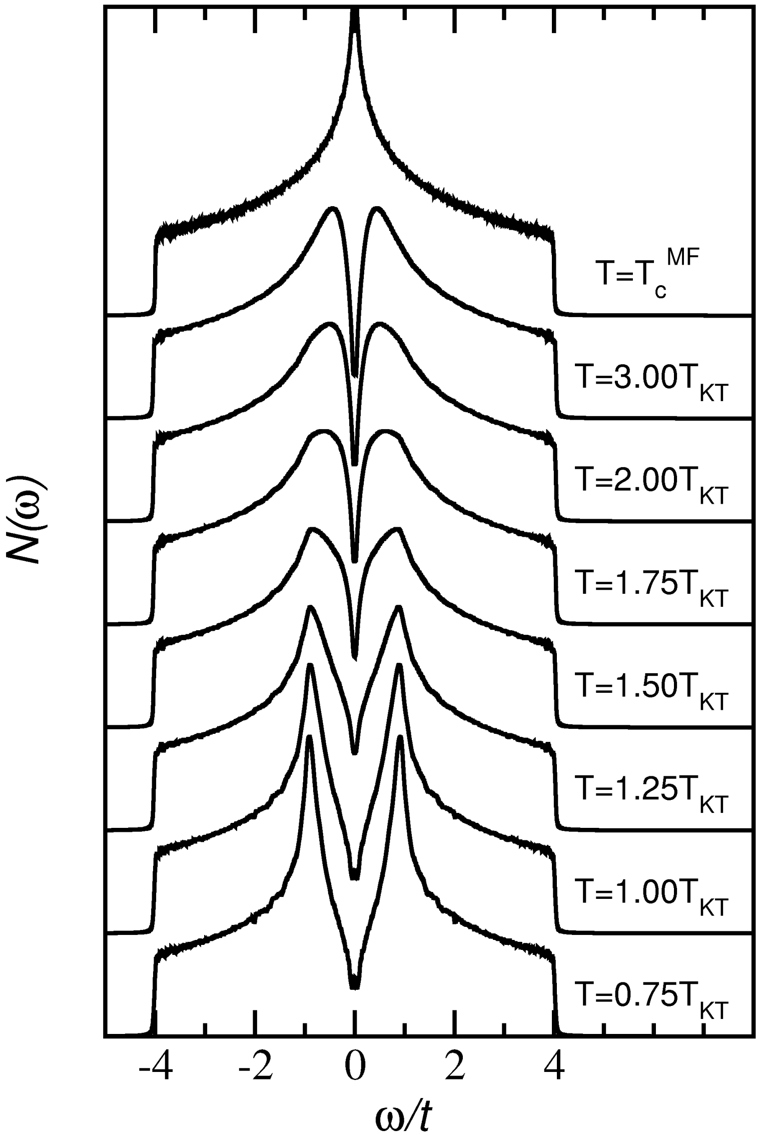

Figure 3.1: Single particle density of states $N(\omega)$ *for different temperatures* T *for a* 32×32 *lattice with* $T_{KT} = 0.1t$. *The* $d_{x^2-y^2}$*-wave gap has the size* $\Delta_{sc} = 1.0t$. *A pseudogap appears below* $T_c^{MF} \simeq 0.42t$ *and coherence peaks develop below* $T \lesssim 1.5T_{KT}$ *as* T *approaches* T_{KT}.

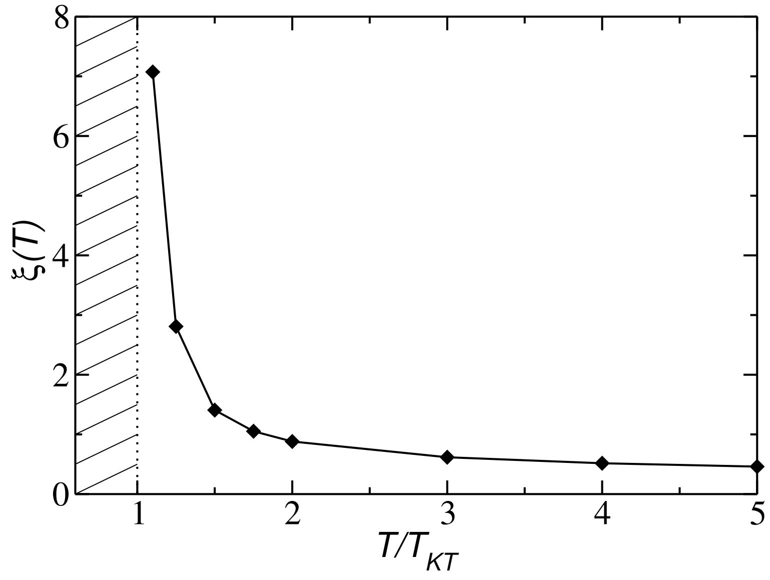

Figure 3.2: The effective correlation length $\xi(T)$ versus T/T_{KT} for the 32×32 lattice. Here $T_c^{MF}/T_{KT} \simeq 4-5$ so that the pseudogap regime which extends from $T/T_{KT} \simeq 1$ to 5 is large compared to the superconducting region which extends from 0 to $T/T_{KT} = 1$. The pronounced increase of $\xi(T)$ occurs over a narrow temperature region ($1 < T/T_{KT} \lesssim 1.5$), on a scale set by T_c^{MF}, as T_{KT} is approached.

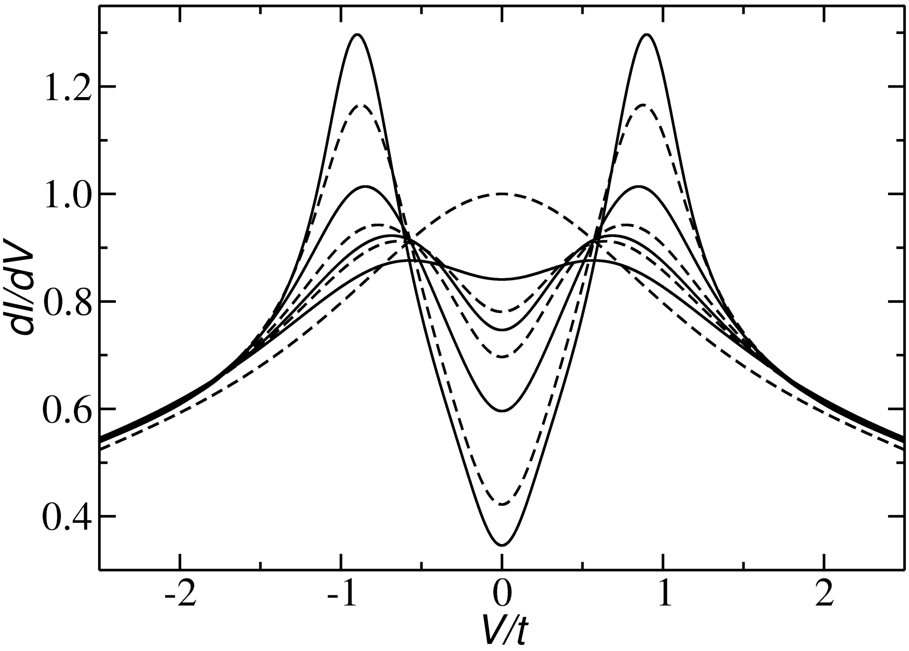

Figure 3.3: Tunneling conductance $\frac{dI}{dV}$ for the $d_{x^2-y^2}$-wave gap, normalized to its value at T_c^{MF} and $V = 0$, for different temperatures. Solid curves are for $T = \{0.75, 1.25, 1.75, 3.00\}\, T_{KT}$, dashed curves for $T = \{1.00, 1.50, 2.00\}\, T_{KT}$ and T_c^{MF} ($\frac{dI}{dV}|_{V=0}$ is increasing with T).

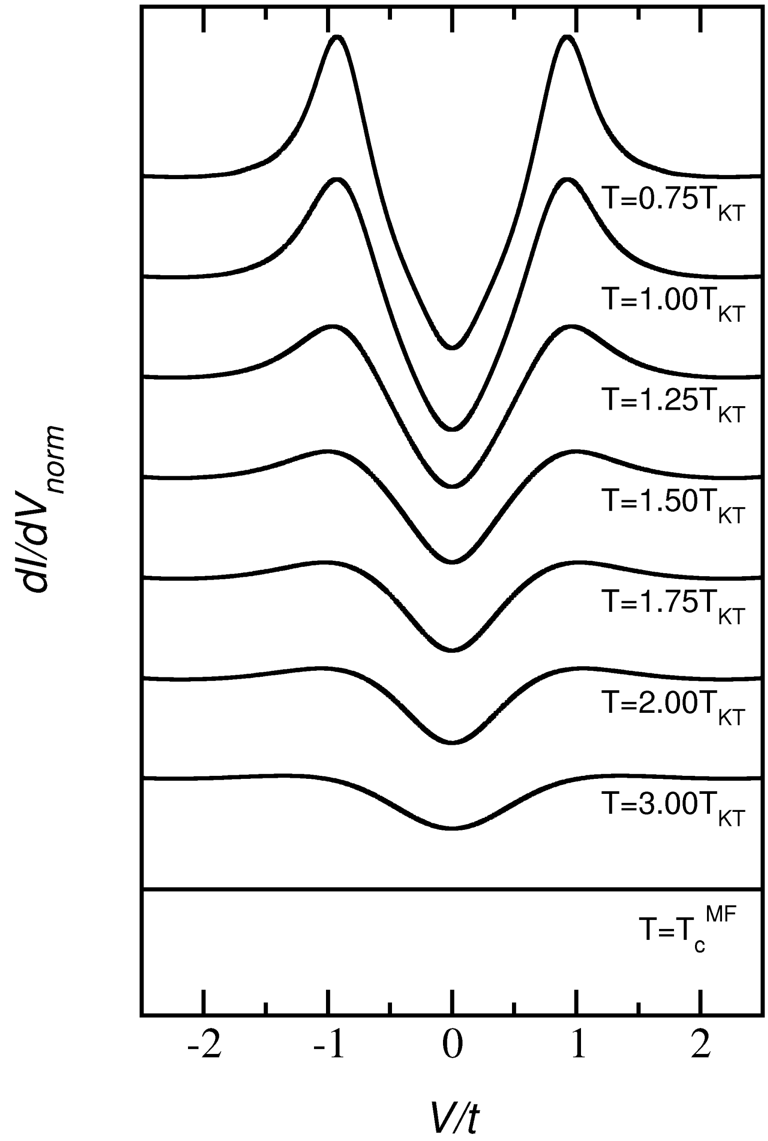

Figure 3.4: Normalized tunneling conductance dI/dV_{norm} for the $d_{x^2-y^2}$-wave gap for different temperatures. All tunneling spectra have been divided by the $T = T_c^{MF}$ spectrum, in order to get rid of the band-structure effects (van Hove peak) and for a better comparison with the experimental data of Ref. [26].

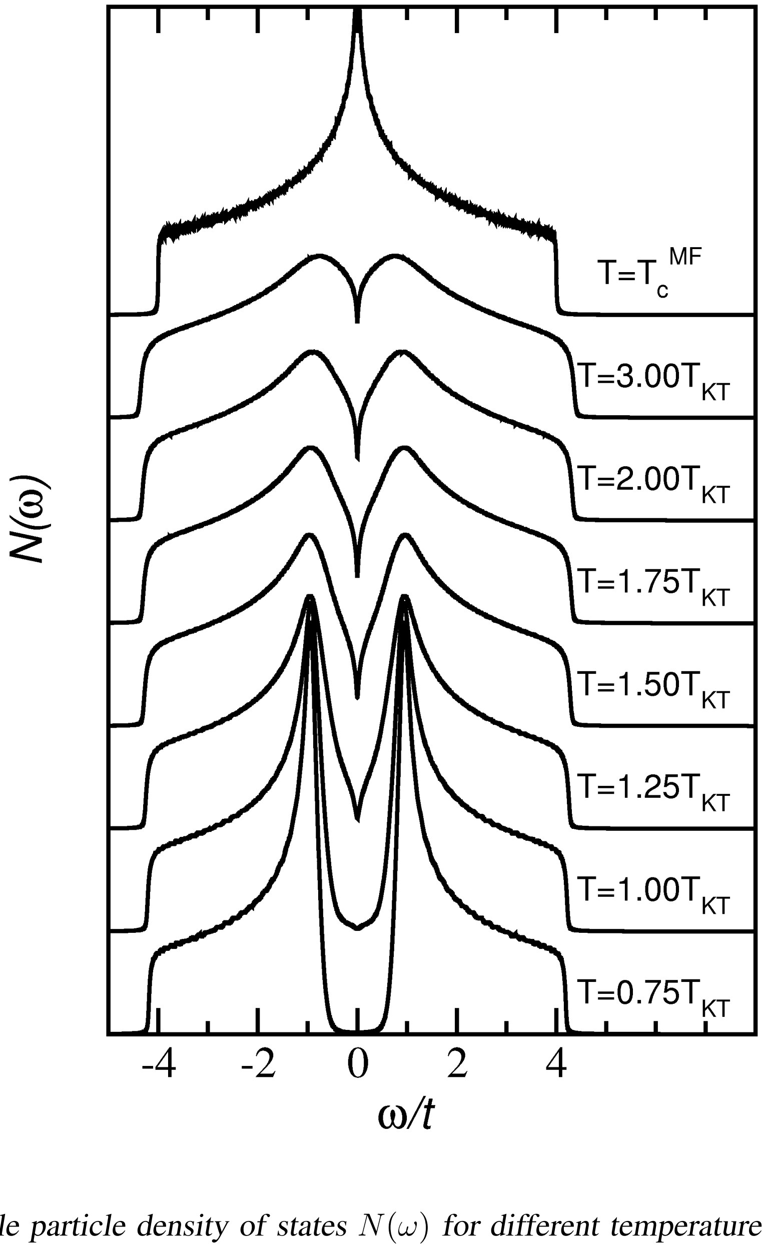

Figure 3.5: Single particle density of states $N(\omega)$ for different temperatures T for a 32×32 lattice with $T_{KT} = 0.1t$. The s-wave gap has the size $\Delta_{sc} = 1.0t$. A pseudogap appears below $T_c^{MF} \simeq 0.54t$ and coherence peaks develop below $T \lesssim 1.5T_{KT}$ as T approaches T_{KT}.

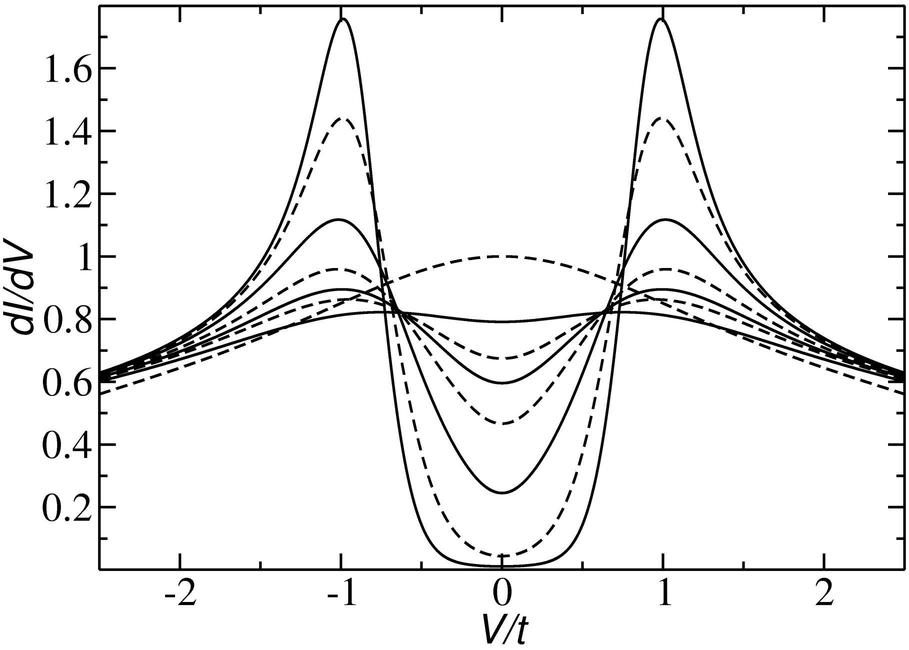

Figure 3.6: Tunneling conductance $\frac{dI}{dV}$ for the s-wave gap, normalized to its value at T_c^{MF} and $V=0$, for different temperatures. Solid curves are for $T=\{0.75, 1.25, 1.75, 3.00\}\ T_{KT}$, dashed curves for $T=\{1.00, 1.50, 2.00\}\ T_{KT}$ and T_c^{MF} ($\frac{dI}{dV}|_{V=0}$ is increasing with T).

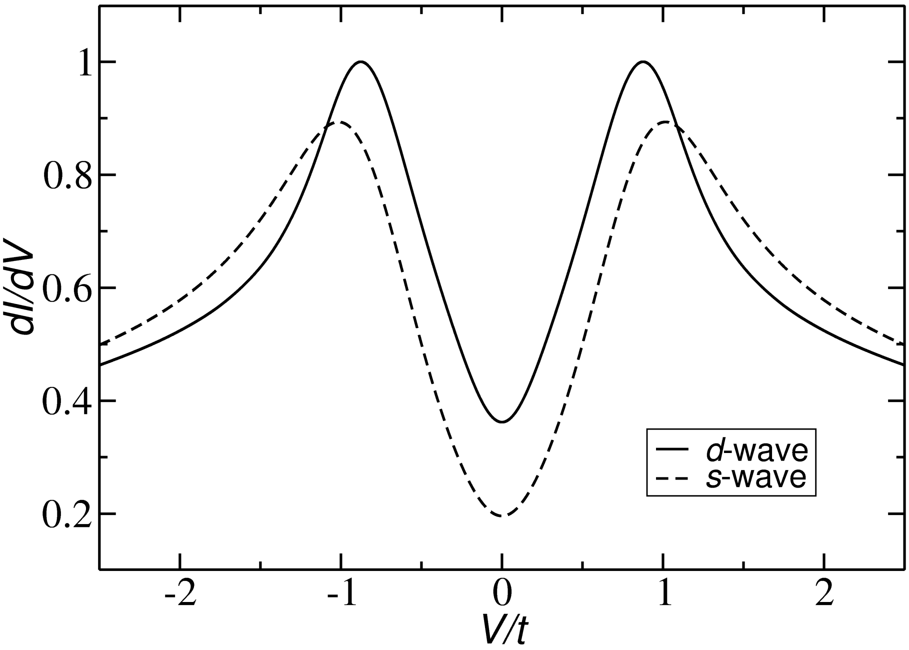

Figure 3.7: Normalized tunneling conductance $\frac{dI}{dV}$. The solid curve is for the $d_{x^2-y^2}$-wave gap at $T=1.0T_{KT}$. The dashed curve for s-wave gap at $T=1.25T_{KT}$. Both curves have a nearly identical shape.

3.2 Spectral weight $A(\boldsymbol{k},\omega)$

The quantity which is usually compared with angle resolved photoemission spectroscopy (ARPES) experiments is the spectral weight $A(\boldsymbol{k},\omega)$. It can be calculated from the retarded single-particle Green's function $G^R_\sigma(\boldsymbol{k},\omega)$ as

$$A_\sigma(\boldsymbol{k},\omega) = -\frac{1}{\pi}\Im\{G^R_\sigma(\boldsymbol{k},\omega)\}. \tag{3.3}$$

However, its connection to the photoemission intensities $I(\boldsymbol{k},\omega)$ is not straightforward, although one commonly assumes $I(\boldsymbol{k},\omega) \sim A(\boldsymbol{k},\omega)$.

The photoemission process can be described by the three-step model [100]: (i) photoexcitation of an electron, (ii) transport of that electron to the surface without inelastic scattering, and (iii) escape of the electron into the vacuum. In the first step matrix elements of the electric dipole operator between the initial and final electronic states have to be considered in addition to the spectral weight [146, 147]. In the third step surface resonances might play an important role [147]. The final photocurrent $I(\boldsymbol{k},\omega)$ is then given as a product of the matrixelements from all three steps. In addition, there is a (large) background from inelastically *and* elastically scattered electrons which adds to the primary photocurrent $I(\boldsymbol{k},\omega)$.

Thus, due to the various matrix-element effects, only relative and no absolute photoemission intensities are available. Furthermore, by tuning the polarization and photon energy of the incoming light, different bands/orbitals contribute to the photocurrent. However, the *position* and *shape* of the spectral lines in the primary photocurrent $I(\boldsymbol{k},\omega)$ are well defined and can be compared with the calculated spectral weight $A(\boldsymbol{k},\omega)$. Finally, at finite temperatures the spectral functions have to be multiplied with the Fermi function, which means that one obtains spectral weight also from bands above the Fermi energy E_F and a reduction of intensity from bands below E_F.

Most ARPES experiments were carried out on Bi2212, which is a bilayer cuprate superconductor [14, 101]. Early photoemission experiments indicated a peak-dip-hump structure of the photoemission peaks which was taken as evidence for the coupling of the quasiparticles to a collective mode [14]. However, it turned out that this peak-dip-hump structure is mostly due to bilayer-splitting of the nearest-neighbor copper oxide planes. In changing the energy and polarization of the incoming light one is now able to focus on the bonding or anti-bonding bands respectively [101]. In the following, we are only interested in low energy characteristics of order $\sim \Delta_{sc}$ of the spectral functions.

3.2.1 Quasiparticle dispersion

d-wave gap

Fig. 3.8 shows the spectral weight $A(\boldsymbol{k},\omega)$ in a greyscale plot for the $d_{x^2-y^2}$-wave superconducting gap with phase fluctuations at 10% doping ($\langle n\rangle = 0.9$) with $t' = 0$ along the standard way $((0,0) \to (\pi,0) \to (\pi,\pi) \to (0,0))$ through the 2D Brillouin zone (BZ). One can clearly see that we obtain the characteristic BCS band structure below $T_c \equiv T_{KT}$. The BCS band structure starts to appear, as soon as the effective phase correlation length ξ on our finite lattice gets much larger than the pair-size coherence length ξ_0 ($\xi \gg \xi_0$). The spectral peaks in the $(\pi,0)$-region are somewhat broadened due to the phase fluctuations already present below T_c. In the pseudogap state above T_c, where $\xi \sim \xi_0$, the dispersion completely changes. The characteristic BCS bands have disappeared and the spectral weight in the $(\pi,0)$-region has become completely incoherent, whereas the nodal $(\frac{\pi}{2},\frac{\pi}{2})$-peak is only very slightly broadened and the dispersion remains unchanged in that region of the BZ. The incoherent spectral weight starts to fill-in the pseudogap at $\boldsymbol{k} = (\pi,0)$.

The band structure of the cuprates is usually described very well by including also the next-nearest-neighbor hopping integral $t' \neq 0$ into the non-interacting dispersion. Typical values for t' are $0 > t'/t > -0.4$, depending on the copper-oxide compound [149]. The purpose of t' is to produce a very flat dispersion along the $(0,0) \rightarrow (\pi,0)$ direction of the BZ. Fig. 3.9 shows the spectral weight $A(\boldsymbol{k},\omega)$ for the $d_{x^2-y^2}$-wave superconducting gap with $t' = -0.4t$ and 10% doping ($\langle n \rangle = 0.9$). Like in the case where $t' = 0$, we obtain a BCS-like bandstructure below T_c, which completely disappears in the pseudogap state above T_c. As before, the spectral weight in the anti-nodal $(\pi,0)$-region is getting very incoherent and fills-in the pseudogap above T_c whereas the rest of the dispersion remains unchanged and the nodal $(\frac{\pi}{2},\frac{\pi}{2})$-peak only slightly broadens with increasing temperature. Thus, t' is not an important parameter in our model.

On the other hand, since in Bi2212 the SC gap in the $(\pi,0)$-region of the BZ opens at a location where the dispersion is already very steep, which is masked in our calculations with $t' = -0.4t$ due to our large SC gap, we use in the following always $t' = 0$ to compare our calculations with ARPES experiments. In Fig. 3.10 we show in more detail what actually happens close to $\boldsymbol{k} = (\pi,0)$. Fig. 3.10 displays the quasiparticle dispersion calculated from our phenomenological phase fluctuation model for $t' = 0$ and 10% doping ($\langle n \rangle = 0.9$). The spectral weight is plotted along the $(0,0) \rightarrow (\pi,0) \rightarrow (\pi,\pi)$ direction through the Brillouin zone (BZ). The free dispersion would cross the Fermi surface close to the $(\pi,0)$-point. One can clearly see that the characteristic (back-turning) Bogoliubov quasiparticle band disappears in the pseudogap state above T_c. Instead, one obtains a sharp quasiparticle dispersion which runs straight towards the Fermi energy and than fades out at a distance of the order of the superconducting (SC) gap Δ_{sc}. This is in complete agreement with the experimentally observed dispersion in underdoped Pb-Bi2212 which is shown in Fig. 3.11.

The angle resolved data for underdoped Pb-Bi2212 presented in Fig. 3.11 provide an insight into how the pseudogap is actually created near k_F. In the superconducting state a characteristic BCS-like back-dispersion is easily seen. This clarity is achieved by the careful choice of the excitation photon energy. Exactly near hν=38 eV the emission probability for the bonding band is much higher than for the anti-bonding band [150, 151] and bilayer-related complications are thus avoided. Above T_c in the pseudogap state the characteristic BCS behavior is replaced by the straight dispersion and strong depletion of the spectral weight towards E_F, which, as will be shown below, still leaves the energy gap in the spectrum.

Furthermore, Fig. 3.10 shows very clearly that the sharp quasiparticle features close to the $(\pi,0)$-point are getting lost above T_c within the phase fluctuation model. The sharp coherent $(\pi,0)$-peaks dissappear and broad incoherent weight *fills-in* the gap. Exactly this behavior was observed before in photoemission studies of the pseudogap [41, 152–155] and is also responsible for the characteristic temperature dependence of the scanning tunneling gap in the underdoped cuprates [26, 156], where the pseudogap fills-in instead of closing. Interestingly, not only SC fluctuations [157], but also staggered flux fluctuations [158] can lead to this strong broadening and destruction of the $(\pi,0)$-photoemission-peaks with increasing temperature while the sharp quasiparticle peaks near the nodes of the d-wave gap are preserved.

The disappearance of the characteristic BCS bands above T_c within the phase fluctuation picture can be understood by the fact, that the BCS wave-function is a coherent superposition of wave functions with different number of electron pairs [7]

$$|\Psi_{BCS}\rangle = \prod_k (u_k + v_k c^\dagger_{k\uparrow} c^\dagger_{-k\downarrow})|\phi_0\rangle = \sum_N \lambda_N |\Psi_N\rangle, \tag{3.4}$$

where $|\Psi_N\rangle$ is a N-particle wavefunction. The quantum mechanical uncertainty in the particle number is given by:

$$(\Delta N)^2 = 4\sum_k u_k^2 v_k^2. \tag{3.5}$$

Now $v_k^2 = 1 - u_k^2$ is the momentum distribution function for $T = 0$ and the weight of a quasiparticle peak at momentum k is given by v_k^2 (u_k^2) for $E < E_F$ ($E > E_F$).

In the normal metallic state with $\Delta = 0$, one gets a sharp cut-off in v_k^2 (u_k^2) at the Fermi-wavevector $k = k_F$ so that $(\Delta N)^2 \equiv 0$. In the BCS-superconducting state, however, v_k^2 (u_k^2) are finite also beyond the Fermi-wavevector k_F, which means that also for $k > k_F$ ($k < k_F$) one gets spectral weight at $E < E_F$ ($E > E_F$). This produces the characteristic BCS band structure, with bands approaching E_F from below (above) and then turning back to higher binding (quasiparticle) energies.

Now what happens if one introduces an arbitrary phase factor into the BCS wave function [7]

$$|\Psi_\varphi\rangle = \prod_k (|u_k| + |v_k| e^{i\varphi} c^\dagger_{k\uparrow} c^\dagger_{-k\downarrow})|\phi_0\rangle. \tag{3.6}$$

Integrating over all possible phases yields [7]

$$\begin{aligned} |\Psi_N\rangle &= \int_0^{2\pi} d\varphi\, e^{-iN\varphi/2} \prod_k (|u_k| + |v_k| e^{i\varphi} c^\dagger_{k\uparrow} c^\dagger_{-k\downarrow})|\phi_0\rangle \\ &= \int_0^{2\pi} d\varphi\, e^{-iN\varphi/2} |\Psi_\varphi\rangle. \end{aligned} \tag{3.7}$$

This means, that one projects into an exact particle-number eigenstate by making the relative phase of the Cooper-pairs completely uncertain. Eq. (3.5) is a special case of the general uncertainty relation between phase and particle number

$$\Delta N \Delta\varphi \gtrsim 1. \tag{3.8}$$

The above described behavior corresponds to what is happening in the phase-fluctuation model as a function of temperature. Starting from a phase coherent state at $T = 0$ with $\Delta\varphi = 0$, the particle number is completely uncertain with ΔN given by Eq. 3.5. With increasing temperature, one *gradually projects into a state with exact particle number* N. In the temperature range, where the phases are completely uncorrelated ($\xi \sim \xi_0$), one then obtains $\Delta N = 0$, and the back-turning BCS-bands must completely dissappear (loose weight for $k > k_F$, as seen in Figs. 3.10 and 3.11). At finite temperatures, this situation corresponds to a classical grand canonical average over ensembles with different number of particles, where each state has a well defined particle number and is no longer a coherent quantum-mechanical superposition of states with different number of particles. Thus, we obtain a crossover from a BCS-like phase-ordered band structure below T_c, which was also very nicely observed in ARPES experiments on overdoped Bi2223 [159], to a completely new phase-disordered *pseudo-gapped* band structure.

s-wave gap

Fig. 3.12 shows the spectral weight $A(\boldsymbol{k},\omega)$ in a greyscale plot for the s-wave superconducting gap with phase fluctuations at half-filling ($\langle n \rangle = 1.0$) with $t' = 0$ along the standard way $((0,0) \to (\pi,0) \to (\pi,\pi) \to (0,0))$ through the Brillouin zone (BZ). Like in the d-wave case, the characteristic BCS Bogoliubov quasiparticle bands can be observed only below T_c, whereas in the pseudogap state above T_c not only the spectral weight in the $(\pi,0)$ region is getting very incoherent, but also the spectral weight at the $(\frac{\pi}{2},\frac{\pi}{2})$ Fermi level crossing. Furthermore, the gap starts closing at $(\frac{\pi}{2},\frac{\pi}{2})$, while it is still open at $(\pi,0)$. This can be seen much clearer in Fig. 3.13, which also shows very nicely the disappearance of BCS bands for $T > T_c$. The temperature, where the gap starts closing at $(\frac{\pi}{2},\frac{\pi}{2})$ coincides with the temperature where the s-wave STM spectra start looking very similar to the d-wave STM spectra (see Fig. 3.7).

The fact that the effects of phase fluctuations on the gap size are stronger near the $(\frac{\pi}{2},\frac{\pi}{2})$ region than at $(\pi,0)$ (Fig. 3.13) can be understood in the following way [36, 160]: In our model we have three important length scales, the phase correlation length ξ, the Cooper-pair size (coherence length) $\xi_0 \sim \frac{v_F}{\Delta_{sc}}$ and the thermal de Broglie wavelength $\xi_{th} \sim \frac{v_F}{T}$. The thermal de Broglie wavelength is a measure for the size of the quasiparticle wave packets. As soon as the mean distance d of the quasiparticles becomes of order $d \simeq \xi_{th}$, quantum mechanical effects have to be taken into account, while at very high temperatures with $d \gg \xi_{th}$ a quasi-classical description is possible .

As discussed in Sec. 2.5, we always have $\xi \geq \xi_0$ in our model, since we only consider pair center-of-mass phase fluctuations. Starting from high temperatures, the pseudogap of size Δ_{sc} begins to open as soon as $\xi_{th} > \xi_0$. The thermal de Broglie wavelength increases as $1/T$, whereas the phase correlation length ξ shows hardly any change over wide temperature range ($1.5 T_{KT} < T < T_c^{MF} \equiv T^*$) and then suddenly diverges close to $T_{KT} \equiv T_c$ (see Fig. 3.2). As long as $\xi_{th} > \xi$, the behavior of the system is dominated by incoherent quasiparticles of "size" ξ_{th}. As soon as $\xi > \xi_{th}$ we start seeing the effects of phase ordering in the spectral weight. Due to the different Fermi velocities — the $(\pi,0)$-region is close to a saddle point with relatively flat dispersion compared to the nodal $(\frac{\pi}{2},\frac{\pi}{2})$-points — we always have $\xi_{th}(\frac{\pi}{2},\frac{\pi}{2}) > \xi_{th}(\pi,0)$ for fixed T. Hence, the phase ordering effect sets in at lower temperatures at $(\frac{\pi}{2},\frac{\pi}{2})$ than at $(\pi,0)$. One can put this in a more simple way: the effective phase-fluctuation temperature $T_{ph} \sim v_F/\xi$ at $(\frac{\pi}{2},\frac{\pi}{2})$ is higher than at $(\pi,0)$, therefore the gap starts closing first at $(\frac{\pi}{2},\frac{\pi}{2})$.

3.2.2 Superconducting gap and pseudogap

Next, we want to elucidate in detail the effect of phase fluctuations on the $\boldsymbol{k}$-dependence of the quasiparticle pairing gap. Therefore, we have plotted in Fig. 3.14 the quasiparticle dispersion obtained from MC simulations of the phase fluctuation model with $d_{x^2-y^2}$-wave gap along the Fermi surface of the free dispersion $\epsilon(\boldsymbol{k})$ at half-filling ($\langle n\rangle = 1.0$, $t' = 0$). This gives us effectively the gap function $\Delta(\boldsymbol{k})$. As can be seen in Fig. 3.14, below T_c one obtains the characteristic V-shape of a gap with $d_{x^2-y^2}$ pairing symmetry. As temperature is raised, the quasiparticles peaks are getting broader. In the pseudogap state above T_c, the spectral weight is getting rather incoherent close the the $\boldsymbol{k} = (\pi, 0)$ as was pointed out before. However, close to the nodal point of the gap function one still obtains a sharp quasiparticle dispersion. There, one can clearly see spectral weight shifting to lower binding energies which produces an *extended gapless region* in the pseudogap state close to $\boldsymbol{k} = (\frac{\pi}{2}, \frac{\pi}{2})$ instead of the nodal point in the superconducting state below T_c. This behavior is in complete agreement with photoemission experiments [152, 155, 162, 163] which show that the pseudogap starts closing from $\boldsymbol{k} = (\frac{\pi}{2}, \frac{\pi}{2})$ where one obtains a finite Fermi-arc but rather *fills in* at $\boldsymbol{k} = (\pi, 0)$ exactly as in Fig. 3.14 (top).

Furthermore, the pseudogap $\Delta(\boldsymbol{k})$ obtained from phase fluctuations of the local $d_{x^2-y^2}$ pairing-amplitude rather has a U-like shape (see Fig. 3.14, top) than the characteristic V-shape of a BCS $d_{x^2-y^2}$-gap. For comparison, Fig. 3.15 shows the pseudogap experimentally observed in underdoped Pb-Bi2212 [148]. One can clearly see that the experimental pseudogap has exactly the U-like form that we have obtained from the phase-fluctuation model. This deviation from the pure $d_{x^2-y^2}$-wave form was also observed in the superconducting state of very underdoped cuprates and interpreted as higher harmonic contributions to the pairing function, which might be due to a change in the pairing interaction in the proximity of the antiferromagnetic (AF) insulating phase [161, 164]. On the other hand, our picture suggests that these experimental results just might indicate the relevance of quantum phase fluctuations in this region of the phase diagram.

This characteristic temperature dependence of the pseudogap is also confirmed by theoretical calculations employing a sum-rule approach to a d-wave pairing model [165]. Besides the "low-energy" leading edge pseudogap[1] of size Δ_{sc} [166], also a "high-energy" pseudogap is observed in photoemission experiments of underdoped cuprates which is nearly an order of magnitude larger than Δ_{sc} [167]. This "high-energy" pseudogap is possibly of spin-fluctuation origin [38].

In Fig. 3.16 the gap function $\Delta(\boldsymbol{k})$ of the phase fluctuation model with s-wave gap ($\langle n\rangle = 1.0$, $t' = 0$) is shown. It was obtained in the same way as the d-wave gap function in plotting the dispersion along the Fermi surface of the non-interacting system. Unlike in the case of the d-wave gap, the quasiparticle peaks along the whole Fermi surface are getting very incoherent above T_c. This incoherent spectral weight continously fills-in the pseudogap. Moreover, Fig. 3.16 clearly shows that the pseudogap has an anisotropic s-wave form despite the isotropic superconducting BCS gap. In contrast to the d-wave case, where also the nodal lines of the $d_{x^2-y^2}$-wave gap play an important role, the anisotropy in the size of the s-wave gap with increasing temperature is solely determined by the $\boldsymbol{k}$-dependent Fermi-velocity $v_F(\boldsymbol{k})$ of the underlying free quasiparticle dispersion $\epsilon(\boldsymbol{k})$ (see discussion in Sec. 3.2.1 and Refs. [36, 160]).

---

[1] One way to identify this low-energy pseudogap in ARPES is to analyze the spectral weight suppression near the Fermi energy in symmetrized ARPES spectra ($A_{\text{sym}}(\boldsymbol{k},\omega) = A(\boldsymbol{k},\omega) + A(\boldsymbol{k},-\omega)$).

The results for the s-wave pairing gap with phase fluctuations could also be of some relevance for electron doped cuprates [141], where — as discussed in Sec. 3.1 — a possible crossover from an anisotropic s-wave (or $d_{x^2-y^2}$-wave) to a pure s-wave symmetry of the SC gap as a function of electron doping was observed [142, 143]. In fact, these experiments could be an indication for the increasing relevance of (quantum) phase fluctuations in the proximity of the AF Mott insulating state also in electron doped cuprates.

3.2.3 $(\pi, 0)$-peak

ARPES experiments on Bi2212 show that the superconducting $(\pi, 0)$-photoemission-peak is very sensitive to the superfluid density ρ_s [41]. The extracted peak weight z tracks the superfluid density as a function of temperature as well as a function of doping. The superconducting $(\pi, 0)$-peak disappears slightly above T_c, while the leading edge gap (LEG) is visible up to much higher temperatures, where the gap continously fills-in. Even up to the overdoped regime a clear correlation between the SC properties and the $(\pi, 0)$-weight was observed [168].

Contrary to this interpretation of the photoemission data, the authors of Ref. [153] argue, that the peak-weight z remains nearly constant as a function of temperature whereas the peak completely looses integrity close to T_c due to a "lifetime catastrophe", where the width of the superconducting peak at $(\pi, 0)$ is getting very large. However, this effect is masked by the dip-feature of the ARPES spectra, so that it looks like the peak is loosing weight.

The differing conclusions are due to the problem of how to extract the quasiparticle peak from a background with broad hump features in the presence of bilayer splitting. The controversy, however, only concerns the way of how the superconducting $(\pi, 0)$-photoemission-peak actually disappears slightly above T_c and not the other conclusions discussed in this section. Further evidence for a connection between the low temperature $(\pi, 0)$-peak weight and T_c in Bi2212 is given in Ref. [169]. There it is shown, that T_c follows in the underdoped regime the increasing coherent $(\pi, 0)$-peak-weight z as a function of doping, while in the overdoped regime T_c follows — rather BCS-like — the decreasing SC gap magnitude Δ_{sc}, so that $T_c \sim z\Delta_{sc}$.

In comparing the different high-T_c superconductors of the Bi-family, a clear correlation of their SC properties at optimal doping with the spectral weight at $(\pi, 0)$ was observed in Bi2201, Bi2212 and Bi2223 as a function of layers per unit cell [154, 155]. Across these cuprates, the superconducting $(\pi, 0)$-peak-weight z at optimal doping as well as the leading edge SC gap Δ_{sc} scale linear with $T_{c,max}$. This clearly indicates that the critical temperature T_c in all Bi-based cuprates is determined by two ingredients — *phase coherence and pairing strength* — as will be explicated below.

We have already seen, that within our phase fluctuation model the $(\pi, 0)$-region reacts most sensitive to phase coherence in case of a $d_{x^2-y^2}$-wave gap. But before we continue and compare our results with the experimental data, we first discuss the expected properties of the SC $(\pi, 0)$-peak within the BCS mean-field picture. In BCS theory the weight z of the sharp Bogoliubov quasiparticle peaks depends on the gap size $\Delta(\boldsymbol{k})$ and the distance of the free dispersion $\epsilon(\boldsymbol{k})$

from the chemical potential μ:

$$z = v_k^2 = \frac{1}{2}\left(1 - \frac{\xi(\boldsymbol{k})}{E(\boldsymbol{k})}\right), \tag{3.9}$$

with $\xi(\boldsymbol{k}) = \epsilon(\boldsymbol{k}) - \mu$ and $E(\boldsymbol{k}) = \sqrt{\xi^2(\boldsymbol{k}) + \Delta^2(\boldsymbol{k})}$. If the free dispersion at $(\pi,0)$ lies above the chemical potential, then we obtain $\xi(\boldsymbol{k}) > 0$ and the superconducting BCS peak at $(\pi,0)$ would dissappear *exactly at* T_c (see Fig. 3.17) and not *slightly above* T_c as observed in experiment.

Furthermore, the weight z of the superconducting peak below T_c, which is a result of particle-hole mixing of the Bogoliubov bands (see Fig. 3.17), would monotonously decrease as a function of hole-doping, since the distance from the chemical potential continously increases with hole-doping and at the same time the gap-size decreases. This doping dependence of z is contrary to what is observed in the underdoped region but in accordance with the overdoped region.

To better understand the properties of the superconducting $(\pi,0)$-photoemission-peak in the underdoped region of the cuprate phase diagram we show in Fig. 3.18 the detailed temperature dependence of the $(\pi,0)$-peak for our phase fluctuation model with $d_{x^2-y^2}$-wave gap ($t' = 0$, $\langle n \rangle = 0.9$). For comparison we also show the BCS $(\pi,0)$-peak as a dashed curve in Fig. 3.18, which again demonstrates how very sensitive the $\boldsymbol{k} = (\pi,0)$-region reacts to phase coherence.

Fig. 3.18 clearly shows that the coherent SC $(\pi,0)$-peak is also visible above T_c within the phase fluctuation model. It continously looses weight with increasing temperature and disappears at $T \simeq 1.5T_c$, exactly as observed in the experiments of Ref. [41]. On the other hand, if we look at the *total* $(\pi,0)$-weight below the chemical potential ($\omega < \mu$), this weight is reduced only by approximately 8% between $T = 0.75T_c$ and $T = 2.0T_c$. Furthermore, it looks as if the coherent SC $(\pi,0)$-peak continously transforms into the very broad incoherent spectral weight, which is visible up to highest temperatures, exactly as argued in Ref. [153]. Thus, the controversy between Ref. [41] and Ref. [153] can be resolved by the fact that the former group extracts only the coherent $(\pi,0)$-weight from the photoemission data, while the latter group extracts the coherent *and* incoherent weight. Hence, both experiments are in complete accordance with the phase fluctuation scenario.

Finally, in Fig. 3.18 is also shown the temperature dependence of the nodal $(\frac{\pi}{2},\frac{\pi}{2})$-peak. The nodal peak changes only slightly with increasing temperature compared to the $(\pi,0)$-peak. The strong dependence of the $(\pi,0)$-peak on the phase coherence moreover implies an increasing coherent SC $(\pi,0)$-peak weight z with increasing phase stiffness (superfluid density ρ_s). This could explain the experimentally observed increase of z with hole-doping in the underdoped Bi-based cuprates and also the increase of z with the number of copper-oxide layers per unit cell, which — due to the coupling between the layers within a unit cell — can reduce phase fluctuations at low temperatures, where a 2D to 3D crossover occurs.

For completeness, we show in Fig. 3.19 the detailed temperature dependence of the spectral peaks at $\boldsymbol{k} = (\pi,0)$ and $\boldsymbol{k} = (\frac{\pi}{2},\frac{\pi}{2})$ for our phase fluctuation model with s-wave gap at half-filling. Contrary to the d-wave case, the spectral peaks at $(\pi,0)$ are visible nearly up to $T \simeq 2.0T_c$, whereas the $(\frac{\pi}{2},\frac{\pi}{2})$-peaks are completely washed out already above $T \simeq 1.5T_c$. The anisotropic temperature dependence of the spectral peaks for the s-wave gap is solely caused by the different Fermi velocities, as discussed in Sec. 3.2.1.

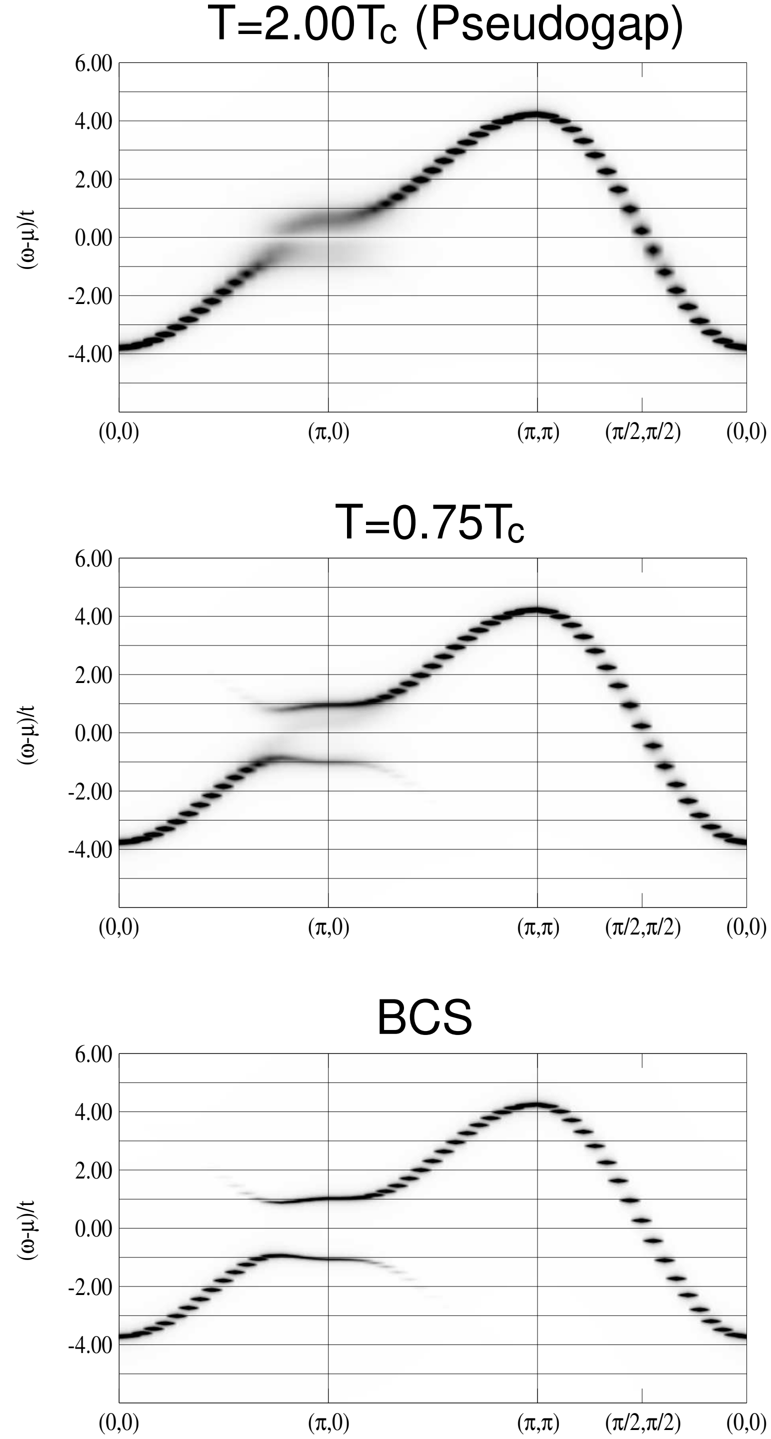

Figure 3.8: Spectral weight $A(\boldsymbol{k},\omega)$ in a greyscale plot for the $d_{x^2-y^2}$-wave superconducting gap with phase fluctuations at finite doping ($t' = 0.0t$, $\langle n\rangle = 0.9$). The figures display the spectral weight in the pseudogap state for $T = 2.00T_c$ (top) and in the superconducting state slightly below T_c ($T = 0.75T_c$, middle). For comparison we also show the phase coherent BCS limit (bottom).

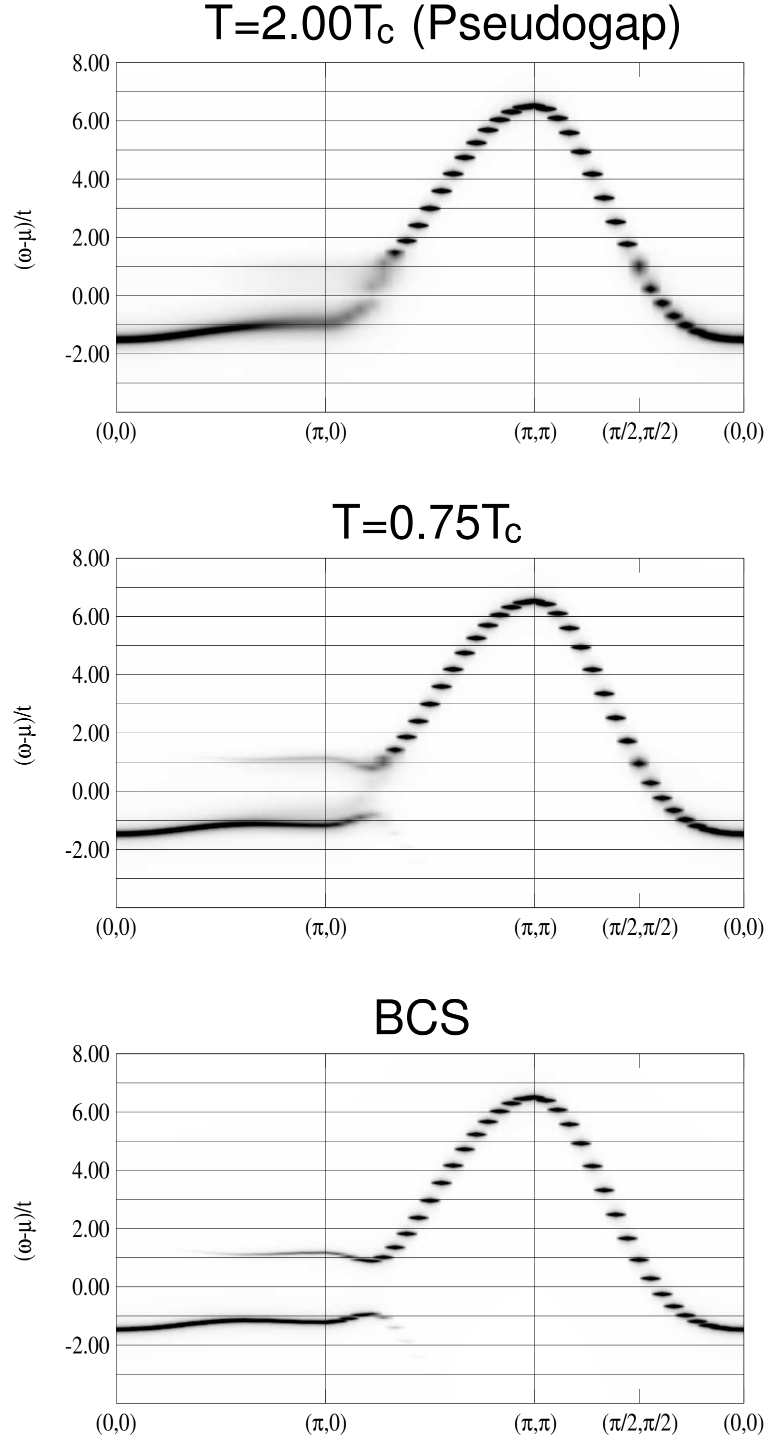

Figure 3.9: Spectral weight $A(\boldsymbol{k},\omega)$ in a greyscale plot for the $d_{x^2-y^2}$-wave superconducting gap with phase fluctuations and next-nearest neighbor-hopping t' at finite doping ($t' = -0.4t$, $\langle n \rangle = 0.9$). The figures display the spectral weight in the pseudogap state for $T = 2.00\,T_c$ (top) and in the superconducting state slightly below T_c ($T = 0.75\,T_c$, middle). For comparison we also show the phase coherent BCS limit (bottom).

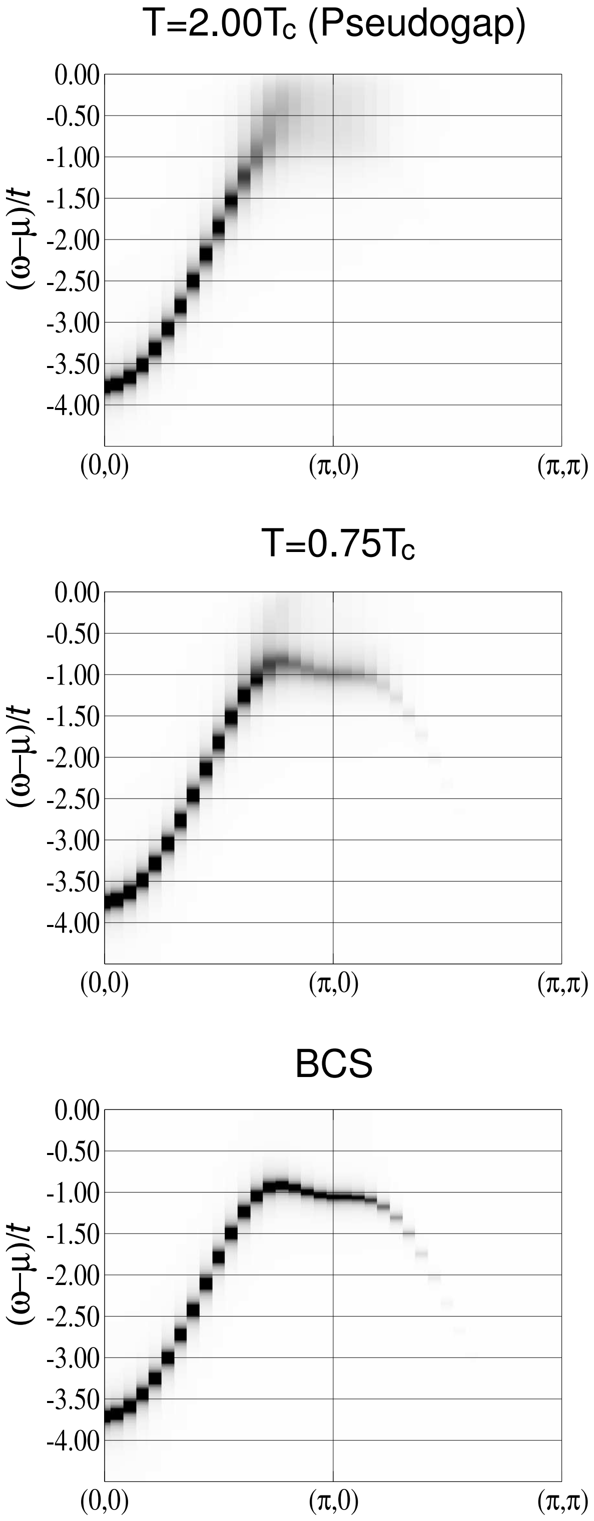

Figure 3.10: Spectral weight $A(\boldsymbol{k},\omega)$ in the pseudogap state ($T = 2.0\,T_c$, top) and in the superconducting state slightly below T_c ($T = 0.75\,T_c$) calculated from the phase fluctuation model with $d_{x^2-y^2}$-wave gap. For comparison we also show the spectral weight for the phase coherent BCS limit (bottom).

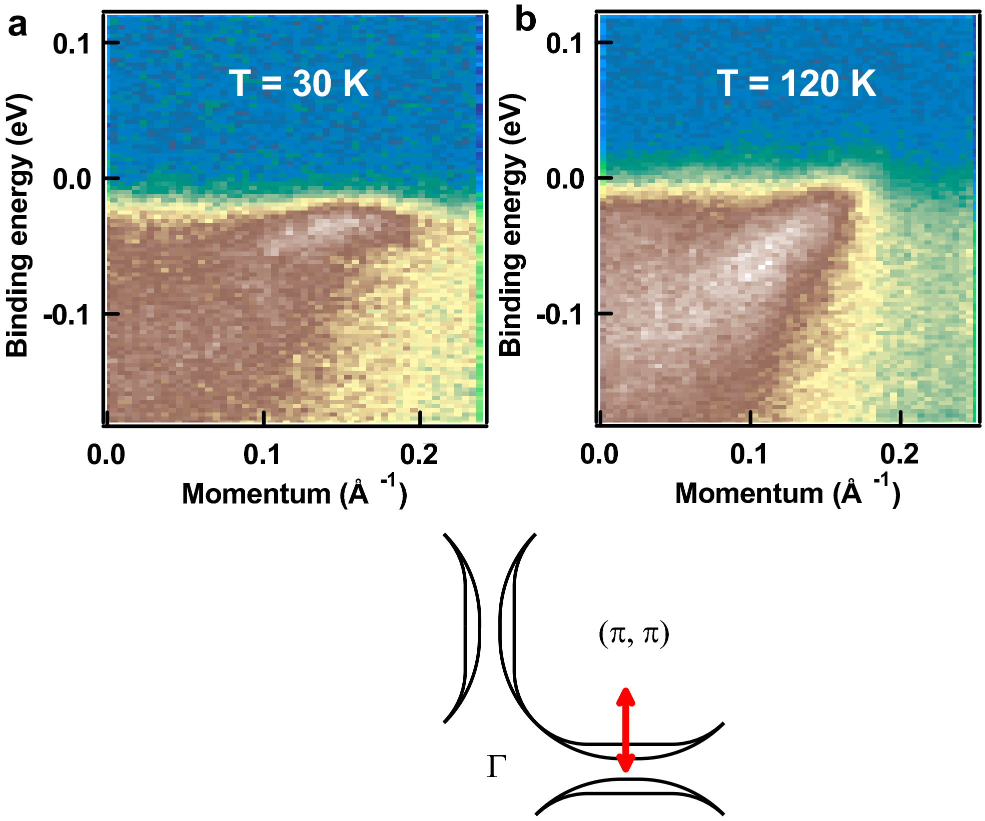

Figure 3.11: Experimental angle resolved photoemission (ARPES) results for the quasiparticle dispersion in underdoped Pb-Bi2212 ($T_c = 77K$) from Ref. [148]. a) Superconducting state. Energy distribution of the photoemission intensity along the direction shown as arrow on the sketch below. The BCS-like dispersion is clearly observed for the bonding band. b) Pseudogap state. No more bending back of the dispersion is observed. Instead, spectral weight fades upon approaching the Fermi level.

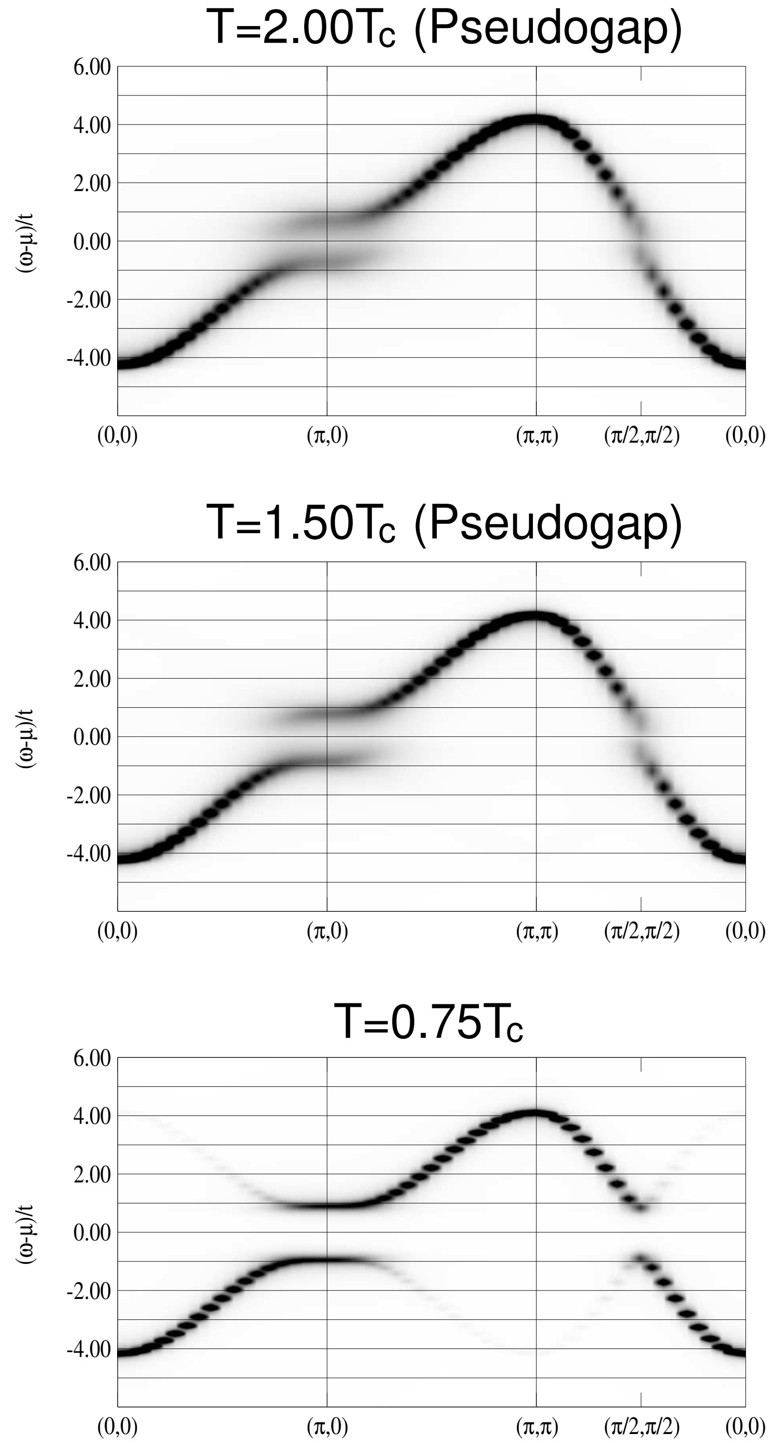

Figure 3.12: Spectral weight $A(\boldsymbol{k},\omega)$ in a greyscale plot for the isotropic s-wave superconducting gap with phase fluctuations at half-filling ($t' = 0.0t$, $\langle n \rangle = 1.0$). The figures display the spectral weight in the pseudogap state for $T = 2.00\,T_c$ (top) and $T = 1.50\,T_c$ (middle) and in the superconducting state slightly below T_c ($T = 0.75\,T_c$, bottom).

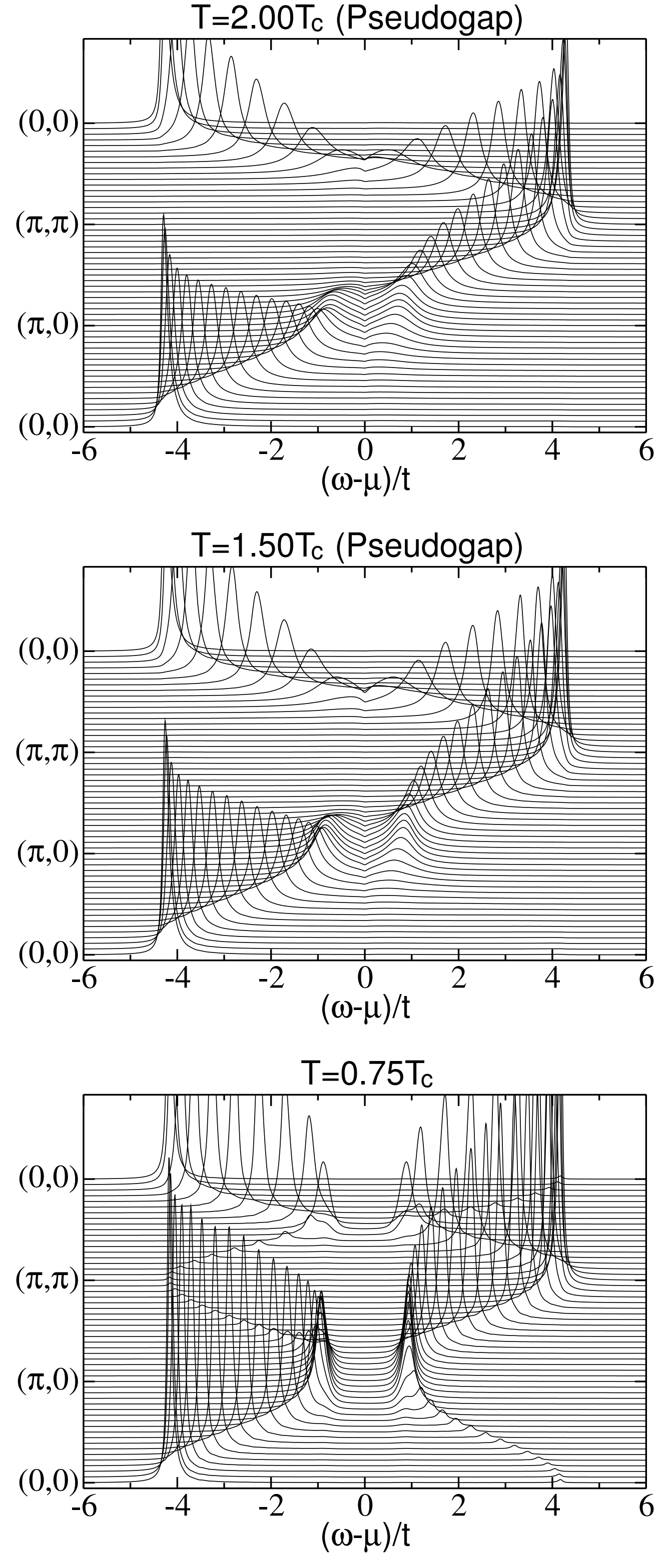

Figure 3.13: Spectral weight $A(\boldsymbol{k},\omega)$ for the isotropic s-wave superconducting gap with phase fluctuations at half-filling ($t' = 0.0t$, $\langle n\rangle = 1.0$). The figures display the spectral weight in the pseudogap state for $T = 2.00T_c$ (top) and $T = 1.50T_c$ (middle) and in the superconducting state slightly below T_c ($T = 0.75T_c$, bottom). One can clearly see that the pseudogap closes anisotropically.

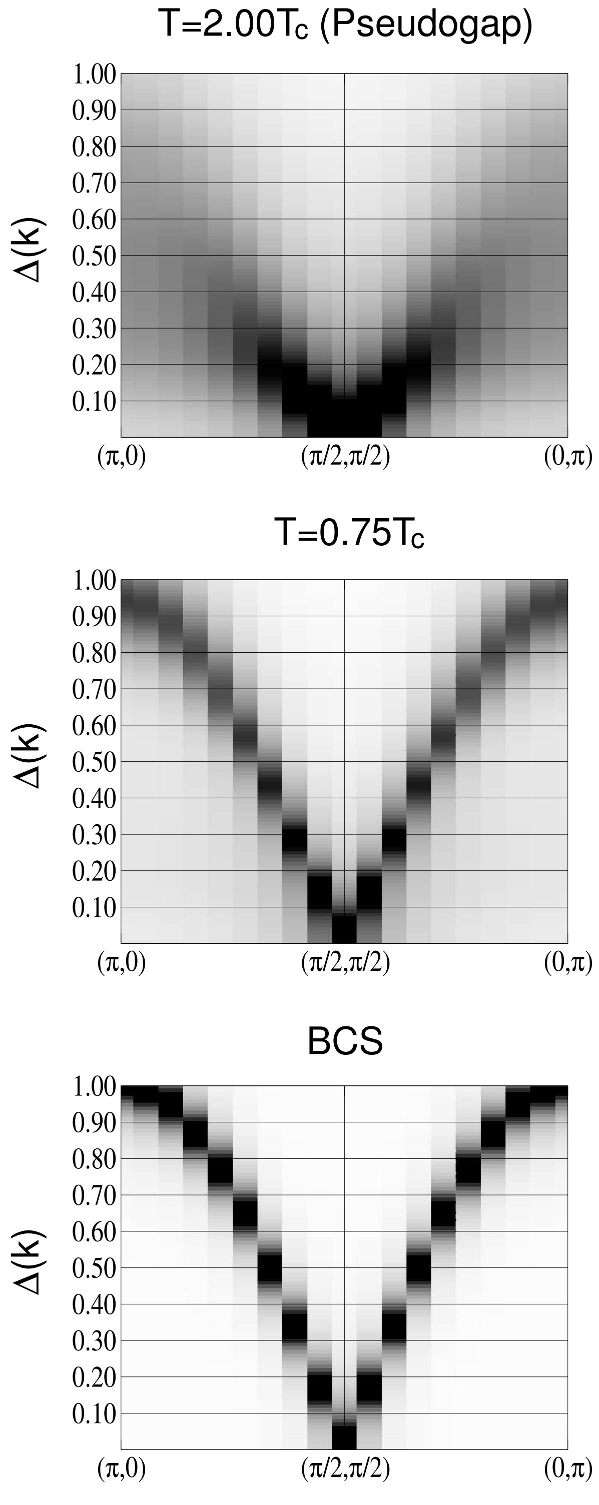

Figure 3.14: Gap function $\Delta(\boldsymbol{k})$ in the pseudogap state ($T = 2.0T_c$, top) and in the superconducting state slightly below T_c ($T = 0.75T_c$) calculated from the phase fluctuation model with $d_{x^2-y^2}$-wave gap. For comparison we also show the BCS gap function (bottom).

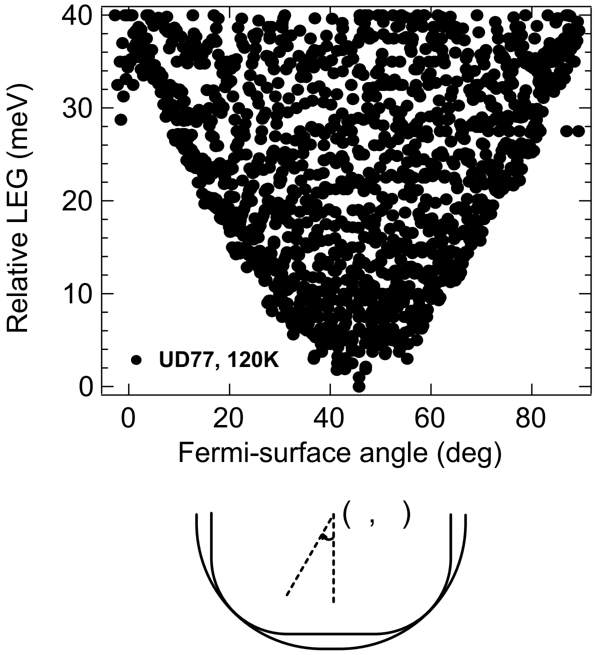

Figure 3.15: Experimental values of the leading edge (pseudo-)gap (LEG) as a function of the Fermi surface angle within the quadrant of the Brillouin zone (see lower panel) given with respect to the binding energy of the leading edge of a nodal energy distribution curve for underdoped Pb-Bi2212 ($T_c = 77K$) from Ref. [148]. The curve joining the low-gap extremity of these data points would represent the $\boldsymbol{k}$*-dependence of the pseudogap. For details see Ref. [161].*

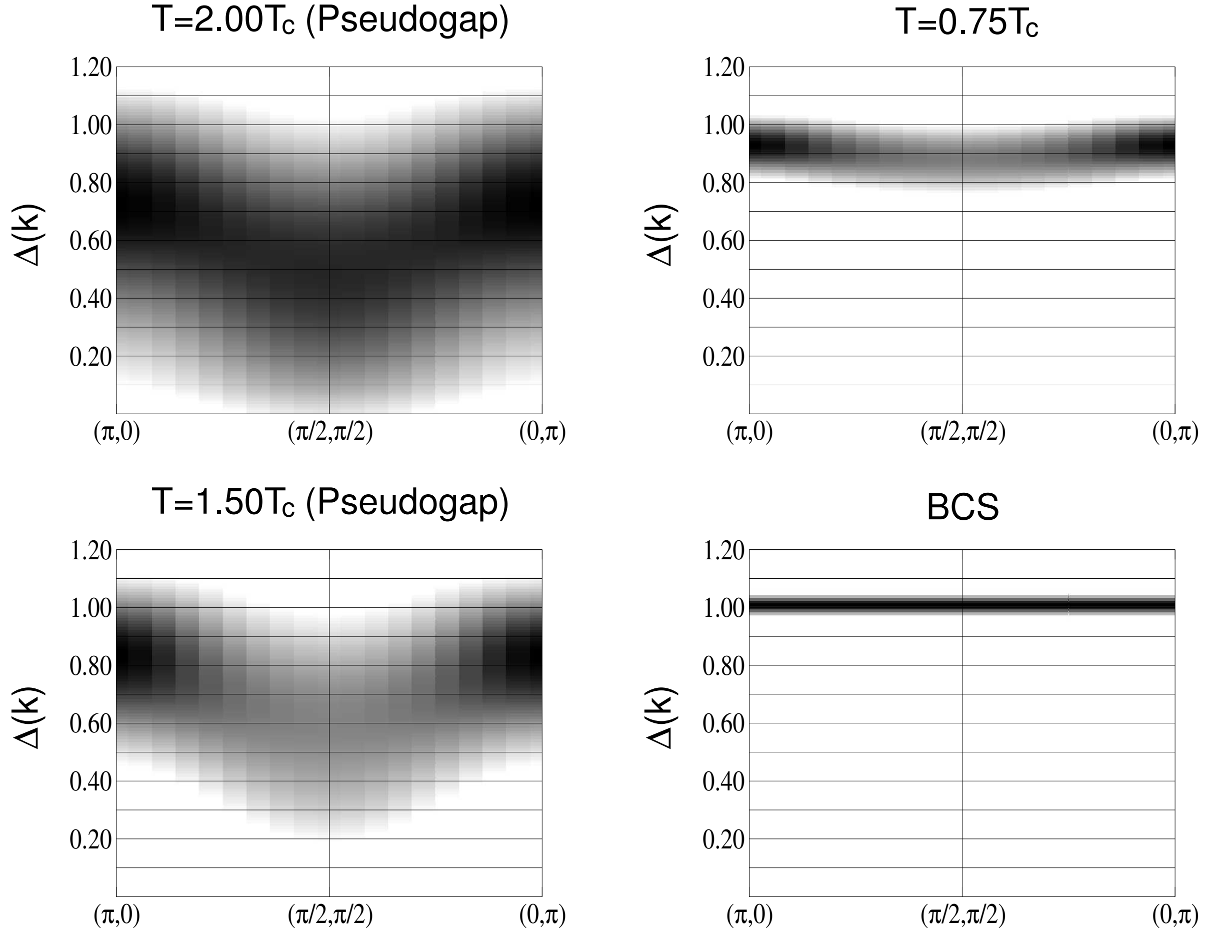

Figure 3.16: Gap function $\Delta(\boldsymbol{k})$ in the pseudogap state (left) for $T = 2.0T_c$ (top) and $T = 1.5T_c$ (bottom) and in the superconducting state (right) slightly below T_c ($T = 0.75T_c$) calculated from the phase-fluctuation model with s-wave gap. For comparison we also show the BCS gap function (bottom, right).

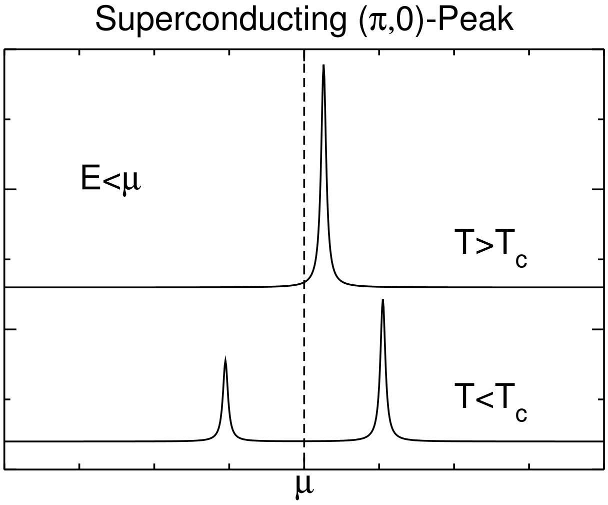

Figure 3.17: Sketch of the superconducting $(\pi,0)$-peak. Within BCS mean-field theory, this quasiparticle peak would be absent in the normal state above T_c in photoemission experiments. In the superconducting state ($T < T_c$), however, this peak becomes visible below the chemical potential μ at an energy $E < \mu$ (left side of panel) due to particle-hole mixing of the Bogoliubov bands.

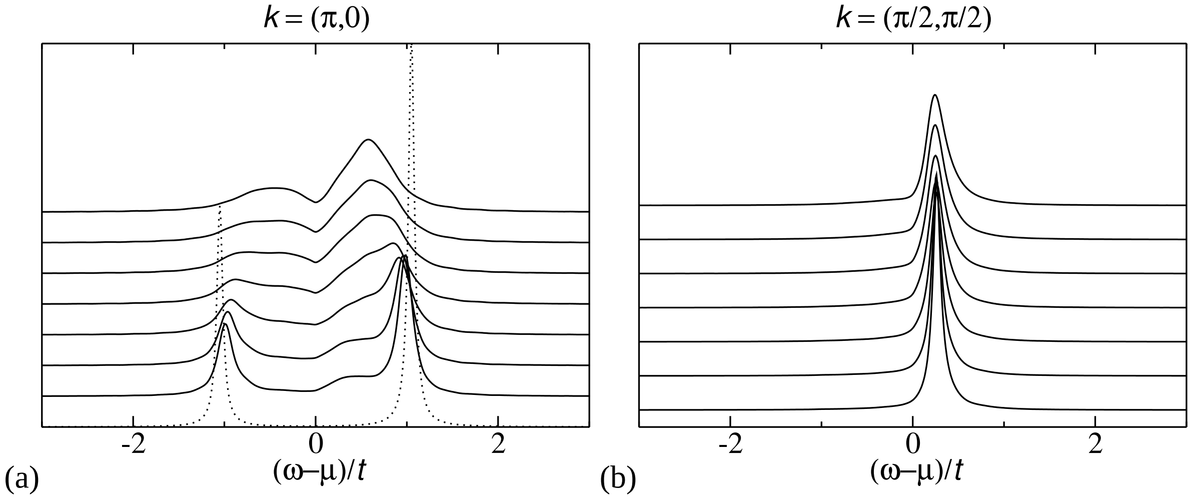

Figure 3.18: Temperature dependence of the spectral peaks at $\boldsymbol{k} = (\pi,0)$ (a) and $\boldsymbol{k} = (\frac{\pi}{2},\frac{\pi}{2})$ (b) for the $d_{x^2-y^2}$-wave gap at finite doping ($t' = 0.0t$, $\langle n\rangle = 0.9$). The temperatures are $T = 0.75T_c$, $T = 1.00T_c$, $T = 1.25T_c$, $T = 1.50T_c$, $T = 1.75T_c$, $T = 2.00T_c$ and $T = 3.00T_c$ (from bottom to top). Notice, that the superconducting $(\pi,0)$-peak disappears above $T \simeq 1.5T_c$, whereas incoherent weight is visible up to highest temperatures below the chemical potential. For comparison we also show the BCS $(\pi,0)$-peak (dashed curve).

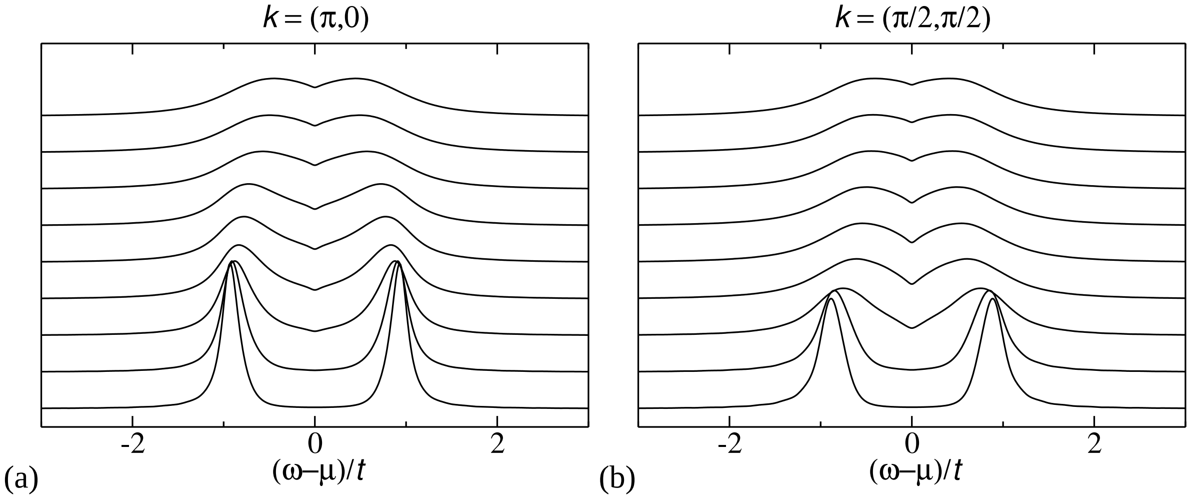

Figure 3.19: Temperature dependence of the spectral peaks at $\mathbf{k} = (\pi, 0)$ *(a) and* $\mathbf{k} = (\frac{\pi}{2}, \frac{\pi}{2})$ *(b) for the* s*-wave gap at half-filling (*$t' = 0.0t$*,* $\langle n \rangle = 1.0$*). The temperatures are* $T = 0.75T_c$*,* $T = 1.00T_c$*,* $T = 1.25T_c$*,* $T = 1.50T_c$*,* $T = 1.75T_c$*,* $T = 2.00T_c$*,* $T = 3.00T_c$*,* $T = 4.00T_c$ *and* $T = 5.00T_c$ *(from bottom to top). The* $(\frac{\pi}{2}, \frac{\pi}{2})$*-peaks are completely washed out above* $T \simeq 1.5T_c$*, whereas the* $(\pi, 0)$*-peaks are visible up to* $T \simeq 2.0T_c$*.*

3.3 The CPA as a high-temperature approximation?

In the preceding sections we have seen that over a wide temperature range in the pseudogap state, we have $\xi \sim \xi_0$ (see Fig. 3.2). Thus, one might ask whether a less computing time intensive high-temperature approximation is possible, where one treats the phases $\varphi_{\boldsymbol{i}}$ as random numbers instead of performing a MC simulation with the XY free energy and diagonalizing the whole Hamiltonian for each phase configuration. A standard procedure of treating randomly disordered crystals is the coherent potential approximation (CPA) [170].

The CPA defines three different Green's functions. The Green's function of the free system without disorder

$$\left(i\omega_n \mathbf{1} - \widehat{H}_0\right) \widehat{G}_0 = \mathbf{1}, \tag{3.10}$$

the impurity Green's function for a single configuration of impurity potentials $\widehat{V}^{imp}$,

$$\left(i\omega_n \mathbf{1} - \widehat{H}_0 - \widehat{V}^{imp}\right) \widehat{G}^{imp} = \mathbf{1}, \tag{3.11}$$

and finally the CPA Green's function

$$\left(i\omega_n \mathbf{1} - \widehat{H}_0 - \widehat{\Sigma}^{CPA}\right) \widehat{G}^{CPA} = \mathbf{1}. \tag{3.12}$$

The CPA self-energy $\widehat{\Sigma}^{CPA}$ is defined by the requirement, that the disorder averaged impurity Green's function $\langle \widehat{G}^{imp} \rangle$ is equal to the CPA Green's function $\widehat{G}^{CPA} = \langle \widehat{G}^{imp} \rangle$. Hence, the CPA self-consistency equation for $\widehat{\Sigma}^{CPA}$ takes the form

$$\langle \widehat{G}^{imp} \rangle \equiv \left\langle \left(\mathbf{1} - \widehat{G}^{CPA} \left(\widehat{V}^{imp} - \widehat{\Sigma}^{CPA}\right)\right)^{-1} \widehat{G}^{CPA} \right\rangle = \widehat{G}^{CPA}, \tag{3.13}$$

with

$$(\widehat{G}^{CPA})^{-1} = (\widehat{G}_0)^{-1} - \widehat{\Sigma}^{CPA}. \tag{3.14}$$

In our case the impurity potential $\widehat{V}^{imp}$ is given by the local BCS-like pairing terms in H_1 (see Sec. 2.1), with fixed amplitude Δ and randomly distributed phases $\varphi_{\boldsymbol{i}}$.

Thus far everything is exact — we have just reformulated the problem. Solving the self-consistency Eq. (3.13) would be as cumbersome as the repeated diagonalization of our phase fluctuation Hamiltonian for random phase configurations. However, one can now very easily exploit the fact, that the system is randomly disordered. Random disorder means, that what happens at one lattice site is completely uncorrelated to what happens on neighboring lattice sites. Thus, the electronic properties are solely determined by the local environment and the disorder caused by random impurity potentials can be taken into account in a mean-field-like manner.

Usually, the self-consistency Eq. (3.13) is solved for a finite submatrix in real space, like a single lattice site. This is the single-site or local aspect of $\widehat{\Sigma}^{CPA}$. In our case, we solved the CPA Eq. (3.13) for an on-site 2×2 Nambu Green's function matrix $\widehat{G}_{\boldsymbol{ii}}^{CPA}$ with the local s-wave impurity potential $\widehat{V}_{imp} = \Delta\, e^{i\phi}\, c_{\boldsymbol{i}\downarrow} c_{\boldsymbol{i}\uparrow} + h.c.$, where the phase ϕ can take all random values between 0 and 2π. The inversion of the Green's functions in Eq. (3.14) was done for the exact Green's function matrices by means of a Fourier transformation.

Fig. 3.20 shows the result of our CPA calculation for on-site s-wave pairing with $\Delta = 1.0t$ at half-filling ($\langle n \rangle = 1.0$). There, the CPA density of states (DOS) $N(\omega)$ is compared with the result of the exact XY-MC calculation at high temperature ($T = 3T_{KT}$), where $\xi \sim \xi_0$. Both $N(\omega)$ curves have a very similar shape. The pseudogap is filled-in somewhat more in the CPA calculation and the CPA DOS shows additional features at $\omega = \pm 4.0t$ which are possibly caused by the spatial cut-off in the Green's function matrices. In Fig. 3.21 the CPA spectral weight $A(\boldsymbol{k}, \omega)$ is displayed in a greyscale plot for the same parameters. Again, the spectral weight looks very similar to the results of the exact XY-MC calculation at very high temperatures shown in Fig. 3.12. However, we loose the $\boldsymbol{k}$-selectivity of the exact result, due to the purely local CPA self-energy $\Sigma^{CPA}(\omega)$. This produces pseudogaps of the same size at $\boldsymbol{k} = (\pi, 0)$ and $\boldsymbol{k} = (\frac{\pi}{2}, \frac{\pi}{2})$ in the CPA spectral weight. In addition, we obtain a rather sharp change in the dispersion at energies $\omega = \pm 4.0t$, which is responsible for the features in the CPA DOS at the same energies.

The CPA only yields relatively good results for diagonal disorder. For off-diagonal disorder, like next-neighbor $d_{x^2-y^2}$-wave pairing, the spatial cut-off in the Green's function matrices causes serious problems. One might, however, improve the results by the consideration of bigger clusters in the CPA self-consistency Eq. (3.13).

Like all mean-field approximations, the CPA is supposed to become exact in infinite dimensions. Instead of increasing the number of spatial dimensions, we increase in the following the number of hopping terms. This is done by choosing a free parabolic dispersion $\sim \boldsymbol{k}^2$ on our 2D square lattice with bandwidth $W = 2.0t$ (Fig. 3.22 (a)). In the presence of a local s-wave pairing potential $\widehat{V}_{imp} = \Delta\, e^{i\phi} c_{\boldsymbol{i}\downarrow} c_{\boldsymbol{i}\uparrow} + h.c.$ (Fig. 3.22 (b)), with random phase ϕ and magnitude $\Delta = W = 2.0t$, a well defined quasiparticle gap of width $\sim 2\Delta$ opens at the chemical potential ($\mu = 0.5t$, which is somewhat below half-filling).

The CPA result obtained for the *constant* free density of states (parabolic dispersion) shown in Fig. 3.22 (b) is in complete accordance with the results of Ref. [171]. Thus, one might speculate that in higher dimensions, also incoherent local pairing can lead to a *real gap* in the DOS. This is in contrast to the results for the tight-binding dispersion in 2D, where incoherent local pairing produces only a *pseudogap* in the DOS, and where the formation of a *real gap* is accompanied by the development of global phase coherence. However, please note that in contrast to all previous calculations, the chosen parameters $\Delta = W = 2.0t$ are already in the strong-coupling Bose-Einstein-pair limit!

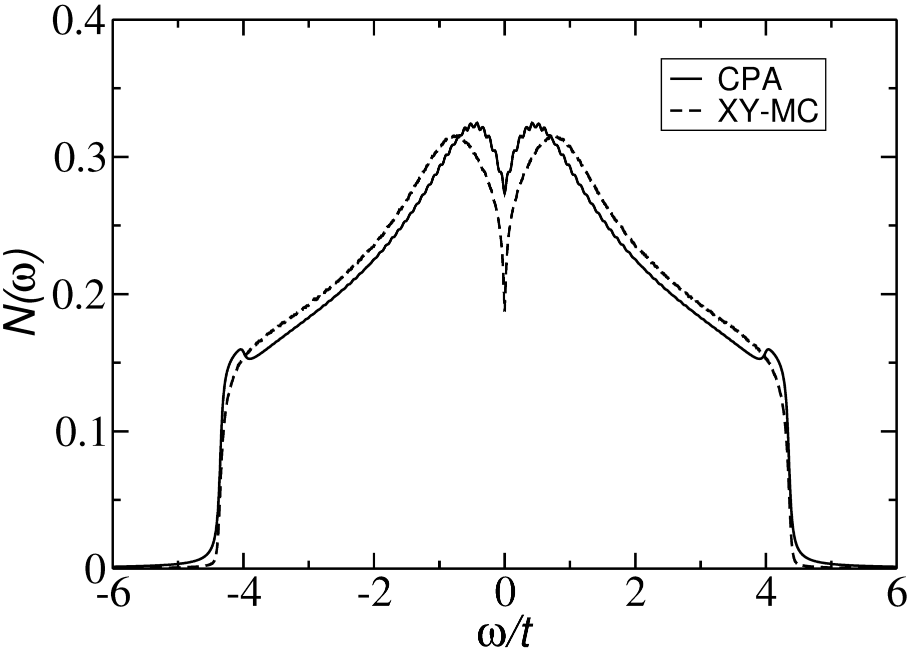

Figure 3.20: Single particle density of states $N(\omega)$ calculated with the CPA (straight line) for a local impurity s-wave pairing-potential $\hat{V}^{imp} \sim \Delta e^{i\phi}$ with random phase ϕ ($\Delta = 1.0t$, for details see text). For comparison we also show $N(\omega)$ calculated from the XY-MC simulation of our phase-fluctuation model with s-wave gap (dashed line) at $T = 3T_{KT}$.

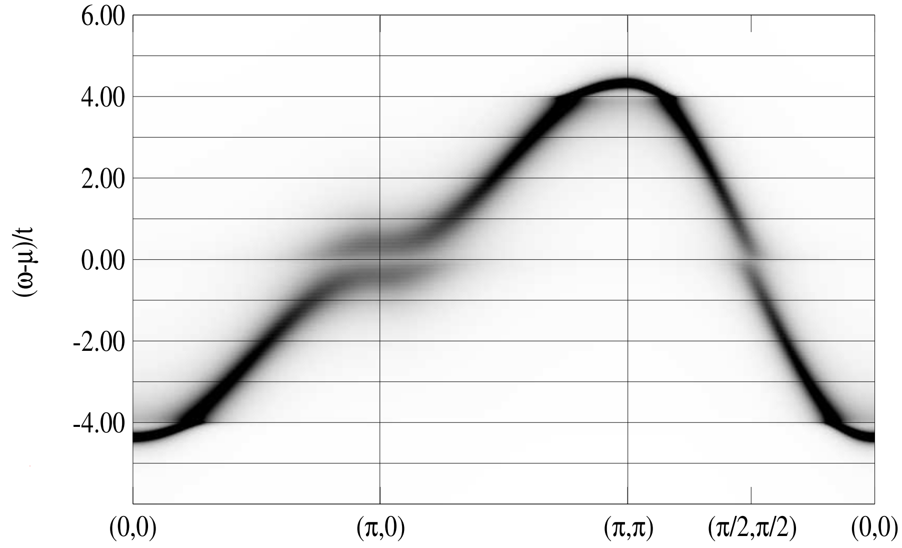

Figure 3.21: Spectral weight $A(\mathbf{k},\omega)$ in a greyscale plot calculated with the CPA for a local impurity s-wave pairing-potential $\hat{V}^{imp} \sim \Delta e^{i\phi}$ with random phase ϕ ($\Delta = 1.0t$). The overall features look similar to the results obtained for our phase-fluctuation model with s-wave gap at very high temperatures (see Fig. 3.12).

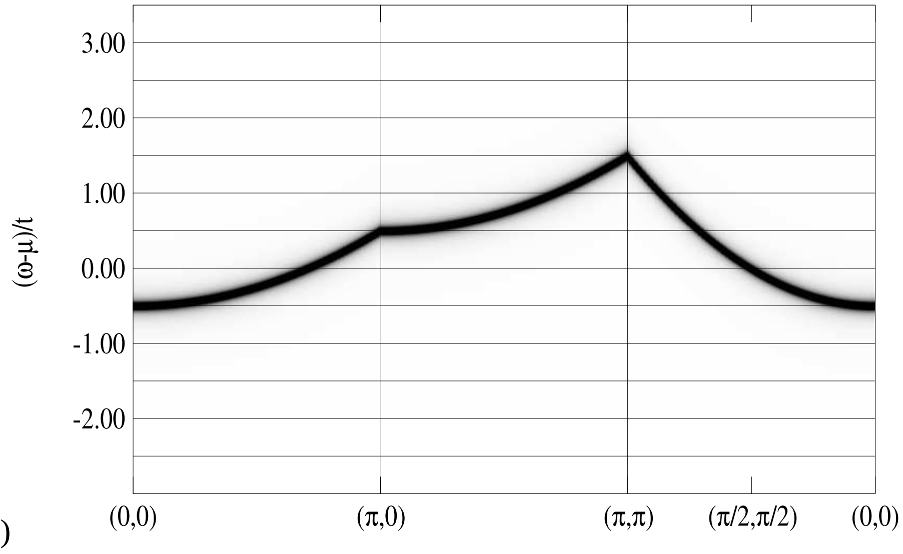

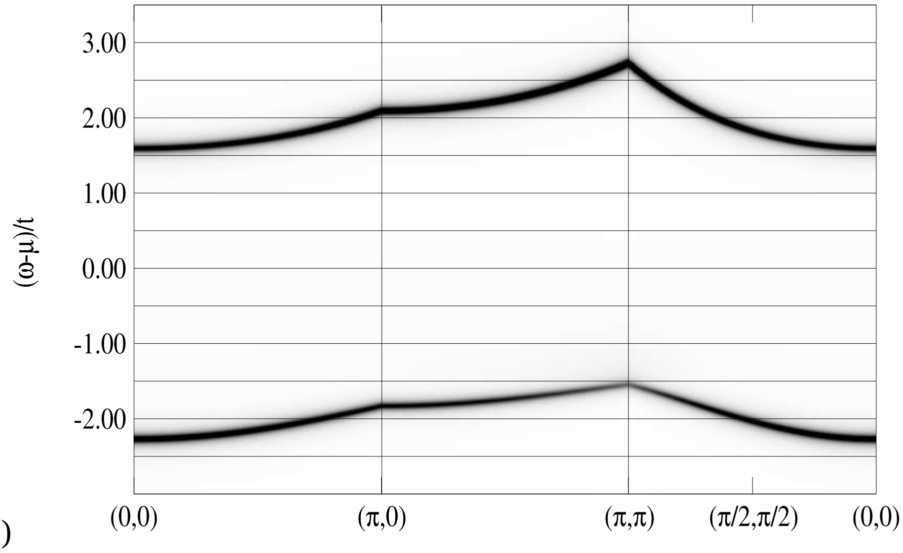

Figure 3.22: (a) Spectral weight $A(\mathbf{k},\omega)$ in a greyscale plot for a free parabolic dispersion $\epsilon(\mathbf{k}) \sim \mathbf{k}^2$ with bandwidth $W = 2.0t$ ($\mu = 0.5t$). (b) $A(\mathbf{k},\omega)$ calculated with the CPA for the same dispersion in the presence of a local impurity s-wave pairing-potential $\hat{V}^{imp} \sim \Delta e^{i\phi}$ with random phase ϕ and $\Delta = W = 2.0t$ ($\mu = 0.5t$). One can clearly see that local pairing can lead to a well defined gap at the chemical potential even without global phase coherence.

4

Optical properties

In this chapter we apply our phenomenological phase-fluctuation model to optical and high-frequency conductivity experiments in the underdoped cuprates. First, we discuss the coupling of an electromagnetic field to the Hamiltonian and elaborate the current response of the quantum many-particle system. Next, we derive the general properties of the current-current correlation function and the optical conductivity. We point out the important differences between a continuum Hamiltonian and an effective lattice Hamiltonian. Then, we analyze experiments on the optical sum-rule in terms of our phase fluctuation scenario, which might shed some light on the temperature dependence of the kinetic energy and in particular its change at the superconducting transition temperature T_c. Finally, the detailed temperature and frequency dependence of the optical conductivity is discussed.

4.1 The current-current correlation function

The current response of a many-particle system to an applied electromagnetic field can be obtained from the current-current correlation function $D_c(\boldsymbol{q}, \omega)$. Thereby, some important differences arise between a continuum model and an effective lattice model. Therefore we start with the continuum description.

4.1.1 Continuum model

Consider the non-interacting continuum Hamiltonian

$$H_0 = \int \hat{\psi}^\dagger(\boldsymbol{x}) \left(-\frac{\hbar^2}{2m} \nabla^2 \right) \hat{\psi}(\boldsymbol{x}) \, dx, \tag{4.1}$$

where $\hat{\psi}^\dagger(\boldsymbol{x})$, $\hat{\psi}(\boldsymbol{x})$ are the usual field operators [172]. The electromagnetic field is coupled to the Hamiltonian by means of the substitution

$$\hat{p} = -i\hbar\nabla \quad \longrightarrow \quad \hat{p} - \frac{e}{c}\boldsymbol{A}(\boldsymbol{x}), \tag{4.2}$$

with $e < 0$ being the charge of the electron. The new Hamiltonian H_0' in the presence of the vector potential $\boldsymbol{A}(\boldsymbol{x})$ is then given by

$$H_0' = \frac{1}{2m} \int \hat{\psi}^\dagger(\boldsymbol{x}) \left(-i\hbar\nabla - \frac{e}{c}\boldsymbol{A}(\boldsymbol{x})\right)^2 \hat{\psi}(\boldsymbol{x})\, dx. \tag{4.3}$$

If the vector potential $\boldsymbol{A}(\boldsymbol{x})$ has Coulomb gauge ($\nabla\boldsymbol{A}(\boldsymbol{x}) = 0$), then the Hamiltonian can be decomposed into three terms:

$$H_0' = H_0 + H_{\text{diamag}}(\boldsymbol{A}) + H_{\text{paramag}}(\boldsymbol{A}). \tag{4.4}$$

The diamagnetic term

$$H_{\text{diamag}}(\boldsymbol{A}) = \frac{e^2}{2mc^2} \int \boldsymbol{A}^2(\boldsymbol{x})\, \hat{\rho}(\boldsymbol{x})\, dx \tag{4.5}$$

is quadratic in $\boldsymbol{A}(\boldsymbol{x})$. There, the vector potential couples to the particle-density operator $\hat{\rho}(\boldsymbol{x}) = \hat{\psi}^\dagger(\boldsymbol{x})\hat{\psi}(\boldsymbol{x})$. Whereas the paramagnetic term

$$H_{\text{paramag}}(\boldsymbol{A}) = -\frac{1}{c} \int \boldsymbol{A}(\boldsymbol{x})\, \hat{\boldsymbol{j}}^p(\boldsymbol{x})\, dx \tag{4.6}$$

is linear in $\boldsymbol{A}(\boldsymbol{x})$ and the vector potential couples to the paramagnetic current operator $\hat{\boldsymbol{j}}^p(\boldsymbol{x})$, which is given by

$$\hat{\boldsymbol{j}}^p(\boldsymbol{x}) = \frac{\hbar e}{2mi} [\hat{\psi}^\dagger(\boldsymbol{x})\nabla\hat{\psi}(\boldsymbol{x}) - (\nabla\hat{\psi}^\dagger(\boldsymbol{x}))\hat{\psi}(\boldsymbol{x})]. \tag{4.7}$$

The total current density can be obtained as a functional derivative of H_0' with respect to the vector potential $\boldsymbol{A}(\boldsymbol{x})$:

$$\hat{\boldsymbol{j}}(\boldsymbol{x}) = -c\,\frac{\delta H_0'}{\delta \boldsymbol{A}(\boldsymbol{x})} = \hat{\boldsymbol{j}}^p(\boldsymbol{x}) - \frac{e^2}{mc}\boldsymbol{A}(\boldsymbol{x})\hat{\rho}(\boldsymbol{x}). \tag{4.8}$$

Here, the first term is the paramagnetic contribution and the second term the diamagnetic contribution to the total current.

4.1.2 Linear response theory — Kubo formula

For an external perturbation at $t_0 = -\infty$, the linear current response is given by [172]

$$\delta\langle\hat{\boldsymbol{j}}(\boldsymbol{x},t)\rangle = \frac{i}{\hbar}\int dt'\, \langle[\hat{H}_H^{ex}(t'), \hat{\boldsymbol{j}}_H(\boldsymbol{x},t)]\rangle\, \Theta(t-t'), \tag{4.9}$$

where $\langle\cdots\rangle$ is the quantum mechanical expectation value with respect to the exact unperturbed Hamiltonian $\hat{H}$ and $[\cdots,\cdots]$ is the commutator. In our case, the perturbing Hamiltonian is $\hat{H}^{ex} = \hat{H}_{\text{diamag}}(\boldsymbol{A}) + \hat{H}_{\text{paramag}}(\boldsymbol{A})$. All operators in Eq. (4.9) have to be in the Heisenberg picture, which means

$$\hat{H}_H^{ex}(t) = e^{\frac{i}{\hbar}\hat{H}t}\left(\hat{H}_{\text{diamag}}(\boldsymbol{A}) + \hat{H}_{\text{paramag}}(\boldsymbol{A})\right)e^{-\frac{i}{\hbar}\hat{H}t} \tag{4.10}$$

and

$$\hat{\boldsymbol{j}}_H(\boldsymbol{x},t) = e^{\frac{i}{\hbar}\hat{H}t}\left(\hat{\boldsymbol{j}}^p(\boldsymbol{x}) - \frac{e^2}{mc}\boldsymbol{A}(\boldsymbol{x},t)\hat{\rho}(\boldsymbol{x})\right)e^{-\frac{i}{\hbar}\hat{H}t}. \tag{4.11}$$

Since the diamagnetic current is already linear in $\boldsymbol{A}(\boldsymbol{x},t)$, the linear response formula has to be applied only to the paramagnetic current. Collecting all terms linear in $\boldsymbol{A}(\boldsymbol{x},t)$, one finally obtains

$$\begin{aligned}\delta\langle\hat{\boldsymbol{j}}(\boldsymbol{x},t)\rangle = &-\frac{i}{\hbar c}\int dt'\,dx'\,\boldsymbol{A}(\boldsymbol{x}',t')\,\langle[\hat{\boldsymbol{j}}^p_H(\boldsymbol{x}',t'),\hat{\boldsymbol{j}}^p_H(\boldsymbol{x},t)]\rangle\,\Theta(t-t')\\ &-\frac{e^2}{mc}\boldsymbol{A}(\boldsymbol{x},t)\langle\hat{\rho}(\boldsymbol{x})\rangle.\end{aligned} \tag{4.12}$$

For a translational invariant system one has

$$\langle\hat{\rho}(\boldsymbol{x})\rangle = \rho_0 \tag{4.13}$$

and hence

$$\begin{aligned}\delta\langle\hat{\boldsymbol{j}}(\boldsymbol{x},t)\rangle = &\frac{i}{c}\int dt'\,dx'\,\bar{\sigma}(\boldsymbol{x}-\boldsymbol{x}',t-t')\,\boldsymbol{A}(\boldsymbol{x}',t')\\ &-\frac{e^2\rho_0}{mc}\boldsymbol{A}(\boldsymbol{x},t),\end{aligned} \tag{4.14}$$

where

$$\bar{\sigma}(\boldsymbol{x}-\boldsymbol{x}',t-t') = \frac{1}{\hbar}\Theta(t-t')\,\langle[\hat{\boldsymbol{j}}^p_H(\boldsymbol{x},t),\hat{\boldsymbol{j}}^p_H(\boldsymbol{x}',t')]\rangle. \tag{4.15}$$

Fourier transformation of Eq. (4.14) yields

$$\begin{aligned}\delta\langle\hat{\boldsymbol{j}}(\boldsymbol{k},\omega)\rangle = &\frac{i}{c}\,\bar{\sigma}(\boldsymbol{k},\omega)\,\boldsymbol{A}(\boldsymbol{k},\omega)\\ &-\frac{e^2\rho_0}{mc}\boldsymbol{A}(\boldsymbol{k},\omega).\end{aligned} \tag{4.16}$$

Eq. (4.16) describes the linear response to a vector potential. The conductivity, however, is defined as the linear response to an applied electric field $\boldsymbol{E}(\boldsymbol{x},t)$. For Coulomb gauge, we have $\boldsymbol{E}(\boldsymbol{x},t) = -\frac{1}{c}\frac{\partial\boldsymbol{A}(\boldsymbol{x},t)}{\partial t}$ and thus

$$\boldsymbol{E}(\boldsymbol{k},\omega) = \frac{i}{c}\,(\omega+i\eta)\,\boldsymbol{A}(\boldsymbol{k},\omega), \tag{4.17}$$

where $\eta = 0^+$ is required due to the adiabatic switch-on of the external perturbation at $t_0 = -\infty$. With the definition of the electrical conductivity

$$\delta\langle\hat{\boldsymbol{j}}(\boldsymbol{k},\omega)\rangle = \sigma(\boldsymbol{k},\omega)\,\boldsymbol{E}(\boldsymbol{k},\omega) \tag{4.18}$$

and

$$\sigma(\boldsymbol{k},\omega) = \sigma_{para}(\boldsymbol{k},\omega) + \sigma_{dia}(\boldsymbol{k},\omega), \tag{4.19}$$

we finally obtain

$$\sigma_{dia}(\boldsymbol{k},\omega) = \frac{ie^2\rho_0}{m(\omega+i\eta)} \tag{4.20}$$

and

$$\sigma_{para}(\boldsymbol{k},\omega) = \frac{1}{\omega+i\eta} \int dt\, dx\, \bar{\sigma}(\boldsymbol{x},t)\, e^{-i(\boldsymbol{k}\boldsymbol{x}-\omega t)}. \tag{4.21}$$

At finite temperatures, the retarded current-current correlation function is defined by [172]

$$iD_c(\boldsymbol{x}t,\boldsymbol{x}'t') = \mathrm{Tr}\{\hat{\rho}_G[\hat{\boldsymbol{j}}^p_H(\boldsymbol{x},t),\hat{\boldsymbol{j}}^p_H(\boldsymbol{x}',t')]\}\,\Theta(t-t'), \tag{4.22}$$

where $\hat{\rho}_G = \frac{1}{Z}\, e^{\beta(\hat{H}-\mu\hat{N})}$ is the grand canonical statistical operator. The Matsubara current-current correlation function is given by

$$\mathcal{D}_c(\boldsymbol{x}\tau,\boldsymbol{x}'\tau') = -\mathrm{Tr}\{\hat{\rho}_G\,\mathrm{T}_\tau[\hat{\boldsymbol{j}}^p_H(\boldsymbol{x},\tau)\,\hat{\boldsymbol{j}}^p_H(\boldsymbol{x}',\tau')]\}, \tag{4.23}$$

where $\mathrm{T}_\tau[\cdots]$ is the imaginary time-ordering operator. For a translational invariant system, we have

$$\bar{\sigma}(\boldsymbol{x}-\boldsymbol{x}',t-t') = \frac{i}{\hbar}\, D_c(\boldsymbol{x}t,\boldsymbol{x}'t'). \tag{4.24}$$

The paramagnetic conductivity can now be written as

$$\begin{aligned}\sigma_{para}(\boldsymbol{k},\omega) &= \frac{i}{\hbar(\omega+i\eta)} \int dt\, dx\, D_c(\boldsymbol{x}t,00)\, e^{-i(\boldsymbol{k}\boldsymbol{x}-\omega t)}\\ &= \frac{i}{\hbar(\omega+i\eta)}\, D_c(\boldsymbol{k},\omega)\\ &= \frac{i}{\hbar(\omega+i\eta)}\, \mathcal{D}_c(\boldsymbol{k},\omega+i\eta),\end{aligned} \tag{4.25}$$

with $\mathcal{D}_c(\boldsymbol{k},i\nu_n)$ the Fourier transformed Matsubara current-current correlation function

$$\mathcal{D}_c(\boldsymbol{k},i\nu_n) = \int dx \int_0^\beta d\tau\, \mathcal{D}_c(\boldsymbol{x}\tau,00)\, e^{-i(\boldsymbol{k}\boldsymbol{x}-\nu_n\tau)}. \tag{4.26}$$

Putting everything together, we finally obtain

$$\begin{aligned}\sigma(\boldsymbol{k},\omega) &= \sigma_{dia}(\boldsymbol{k},\omega)+\sigma_{para}(\boldsymbol{k},\omega)\\ &= \frac{ie^2\rho_0}{m(\omega+i\eta)} + \frac{i}{\hbar(\omega+i\eta)}\, \mathcal{D}_c(\boldsymbol{k},\omega+i\eta).\end{aligned} \tag{4.27}$$

4.1.3 Lattice model — Peierls-Factors, Part II

For the effective lattice model, we use units such that $\hbar = c = 1$ and all length scales are defined in terms of the lattice constant $a = 1$. In some important formulas, we give the neglected constants in brackets $[\cdots]$ at the end of the formula, which allows us to compare our results quantitatively with experiments later on.

Now, consider the tight-binding hopping term of H_0 (Eq. (2.2)) with next-neighbor hopping only

$$T = -t \sum_{\langle \boldsymbol{ij} \rangle, \sigma} (c^\dagger_{\boldsymbol{i}\sigma} c_{\boldsymbol{j}\sigma} + c^\dagger_{\boldsymbol{j}\sigma} c_{\boldsymbol{i}\sigma}). \tag{4.28}$$

In Sec. 2.6.2 we saw, that in the presence of a static magnetic field, one has to make the substitution

$$c^\dagger_{\boldsymbol{i}\sigma} c_{\boldsymbol{j}\sigma} \longrightarrow \; e^{ie\int_{\boldsymbol{j}}^{\boldsymbol{i}} \boldsymbol{A}(\boldsymbol{l})\, d\boldsymbol{l}} \; c^\dagger_{\boldsymbol{i}\sigma} c_{\boldsymbol{j}\sigma}, \tag{4.29}$$

where the integral formulation was very important because of the phase acquired by an electron moving on a closed path through the $\boldsymbol{B}$-field, which is proportional to the enclosed magnetic flux. Here, we are only interested in the linear response to an applied electric field $\boldsymbol{E}(\boldsymbol{q},\omega)$ in the long wavelength limit of $\boldsymbol{q} \to 0$, which actually means $\frac{2\pi}{|\boldsymbol{q}|} \gg a$. The electric field is coupled through the vector potential to the Hamiltonian. Thus, the vector potential is nearly constant over a distance of size a. For an electric field in x-direction $E_x = -\frac{1}{c}\frac{\partial A_x}{\partial t}$, we can thus approximately make the substitution

$$c^\dagger_{\boldsymbol{l}+\boldsymbol{e}_x,\sigma} c_{\boldsymbol{l},\sigma} \longrightarrow \; e^{ieA_x(\boldsymbol{l})} \; c^\dagger_{\boldsymbol{l}+\boldsymbol{e}_x,\sigma} c_{\boldsymbol{l},\sigma}. \tag{4.30}$$

The approximation of the vector potential between $\boldsymbol{l}+\boldsymbol{e}_x$ and $\boldsymbol{l}$ by its value at $\boldsymbol{l}$ is somewhat arbitrary. The consequences of this choice will be discussed later.

Interestingly, in the limit where the vector potential varies on a scale Λ, which is much larger than the extent λ of the tightly bound electronic orbitals, the Peierls factors in the form Eq. (4.30) can also be motivated in a different way. Starting from the Schrödinger equation

$$H\,\psi_{\boldsymbol{i}}(\boldsymbol{x}) = \frac{1}{2m}\left(-i\hbar\nabla - \frac{e}{c}\boldsymbol{A}(\boldsymbol{x})\right)^2 \psi_{\boldsymbol{i}}(\boldsymbol{x}) + V(\boldsymbol{x})\,\psi_{\boldsymbol{i}}(\boldsymbol{x}) = E\,\psi_{\boldsymbol{i}}(\boldsymbol{x}) \tag{4.31}$$

with $\psi_{\boldsymbol{i}}(\boldsymbol{x})$ being the wave function of a tightly bound electron at lattice site $\boldsymbol{i}$, one can eliminate $\boldsymbol{A}(\boldsymbol{x})$ approximately by the gauge transformation

$$\psi_{\boldsymbol{i}}(\boldsymbol{x}) \longrightarrow e^{i\frac{e}{\hbar c}\,\boldsymbol{x}\boldsymbol{A}(\boldsymbol{i})}\;\psi_{\boldsymbol{i}}(\boldsymbol{x}), \tag{4.32}$$

whereby the error is of order $\sim \frac{\lambda}{\Lambda}$. In the language of second quantization, this means that the coupling to a slowly varying $\boldsymbol{A}(\boldsymbol{x})$ can be absorbed by the substitution

$$c^\dagger_{\boldsymbol{l}\sigma} \longrightarrow e^{i\frac{e}{\hbar c}\,\boldsymbol{l}\boldsymbol{A}(\boldsymbol{l})}\; c^\dagger_{\boldsymbol{l}\sigma}, \tag{4.33}$$

which is completely equivalent to Eq. (4.30).

Expansion of the exponential up to order $A_x^2(\boldsymbol{l})$ yields for the next-neighbor hopping terms in H_0:

$$T_A = T - \sum_{\boldsymbol{l}}\left[e\, j_x^p(\boldsymbol{l})\; A_x(\boldsymbol{l},t) + \frac{e^2\, k_x(\boldsymbol{l})}{2}\; A_x^2(\boldsymbol{l},t)\right], \tag{4.34}$$

where

$$j_x^p(\boldsymbol{l}) = it\sum_\sigma (c^\dagger_{\boldsymbol{l}+\boldsymbol{e}_x,\sigma} c_{\boldsymbol{l},\sigma} - c^\dagger_{\boldsymbol{l},\sigma} c_{\boldsymbol{l}+\boldsymbol{e}_x,\sigma}) \quad \cdot [\frac{1}{\hbar\, a_\parallel\, a_\perp}] \tag{4.35}$$

is the paramagnetic current density operator and

$$k_x(\boldsymbol{l}) = -t\sum_{\sigma}(c^{\dagger}_{\boldsymbol{l}+\boldsymbol{e}_x,\sigma}\, c_{\boldsymbol{l},\sigma} + c^{\dagger}_{\boldsymbol{l},\sigma}\, c_{\boldsymbol{l}+\boldsymbol{e}_x,\sigma}) \tag{4.36}$$

the operator for the local kinetic energy in x-direction. In Eq. (4.35), $a_{||}$ and $a_{\perp}$ stand for the in-plane and inter-plane lattice-spacing, respectively. As before, the total current density operator is then given by the derivation of the Hamiltonian with respect to $A_x(\boldsymbol{l},t)$:

$$j_x(\boldsymbol{l},t) = -\frac{\delta T_A}{\delta A_x(\boldsymbol{l},t)} = e\, j^p_x(\boldsymbol{l}) + e^2\, k_x(\boldsymbol{l})\, A_x(\boldsymbol{l},t). \tag{4.37}$$

Applying the linear response formula gives

$$\begin{aligned} \delta\langle j_x(\boldsymbol{l},t)\rangle = & -ie^2 \int dt' \sum_{\boldsymbol{l}'} A_x(\boldsymbol{l}',t')\, \langle [j^p_x(\boldsymbol{l}',t'), j^p_x(\boldsymbol{l},t)]\rangle\, \Theta(t-t') \\ & + e^2\, \langle k_x\rangle\, A_x(\boldsymbol{l},t), \end{aligned} \tag{4.38}$$

where $j^p_x(\boldsymbol{l},t)$ is in the Heisenberg picture with respect to the unperturbed Hamiltonian H and $\langle k_x\rangle$ is the expectation value of the local kinetic energy in x-direction for the unperturbed Hamiltonian H. Hence, $\langle k_x\rangle$ has no time or space dependence. With the definition of the retarded current-current correlation function

$$iD_c(\boldsymbol{l}t, \boldsymbol{l}'t') = \mathrm{Tr}\{\hat{\rho}_G\, [j^p_x(\boldsymbol{l},t), j^p_x(\boldsymbol{l}',t')]\}\, \Theta(t-t'), \tag{4.39}$$

one obtains for the current response after a Fourier transformation:

$$\delta\langle j_x(\boldsymbol{k},\omega)\rangle = \{-e^2 D_c(\boldsymbol{k},\omega) + e^2\langle k_x\rangle\}\, A_x(\boldsymbol{k},\omega). \tag{4.40}$$

Thus, the electrical conductivity has the form

$$\sigma_{xx}(\boldsymbol{k},\omega) = e^2\, \frac{\langle k_x\rangle - \mathcal{D}_c(\boldsymbol{k},\omega+i\eta)}{i(\omega+i\eta)} \quad \cdot [\frac{1}{\hbar^2\, a_{\perp}}], \tag{4.41}$$

with the Matsubara current-current correlation function $\mathcal{D}_c(\boldsymbol{k}, i\nu_n)$. The important point here is, that the electron density ρ_0 of the continuum model (see Eq. (4.27)) is replaced by the local kinetic energy $\langle k_x\rangle$ of the effective lattice Hamiltonian.

In the presence of next-nearest neighbor diagonal hopping terms $\sim t'$, one has to make the additional substitution

$$c^{\dagger}_{\boldsymbol{l}+\boldsymbol{e}_x\pm\boldsymbol{e}_y,\sigma}\, c_{\boldsymbol{l},\sigma} \rightarrow\; e^{ieA_x(\boldsymbol{l})}\, c^{\dagger}_{\boldsymbol{l}+\boldsymbol{e}_x\pm\boldsymbol{e}_y,\sigma}\, c_{\boldsymbol{l},\sigma}, \tag{4.42}$$

where the expansion of the hopping terms up to order A^2 now yields

$$T_A = T - \sum_{\boldsymbol{l}} \left[e\, j^p_x(\boldsymbol{l})\, A_x(\boldsymbol{l},t) + \frac{e^2\, \tilde{k}_x(\boldsymbol{l})}{2}\, A^2_x(\boldsymbol{l},t) \right]. \tag{4.43}$$

Here, $\tilde{k}_x(\boldsymbol{l})$ is no longer proportional to the local kinetic energy and given by

$$\begin{aligned} \tilde{k}_x(\boldsymbol{l}) = & -t\sum_{\sigma}(c^{\dagger}_{\boldsymbol{l}+\boldsymbol{e}_x,\sigma}\, c_{\boldsymbol{l},\sigma} + c^{\dagger}_{\boldsymbol{l},\sigma}\, c_{\boldsymbol{l}+\boldsymbol{e}_x,\sigma}) \\ & \quad -t'\sum_{\sigma}(c^{\dagger}_{\boldsymbol{l}+\boldsymbol{e}_x+\boldsymbol{e}_y,\sigma}\, c_{\boldsymbol{l},\sigma} + c^{\dagger}_{\boldsymbol{l}+\boldsymbol{e}_x-\boldsymbol{e}_y,\sigma}\, c_{\boldsymbol{l},\sigma} \\ & \qquad + c^{\dagger}_{\boldsymbol{l},\sigma}\, c_{\boldsymbol{l}+\boldsymbol{e}_x+\boldsymbol{e}_y,\sigma} + c^{\dagger}_{\boldsymbol{l},\sigma}\, c_{\boldsymbol{l}+\boldsymbol{e}_x-\boldsymbol{e}_y,\sigma}). \end{aligned} \tag{4.44}$$

The paramagnetic current density operator in the presence of t',

$$\begin{aligned} j_x^p(\boldsymbol{l}) = it \sum_\sigma (c^\dagger_{\boldsymbol{l}+\boldsymbol{e}_x,\sigma} c_{\boldsymbol{l},\sigma} - c^\dagger_{\boldsymbol{l},\sigma} c_{\boldsymbol{l}+\boldsymbol{e}_x,\sigma}) \\ +it' \sum_\sigma (c^\dagger_{\boldsymbol{l}+\boldsymbol{e}_x+\boldsymbol{e}_y,\sigma} c_{\boldsymbol{l},\sigma} + c^\dagger_{\boldsymbol{l}+\boldsymbol{e}_x-\boldsymbol{e}_y,\sigma} c_{\boldsymbol{l},\sigma} \\ -c^\dagger_{\boldsymbol{l},\sigma} c_{\boldsymbol{l}+\boldsymbol{e}_x+\boldsymbol{e}_y,\sigma} - c^\dagger_{\boldsymbol{l},\sigma} c_{\boldsymbol{l}+\boldsymbol{e}_x-\boldsymbol{e}_y,\sigma}), \end{aligned} \tag{4.45}$$

contains many additional terms, which makes it very cumbersome to calculate the current-current corelation function.

On the other hand, for a translational invariant system with general dispersion $\epsilon(\boldsymbol{k})$, things simplify again and one obtains for the diamagnetic current

$$\langle j_x^D(\boldsymbol{q})\rangle = -e^2 \frac{2}{N} \sum_{\boldsymbol{k}} \frac{\partial^2 \epsilon(\boldsymbol{k})}{\partial k_x^2} n_{\boldsymbol{k}} A_x(\boldsymbol{q}), \tag{4.46}$$

where $n_{\boldsymbol{k}}$ is the momentum distribution function, which for a non-interacting system is given by the Fermi function $n_{\boldsymbol{k}} = f(\epsilon(\boldsymbol{k})) = \frac{1}{e^{\beta(\epsilon(\boldsymbol{k})-\mu)}+1}$. With the paramagnetic current operator given by

$$j_x^p(\boldsymbol{q}) = e \sum_{\boldsymbol{k},\sigma} \frac{1}{2} \left(\frac{\partial \epsilon(\boldsymbol{k})}{\partial k_x} + \frac{\partial \epsilon(\boldsymbol{k}+\boldsymbol{q})}{\partial k_x} \right) c^\dagger_{\boldsymbol{k},\sigma} c_{\boldsymbol{k}+\boldsymbol{q},\sigma}, \tag{4.47}$$

the Matsubara current-current correlation function

$$\mathcal{D}_c(\boldsymbol{q}, \tau - \tau') = -\frac{1}{N} \mathrm{Tr}\{\hat\rho_G \mathrm{T}_\tau [\hat{\boldsymbol{j}}_x^p(\boldsymbol{q},\tau) \hat{\boldsymbol{j}}_x^p(-\boldsymbol{q},\tau')]\} \tag{4.48}$$

can be evaluated exactly for a non-interacting system and one obtains

$$\mathcal{D}_c(\boldsymbol{q}, i\nu_n) = \frac{e^2}{2N} \sum_{\boldsymbol{k}} \left(\frac{\partial \epsilon(\boldsymbol{k})}{\partial k_x} + \frac{\partial \epsilon(\boldsymbol{k}+\boldsymbol{q})}{\partial k_x} \right)^2 \frac{f(\epsilon(\boldsymbol{k})) - f(\epsilon(\boldsymbol{k}+\boldsymbol{q}))}{i\nu_n + \epsilon(\boldsymbol{k}) - \epsilon(\boldsymbol{k}+\boldsymbol{q})}. \tag{4.49}$$

In deriving Eqs. (4.46) – (4.49), we used a symmetric expression for the current operator ($j^p_{x,sym}(\boldsymbol{l}) = \frac{1}{2}(j^p_x(\boldsymbol{l}-\boldsymbol{e}_x) + j^p_x(\boldsymbol{l}))$, see Eq. (4.35)). The result for the current-current correlation function (Eq. (4.49)) differs from the result obtained for the asymmetric $j^p_x(\boldsymbol{l})$ by a factor of $\cos(q_x/2)$ for a next neighbor tight-binding dispersion. This is due to the discreteness of the lattice on the scale a, which can be seen from

$$\cos\left(\frac{q_x}{2}\right) \equiv \cos\left(\frac{q_x a}{2}\right) \xrightarrow[a\to 0]{} 1, \tag{4.50}$$

for fixed q_x. Since we are considering the long-wavelength limit $\frac{2\pi}{|\boldsymbol{q}|} \gg a$, and since additionally for all physical relevant quantities $q_x = 0$ (see below), we have always used the asymmetric expression for the current given in Eq. (4.35), from which the current-current correlation function can be calculated much faster.

This example shows us, that the current obtained from an effective lattice Hamiltonian by means of a Peierls substitution is not a well-defined quantity. This stands in contrast to the first principle continuum Hamiltonian (Eq. (4.3)), which always yields a unique expression for the

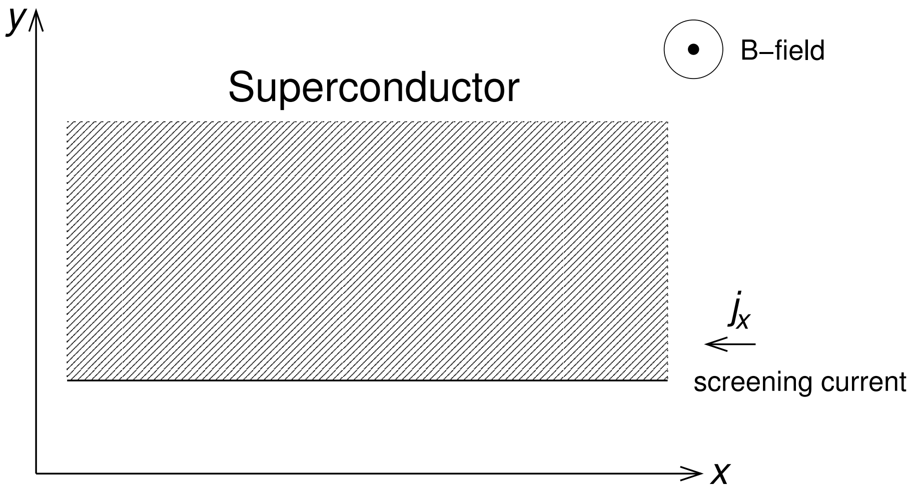

Figure 4.1: Superconducting half-plane with a magnetic field B applied perpendicular to the plane in z-direction. The screening current j_x runs parallel to the plane boundary in x-direction.

current. In fact, the correct way to obtain the effective current operator on the lattice would be to calculate the exact current operator for the original Hamiltonian and then perform the same unitary transformation and projection to the low energy sector that was done to obtain the effective lattice Hamiltonian from the first-principle Hamiltonian [173]. In practice, this is however only possible in an approximative way and always detailed knowledge of the original Hamiltonian is required [173].

4.1.4 General properties of $D_c(\boldsymbol{q},\omega)$ and $\sigma(\omega)$

In this section, we discuss different limits of the current-current correlation function, which determine whether a system is insulating, metallic or superconducting [174]. Furthermore, we present the conductivity sum rule for our effective lattice Hamiltonian and for a general continuum Hamiltonian.

London equations, London penetration depth, and superfluid weight D_s

One of the most characteristic properties of a superconductor — besides superconductivity — is, that it acts like a perfect diamagnet. This so-called Meissner effect can be described by the second London equation [175]

$$\boldsymbol{j}_s(\boldsymbol{x}) = -\frac{n_s e^2}{mc}\boldsymbol{A}(\boldsymbol{x}), \tag{4.51}$$

where n_s is the density of superfluid electrons. For the supercurrent $\boldsymbol{j}_s(\boldsymbol{x})$ to be conserved, one must require $\nabla \boldsymbol{A}(\boldsymbol{x}) = 0$ (or $\boldsymbol{q}\cdot\boldsymbol{A}(\boldsymbol{q}) = 0$), which means that $\boldsymbol{A}(\boldsymbol{x})$ must have transverse (Coulomb) gauge.

Now consider the geometry sketched in Fig. 4.1, with a superconducting half-plane with plane boundary at $y = 0$ and a static screening current running in x-direction parallel to the plane boundary. The magnitude of the screening current is constant in x-direction and varies slowly on a scale set by the lattice constant a in y-direction. The Fourier transformed London equation yields

$$j_x(q_y) = -\frac{c}{4\pi}\frac{1}{\lambda^2}\,A_x(q_y), \tag{4.52}$$

where $A_x(q_y)$ produces a magnetic field $B_z(q_y)$ in z-direction:

$$\boldsymbol{B}(\boldsymbol{x}) = \nabla\times\boldsymbol{A}(\boldsymbol{x}) \quad\Rightarrow\quad B_z(q_y) = -iq_y\,A_x(q_y). \tag{4.53}$$

In the long wavelength limit $q_y \to 0$ ($\lambda \gg a$), we obtain the Meissner effect, with the London penetration depth λ given by [174]

$$\frac{1}{\lambda^2} = \frac{4\pi n_s e^2}{mc^2}. \tag{4.54}$$

More general one can show [175], that in the long wavelength limit of the vector potential, the linear response Kernel can be written as

$$\langle j_i(\boldsymbol{q})\rangle = f(\boldsymbol{q})\,[\delta_{ij} - \frac{q_i q_j}{\boldsymbol{q}^2}]\,A_j(\boldsymbol{q}). \tag{4.55}$$

Here, gauge invariance, charge conservation as well as rotation invariance have been taken into account. For a superconductor one has ($\hbar = c = 1$)

$$\frac{-f(\boldsymbol{q}\to 0)}{e^2} = \left(\frac{n_s}{m}\right)^* = \frac{D_s}{\pi e^2}, \tag{4.56}$$

with D_s the superfluid weight. Comparing Eqs. (4.55) and (4.56) with our linear response formula (Eq. (4.40)) for the 2D lattice with next-neighbor hopping, one gets [174]

$$\frac{D_s}{\pi e^2} = -\langle k_x\rangle + \mathcal{D}_c(q_x = 0, q_y \to 0, i\nu_n = 0) \tag{4.57}$$

and

$$0 = -\langle k_x\rangle + \mathcal{D}_c(q_x \to 0, q_y = 0, i\nu_n = 0). \tag{4.58}$$

The last equation holds only if the system is gauge invariant. In the BCS gauge symmetry broken state also Eq. (4.58) yields D_s [174]. In our phase fluctuation model, on the other hand, we sample at each temperature over all possible phase configurations. Thus, all our results are gauge invariant and Eq. (4.58) should always be satisfied. Even below T_{KT}, we do not get a spontaneous gauge symmetry breaking, as discussed in Chap. 2. However, on the finite lattice we get a quasi long-range phase order and hence $D_s \neq 0$. Therefore, Eqs. (4.57) and (4.58) are an important check for the consistency of our calculations.

Drude weight D_0

Starting from the Drude conductivity

$$\sigma(\omega) = \frac{\sigma_0}{1 - i\omega\tau}, \tag{4.59}$$

with $\sigma_0 = \frac{ne^2\tau}{m}$ and taking the limit $\tau \to \infty$:

$$\sigma(\omega) = \frac{ne^2}{m}\, i\, \frac{1}{\omega + i\frac{1}{\tau}} \xrightarrow[\tau\to\infty]{} \frac{ne^2}{m}\left(\pi\,\delta(\omega) + i\,\frac{1}{\omega}\right), \tag{4.60}$$

the real part of $\sigma(\omega)$ turns into a δ-function

$$\sigma_1(\omega) = D_0\,\delta(\omega). \tag{4.61}$$

Eq. (4.61) defines the Drude weight $D_0 = \frac{\pi ne^2}{m}$. In general, one expects that at $T = 0$, the real part of the optical conductivity $\sigma_1(\boldsymbol{q} = 0, \omega)$ will have the form [174]

$$\sigma_1(\omega) = D_0\,\delta(\omega) + \sigma_1^{reg}(\omega), \tag{4.62}$$

with

$$\frac{D_0}{\pi e^2} = \left(\frac{n}{m}\right)^*. \tag{4.63}$$

Eqs. (4.62) and (4.63) can be generalized to finite temperatures. From the linear response formula (Eq. 4.41) in the limit $\eta \to 0$, one obtains for the 2D lattice with next-neighbor hopping:

$$\begin{aligned}\sigma(\omega) =& -e^2\pi\,(\langle k_x\rangle - \Re\{D_c(\boldsymbol{q}=0,\omega)\})\,\delta(\omega)\\ &-e^2\,\Im\{D_c(\boldsymbol{q}=0,\omega)\}\,\frac{1}{\omega}\\ &-ie^2\,(\langle k_x\rangle - \Re\{D_c(\boldsymbol{q}=0,\omega)\})\,\frac{1}{\omega}\\ &[+i\pi\,\Im\{D_c(\boldsymbol{q}=0,\omega)\}\,\delta(\omega)].\end{aligned} \tag{4.64}$$

Here, we separated the retarded current-current correlation function into real ($\Re\{\cdots\}$) and imaginary ($\Im\{\cdots\}$) part. The term in brackets $[\cdots]$ is zero, since the imaginary part of $D_c(\boldsymbol{q} = 0, \omega)\}$ is antisymmetric in ω. Comparing Eq. (4.62) with Eq. (4.64), one finally gets

$$\frac{D_0}{\pi e^2} = -\langle k_x\rangle + \Re\{D_c(\boldsymbol{q}=0,\omega\to 0)\}. \tag{4.65}$$

To summarize our results: D_s is a measure of the density of superconducting electrons and D_0 is a measure of the density and mobility of normal conducting electrons. Thus, at $T = 0$ an insulator is defined by $D_s = 0$ and $D_0 = 0$, a metal is defined by $D_s = 0$ and $D_0 \neq 0$, and a superconductor is defined by $D_s \neq 0$ and $D_0 \neq 0$. At finite temperature or in the presence of disorder, one can have $D_0 = 0$, but $\sigma(\omega = 0)$ remains finite for a metallic system [174].

Conductivity sum-rule

Integrating Eq. (4.64) over all frequencies, one gets the conductivity sum-rule for the 2D lattice with next-neighbor hopping

$$\int_{-\infty}^{+\infty} \sigma(\omega)\, d\omega = -e^2 \pi \, \langle k_x \rangle. \tag{4.66}$$

This result was obtained due to the symmetry of $\Re\{D_c(\boldsymbol{q}=0,\omega)\}$, which is an even function in ω, and since

$$\int_{-\infty}^{+\infty} \left(\pi\, \Re\{D_c(\boldsymbol{q}=0,\omega)\}\, \delta(\omega) - \Im\{D_c(\boldsymbol{q}=0,\omega)\}\, \frac{1}{\omega} \right) d\omega = 0, \tag{4.67}$$

because of the Kramers-Kronig relation

$$\Re\{D_c(\boldsymbol{q},\omega)\} = \frac{1}{\pi}\, \mathcal{P} \int_{-\infty}^{+\infty} \frac{\Im\{D_c(\boldsymbol{q},\omega')\}}{\omega'-\omega}\, d\omega'. \tag{4.68}$$

For the continuum system, on the other hand, one obtains

$$\int_{-\infty}^{+\infty} \sigma(\omega)\, d\omega = \frac{\pi n e^2}{m}. \tag{4.69}$$

The consequences of these results will be discussed in great detail in the next section.

4.2 Optical sum-rule and kinetic energy

In ordinary BCS superconductors the optical conductivity is suppressed at frequencies within a range of about twice the SC gap. The corresponding low-frequency spectral weight W_{low} is transfered to the zero-frequency delta peak W_D [7], associated with the dissipationless transport (and the superfluid weight D_s) in the SC state. This is the Glover-Ferrell-Tinkham (GFT) sum rule. On the other hand, the *total* frequency integral of the optical conductivity is conserved, when decreasing the temperature across the SC transition, due to the oscillator-strength or f-sum rule [7], i. e.

$$W_{tot}^{sc} = W_{tot}^{n}. \tag{4.70}$$

The full optical integral, when integrated over all frequencies *and* energy bands, is proportional to the carrier density n over the bare mass m

$$W_{tot} \equiv W_D + W_{low} + W_{high} = \int_0^{\infty} Re\ \sigma_{exp}(\omega)\, d\omega = \frac{\pi n e^2}{2m}, \tag{4.71}$$

and thus is conserved. This is exactly the result, which one obtains from the first principle continuum Hamiltonian (Eq. (4.69)). When the optical integral is restricted over a finite (low) range of frequencies Ω, in the HTSC typically of the order of eV, one may consider the weight $W_D + W_{low}$ as being essentially due to a single band around the Fermi energy, i. e.

$$W_D + W_{low} = \int_0^{\Omega} Re\ \sigma_{exp}(\omega)\, d\omega = \int_0^{\infty} Re\ \tilde{\sigma}(\omega)\, d\omega = \pi e^2\, \frac{1}{N} \sum_{\boldsymbol{k}} \frac{\partial^2 \epsilon(\boldsymbol{k})}{\partial k_x^2}\, n_{\boldsymbol{k}}, \tag{4.72}$$

where $\sigma_{exp}(\omega)$ is the experimentally measured low frequency optical conductivity and $\tilde{\sigma}(\omega)$ is the theoretical single-band conductivity. The last equality was obtained from Eq. (4.46), with the Fermi distribution replaced by the momentum distribution $n_{\boldsymbol{k}}$ of the interacting many-particle system. Thus, the frequency integral of the optical conductivity within the single-band assumption, is proportional to the the inverse mass tensor $\frac{\partial^2\epsilon(\boldsymbol{k})}{\partial k_x^2}$ ($\hat{x}$ being the direction in which the conductivity is measured) weighted with the momentum distribution $n_{\boldsymbol{k}}$. It depends upon the bare single-particle band structure $\epsilon(\boldsymbol{k})$, being proportional to minus the kinetic energy $W_D + W_{low} = -\frac{\pi e^2}{4}E_{kin}$ for a (nearest-neighbor) tight-binding (TB) model, while for free electrons it is a constant given by the electron density divided by the effective mass.

In case of our phase-fluctuation model with nearest-neighbor hopping ($t' = 0$), we obtain

$$W_D + W_{low} = -e^2\,\frac{\pi}{2}\,\langle k_x\rangle, \tag{4.73}$$

whereas the inclusion of next-nearest neighbor hopping terms ($t' \neq 0$) yields

$$W_D + W_{low} = -e^2\,\frac{\pi}{2}\,\langle \tilde{k}_x\rangle, \tag{4.74}$$

with k_x and $\tilde{k}_x$ being defined in Eqs. (4.36) and (4.44). Hence, a careful study of the low-frequency single-band optical sum-rule could show, whether the SC transition in the underdoped cuprates is BCS-like. Furthermore, it may reflect the detailed temperature dependence of the kinetic energy, if a nearest-neighbor tight-binding description is appropriate.

Now, recent measurements of the in-plane optical conductivity [176, 177] have indicated a *violation* of the GFT optical sum rule for frequencies up to 2 eV in underdoped $Bi_2Sr_2CaCu_2O_{8+\delta}$ (Bi2212). By entering the superconducting state, not only spectral weight W_{low} from the microwave and far-infrared, but also from the visible optical spectrum i. e. high-frequency spectral weight W_{high} contributes to the superfluid condensate W_D. That is, in contrast to ordinary BCS-superconductors, a "*color* change" is introduced at the superconducting transition. In addition, unusually high energy scales involved in forming the superconducting state were also observed in sum-rule analyses of underdoped $YBa_2Cu_3O_{6+x}$ (YBCO) [178–180].

The interpretation of these unusual results may require the inclusion of local-field effects [181] and other (such as excitonic) many-body effects. Local-field effects are caused by local dipoles, which are induced by an external perturbation with wavevector $\boldsymbol{q}$. The induced secondary fields vary on a atomic scale and produce a response also at wavevector $\boldsymbol{q}+\boldsymbol{G}$, with $\boldsymbol{G}$ being a reciprocal lattice vector. These effects are known to play a crucial role already in weakly-correlated systems (such as semiconductors), and introduce a shift of order of the Coulomb correlation energy between single-particle and two-particle, i. e. optical excitations [182]. Therefore, they may partly account for the "high-energy" features observed in $\sigma(\omega)$. On the other hand, within a tight-binding one-band model, the anomalously large energy scale, which contributes to the superfluid weight, and the corresponding *color* change in Bi2212 can be attributed to a *reduction of kinetic energy* [183] at the superconducting transition. This is rather surprising, since one would expect that in a conventional (BCS) pairing process, it is the potential energy which is reduced at the expense of the kinetic energy, with the latter being increased due to particle-hole mixing. In contrast, a similar analyses for YBCO rather points to an increasing kinetic energy in the SC state [180].

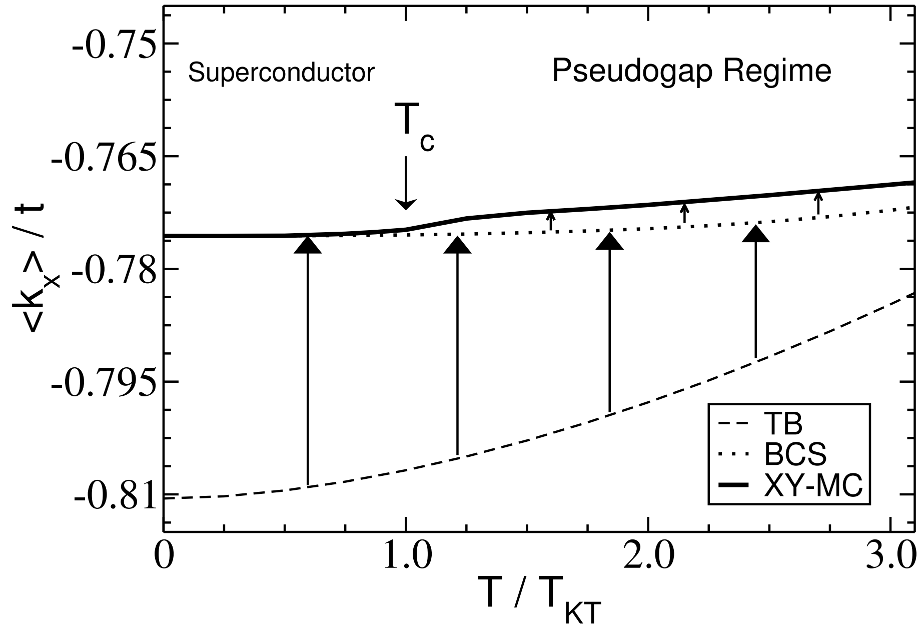

Figure 4.2: Kinetic energy per bond $\langle k_x \rangle$ as a function of temperature for non-interacting tightly-bound electrons (TB), the BCS solution (BCS), and our phase-fluctuation model (XY-MC) at half-filling ($\langle n \rangle = 1$). The large vertical arrows indicate the increase in kinetic energy upon pairing relative to the tight-binding model of non-interacting electrons, and the small arrows indicate the additional increase due to phase fluctuations. This additional phase-fluctuation energy *rapidly vanishes near $T_c \equiv T_{KT}$, which causes the significant change in the optical integral upon entering the superconducting state at T_{KT}. Note that the full line follows the actual kinetic energy encountered in our model, when going from the pseudogap to the superconducting regime.*

In the following, we show that phase fluctuations can contribute to a significant reduction of the in-plane kinetic energy upon entering into the SC phase below T_c, with a magnitude comparable to the experimental results in Bi2212. The physical reason for this kinetic energy lowering is that, due to phase fluctuations and to the associated incoherent motion of Cooper pairs (cf. Fig. 4.2), the pseudogap region has a higher kinetic energy than the simple BCS mean-field state. When long-ranged phase coherence finally develops at T_c, the Cooper-pair motion becomes phase *coherent* and the kinetic energy decreases. The onset of the coherent motion can be seen, for example, from the development of coherence peaks in the tunneling spectrum of $Bi_2Sr_2CuO_{6+\delta}$ compounds (see e. g. [26, 156] and Fig. 3.1). The initial *cost* of kinetic energy, which is needed for pairing, is payed at a mean-field temperature T_c^{MF} considerably higher than T_c. Therefore, the reduction of kinetic energy observed experimentally in Bi2212 [176, 177] can be attributed to a transition from a phase-disordered pseudogap to a phase-ordered superconducting state. We stress that this effect is independent of the particular mechanism leading to pair formation, as long as the superconductor considered is characterized by a small phase stiffness [13].

For the calculation of the optical sum-rule and kinetic energy, we assume a BCS temperature

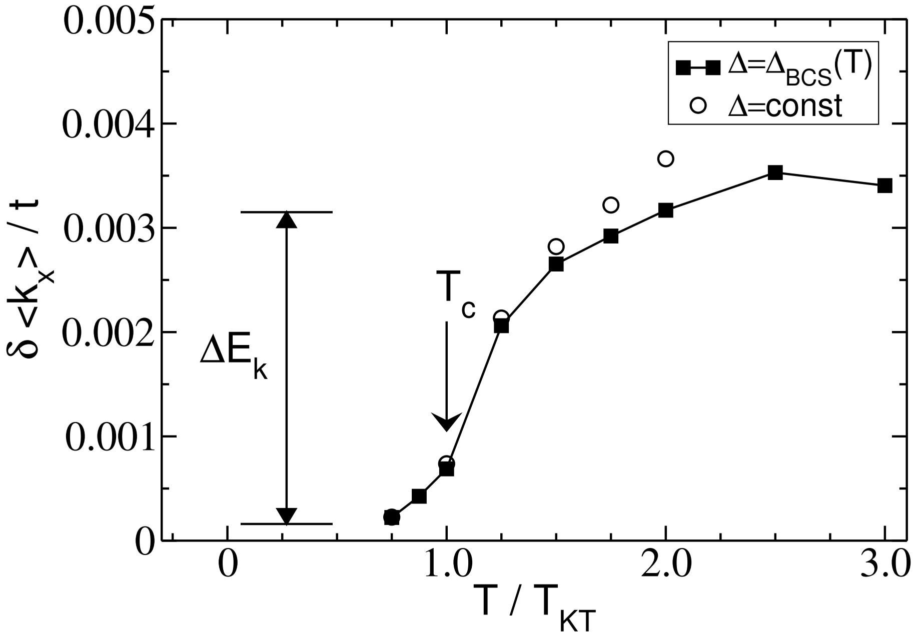

Figure 4.3: Kinetic energy contribution from phase fluctuations $\delta\langle k_x\rangle = \langle k_x\rangle_{XY-MC} - \langle k_x\rangle_{BCS}$. One can clearly see the sharp decrease of the kinetic energy near the Kosterlitz-Thouless transition at $T_{KT} \equiv T_c$. ΔE_k gives an estimate of the kinetic condensation energy at T_c. For comparison, we also show the results for a constant gap as open circles between T_{KT} and $2T_{KT}$.

dependence of the $d_{x^2-y^2}$-wave pairing gap $\Delta(T)$. We have therefore set $\Delta(T=0) = 1.0t$ corresponding to $T_c^{MF} \simeq 0.42t$. The condition that $\xi > \xi_0$ (see Sec. 2.5) is always fulfilled, if we are not too close to T_c^{MF}. Fig. 4.2 displays the kinetic energy $\langle k_x\rangle$ as a function of temperature for non-interacting tight-binding electrons, for BCS electrons, and for our phase-fluctuation model, respectively, at half-filling ($\langle n\rangle = 1$) and with $t' = 0$. One can clearly see that pairing, as expected, produces an overall increase of kinetic energy (indicated as vertical arrows) with respect to the free-electron case. We observe that in the phase-fluctuation model the kinetic energy is further increased (small vertical arrows) due to the incoherent motion of the paired electrons. The kinetic energy is a smoothly decreasing function of temperature for $T \longrightarrow 0$. This is expected from the fact that, at high temperature, more electrons are transferred to higher kinetic energies, and is in agreement with the experimental results [176, 177]. What we are especially interested in, is the rather pronounced change (magnified in Fig. 4.3 by using a different scale for the kinetic energy) near $T_c \equiv T_{KT}$, where the kinetic energy of our phase-fluctuation model rather suddenly reduces to the BCS value. This sudden deviation from the $T \gtrsim T_c$ behavior is also obtained in experiments, which show a kink in the temperature dependence of the low-frequency spectral weight $W_D + W_{low}$ at T_c [176].

This pronounced change of in-plane kinetic energy can be better observed in Fig. 4.3, where we plot the difference between the BCS kinetic energy and the kinetic energy of our phase-fluctuation model $\delta\langle k_x\rangle = \langle k_x\rangle_{XY-MC} - \langle k_x\rangle_{BCS}$. Fig. 4.3 also shows the temperature dependence of the kinetic energy for a constant gap Δ. We see, that the change in kinetic energy close

parameters:	$\langle n\rangle = 1.0, t' = 0$	$\langle n\rangle = 0.9, t' = 0$
$E_{kin}(0.75T_{KT})$	$-1.550713 \pm .000024$	$-1.541022 \pm .000020$
$E_{kin}(2.0T_{KT})$	$-1.542952 \pm .000004$	$-1.533595 \pm .000007$
$E_{kin}^{BCS}(0.75T_{KT})$	-1.550919	-1.540824
$E_{kin}^{BCS}(2.0T_{KT})$	-1.549297	-1.538979
$\delta E_{kin}/10^{-3}$	$7.761 \pm .024$	$7.427 \pm .021$
$\delta E_{kin}^{rel}/10^{-3}$	$6.139 \pm .024$	$5.581 \pm .021$
$\langle\tilde{k}_x\rangle(0.75T_{KT})$	$-0.775357 \pm .000012$	$-0.770511 \pm .000010$
$\langle\tilde{k}_x\rangle(2.0T_{KT})$	$-0.771476 \pm .000002$	$-0.766798 \pm .000004$
$\langle\tilde{k}_x\rangle^{BCS}(0.75T_{KT})$	-0.775460	-0.770412
$\langle\tilde{k}_x\rangle^{BCS}(2.0T_{KT})$	-0.774649	-0.769489
$\delta\langle\tilde{k}_x\rangle/10^{-3}$	$3.881 \pm .012$	$3.714 \pm .011$
$\delta\langle\tilde{k}_x\rangle^{rel}/10^{-3}$	$3.070 \pm .012$	$2.790 \pm .011$

Table 4.1: Kinetic energy per lattice site for the phase-fluctuation model (E_{kin}) and for the BCS model (E_{kin}^{BCS}) at different temperatures. δE_{kin} indicates the absolute change in kinetic energy and $\delta E_{kin}^{rel} = \delta E_{kin} - \delta E_{kin}^{BCS}$ the relative change in kinetic energy of the phase-fluctuation model between $0.75T_{KT}$ and $2.0T_{KT}$. $\langle\tilde{k}_x\rangle$ indicates the corresponding values for the optical integral. With $t' = 0$, we have $\langle\tilde{k}_x\rangle = E_{kin}/2$.

to T_c is almost the same. For higher temperatures, however, a constant gap produces a further increasing kinetic energy, especially close to T_c^{MF}.

As discussed above, the reduction of kinetic energy is due to the onset of phase coherence of the Cooper pairs below the SC transition temperature $T_c \equiv T_{KT}$. This is signaled by the appearance of sharp coherence peaks in the single-particle spectral function upon developing long-range phase coherence [156]. The corresponding result for the density of states $N(\omega)$ displaying these coherence peaks was already shown in Fig. 3.1. Notice that this argument for the reduction of kinetic energy at T_c due to a phase ordering transition is quite robust. For example, we expect it to be valid (and actually to be stronger) in a true three-dimensional system. As a matter of fact, it has been argued [32, 83] that even small interplane couplings play an important role due to the infinite-order nature of the the KT transition.

In order to get a rough estimate of the kinetic condensation energy, we calculate the reduction in kinetic energy near T_c, i. e.

$$\Delta E_k = -\frac{2}{e^2\pi}\int_0^\infty (Re\,\tilde{\sigma}^{sc}(\omega) - Re\,\tilde{\sigma}^{n}(\omega))\,d\omega, \tag{4.75}$$

as indicated by the energy change ΔE_k in Fig. 4.3 and also displayed in Tab. 4.1. Assuming that $t \simeq 250$ meV, we get a condensation energy estimate of 1.5 meV per Copper site, which is in order of magnitude agreement with the experimental results (again assuming a one-band nearest-neighbor TB analysis).

Up to now, to refrain from further approximations, we have set the chemical potential μ equal to zero and have only considered nearest-neighbor hopping. We have checked to some extent,

parameters:	$\langle n\rangle = 1.0$, $t' = -0.4t$	$\langle n\rangle = 0.9$, $t' = -0.4t$
$E_{kin}(0.75T_{KT})$	$-1.611590 \pm .000160$	$-1.515547 \pm .000189$
$E_{kin}(2.0T_{KT})$	$-1.606282 \pm .000017$	$-1.506225 \pm .000014$
$E_{kin}^{BCS}(0.75T_{KT})$	-1.609822	-1.515214
$E_{kin}^{BCS}(2.0T_{KT})$	-1.607755	-1.511573
$\delta E_{kin}/10^{-3}$	$5.308 \pm .161$	$9.322 \pm .190$
$\delta E_{kin}^{rel}/10^{-3}$	$3.241 \pm .161$	$5.681 \pm .190$
$\langle \tilde{k}_x\rangle(0.75T_{KT})$	$-0.853573 \pm .000175$	$-0.776569 \pm .000216$
$\langle \tilde{k}_x\rangle(2.0T_{KT})$	$-0.855927 \pm .000020$	$-0.777414 \pm .000019$
$\langle \tilde{k}_x\rangle^{BCS}(0.75T_{KT})$	-0.849341	-0.773091
$\langle \tilde{k}_x\rangle^{BCS}(2.0T_{KT})$	-0.849921	-0.773596
$\delta\langle \tilde{k}_x\rangle/10^{-3}$	$-2.354 \pm .176$	$-0.845 \pm .217$
$\delta\langle \tilde{k}_x\rangle^{rel}/10^{-3}$	$-1.775 \pm .176$	$-0.340 \pm .217$

Table 4.2: Kinetic energy per lattice site for the phase-fluctuation model (E_{kin}) and for the BCS model (E_{kin}^{BCS}) at different temperatures. δE_{kin} indicates the absolute change in kinetic energy and $\delta E_{kin}^{rel} = \delta E_{kin} - \delta E_{kin}^{BCS}$ the relative change in kinetic energy of the phase-fluctuation model between $0.75T_{KT}$ and $2.0T_{KT}$. $\langle \tilde{k}_x\rangle$ indicates the corresponding values for the optical integral. Note the contrary behavior of E_{kin} and $\langle \tilde{k}_x\rangle$ for $t' = -0.4t$.

how robust these results are with respect to finite doping ($\langle n\rangle \approx 0.9$) and the inclusion of a next-nearest-neighbor hopping-term t' in our Hamiltonian Eq. (2.2). The results are displayed in Tabs. 4.1 and 4.2. Notice that in the case of $t' \neq 0$, the optical integral (Eq. (4.72)) is no longer proportional to the kinetic energy and given by $\sim \langle \tilde{k}_x\rangle$ (see Eqs. (4.44) and (4.74)).

In the cuprates, one typically has $0 > t' > -0.4t$ (see Sec. 3.2.1). For $0 \geq t' \gtrsim -0.3t$, our results for the sum rule *violation* are reduced only by about 20% – 30%. For $t' = -0.4t$, however, the *violation* of the sum rule changes its sign (see Tab. 4.2). On the other hand, the reduction of the kinetic energy at T_c is always of the same order of magnitude. The strong dependence of the optical sum-rule on the dispersion might — besides local-field and other many-particle effects — be a reason for the different temperature dependence of the low-frequency optical sum-rule in Bi2212 and YBCO [180].

On a more general ground, going back to Eq. (4.72), we see that a change of the optical integral is always related to a change in the momentum distribution function $n_{\boldsymbol{k}}$, for a fixed bare single-particle dispersion $\epsilon(\boldsymbol{k})$. Starting from a Fermi liquid at low temperature, one gets a sharp cut-off in $n_{\boldsymbol{k}}$ at $k = k_F$. In the BCS ground state, the momentum distribution function is no longer given by the Fermi function. Instead, we have $n_{\boldsymbol{k}} = v_k^2$ (see Sec. 3.2.1), with v_k^2 being smeared out over an energy of order $2\Delta_{sc}$ due to particle-hole mixing. This occupation of momentum states with $k > k_F$ in the ground state produces, e. g. for a nearest neighbor tight-binding dispersion, the *increase* in kinetic energy in the BCS SC state with respect to the Fermi-liquid normal state.

Therefore, a *reduction* in kinetic energy in the SC state can only happen, if one has a non-

Fermi-liquid-like normal state with a momentum distribution which is smeared out on a even larger scale then the BCS momentum distribution. This can happen, if the normal state spectral functions are rather incoherent and sharp quasiparticle peaks form only below T_c, as in the underdoped high-T_c cuprates [184, 185]. In our case, the non-Fermi-liquid behavior above T_c is caused by a pseudogap with phase fluctuations which produces very incoherent quasiparticle peaks especially at the $(\pi, 0)$-regions of the Brillouin zone (see our results for the spectral weight in Sec. 3.2).

This non-BCS-like behavior is typical for strongly coupled superconductors with a pure electronic pairing mechanism [186]. There, the onset of superconductivity has a strong feedback effect on the electronic structure and can therefore lead to a reduction of kinetic energy [186]. DCA (dynamical cluster approximation) calculations [187] and variational Monte Carlo studies [188] of the 2D Hubbard model have shown, that one indeed obtains a reduction of kinetic energy in the SC state for strong coupling ($U \gg 1$).

In the preceeding discussion, we always used the term “kinetic energy” for $\langle k_x \rangle$ instead of the more appropriate term “expectation value of the nearest-neighbor hopping-operator”. This is usually done to distinguish the hopping (“kinetic”) part of the effective Hamiltonian, which picks up a Peierls phase in a Gauge transformation, from the interacting part. However, a real decomposition into kinetic and potential energy is meaningless for an effective Hamiltonian [189]. This is exactly the same problem that we have encountered in defining a current operator for an effective lattice Hamiltonian by means of the Peierls phase (see Sec. 4.1.3).

Each effective Hamiltonian can, in principle, be obtained from the exact many-particle Hamiltonian by a series of unitary transformations and a subsequent projection into the low energy sector of the Hilbert space. However, what is “kinetic energy” at one level, is “potential energy” on the other level [190]. This becomes more clear, when we look at the Hubbard model. For large Coulomb repulsion ($U \to \infty$), the Hubbard Hamiltonian can be reduced to the effective t-J Hamiltonian, where the exchange interaction is given by $J = 4t^2/U$. Hence, the exchange interaction of the t-J model is nothing but a reflection of the frustrated kinetic energy at the level of the Hubbard model in the $U \to \infty$ limit.

Thus it only makes sense to ask, which term of the effective Hamiltonian is more important in forming the SC state, but it is pure semantics to call one term “kinetic energy” and the other “potential energy” [189]. In fact, even the BCS Hamiltonian is an effective reduced Hamiltonian, where the *kinetic process* of lattice distortion is replaced by an effective electron-electron *potential* energy term.

Finally, we want to annotate, that a kinetic energy reduction as driving mechanism for superconductivity has been discussed some years ago in connection with an interlayer tunneling (ILT) model for the high-T_c cuprates [191]. There, the reduction of kinetic energy is due to the delocalization of Cooper-pairs between the copper-oxide layers. The Cooper-pairs can tunnel much better between layers then normal quasiparticles, especially for momenta close to the $(\pi, 0)$-regions of the Brillouin zone. This effect should be visible in the c-axis conductivity sum-rule [192, 193], in contrast to the in-plane or ab-axis sum-rule discussed in this section.

However, the expected release of frustrated c-axis kinetic energy is only compatible with the experimental c-axis optical sum-rule for some high-T_c compounds [194]. Thus, ILT is not the main driving mechanism for superconductivity in the cuprates but may be an important mechanism to enhance T_c in a mixture with other mechanisms, such as charge imbalance between the layers [195].

Interestingly, the c-axis conductivity is very sensitive to the $(\pi,0)$-properties of the single-particle spectral function [196, 197]. Which means, that also there, the in-plane $(\pi,0)$-scattering rate and incoherent $(\pi,0)$-quasiparticle-peaks play an important role. Only below T_c, coherent tunneling of the (pre-formed) pairs is possible. On the other hand, the *in-plane* (ab-axis) infrared conductivity is most sensitive to the $(\frac{\pi}{2},\frac{\pi}{2})$-direction of the Fermi surface, and *not* $\boldsymbol{k} = (\pi,0)$, where the pseudogap opens.

This is due to the different bare quasiparticle velocities $v(\boldsymbol{k}) = \frac{\partial\epsilon(\boldsymbol{k})}{\partial k_x}$ [198] and can be seen from Eq. (4.49), where in the limit $\boldsymbol{q} \to 0$, the sum over all states $\boldsymbol{k}$ is weighted with a factor $v^2(\boldsymbol{k})$.[1] Furthermore, for small frequencies and temperatures, only states close to the Fermi surface contribute. For the in-plane optical integral, this had no consequences, since we integrated the single-band conductivity $\tilde{\sigma}(\omega)$ from $\omega = 0$ up to $\omega = \infty$. But this $\boldsymbol{k}$-selectivity of the in-plane optical conductivity has important consequences, when one calculates the *low-frequency* conductivity for our phase fluctuation model. This can bee seen, by comparing the results for a $d_{x^2-y^2}$-wave gap with those for a s-wave gap with phase fluctuations, as will be shown in the next section (Sec. 4.3).

4.3 Optical conductivity

In this section we give a thorough discussion of the detailed frequency and temperature dependence of the optical conductivity within our phase fluctuation model. The results for a $d_{x^2-y^2}$-wave gap are complemented with results for a s-wave gap and analyzed in terms of an extended Drude model. Finally, we discuss the precursor effects of the superconducting state above T_c which are visible in the optical conductivity at finite frequencies. These precursor effects are called *paraconductivity*. We compare our results for a $d_{x^2-y^2}$-wave gap with phase fluctuations with microwave conductivity experiments in underdoped $\mathrm{Bi_2Sr_2CaCu_2O_{8+\delta}}$ (Bi2212) [40].

4.3.1 General properties

The optical conductivity $\sigma(\omega)$ is usually written as $\sigma(\omega) = \sigma_1(\omega) + i\,\sigma_2(\omega)$, with $\sigma_1(\omega)$ the real part of $\sigma(\omega)$, and $\sigma_2(\omega)$ the imaginary part. In an ideal BCS superconductor, like our model without phase fluctuations, the real part of the conductivity $\sigma_1(\omega)$ is given by a δ-peak with weight $D_s \sim \left(\frac{n_s}{m}\right)^*$ centered at $\omega = 0$. The imaginary part, on the other hand, falls off as $\frac{1}{\omega}$ with prefactor $D_s \sim \left(\frac{n_s}{m}\right)^*$ [7]. In a real material, the normal conducting electrons already give a contribution *below* T_c to the real part of the conductivity $\sigma_1(\omega)$. In an s-wave superconductor, this contribution to $\sigma_1(\omega)$ becomes visible only at frequencies $\omega \gtrsim 2\Delta_{sc}$, but in a $d_{x^2-y^2}$-wave superconductor, the presence of nodal quasiparticles gives a visible contribution to $\sigma_1(\omega)$ even below $\omega \simeq 2\Delta_{sc}$ and at very low temperatures $T \lesssim T_c$.

---

[1] Note, that also the density of energy states close to $\boldsymbol{k} = (\pi,0)$ is increased, the prefactor of $v^2(\boldsymbol{k})$ strongly suppresses any contribution.

Above T_c, the finite electronic scattering rate strongly suppresses the imaginary part $\sigma_2(\omega)$ at low frequencies, so that it can be completely neglected in the *normal state* of a real material. In our model, however, we obtain without pairing interaction ($\Delta = 0$) a nearest-neighbor-hopping tight-binding metal. This is an *ideal metal* without electron scattering. Hence, also there, the real part of the conductivity is given by a δ-peak at $\omega = 0$ and the imaginary part falls of as $\frac{1}{\omega}$ (see Sec. 4.1.4). However, in the metallic state the superfluid weight D_s is replaced by the Drude weight D_0. In the phase coherent BCS-limit, one has $D_s = D_0$ [174]. Thus, the optical conductivity calculated from our phase fluctuation model solely represents the finite-frequency paraconductivity due to phase fluctuations and has to be added to the regular finite-frequency conductivity of the normal electrons in the cuprates.

The optical conductivity is generally analyzed in terms of the extended Drude model (EDM) [199]. This model is defined by

$$\sigma(\omega) = \frac{ne^2}{m_b} \frac{1}{1/\tau(\omega) - i\omega m_{\text{eff}}(\omega)/m_b}, \tag{4.76}$$

where m_b is the bare electron band mass. From this model one can extract the frequency dependent effective scattering rate as

$$\frac{1}{\tau_{\text{eff}}(\omega)} = \frac{ne^2}{m_b} \Re\left\{\frac{1}{\sigma(\omega)}\right\}, \tag{4.77}$$

and the frequency dependent effective mass as

$$\frac{m_{\text{eff}}(\omega)}{m_b} = -\frac{ne^2}{m_b} \frac{1}{\omega} \Im\left\{\frac{1}{\sigma(\omega)}\right\}. \tag{4.78}$$

For our lattice Hamiltonian with nearest-neighbor hopping one has instead

$$\frac{1}{\tau_{\text{eff}}(\omega)} = -\langle k_x\rangle \Re\left\{\frac{1}{\sigma(\omega)}\right\} \tag{4.79}$$

and

$$\frac{m_{\text{eff}}(\omega)}{m_b} = \langle k_x\rangle \frac{1}{\omega} \Im\left\{\frac{1}{\sigma(\omega)}\right\}. \tag{4.80}$$

Optical conductivity curves acquired from infrared spectroscopy on different high-T_c compounds for various doping levels can be found in Refs. [200–203]. They all show, that the real part of the ab-(in-plane) optical conductivity $\sigma_1(\omega)$ is suppressed in the superconducting state for frequencies $\omega \lesssim 2\Delta_{sc}$. This change in the optical properties is much clearer observable in the scattering rate $1/\tau$. The nearly ω-linear scattering rate is suddenly strongly suppressed for frequencies $\omega \lesssim 2\Delta_{sc}$. This suppression of $1/\tau$ is recovered in the overdoped cuprates *exactly* at the superconducting critical temperature T_c, as expected in a BCS scenario.

In the underdoped cuprates, on the other hand, the scattering rate for $\omega \lesssim 2\Delta_{sc}$ *smoothly* increases for temperatures $T > T_c$, but the ω-linear behavior is not resumed until a temperature $T^* \gg T_c$ [201]. Furthermore, even below T_c, an additional dissipation was observed in the infrared conductivity of Bi2212, which cannot be explained by a normal fluid of nodal quasiparticles alone and might be an indication for the presence of (quantum) phase fluctuations below T_c [204].

Before we discuss our results, a few words on the terminology are in place here. We are only interested in the properties of the *low-frequency* optical conductivity with frequencies $\omega \lesssim 2\Delta_{sc}$. These frequencies correspond to the microwave and infrared part of the electromagnetic spectrum. Whereas the *high-frequency* optical conductivity corresponds to frequencies of the order of the total bandwidth and is usually in the visible and ultraviolet range of the electromagnetic spectrum. However, from the point of view of a *standard* "50 Hz" AC circuit, all these are "high-frequency" conductivity experiments.

All calculations were done for 10% doping ($\langle n \rangle = 0.9$) and without next-nearest neighbor-hopping ($t' = 0$). Fig. 4.4 displays the real part of the optical conductivity $\sigma_1(\omega)$ for the $d_{x^2-y^2}$-wave gap with phase fluctuations. One can clearly see an increase of the finite-frequency conductivity as a function of temperature already below $T_c \equiv T_{KT}$ for frequencies $\omega \lesssim \Delta_{sc}$. This increase is due to the presence of nodal quasiparticles with vanishing excitation energy. Moreover, $\sigma_1(\omega)$ shows a very smooth development as a function of temperature. This smooth temperature dependence can be explained by the $\boldsymbol{k}$-selectivity of the in-plane optical conductivity, which was discussed at the end of Sec. 4.2. There, we have shown that quasiparticles with $\boldsymbol{k}$-vectors in the nodal direction of the Brillouin zone (BZ) dominate the in-plane conductivity. Now, the $(\frac{\pi}{2}, \frac{\pi}{2})$-quasiparticle-peaks only change very slightly with rising temperature (see Figs. 3.14 and 3.18) compared to the dramatic changes of the $(\pi, 0)$-quasiparticle-peaks. The quasiparticles close to $\boldsymbol{k} = (\pi, 0)$, where the $d_{x^2-y^2}$-wave gap is its maximum, however, do not contribute to the in-plane conductivity, which can also be seen from the absence of any paraconductivity in the frequency range $1.5\Delta_{sc} \lesssim \omega < 2\Delta_{sc}$.

In contrast to the $d_{x^2-y^2}$-wave gap, our results for the s-wave gap with phase fluctuations displayed in Fig. 4.5, show a relatively sharp peak at $\omega = 0$ in $\sigma_1(\omega)$, also at higher temperatures. The main difference to the $d_{x^2-y^2}$-wave case is that the optical conductivity has a small maximum at $\omega = 2\Delta_{sc}$ below $T_c \equiv T_{KT}$, whereas in the frequency range $0.5\Delta_{sc} \lesssim \omega \lesssim 1.5\Delta_{sc}$ almost no enhanced conductivity is observable in the SC state. Only for $\omega \lesssim 0.5\Delta_{sc}$ one gets a contribution to the finite frequency conductivity from the slightly broadened δ-peak at $\omega = 0$, which is caused by the Lorentzian representation of the δ-function. But as soon as the temperature is raised above $T \gtrsim 1.25 T_{KT}$, one gets a sudden massive increase of $\sigma_1(\omega)$ for all frequencies $\omega \lesssim 2\Delta_{sc}$.

Again, this reflects the behavior of the quasiparticle peaks at the $(\frac{\pi}{2}, \frac{\pi}{2})$-regions of the BZ (see Figs. 3.13 and 3.19). In contrast to the d-wave case, below $T_c \equiv T_{KT}$ the quasiparticle spectrum is gapped at $\boldsymbol{k} = (\frac{\pi}{2}, \frac{\pi}{2})$. Thus one obtains a finite conductivity only for frequencies $\omega \approx 2\Delta_{sc}$. On the other hand, for $T \gtrsim 1.25 T_{KT}$, the s-wave gap closes at $\boldsymbol{k} = (\frac{\pi}{2}, \frac{\pi}{2})$ and the $(\frac{\pi}{2}, \frac{\pi}{2})$-quasiparticle peaks are completely wiped out. This produces the strong increase of the real part of the finite-frequency conductivity.

The imaginary part of the optical conductivity $\sigma_2(\omega)$ is displayed in Figs. 4.6 and 4.7 for the $d_{x^2-y^2}$-wave gap and the s-wave gap, respectively. In the superconducting state ($T < T_c \equiv T_{KT}$) one obtains the expected $\frac{1}{\omega}$ dependence. For temperatures $T > T_c \equiv T_{KT}$, deviations from this dependence become observable. In case of the $d_{x^2-y^2}$-wave gap, these deviations are limited to frequencies $\omega \lesssim 0.5\Delta_{sc}$. Once more, this exactly reflects the properties of the nodal quasiparticles, which are only slightly scattered by phase fluctuations, as can be seen by the very small increase of the width of the $(\frac{\pi}{2},\frac{\pi}{2})$-quasiparticle peaks above T_c compared to the anti-nodal $(\pi,0)$-peaks (see Fig. 3.18). In contrast to the s-wave case, where also the quasiparticles at the $(\frac{\pi}{2},\frac{\pi}{2})$-regions of the BZ are strongly scattered by phase fluctuations and which, in combination with the finite SC gap at $\boldsymbol{k} = (\frac{\pi}{2},\frac{\pi}{2})$, leads to the very strong reduction of $\sigma_2(\omega)$ for frequencies $\omega \lesssim 1.5\Delta_{sc}$ shown in Fig. 4.7.

A further important quantity to characterize the metallic or superconducting properties of a material is the temperature dependence of the DC resistivity $\rho(T) = 1/\sigma_1(\omega = 0,T)$. Because of severe finite-size effects, especially close to $\omega = 0$, it cannot be obtained directly from the optical conductivity. In order to discuss the resistivity $\rho(T)$, we have therefore calculated the Drude weight D_0, which is a measure of the spectral weight at $\omega = 0$ (see Sec. 4.1.4), and the effective charge carrier mass m_{eff}. Also in calculating the Drude weight with Eq. (4.65), one has to take care of finite-size effects, which become visible for $\omega \lesssim 0.03t$. However, a controlled extrapolation to $\omega = 0$ is possible.[2]

Figs. 4.8 and 4.9 display the Drude weight $D_0(T)$ as a function of temperature for the $d_{x^2-y^2}$-wave and the s-wave gap, respectively. Above $T_c \equiv T_{KT}$, the Drude weight is strongly reduced as soon as the phases become completely uncorrelated ($T \gtrsim 1.5T_{KT}$). This reduction of the Drude weight D_0 in the phase-uncorrelated pseudogap state is even stronger for the s-wave gap with phase fluctuations, as expected from the discussion of the optical conductivity. Whereas below T_c, the Drude weight D_0 converges to the superfluid weight D_s, which is somewhat larger for the s-wave gap.

Figs. 4.10 and 4.11 display the corresponding effective (renormalized) electron mass m_{eff} as a function of frequency for different temperatures. Over nearly the complete bandwidth $W = 8t$, the bare band mass m_b is only weakly renormalized. Only close to $\omega = 0$, the effective mass is strongly enhanced for $T \gtrsim 1.5T_{KT}$. Interestingly, for the s-wave gap, the closing of the quasiparticle gap at $\boldsymbol{k} = (\frac{\pi}{2},\frac{\pi}{2})$ becomes clearly observable in the qualitative change of the $m_{\text{eff}}(\omega)$ curves above T_c (see Fig. 4.11). The strong enhancement of the zero-frequency effective mass in addition to the very small Drude weight D_0, compared to the tight-binding metal, implies a bad metallic behavior of the resistivity $\rho(T)$ in the pseudogap state.

Finally, the finite-frequency optical scattering rate is shown in Figs. 4.12 and 4.13 for the $d_{x^2-y^2}$-wave and the s-wave gap, respectively. For the $d_{x^2-y^2}$-wave gap, $1/\tau_{\text{eff}}(\omega)$ smoothly increases as a function of temperature with the maximal scattering rate below $\omega = 2\Delta_{sc}$. The continuous increase of $1/\tau_{\text{eff}}(\omega)$ in the pseudogap state for frequencies $\omega \lesssim 2\Delta_{sc}$ is in accordance with experiment [201]. Using, as before, $t = 250$meV, we obtain a phase fluctuation contribution to the low-frequency ($\omega \lesssim 2\Delta_{sc}$) optical scattering rate, which is about half the experimentally observed value. If we express the scattering rate in units of the SC gap size (Δ_{sc}), it is however only 1/8 of the observed value. Hence, phase fluctuations can only partially contribute to the low-frequency in-plane scattering rate in the pseudogap state of the underdoped cuprates.

---

[2] Above $\omega \approx 0.03t$, finite-size effects are suppressed by using Assaad's technique. But below $\omega \approx 0.03t$, the different limits of the current-current correlation function $D_c(\boldsymbol{q},\omega)$ (see Sec. 4.1.4) cause an uncontrolled behavior of $D_c(\boldsymbol{q} = 0,\omega)$ close to $\omega = 0$.

On the other hand, for the s-wave gap with phase fluctuations, the low-frequency optical scattering rate in the pseudogap state is about 3 times larger. This is closely connected to the disappearance of the $(\frac{\pi}{2},\frac{\pi}{2})$-quasiparticle-peaks in the single-particle spectral weight. Below $T_c \equiv T_{KT}$, where one still has a well-defined s-wave quasiparticle gap in the $(\frac{\pi}{2},\frac{\pi}{2})$-region of the Brillouin zone, the scattering rate is strongly reduced for frequencies $\omega \lesssim 2\Delta_{sc}$. In contrast to the $d_{x^2-y^2}$-wave case, where the presence of nodal quasiparticles produces a finite phase fluctuation induced scattering rate even in the superconducting state for frequencies $\omega \lesssim 2\Delta_{sc}$, in qualitative agreement with the experiments of Ref. [204].

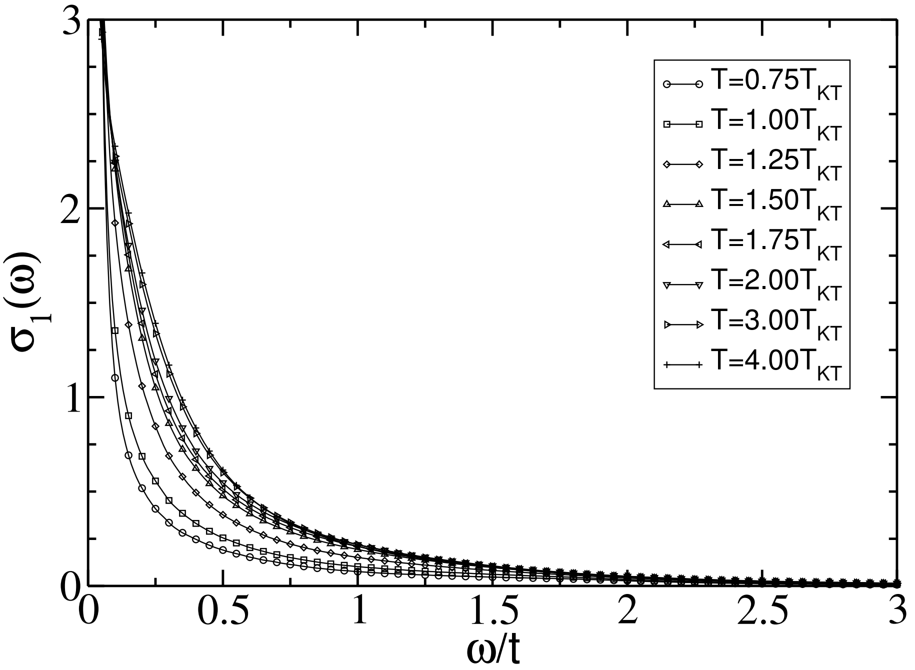

Figure 4.4: Real part of the low-frequency optical conductivity $\sigma_1(\omega)$, for a $d_{x^2-y^2}$-wave gap with phase fluctuations at different temperatures ($\Delta_{sc} = 1.0t$). The conductivity is measured in units of e^2 ($\hbar = c = a = 1$).

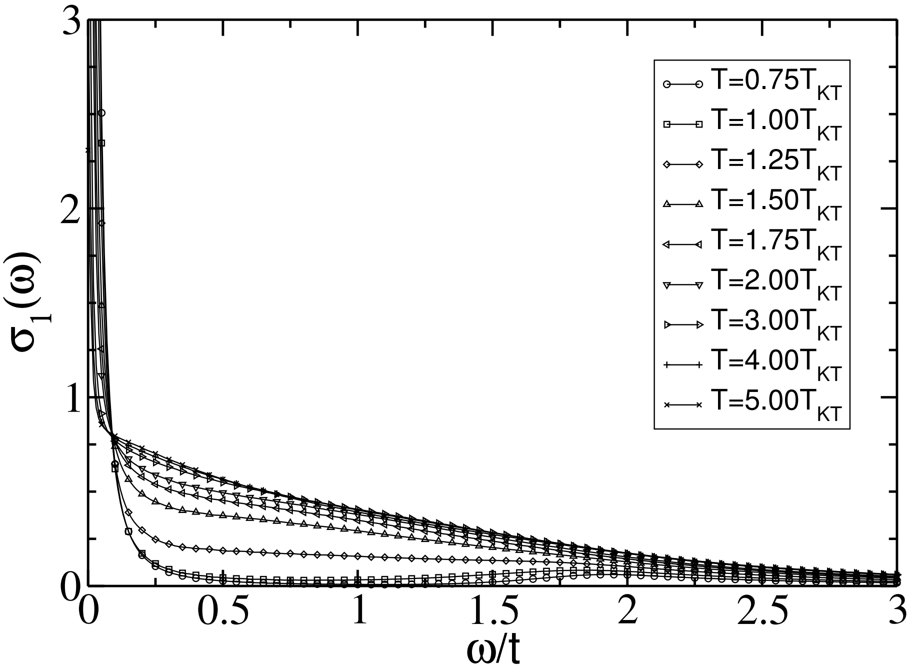

Figure 4.5: Real part of the low-frequency optical conductivity $\sigma_1(\omega)$, for a s-wave gap with phase fluctuations at different temperatures ($\Delta_{sc} = 1.0t$). The conductivity is measured in units of e^2 ($\hbar = c = a = 1$).

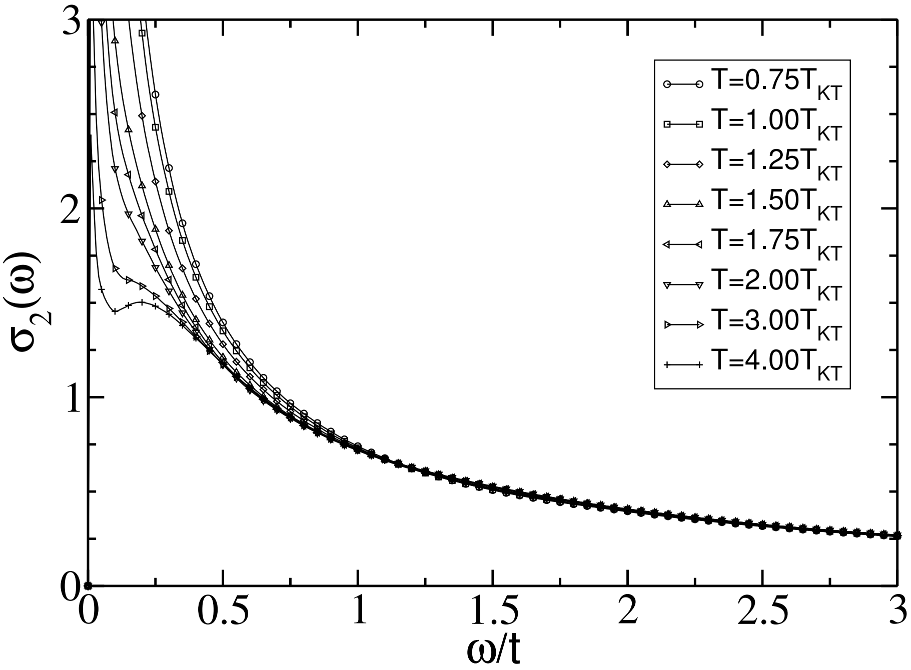

Figure 4.6: Imaginary part of the low-frequency optical conductivity $\sigma_2(\omega)$*, for a* $d_{x^2-y^2}$*-wave gap with phase fluctuations at different temperatures (*$\Delta_{sc} = 1.0t$*). The conductivity is measured in units of* e^2 *(*$\hbar = c = a = 1$*).*

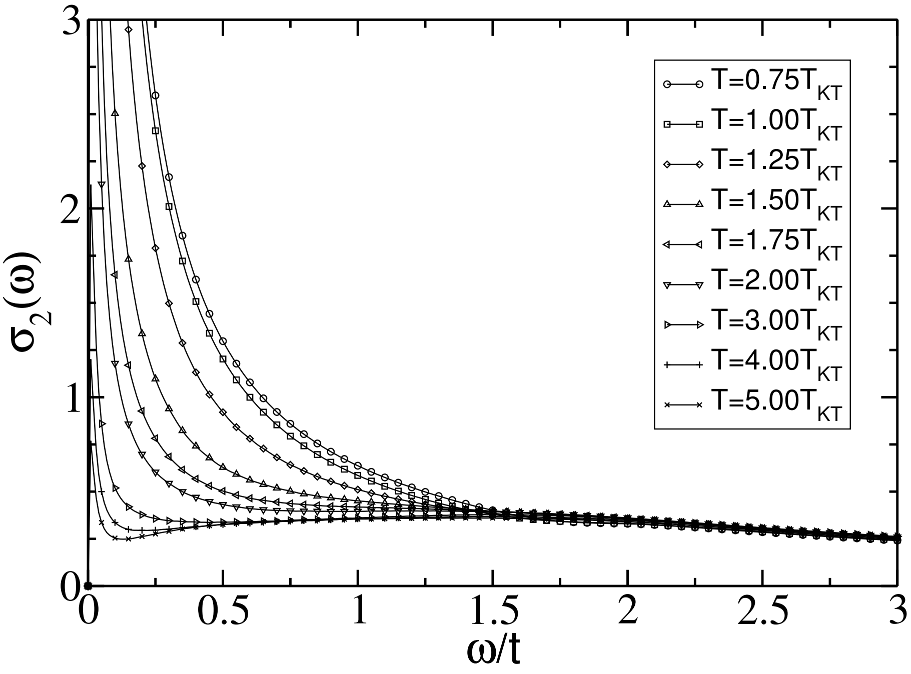

Figure 4.7: Imaginary part of the low-frequency optical conductivity $\sigma_2(\omega)$*, for a* s*-wave gap with phase fluctuations at different temperatures (*$\Delta_{sc} = 1.0t$*). The conductivity is measured in units of* e^2 *(*$\hbar = c = a = 1$*).*

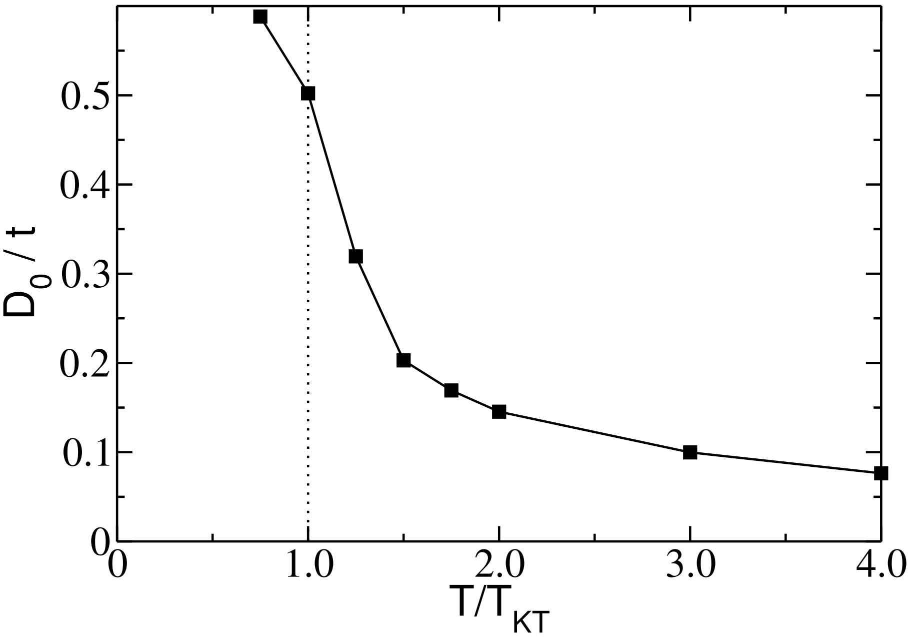

Figure 4.8: Drude weight D_0 in units of πe^2 as a function of temperature for a $d_{x^2-y^2}$-wave gap with phase fluctuations. The dotted vertical line indicates $T_c \equiv T_{KT}$.

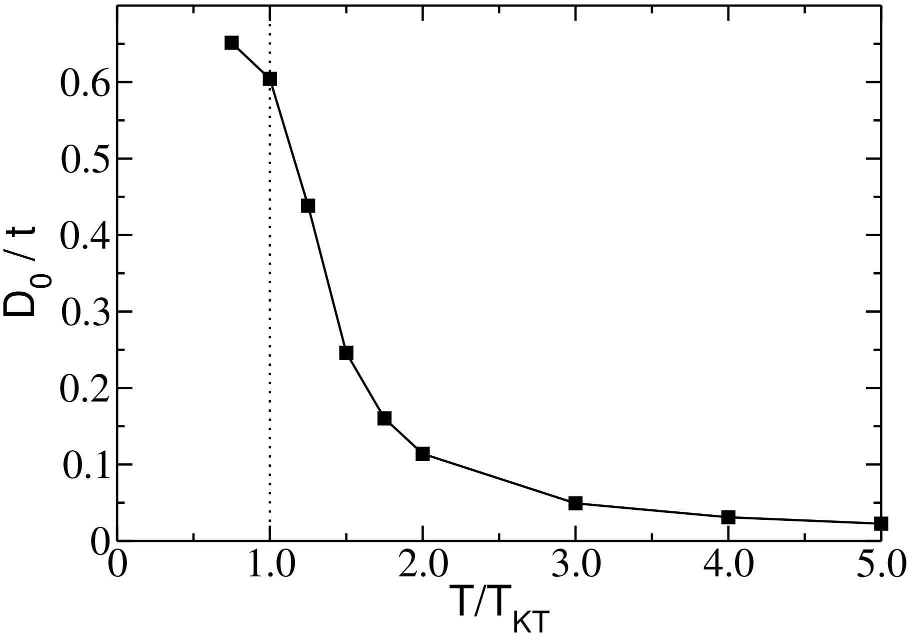

Figure 4.9: Drude weight D_0 in units of πe^2 as a function of temperature for a s-wave gap with phase fluctuations. The dotted vertical line indicates $T_c \equiv T_{KT}$.

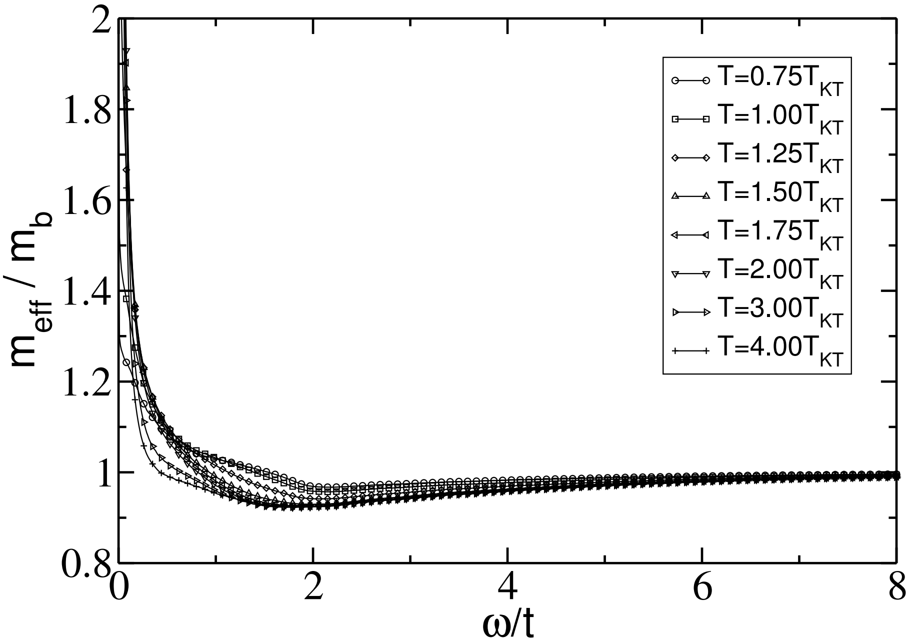

Figure 4.10: Effective electron mass m_{eff} in units of the bare band mass m_b as a function of frequency for a $d_{x^2-y^2}$-wave gap with phase fluctuations at different temperatures ($\Delta_{sc} = 1.0t$).

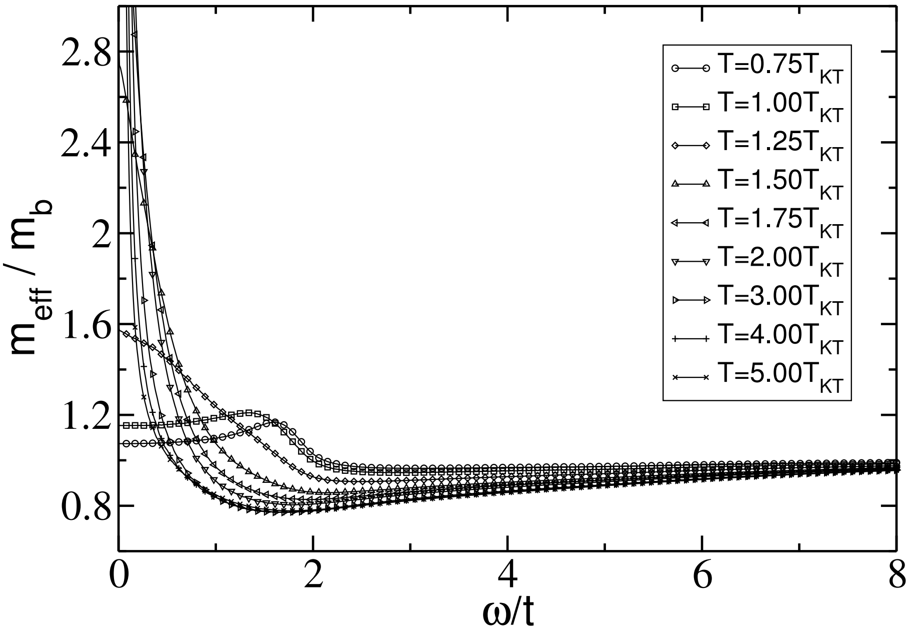

Figure 4.11: Effective electron mass m_{eff} in units of the bare band mass m_b as a function of frequency for a s-wave gap with phase fluctuations at different temperatures ($\Delta_{sc} = 1.0t$).

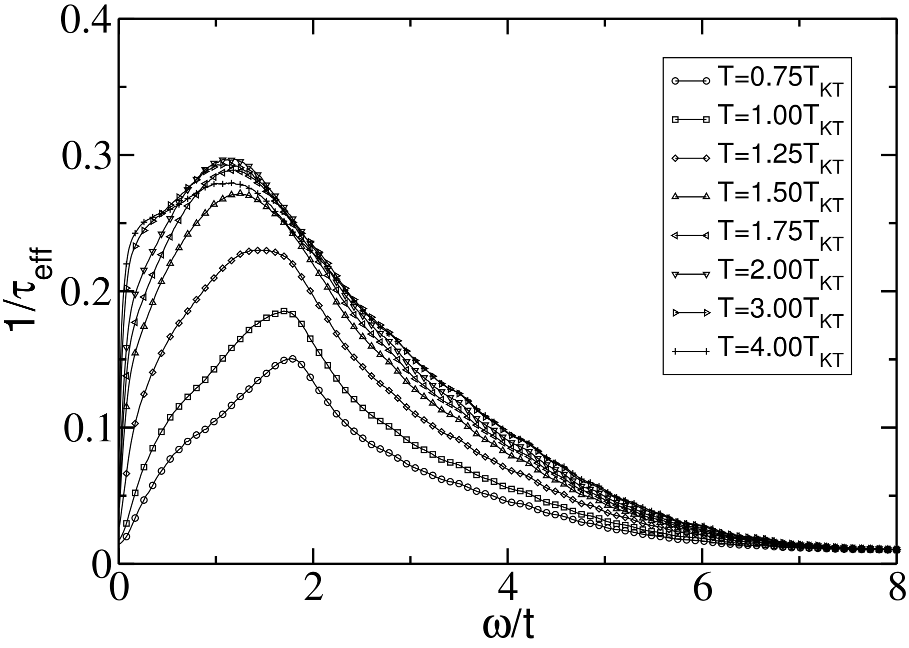

Figure 4.12: Effective optical scattering rate $1/\tau_{\text{eff}}$, in units of t as a function of frequency for a $d_{x^2-y^2}$-wave gap with phase fluctuations at different temperatures ($\Delta_{sc} = 1.0t$).

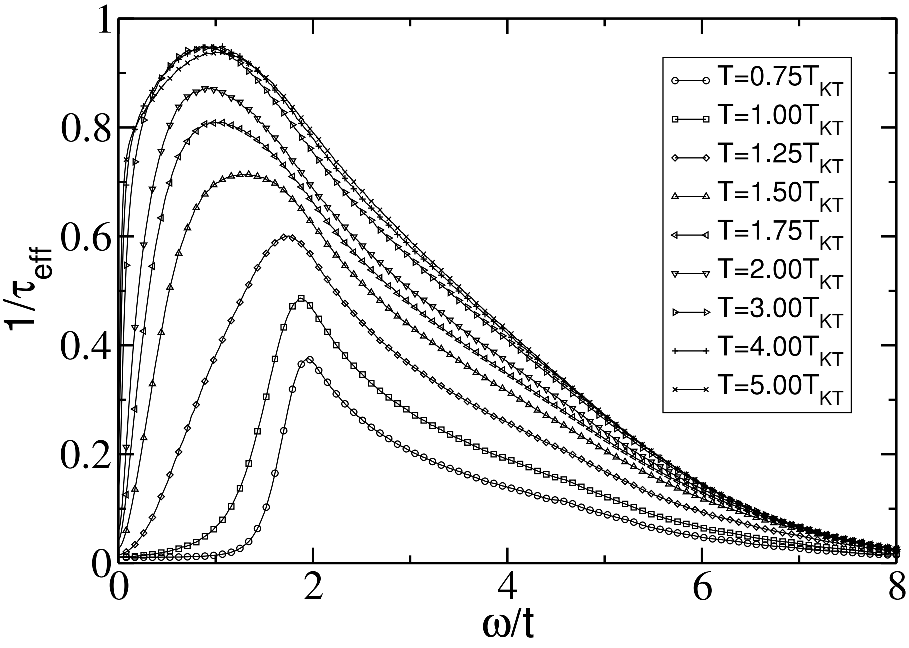

Figure 4.13: Effective optical scattering rate $1/\tau_{\text{eff}}$, in units of t as a function of frequency for a s-wave gap with phase fluctuations at different temperatures ($\Delta_{sc} = 1.0t$).

4.3.2 Paraconductivity

In a conventional BCS superconductor, superconducting (SC) fluctuations with short-range phase coherence survive no more than 1K above T_c. Within a phase fluctuation scenario for the underdoped cuprates, one would expect that pairing remains over a wide temperature range above T_c, together with phase correlations which are of finite range in space and time. Hence, although the system is in the normal state, signatures of the ideal SC state should still be observable considerably above T_c, *if* the experiments probe short enough time scales. A likely candidate to observe these effects are high-frequency conductivity experiments.

Microwave conductivity experiments on underdoped Bi2212 [40] indeed were able to track the phase-correlation time in the normal state up to 25K above T_c. These experiments show, that the SC transition is "smeared out" over a considerable temperature range, when viewed at high-enough frequencies (short-enough time scales). The imaginary part of the conductivity finally disappears more than 25K above $T_c \simeq$ 74K and shows a superconducting scaling behavior already above T_c. The real part of the conductivity displays a characteristic peak near T_c at finite frequencies, on top of a background of normal conducting electrons. This peak was interpreted by the authors of Ref. [40] as signature of the partially phase coherent electrons.

All experiments were carried out with frequencies of a few hundred GHz, which corresponds to $\omega \lesssim 0.01t$. In order to compare these experiments with our phase fluctuation model, some compromise had to be made, since finite-size effects become important below $\omega_{low} \simeq 0.03t$. Therefore, we have chosen a set of frequencies $\omega = \{0.1t, 0.2t, 0.3t, 0.4t\}$, which are, on the one hand, much larger than ω_{low}, and on the other hand much smaller than the SC gap size in our model ($\Delta_{sc} = 1.0t$). Thus, in the following, one always should keep in mind that the frequency closest to experiment is $\omega = 0.1t$.

Fig. 4.14 displays the real part of the optical conductivity $\sigma_1(\omega,T)$ as a function of temperature for different frequencies $\omega < \Delta_{sc}$. One can clearly see that the finite frequency paraconductivity increases above $T_c \equiv T_{KT}$ and remains nearly constant over a wide temperature range $T \gtrsim 1.5T_{KT}$ up to the pseudogap temperature T^*. This sudden increase of $\sigma_1(\omega,T)$ above $T_c \equiv T_{KT}$ becomes less pronounced at higher frequencies. The strong finite frequency paraconductivity over almost the whole pseudogap phase up to $T^* \gg T_c$ stands in contradiction to the experimental observations [40].

This contradiction can be solved by recalling that our model consists of "ideal" electrons, which are only scattered by phase fluctuations. To get into closer touch with experiment, we have therefore replaced the infinitesimal damping factor $\eta = 0^+$ in the response formulas by a *finite* marginal-Fermi-liquid-like damping-factor $\eta = \lambda\sqrt{\omega^2 + \pi^2 T^2}$, with λ a free parameter, which can be obtained from experiment. The marginal Fermi liquid (MFL) theory is a phenomenological theory which accounts for many experimental features of the underdoped cuprates and simply relies on assuming a special form of the single-particle self-energy $\Sigma(\boldsymbol{k},\omega)$, with a damping factor $\eta = 1/\tau \sim \max(|\omega|,T)$ [205, 206].

We have already seen in the previous section (Sec. 4.3.1), that phase fluctuations can only partially contribute to the low-frequency scattering rate observed in optical experiments. Hence, it is quite natural to include the additional scattering rate "by hand" into the theoretical response formulas for the optical conductivity. Fig. 4.15 shows the result of this procedure. The finite-frequency paraconductivity now is suppressed at higher temperatures. In addition, all $\sigma_1(\omega,T)$ curves display a maximum at a temperature $T \geq T_c$. This maximum is getting more pronounced and moves closer to T_c, the lower the frequency.

Hence, our explanation for the high-frequency conductivity experiments of Ref. [40] is that as soon as phase coherence gets lost at $T_c \equiv T_{KT}$, spectral weight from the superfluid δ-peak at $\omega = 0$ is transfered to finite frequencies. This transfer of spectral weight causes the finite-frequency paraconductivity effects in $\sigma_1(\omega,T)$, which set in more rapidly above T_c, the lower the frequencies. At higher temperatures, the finite frequency paraconductivity is suppressed by normal quasiparticle-scattering in the pseudogap state. This produces a peak in the real-part of the optical conductivity near T_c, which is more distinct at smaller frequencies.

Please note, that in order to obtain the results shown in Fig. 4.15, we used $\lambda = 0.2$. This differs from the value derived from optical experiments in underdoped Bi2212, which is $\lambda \approx 0.85$ [201]. A larger value for λ, however, would have completely wiped out all phase-fluctuation features in the optical conductivity. This discrepancy is not surprising, since we used a larger bandwidth to gap ratio in our calculations and also higher frequencies, for which the MFL scattering-rate is stronger. The important point is, that we can qualitatively explain the characteristic peak-feature in the real part of the optical conductivity as being due to phase fluctuations.

Fig. 4.16 displays the imaginary part of the optical conductivity $\sigma_2(\omega,T)$ as a function of temperature for different frequencies $\omega < \Delta_{sc}$. Exactly as in the experiments of Ref. [40], the superconductivity induced change in the imaginary part of the optical conductivity extends over a large temperature interval $T_c \lesssim T \lesssim 2T_c$ into the normal state, with the strongest increase below $T \simeq 1.5T_c$. The change of $\sigma_2(\omega,T)$ is more pronounced at lower frequencies. However, in our model the imaginary part does not go to zero in the normal state but rather converges towards a finite value. Again this is due to the missing quasiparticle scattering in the normal states besides phase fluctuation caused scattering. Here, the inclusion of a MFL scattering-rate would further reduce $\sigma_2(\omega,T)$ above $T \simeq 2T_c$, without changing its properties at the SC transition ($T \lesssim 2T_c$) qualitatively.

In Fig. 4.17 we plot the re-scaled imaginary part of the optical conductivity $\omega\sigma_2(\omega,T)$ as a function of temperature for the same frequencies $\omega < \Delta_{sc}$ as before. In the superconducting state, all re-scaled curves should collapse onto a single curve (see Sec. 4.3.1). One can clearly see that this collapse already begins in the normal state above $T_c \equiv T_{KT}$, starting with the highest frequencies, exactly as in Ref. [40]. Also here, the inclusion of an additional MFL scattering-rate would reduce the optical conductivity curves above $T \simeq 2T_c$, but it does not change the SC high-frequency scaling-behavior below $T \lesssim 1.5T_c$ significantly.

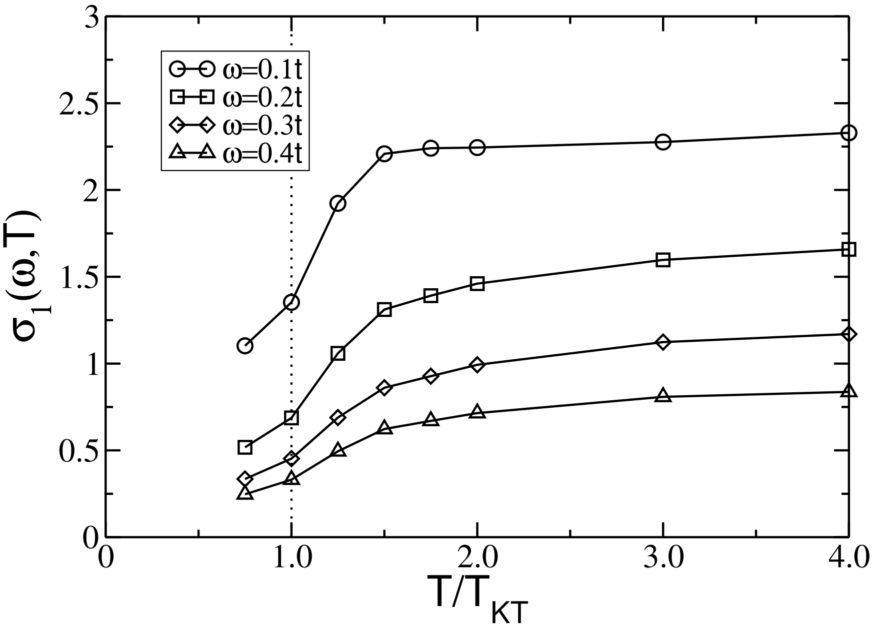

Figure 4.14: Real part of the low-frequency optical conductivity $\sigma_1(\omega,T)$, as a function of temperature for different frequencies $\omega < \Delta_{sc}$ ($\Delta_{sc} = 1.0t$). The dotted vertical line indicates $T_c \equiv T_{KT}$. Note, that the sharp transition at $T_c \equiv T_{KT}$ is washed out at higher frequencies.

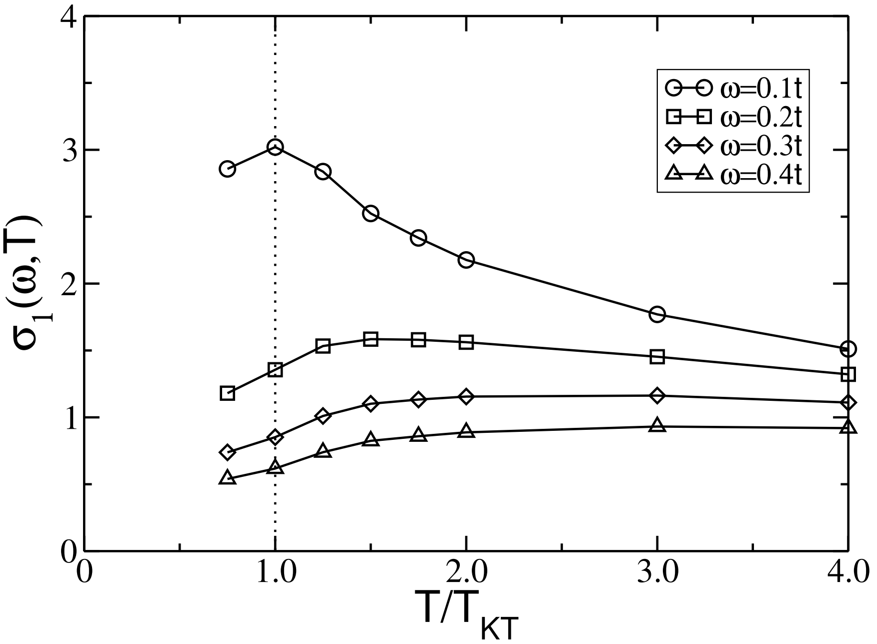

Figure 4.15: Real part of the low-frequency optical conductivity $\sigma_1(\omega,T)$ with a finite marginal-Fermi-liquid (MFL) damping-factor $\eta = \lambda\sqrt{\omega^2 + \pi^2 T^2}$ ($\lambda = 0.2$, for details see text), as a function of temperature for different frequencies $\omega < \Delta_{sc}$ ($\Delta_{sc} = 1.0t$). The dotted vertical line indicates $T_c \equiv T_{KT}$. Note, that a clear maximum develops close to $T_c \equiv T_{KT}$ for low frequencies.

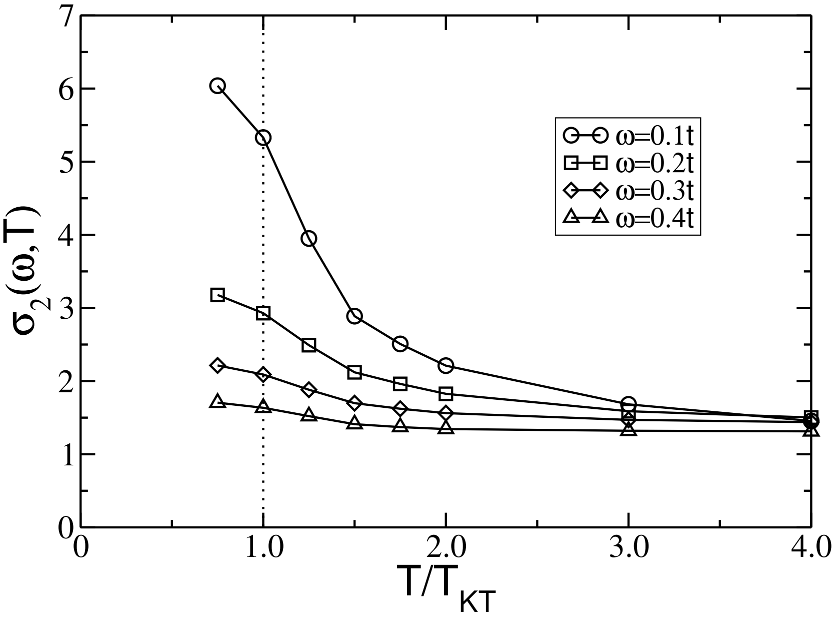

Figure 4.16: Imaginary part of the low-frequency optical conductivity $\sigma_2(\omega,T)$*, as a function of temperature for different frequencies* $\omega < \Delta_{sc}$ *(*$\Delta_{sc} = 1.0t$*). The dotted vertical line indicates* $T_c \equiv T_{KT}$*. Note, that the change of* $\sigma_2(\omega,T)$ *at the superconducting transition* $T_c \equiv T_{KT}$ *becomes less pronounced at higher frequencies and is smeared out over a finite range of temperatures* $T > T_c \equiv T_{KT}$*.*

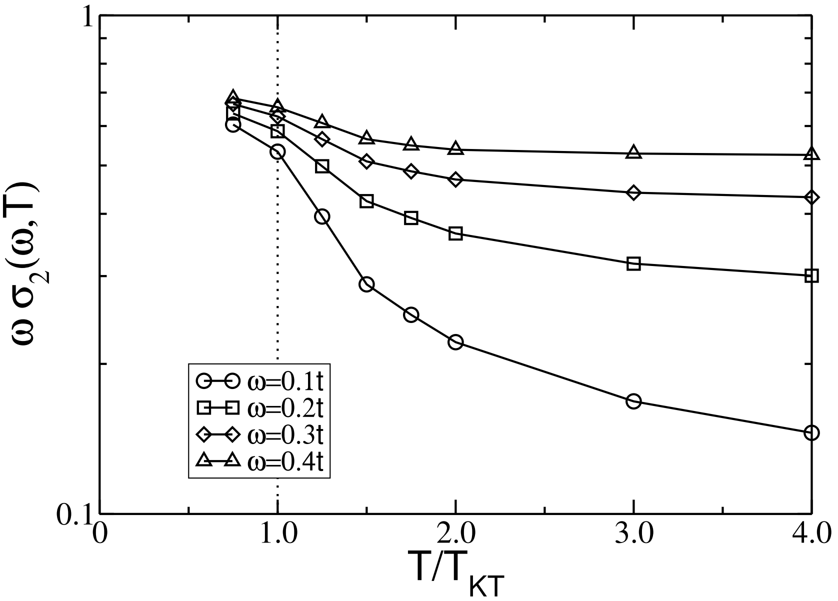

Figure 4.17: Scaling behavior of the imaginary part of the optical conductivity $\sigma_2(\omega,T)$*. In the superconducting state* $\sigma_2(\omega,T) \sim 1/\omega$*, thus all* $\omega\ \sigma_2(\omega,T)$ *curves should collapse onto a single curve. Note, that the higher the frequency, the earlier this collapse starts in the normal state for temperatures* $T > T_c \equiv T_{KT}$*. The logarithmic scale was chosen for a better comparison with the experimental data of Ref. [40].*

5

Magnetic properties

A superconductor is not only a perfect conductor, it is *in addition* a perfect diamagnet which becomes visible in the Meissner effect. Since, in the phase fluctuation scenario, the pseudogap is due to phase fluctuations of the SC order parameter, one might ask, how much of the characteristic magnetic properties of a superconductor are still observable in the pseudogap state of the underdoped cuprates.

These magnetic precursor effects of the ideal superconducting state are twofold. Firstly, one would expect a form of fluctuating diamagnetism which partially screens an applied magnetic field already above T_c. The diamagnetic activities in the pseudogap state are most probably closely connected to the phase coherence among the pairs. Secondly, one would also expect that the paramagnetic spin (or Pauli) susceptibility is reduced in a characteristic way below T^* due to the formation of incoherent singlet-pairs, accompanied by the reduction of spectral weight at the Fermi surface.

The magnetic susceptibility is usually obtained directly from magnetization experiments or indirectly from the characteristic *Knight shift* of the resonance lines in nuclear magnetic resonance (NMR) experiments. All these experiments give a *net* magnetic susceptibility which is the sum of all diamagnetic and paramagnetic contributions.[1] The different magnetic contributions to the total susceptibility can only be disentangled, if one form of magnetism dominates a special region of the phase diagram.

5.1 Diamagnetic susceptibility

The diamagnetic susceptibility can be obtained from the following consideration [207]. An externally applied magnetic field $\boldsymbol{H}_0$, generated by the external current density $\boldsymbol{j}_0$, with

$$\nabla \times \boldsymbol{H}_0 = \frac{4\pi}{c} \langle \boldsymbol{j}_0 \rangle, \tag{5.1}$$

---

[1] We neglect for the moment anti-ferromagnetic fluctuations, which are surely also present in the underdoped cuprates.

produces a total magnetic field $\boldsymbol{H}$ in the sample, which is given by

$$\nabla \times \boldsymbol{H} = \frac{4\pi}{c} \langle \boldsymbol{j}_0 + \boldsymbol{j} \rangle. \tag{5.2}$$

Here, $\boldsymbol{j}$ is the diamagnetic screening-current density. The total field $\boldsymbol{H}$ is the sum of the external field $\boldsymbol{H}_0$ and the magnetization $\boldsymbol{M}$ of the sample:[2]

$$\boldsymbol{H} = \boldsymbol{H}_0 + 4\pi \boldsymbol{M}. \tag{5.3}$$

The magnetization is proportional to the externally applied field,

$$\boldsymbol{M} = \chi_{Dia}\, \boldsymbol{H}_0, \tag{5.4}$$

which defines the diamagnetic susceptibility χ_{Dia}.

With $\boldsymbol{H} = \nabla \times \boldsymbol{A}$ and $\langle \boldsymbol{j} \rangle = c\, \nabla \times \boldsymbol{M}$, one obtains after a Fourier transformation

$$\chi_{Dia}(\boldsymbol{q}) = -\frac{1}{4\pi} \frac{\langle \boldsymbol{j}(\boldsymbol{q}) \rangle}{\langle \boldsymbol{j}(\boldsymbol{q}) \rangle - \frac{c\boldsymbol{q}^2}{4\pi} \boldsymbol{A}(\boldsymbol{q})}, \tag{5.5}$$

where $\boldsymbol{A}$ has to be given in a transverse gauge ($\nabla \cdot \boldsymbol{A} = 0$). Using the linear response formula for the current derived in Sec. 4.1.2, one finally gets

$$\chi_{Dia}(\boldsymbol{q}) = -\frac{1}{4\pi} \frac{\frac{e^2 \rho_0}{mc} + \frac{1}{\hbar c} D_c(\boldsymbol{q})}{\frac{e^2 \rho_0}{mc} + \frac{1}{\hbar c} D_c(\boldsymbol{q}) + \frac{c\boldsymbol{q}^2}{4\pi}}. \tag{5.6}$$

The static uniform diamagnetic susceptibility is defined by

$$\chi_{Dia} = \chi_{Dia}(q_x = 0, q_y \to 0, \omega = 0), \tag{5.7}$$

where the geometry is the same as in the discussion of the London penetration depth in Sec. 4.1.4.

For our lattice model with nearest-neighbor hopping ($\hbar = c = a = 1$), Eq. (5.6) changes to

$$\chi_{Dia}(\boldsymbol{q}) = -\frac{1}{4\pi} \frac{\langle k_x \rangle - D_c(\boldsymbol{q})}{\langle k_x \rangle - D_c(\boldsymbol{q}) - \frac{1}{4\pi e^2} \boldsymbol{q}^2}, \tag{5.8}$$

with $e^2 = \alpha \approx \frac{1}{137}$. A series expansion for $q_x = 0$ and $q_y \ll 1$ yields

$$\begin{aligned} \langle k_x \rangle - D_c(\boldsymbol{q}) = & \langle k_x \rangle - D_c(q_x = 0, q_y \to 0) \\ & - \frac{1}{2} q_y^2\, D_c''(q_x = 0, q_y \to 0) \\ & + O(q_y^4), \end{aligned} \tag{5.9}$$

where, $D_c''(\boldsymbol{q}) \equiv \frac{\partial^2 D_c(\boldsymbol{q})}{\partial q_y^2}$. In Eq. (5.9) no odd terms in q_y appear, due to space-inversion symmetry. Using Eq. (4.57), one can finally write

$$\langle k_x \rangle - D_c(\boldsymbol{q}) \approx -\frac{D_s}{\pi e^2} - \frac{1}{2} q_y^2\, D_c''(q_x = 0, q_y \to 0). \tag{5.10}$$

---

[2] The total magnetic field $\boldsymbol{H}$ is generally also called magnetic induction $\boldsymbol{B}$.

In a superconductor one has $D_s \neq 0$, thus

$$\chi_{Dia} = -\frac{1}{4\pi}, \tag{5.11}$$

whereas in a normal conductor with $D_s \equiv 0$ one obtains

$$\chi_{Dia} = -\frac{1}{4\pi} \, \frac{D_c''(q_x = 0, q_y \to 0)}{D_c''(q_x = 0, q_y \to 0) + \frac{1}{2\pi e^2}}. \tag{5.12}$$

This can be further simplified to

$$\chi_{Dia} \approx -\frac{e^2}{2} \, D_c''(q_x = 0, q_y \to 0) \quad \cdot [\frac{a_\parallel^2}{\hbar^2 \, c^2 \, a_\perp}] \tag{5.13}$$

for $D_c''(q_x = 0, q_y \to 0) \ll \frac{1}{2\pi e^2} \approx \frac{137}{2\pi} \approx 22$, which is usually the case.

Alternatively to directly calculating the derivative $D_c(\boldsymbol{q})$, one can start from the current-current correlation function in coordinate space $D_c(\boldsymbol{i}, \boldsymbol{j})$ and write

$$D_c(\boldsymbol{q}) = \frac{1}{N} \sum_{\boldsymbol{i},\boldsymbol{j}} e^{-i\boldsymbol{q}(\boldsymbol{i}-\boldsymbol{j})} D_c(\boldsymbol{i}, \boldsymbol{j}). \tag{5.14}$$

Expanding the exponential in powers of q_y for $q_x = 0$, $q_y \to 0$, one gets

$$D_c''(q_x = 0, q_y \to 0) = -\frac{1}{N} \sum_{\boldsymbol{i},\boldsymbol{j}} (i_y - j_y)^2 \, D_c(\boldsymbol{i}, \boldsymbol{j}). \tag{5.15}$$

Eq. (5.15) saves the computing time needed for a Fourier transformation, since the MC simulation always gives at first $D_c(\boldsymbol{i}, \boldsymbol{j})$.

The problem now is the calculation of the curvature $D_c''(q_x = 0, q_y \to 0)$ on our 16×16 lattice. Already the correlation function $D_c(\boldsymbol{q})$ shows strong finite size effects, especially close to $\boldsymbol{q} = 0$. In contrast to the optical ($\boldsymbol{q} = 0$) conductivity calculation, we cannot use Assaad's technique to reduce finite size effects. The situation is even worse, because of the different limits of the current-current correlation function, which depend upon the path in $(\boldsymbol{q}, \omega)$-space on which the $(q_x = 0, q_y = 0, \omega = 0)$-point is approached (see Sec. 4.1.4). Therefore, we have tested different methods to extract the curvature $D_c''(q_x = 0, q_y \to 0)$ from our data.

First we have calculated the diamagnetic susceptibility for the non-interacting 2D tight-binding model with nearest-neighbor hopping at half-filling ($\langle n \rangle = 1$). The susceptibility diverges logarithmically at $T = 0$ as a result of the van-Hove-peak in the density of states. For this case, the diamagnetic susceptibility can be calculated to any accuracy. Fig. 5.1 displays the result of this calculation. The first point worth noting is the well-known fact that the magnetic response of the current actually is paramagnetic. Therefore we call the result of Eq. (5.13) in the following *magnetic susceptibility* χ_{mag}.

For a free electron dispersion, the magnetic response of the current is always diamagnetic. In tight-binding lattices, there is a crossover from diamagnetism to paramagnetism as a function of doping [208]. At very small filling ($\langle n \rangle \ll 1$), the response is diamagnetic. In general, the outcome of Eq. (5.13) depends in a complicated way on the electronic band structure.

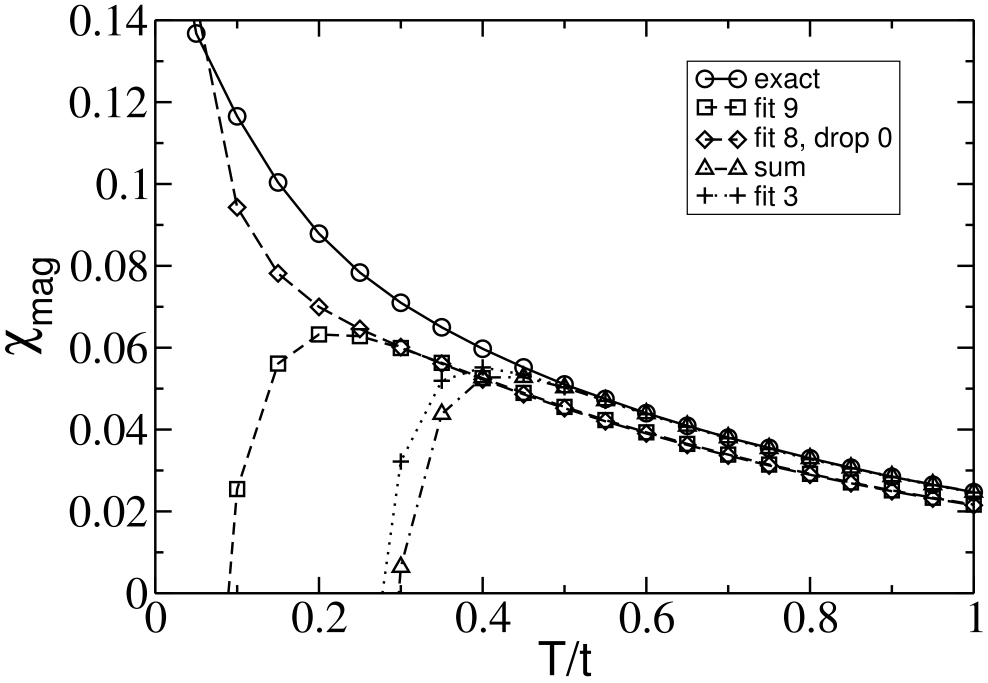

Figure 5.1: Magnetic susceptibility χ_{mag} in units of te^2 ($\hbar = c = a = 1$) calculated from the current response of the 2D tight-binding model at half-filling ($\langle n \rangle = 1$). The full line shows the exact result for the infinite lattice as a function of temperature (exact). The broken lines display the results of different approximative schemes for the calculation of χ_{mag} on a 16×16 lattice: 9-point-fit including $q_y = 0$ (fit 9), 8-point-fit without $q_y = 0$ (fit 8, drop 0), using the sum of Eq. (5.15) (sum), and finally a 3-point-fit including $q_y = 0$ (fit 3). (For details see text.)

Next, we tried to reproduce the exact result as good as possible on our finite 16×16 lattice. We started with the expression of the magnetic susceptibility given in Eq. (5.15). In Fig. 5.1 one can see that this expression reproduces excellently the exact result for high temperatures but then suddenly strongly diverges below $T \simeq 0.4t$. Using a parabolic 3-point fit to obtain the curvature $D''_c(q_x = 0, q_y \to 0)$, with the smallest q_y-values to the left and right of $q_y = 0$, including $q_y = 0$, nearly gives the same result (see Fig. 5.1).[3]

In order to stabilize the fit procedure for small temperatures, we have also performed a parabolic fit of $D_c(\boldsymbol{q})$ using the 9 smallest q_y-points between $-\frac{\pi}{2} \leq q_y \leq \frac{\pi}{2}$, including $q_y = 0$. Fig. 5.1 shows that this procedure yields a systematic deviation at high temperatures, but on the other hand closely follows the exact result down to $T \simeq 0.2t$, where it suddenly diverges to negative values.

In our phase-fluctuation simulation we are interested in the temperature range $0.1t \lesssim T \lesssim 0.4t$. Especially below $T \simeq 0.2t$, we expect many interesting things to happen. Since the finite-size effects in $D_c(\boldsymbol{q})$ are strongest at $\boldsymbol{q} = 0$, we dropped the $q_y = 0$ point and finally performed a parabolic 8-point fit with the 4 smallest q_y-points to the left and right of $q_y = 0$. As can be seen in Fig. 5.1, this procedure yields the best agreement with the exact result over the whole temperature range. Hence, in the following the magnetic susceptibility is always obtained from the parabolic 8-point fit to $D_c(\boldsymbol{q})$.[4]

---

[3] Actually for 3 points $q_y = \pm\frac{\pi}{8}$ and $q_y = 0$ this procedure is exact. We call it however fit because of the finite-lattice approximation.

We have seen in the preceeding discussion of the diamagnetic susceptibility, that the curvature $D_c''(q_x = 0, q_y \to 0)$ is a meaningful quantity, only if the superfluid weight D_s vanishes. Therefore, we first have to calculate D_s on our finite lattice. Fig. 5.2 displays $-\langle k_x \rangle + \mathcal{D}_c(q_x = 0, q_y, i\nu_n = 0)$ as a function of q_y, for our phase fluctuation model with a $d_{x^2-y^2}$-wave gap at different temperatures ($\langle n \rangle = 0.9$). In the limit of $q_y \to 0$ one obtains the superfluid weight (see Eq. (4.57)).

As can be seen from Fig. 5.2, this limit alway yields a finite positive value for D_s. This is due to the fact that the single-particle expectation value $\langle k_x \rangle$ converges much faster with increasing lattice size than the two-particle correlation function $\mathcal{D}_c(q_x = 0, q_y, i\nu_n = 0)$. To get an estimate for this finite-size error, we plot in Fig. 5.3 the corresponding q_x-limit: $-\langle k_x \rangle + \mathcal{D}_c(q_x, q_y = 0, i\nu_n = 0)$ as a function of q_x. For $q_x \to 0$, $-\langle k_x \rangle$ and $\mathcal{D}_c(q_x, q_y = 0, i\nu_n = 0)$ should cancel each other exactly (see Eq. (4.58)).

Comparing Fig. 5.2 with Fig. 5.3, one can see that D_s is of the order of the finite-size error for temperatures $T \gtrsim 1.5T_{KT}$. Furthermore, $\mathcal{D}_c(q_x = 0, q_y, i\nu_n = 0)$ displays an upward curvature for temperatures $T \lesssim 1.25T_{KT}$ (see Fig. 5.2), whereas at higher temperatures, it changes to downward curvature that looks qualitatively very similar to the results obtained for the nearest-neighbor tight-binding model. Hence, we expect reliable results for the diamagnetic susceptibility for temperatures $T \gtrsim 1.5T_{KT}$.

Fig. 5.4 now displays the results for the magnetic susceptibility χ_{mag} as a function of temperature for our phase-fluctuation model with a constant $d_{x^2-y^2}$-wave gap at finite doping ($\langle n \rangle = 0.9$). For comparison we also show the magnetic susceptibility χ_{mag} for the nearest-neighbor tight-binding model. Over a wide temperature range $2.0T_{KT} \lesssim T \lesssim 4.0T_{KT}$, both susceptibilities are nearly identical. A small phase fluctuation induced reduction of χ_{mag} becomes visible only for $T \lesssim 2.0T_{KT}$. Below $T \simeq 1.5T_{KT}$, we see an unphysical sudden increase of χ_{mag} in the phase fluctuation model because of the aforementioned strong finite size effects.

The phase-fluctuation-induced diamagnetic susceptibility can be defined by the difference of the magnetic susceptibilities of phase fluctuation (XY-MC) and tight-binding (TB) model $\chi_{Dia} = \chi_{mag}^{XY-MC} - \chi_{mag}^{TB}$. Fig. 5.5 shows χ_{Dia} as a function of temperature. The fluctuating diamagnetism is a small effect compared to the lattice paramagnetism, which is more than one order of magnitude larger. It is only important below $T \simeq 1.5T_{KT}$, where one expects χ_{Dia} to strongly increase close to T_c, but it does not play any role over most part of the pseudogap phase. Fig. 5.5 also shows the fluctuating diamagnetism χ_{Dia} for a BCS-temperature-dependent gap with phase fluctuations ($\Delta = \Delta_{BCS}(T)$). At low temperatures this gives us an estimate for the MC error, and at high temperatures it exhibits the influence of a temperature-dependent gap that smoothly goes to zero at $T_c^{MF} \equiv T^*$. Fig. 5.5 clearly shows that both effects are small and of the order of the symbol size.

On the experimental side, the c-axis[5] magnetic susceptibility of *optimally* doped $YBa_2Cu_3O_{7-\delta}$

---

[4] Although we tested this technique only for the tight-binding model at half-filling, we expect it to work equally well in the pseudogap state of the phase fluctuation model, where the current-current correlation function qualitatively looks very similar.

[5] $\boldsymbol{B} \perp$ copper-oxide planes.

(YBCO) is nearly constant above T_c, without the slightest sign of any fluctuating diamagnetism [209]. In *underdoped* YBCO, a clear diamagnetic response was observed up to 15K above T_c ($T \approx 1.2\,T_c$) for chain-disordered YBCO [210, 211]. In *chain-ordered* YBCO, the diamagnetic response is even stronger and increases rather linearly with decreasing temperature above T_c [210, 211], whereas in *chain-disordered* YBCO, where only the copper-oxide planes are supposed to contribute to the diamagnetic susceptibility, it can be perfectly fitted by an exponential temperature dependence [212]. Interestingly, magnetization measurements on YBCO *powders* indicate a form of fluctuating diamagnetism above T_c also in *overdoped* YBCO, which could be caused by charge inhomogeneities and the formation of superconducting droplets [213]. Recently, precursor diamagnetism was observed in underdoped $La_{1.9}Sr_{0.1}CuO_4$ (LSCO) up to 2K above T_c ($T \approx 1.1\,T_c$) [214]. All these experimental observations are in complete agreement with our theoretical results, indicating a limitation of the diamagnetic precursor effects above T_c to temperatures of a small fraction of T_c.

In the following, we want to obtain some quantitative numbers for the susceptibility. From Fig. 5.5 we get $\chi_{Dia}(T = 1.5\,T_{KT}) \approx -0.003\,te^2$ in units where $\hbar = c = a = 1$. Using Eq. (5.13) with the typical parameters for YBCO ($a_{\|} = 3.86 \cdot 10^{-8}$ cm, $a_{\perp} = 5.88 \cdot 10^{-8}$ cm) and as before $t = 250$ meV, one obtains the cgs diamagnetic-susceptibility $\chi_{Dia}(T = 1.5\,T_{KT}) \approx 7 \cdot 10^{-9}$. The diamagnetic susceptibility in SI units can be obtained by multiplying the cgs susceptibility with 4π. Experimental susceptibilities are often measured in units of emu/mol.[6] The diamagnetic susceptibility in units of emu/mol can be obtained by multiplying the cgs susceptibility with the molar volume of YBCO. For our phase fluctuation model, we get $\chi_{Dia}(T = 1.5\,T_{KT}) \approx -10^{-6}$ emu/mol. This value for the fluctuating diamagnetism is tiny and experimentally not observable. Thus, our results are consistent with experiments, which measure a paramagnetic susceptibility of $\sim 10^{-4}$ emu/mol at the same temperature [209, 211], with no sign of any fluctuating diamagnetism in the static magnetic susceptibility.

Finally, we want to annotate, that also the precursor effects of the ideal diamagnetism are limited for the static uniform susceptibility to temperatures close to T_c, evidence for diamagnetic precursor activities up to T^* was found when looking on small length scales and high frequencies.[7] Scanning SQUID microscopy experiments on thin films of underdoped LSCO show, that the vortex pattern below $T_c = 18\,$K develops out of diamagnetic precursor domains which are observable up to $T = 80\,$K [216]. AC susceptibility measurements on slightly underdoped LSCO have shown a diamagnetic response up to T^* for frequencies of 0.1–10 kHz [217].

Next, we discuss our results for the s-wave gap with phase fluctuations. Due to the fully gaped quasiparticle excitations below T_c, we expect a qualitatively different diamagnetic current response of the quasiparticles. Fig. 5.6 displays $-\langle k_x\rangle + \mathcal{D}_c(q_x = 0, q_y, i\nu_n = 0)$ as a function of q_y, for the s-wave gap at different temperatures ($\langle n\rangle = 0.9$). As before, the superfluid weight can be obtained in the limit of $q_y \to 0$.

---

[6] **Emu is not a real unit**, in fact one has $\chi_{cgs} = \chi_{cgs}[cm^3/cm^3] = \chi_{cgs}[emu/cm^3]$. In experiments one often measures the total magnetic moment of a sample in place of the magnetization. The magnetic moment is then divided by the applied magnetic field and the sample quantity (either in units of mol or $gram$) in order to obtain a generalized material dependent susceptibility $\chi_{cgs}[emu/mol]$ or $\chi_{cgs}[emu/gram]$. These material dependent susceptibilities can be obtained from the usual cgs susceptibility in dividing the dimensionless cgs susceptibility by the molar density or mass density of the sample. Typical values of diamagnetic susceptibilities in emu/mol can be found in [215]. Please note, that the unit for magnetic moment is also called emu. For magnetic moments one has $emu = erg/gauss$, but for magnetic susceptibilities one has $emu = cm^3$, which should not be confused! In SI units there is no comparable confusion, but the units are less familiar to many scientists.

[7] Note that also paraconductivity was observed only at finite frequencies (see Sec. 4.3).

We see two completely different regimes in Fig. 5.6. For $T \lesssim 1.0T_{KT}$, we get an upward curvature of the current correlation function and the superfluid weight D_s has a rather large positive value compared to the $d_{x^2-y^2}$-wave case. For $T \gtrsim 2.0T_{KT}$ the current correlation function shows the characteristic tight-binding-like downward curvature and the superfluid weight D_s approaches zero. Between these to regimes, we obtain a very strong downward curvature of $\mathcal{D}_c(q_x = 0, q_y, i\nu_n = 0)$ close to $q_y = 0$, in particular for $T = 1.25T_{KT}$ and $T = 1.5T_{KT}$. It is not clear whether this is a finite-size effect or the indication of a true lattice diamagnetism. Surely it is related to the anisotropic closing of the s-wave gap above T_c (see Sec. 3.2).

To get an estimate of the finite-size error, Fig. 5.7 shows $-\langle k_x\rangle + \mathcal{D}_c(q_x, q_y = 0, i\nu_n = 0)$ as a function of q_x. For $q_x \to 0$, this function should approach zero for all temperatures. One can clearly see in Fig. 5.7 that the finite-size errors are much larger than in case of the $d_{x^2-y^2}$-wave gap (cf. Fig. 5.3), especially for temperatures $T \lesssim 1.75T_{KT}$. Putting everything together, we conclude that we get reliable results for the magnetic susceptibility only for temperatures $T \gtrsim 2.0T_{KT}$.

Fig. 5.8 displays the magnetic susceptibility χ_{mag} as a function of temperature for a constant s-wave gap with phase fluctuations at finite doping ($\langle n\rangle = 0.9$). For comparison, we also show the magnetic susceptibility χ_{mag} for the nearest-neighbor tight-binding model. In contrast to the $d_{x^2-y^2}$-wave gap, we have a phase fluctuation induced reduction of χ_{mag} up to highest temperatures. In Fig. 5.9 the corresponding fluctuating diamagnetism $\chi_{Dia} = \chi_{mag}^{XY-MC} - \chi_{mag}^{TB}$ is displayed as a function of temperature. It has a finite value at all temperatures in the pseudogap phase and does not show the characteristic on-set behavior observed for the $d_{x^2-y^2}$-wave gap (cf. Fig. 5.5).

Using a BCS-temperature-dependent gap does not change the properties of χ_{Dia} significantly (see Fig. 5.9). It only causes χ_{Dia} to diminish smoothly as one approaches $T^* \equiv T_c^{MF}$. Hence, a local s-wave gap with phase fluctuations leads to diamagnetic precursor effects over the whole temperature range $T_c < T < T^*$, but the fluctuating diamagnetism is only about 1/3 of the tight-binding lattice paramagnetism and still one order of magnitude smaller than the experimentally observed values for the paramagnetic susceptibility in the pseudogap state of the cuprates.

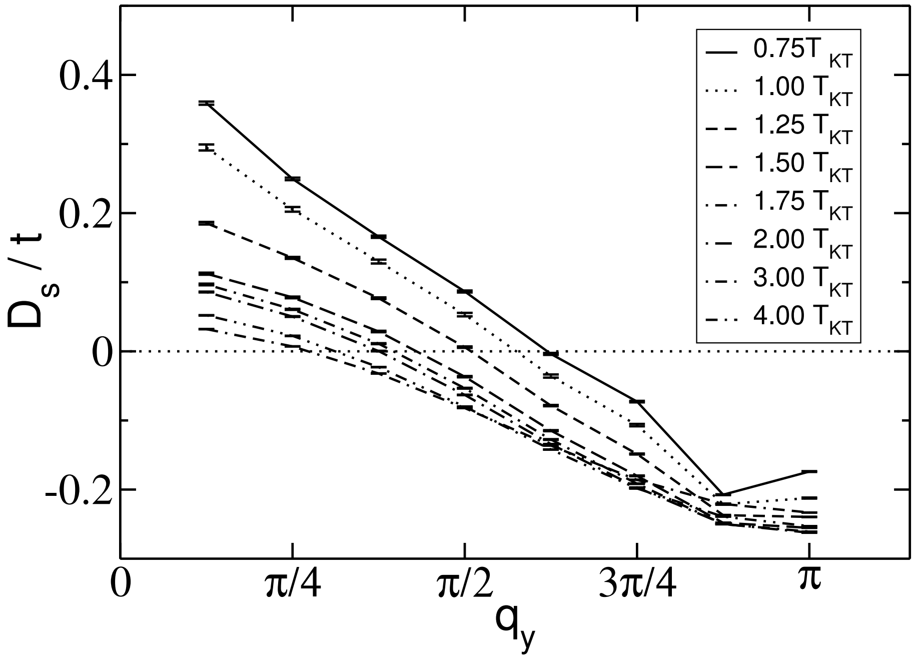

Figure 5.2: $-\langle k_x \rangle + \mathcal{D}_c(q_x = 0, q_y, i\nu_n = 0)$ *as a function of* q_y*, calculated for the* $d_{x^2-y^2}$*-wave gap with phase fluctuations at different temperatures (*$\langle n \rangle = 0.9$*). The limit* $q_y \to 0$ *yields the superfluid weight* D_s *in units of* πe^2*. (For details see text.)*

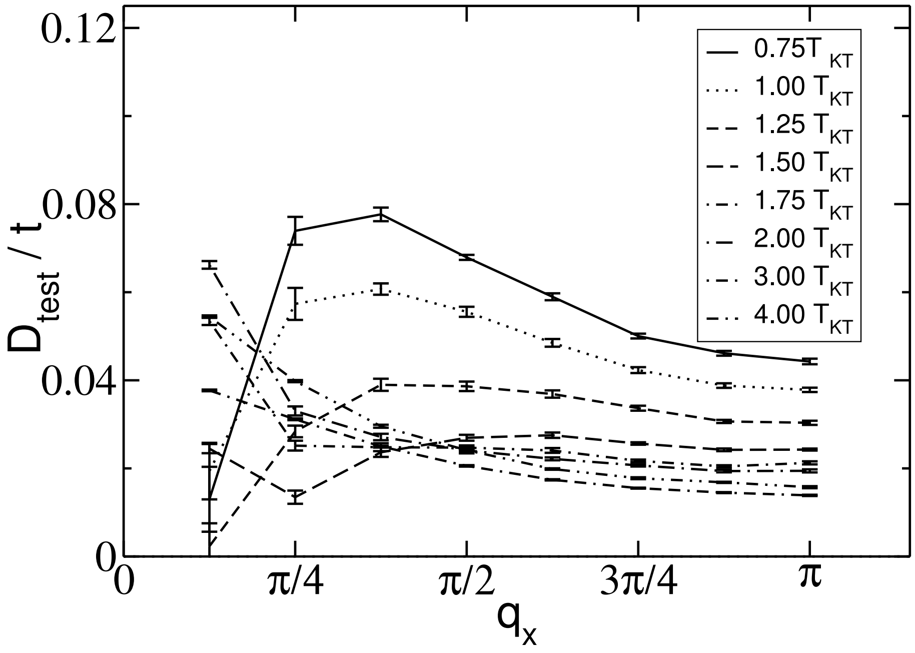

Figure 5.3: $-\langle k_x \rangle + \mathcal{D}_c(q_x, q_y = 0, i\nu_n = 0)$ *as a function of* q_x*, calculated for the* $d_{x^2-y^2}$*-wave gap with phase fluctuations at different temperatures (*$\langle n \rangle = 0.9$*). The limit* $q_x \to 0$ *yields* D_{test} *in units of* πe^2*. For a Gauge invariant Hamiltonian one has* $D_{test} \equiv 0$*. (For details see text.)*

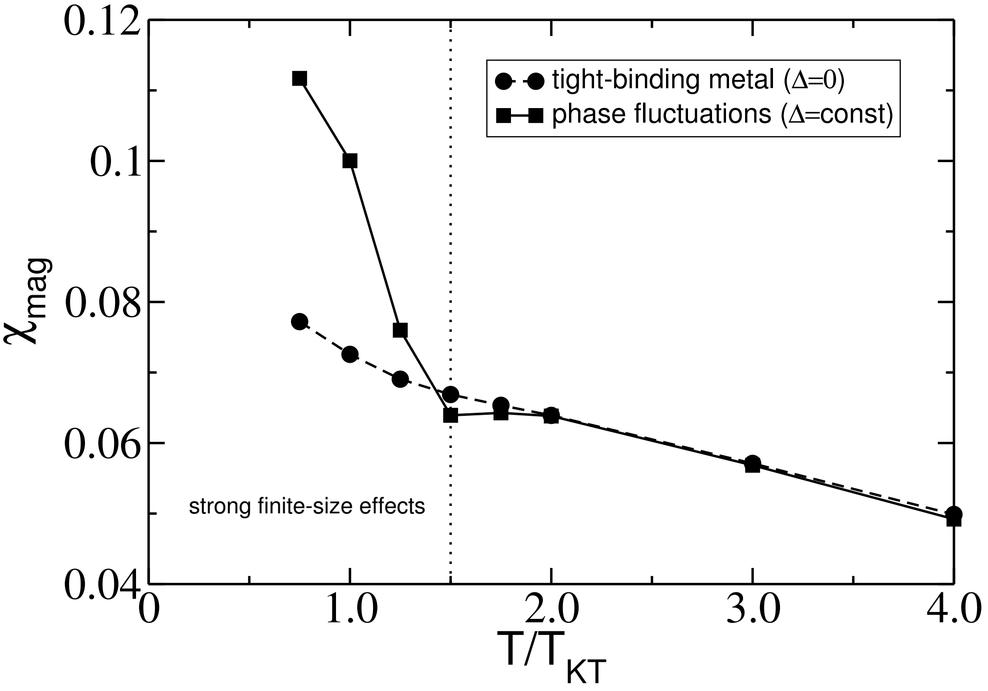

Figure 5.4: Magnetic susceptibility χ_{mag} in units of te^2 ($\hbar = c = a = 1$) as a function of temperature, calculated from the current response of our phase-fluctuation model with a constant $d_{x^2-y^2}$-wave gap ($\langle n \rangle = 0.9$). For comparison we also show the magnetic susceptibility χ_{mag} for the tight-binding model ($\Delta = 0$). The dotted vertical line indicates the temperature above which we expect reliable results for χ_{mag} in our phase-fluctuation model. Below this temperature, we obtain an unphysical sudden increase of χ_{mag} in the phase-fluctuation model due to strong finite-size effects.

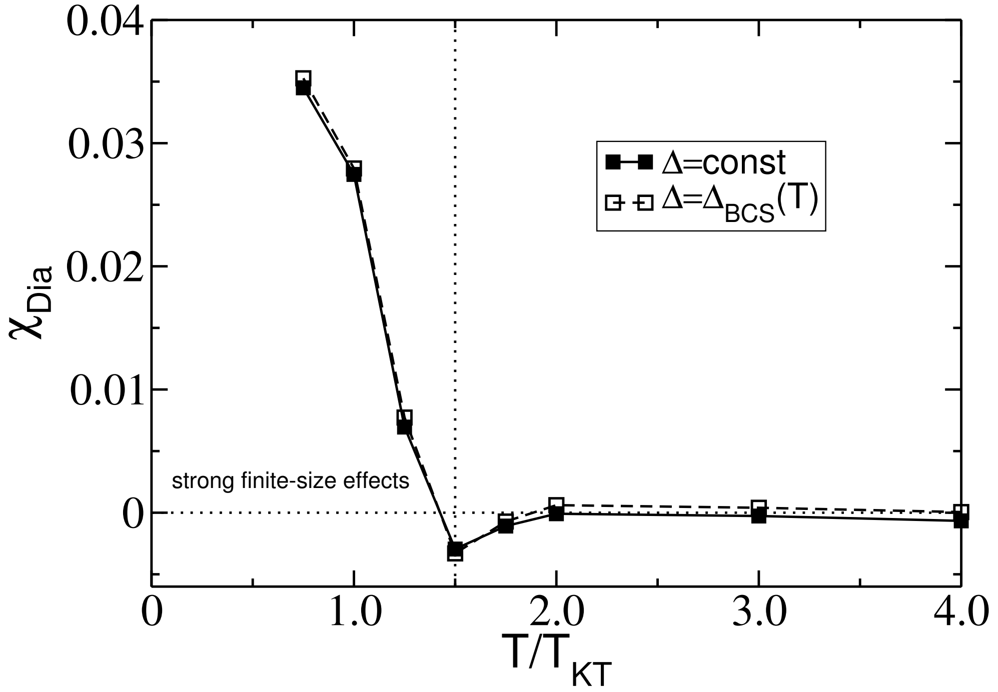

Figure 5.5: Diamagnetic susceptibility $\chi_{Dia} = \chi_{mag}^{XY-MC} - \chi_{mag}^{TB}$ *in units of* te^2 $(\hbar = c = a = 1)$ *as a function of temperature for a constant* $d_{x^2-y^2}$*-wave gap with phase fluctuations* $(\langle n \rangle = 0.9)$*. For comparison we also show the diamagnetic susceptibility* χ_{Dia} *for a BCS-temperature-dependent gap with phase fluctuations* $(\Delta = \Delta_{BCS}(T))$*. The dotted vertical line indicates the temperature above which we expect reliable results for* χ_{Dia}*. Below this temperature, we obtain an unphysical sudden increase of* χ_{mag} *due to strong finite-size effects. (For details see text.)*

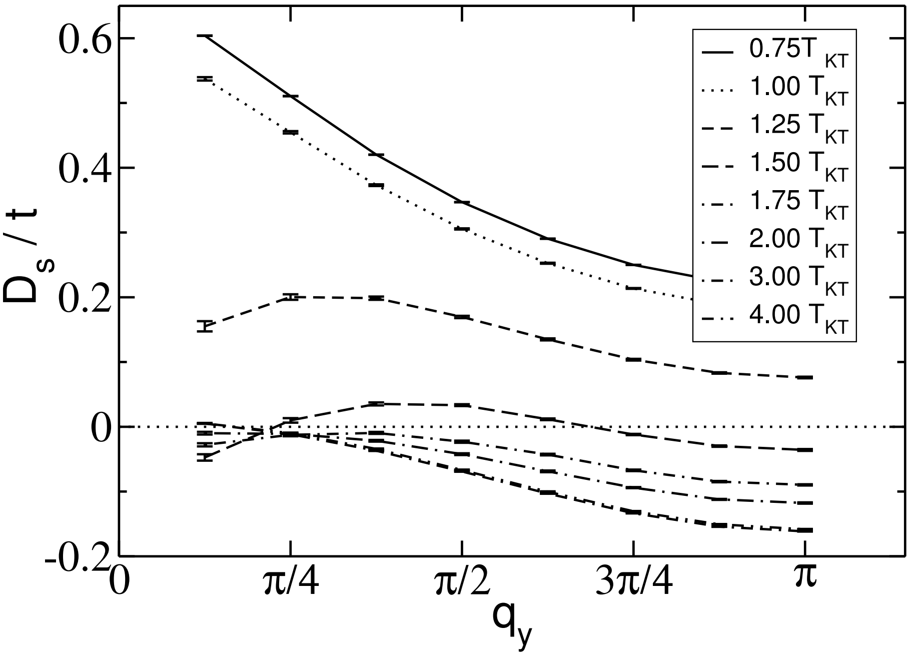

Figure 5.6: $-\langle k_x \rangle + \mathcal{D}_c(q_x = 0, q_y, i\nu_n = 0)$ as a function of q_y, calculated for the s-wave gap with phase fluctuations at different temperatures ($\langle n \rangle = 0.9$). The limit $q_y \to 0$ yields the superfluid weight D_s in units of πe^2. (For details see text.)

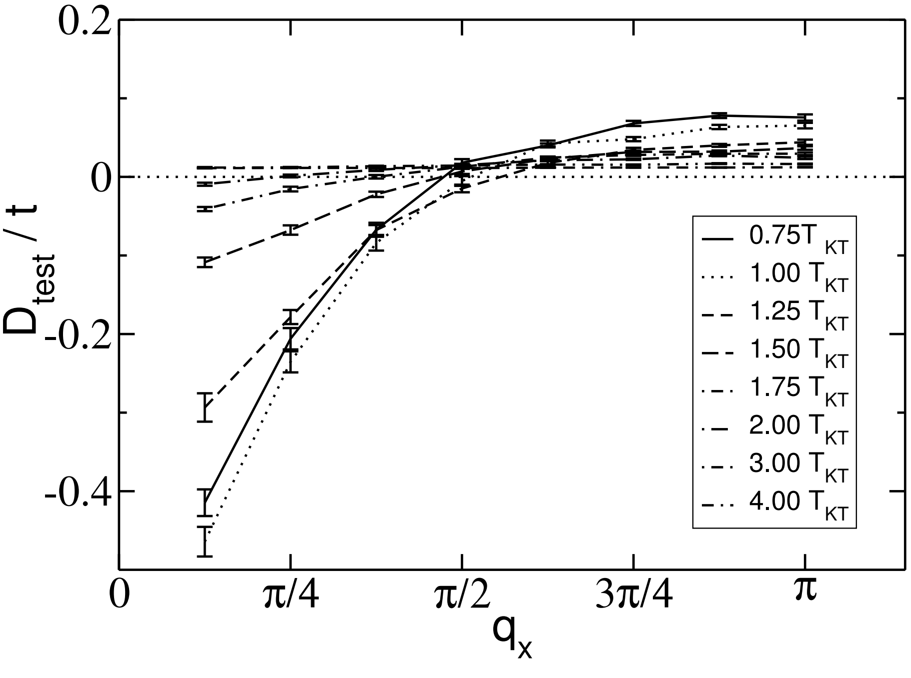

Figure 5.7: $-\langle k_x \rangle + \mathcal{D}_c(q_x, q_y = 0, i\nu_n = 0)$ as a function of q_x, calculated for the s-wave gap with phase fluctuations at different temperatures ($\langle n \rangle = 0.9$). The limit $q_x \to 0$ yields D_{test} in units of πe^2. For a Gauge invariant Hamiltonian one has $D_{test} \equiv 0$. (For details see text.)

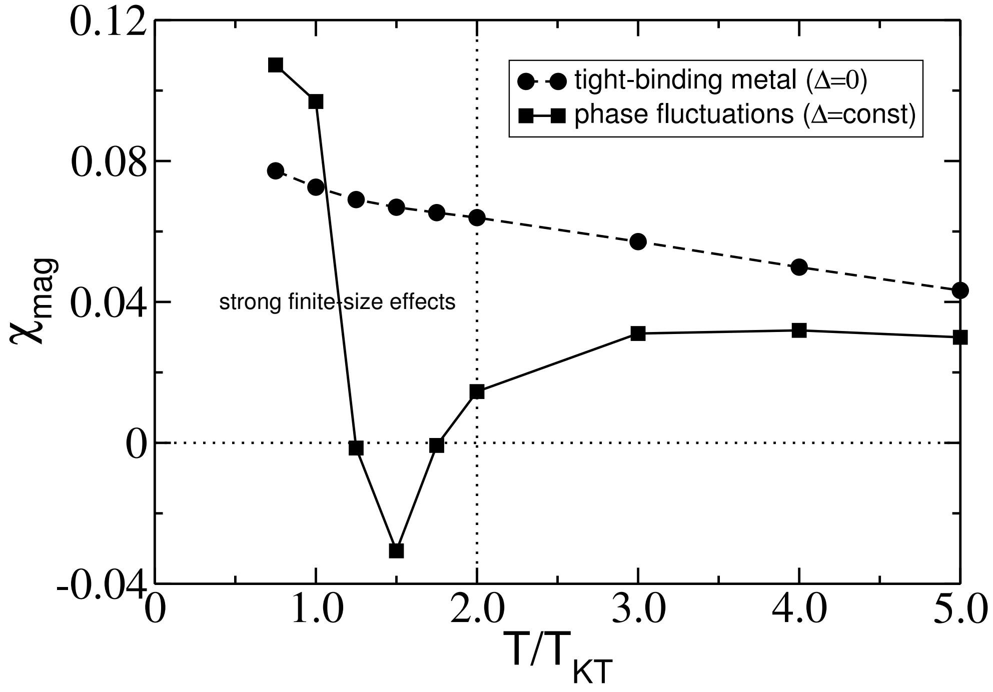

Figure 5.8: Magnetic susceptibility χ_{mag} in units of te^2 ($\hbar = c = a = 1$) as a function of temperature, calculated from the current response of our phase-fluctuation model with a constant s-wave gap ($\langle n \rangle = 0.9$). For comparison we also show the magnetic susceptibility χ_{mag} for the tight-binding model ($\Delta = 0$). The dotted vertical line indicates the temperature above which we expect reliable results for χ_{mag} in our phase-fluctuation model. Below this temperature, we obtain an unphysical sudden increase of χ_{mag} in the phase-fluctuation model due to strong finite-size effects.

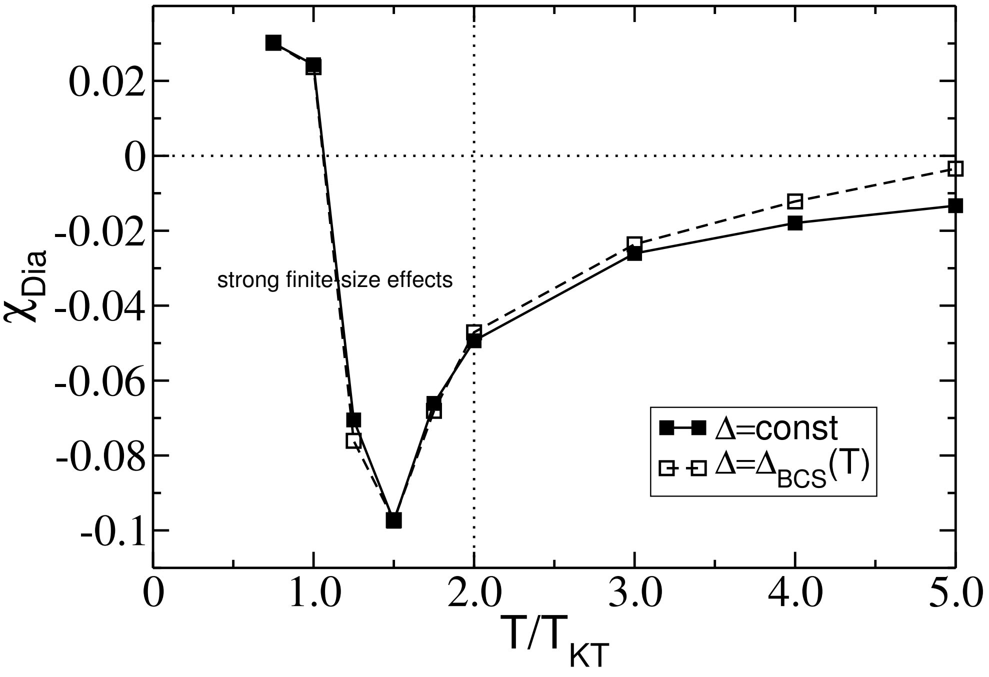

Figure 5.9: *Diamagnetic susceptibility* $\chi_{Dia} = \chi_{mag}^{XY-MC} - \chi_{mag}^{TB}$ *in units of* te^2 *(*$\hbar = c = a = 1$*) as a function of temperature for a constant* s*-wave gap with phase fluctuations (*$\langle n \rangle = 0.9$*). For comparison we also show the diamagnetic susceptibility* χ_{Dia} *for a BCS-temperature-dependent gap with phase fluctuations (*$\Delta = \Delta_{BCS}(T)$*). The dotted vertical line indicates the temperature above which we expect reliable results for* χ_{Dia}*. Below this temperature, we obtain an unphysical sudden increase of* χ_{mag} *due to strong finite-size effects. (For details see text.)*

5.2 Spin susceptibility

The spin (or Pauli) susceptibility can be obtained from the coupling of the magnetic field $\boldsymbol{B}$ to the spin degrees of freedom. For a field perpendicular to the 2D planes ($\boldsymbol{B} \parallel \hat{\boldsymbol{z}}$), one gets

$$\hat{H}_H^{ex}(t) = \int dx' \, g \, \frac{\mu_B}{\hbar} \, s_z(\mathbf{x}',t) \, B(\mathbf{x}',t), \tag{5.16}$$

with μ_B Bohr's magneton and $g \approx 2$ the electronic g-factor. The magnetization field $M(\mathbf{x},t)$ is given by

$$\begin{aligned} M(\mathbf{x},t) &= -\frac{N}{V} \, g \, \frac{\mu_B}{\hbar} \, \langle s_z(\mathbf{x},t) \rangle \\ &= \int dx' \, dt' \, \chi_{spin}(\mathbf{x},t,\mathbf{x}',t') \, H(\mathbf{x}',t'), \end{aligned} \tag{5.17}$$

where the last line defines the spin susceptibility as response to the externally applied magnetic field $H(\mathbf{x}',t')$. The expectation value of the spin in z-direction can be decomposed into

$$\langle s_z(\mathbf{x},t) \rangle = \langle s_z^0(\mathbf{x},t) \rangle + \delta \langle s_z(\mathbf{x},t) \rangle. \tag{5.18}$$

Here $\langle s_z^0(\mathbf{x},t) \rangle$ is the expectation value without magnetic field. For a diamagnet or paramagnet one has $\langle s_z^0(\mathbf{x},t) \rangle = 0$. The magnetic field caused spin polarization $\delta \langle s_z(\mathbf{x},t) \rangle$ can be obtained by means of

$$\delta \langle s_z(\mathbf{x},t) \rangle = g \, \frac{\mu_B}{\hbar} \, \frac{i}{\hbar} \int dt' \, dx' \, B(\mathbf{x}',t') \, \mathrm{Tr}\{\hat{\rho}_G [s_z(\mathbf{x}',t'), s_z(\mathbf{x},t)]\} \, \Theta(t-t'), \tag{5.19}$$

which is the usual linear response formula that was already used for the current in the preceding paragraphs. Using

$$B(\mathbf{x},t) = H(\mathbf{x},t) + 4\pi M(\mathbf{x},t) \approx H(\mathbf{x},t), \tag{5.20}$$

one finally gets

$$\chi_{spin}(\mathbf{x},t,\mathbf{x}',t') = -\frac{N}{V} \, g^2 \, \frac{\mu_B^2}{\hbar^2} \, \frac{1}{\hbar} \, D_{zz}(\mathbf{x},t,\mathbf{x}',t'), \tag{5.21}$$

with

$$D_{zz}(\mathbf{x},t,\mathbf{x}',t') = -i \, \mathrm{Tr}\{\hat{\rho}_G [s_z(\mathbf{x},t), s_z(\mathbf{x}',t')]\} \, \Theta(t-t') \tag{5.22}$$

the spin correlation function.

Note, that we replaced $B(\mathbf{x},t)$ by $H(\mathbf{x},t)$ in the linear response formula, since we are only interested in the lowest order perturbation and $\chi_{spin} \ll 1$. A Fourier transformation yields

$$\chi_{spin}(\boldsymbol{q},\omega) = -\frac{N}{V} \, g^2 \, \frac{\mu_B^2}{\hbar^2} \, \frac{1}{\hbar} \, D_{zz}(\boldsymbol{q},\omega). \tag{5.23}$$

The static uniform susceptibility is defined by $\chi_{spin} = \chi_{spin}(\boldsymbol{q} \to 0, \omega = 0)$. For a non-interacting system with a general dispersion $\epsilon(\boldsymbol{k})$, the static uniform spin (or Pauli) susceptibility is given by

$$\chi_{spin}(\boldsymbol{q} \to 0, \omega = 0) = -\frac{1}{V} \, \frac{1}{2} \, g^2 \, \mu_B^2 \sum_{\boldsymbol{k}} \frac{\partial f(\epsilon(\boldsymbol{k}) - \mu)}{\partial \epsilon(\boldsymbol{k})}, \tag{5.24}$$

with $f(\epsilon(\boldsymbol{k})-\mu)$ the Fermi function. For $T \rightarrow 0$, the static uniform susceptibility is proportional to the density of states at the Fermi surface.

Fig. 5.10 displays the spin susceptibility χ_{spin} as a function of temperature for a constant $d_{x^2-y^2}$-wave gap with phase fluctuations at finite doping ($\langle n \rangle = 0.9$). In Sec. 5.1, we have seen that the fluctuation-induced diamagnetism is only important below $T \simeq 1.5\,T_c$ and that, at higher temperatures, χ_{Dia} is at least two orders of magnitude smaller than the paramagnetic current response of the tight-binding electrons. Furthermore, expressing the susceptibilities in cgs-units and using the typical lattice parameters of YBCO (see Sec. 5.1), one obtains that the paramagnetic spin response is 5 times larger than the paramagnetic current response of the tight-binding electrons. In addition, the magnetic current response is only weakly temperature dependent. Moreover, the experimentally observed diamagnetic susceptibility close to T_c can be perfectly fitted by an exponential function, which also indicates that the fluctuating diamagnetism is exponentially suppressed at higher temperatures [212]. Hence, we expect that the temperature dependence of the experimentally observed paramagnetic susceptibility is dominated by the spin susceptibility χ_{spin} over almost the the entire pseudogap phase.[8]

In Fig. 5.10 we have also plotted χ_{spin} for the nearest-neighbor tight-binding model and for the BCS-model with a constant superconducting gap. The phase-fluctuation model exhibits a characteristic temperature dependence of the spin susceptibility, which differs qualitatively from the tight-binding model as well as from the BCS-model. This becomes even more clear for a BCS-temperature-dependent gap, as shown in Fig. 5.11. From Fig. 5.11 we can also infer, that a temperature dependent pairing-gap only slightly modifies the temperature dependence of χ_{spin} in our phase fluctuation model. χ_{spin} always slightly decreases nearly linear below $T^* \equiv T_c^{MF}$ and then displays a characteristic downward bending at $T \simeq 2\,T_{KT}$.

These results are very similar to the experimentally observed temperature dependence of the NMR Knight-shift and the magnetic susceptibility in the pseudogap state of various underdoped high-T_c compounds [218–221]. In the pseudogap state, the temperature variation of the NMR Knight-shift scales linearly with the macroscopic magnetic susceptibility [222]. In underdoped $Bi_2Sr_2CaCu_2O_{8+\delta}$ (Bi2212) single-crystals, two characteristic temperature scales can be identified in the temperature dependence of the Knight-shift [218]. A higher temperature T_{mK}, where the Knight-shift starts to decrease from the nearly constant high-temperature value, and a lower temperature $T_K^* > T_c$, where it starts to decrease very steeply [218]. These two temperatures are however difficult to define exactly. This can be seen from the scaled Knight-shift date of YBCO shown in Ref. [223] and also from our numerical results displayed in Fig. 5.10 and Fig. 5.11, since the change as a function of temperature is continuous.

For completeness, we report in Fig. 5.12 and Fig. 5.13, respectively, results on the temperature dependence of the spin susceptibility χ_{spin} for a constant and a BCS-temperature-dependent s-wave gap with phase fluctuations at finite doping ($\langle n \rangle = 0.9$). Our results for the s-wave gap are very similar to the results for the $d_{x^2-y^2}$-wave gap, indicating that the temperature dependence of χ_{spin} has a characteristic unique fingerprint in the presence of phase fluctuations. The only difference is the much stronger reduction of χ_{spin} at $T = T_{KT}$. Interestingly, a comparable temperature dependence of the uniform spin susceptibility was obtained in QMC simulations of the attractive Hubbard model [224].

---

[8] Again, we neglect in our discussion the influence of antiferromagnetic spin fluctuations.

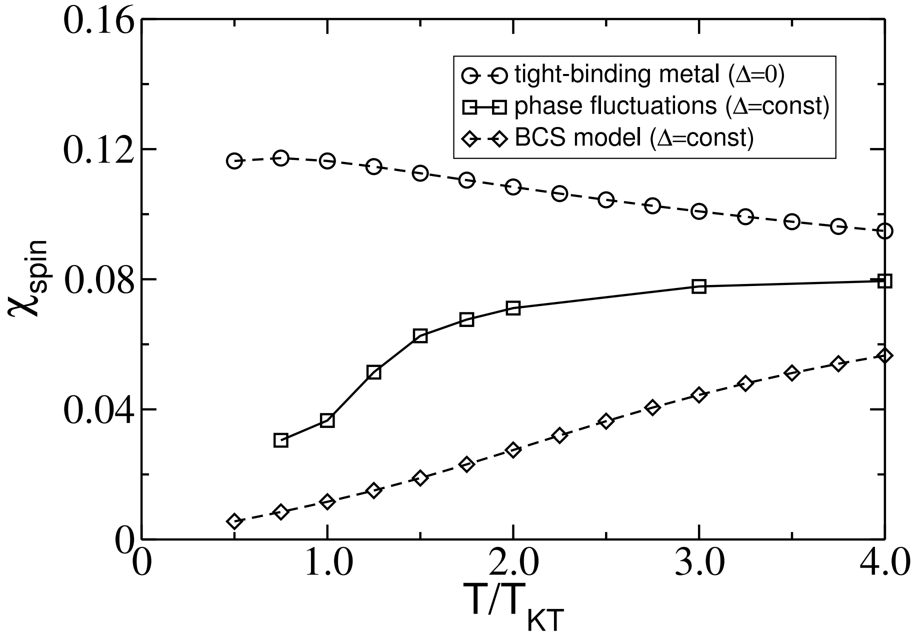

Figure 5.10: Spin susceptibility χ_{spin} in units of $g^2\mu_B^2/t$ ($\hbar = c = a = 1$) as a function of temperature for a constant $d_{x^2-y^2}$-wave gap with phase fluctuations ($\langle n\rangle = 0.9$). For comparison we also show the temperature dependence of the spin susceptibility χ_{spin} for a BCS-superconductor with a constant gap and for the tight-binding model ($\Delta = 0$).

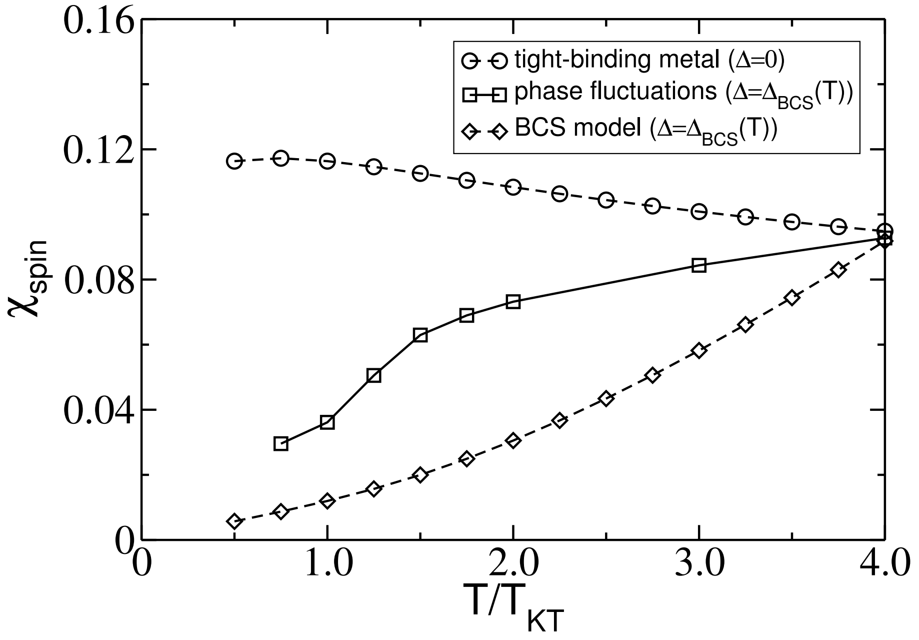

Figure 5.11: Spin susceptibility χ_{spin} in units of $g^2\mu_B^2/t$ ($\hbar = c = a = 1$) as a function of temperature for a BCS-temperature-dependent $d_{x^2-y^2}$-wave gap with phase fluctuations ($\langle n\rangle = 0.9$). For comparison we also show the temperature dependence of the spin susceptibility χ_{spin} for a BCS-superconductor and for the tight-binding model ($\Delta = 0$).

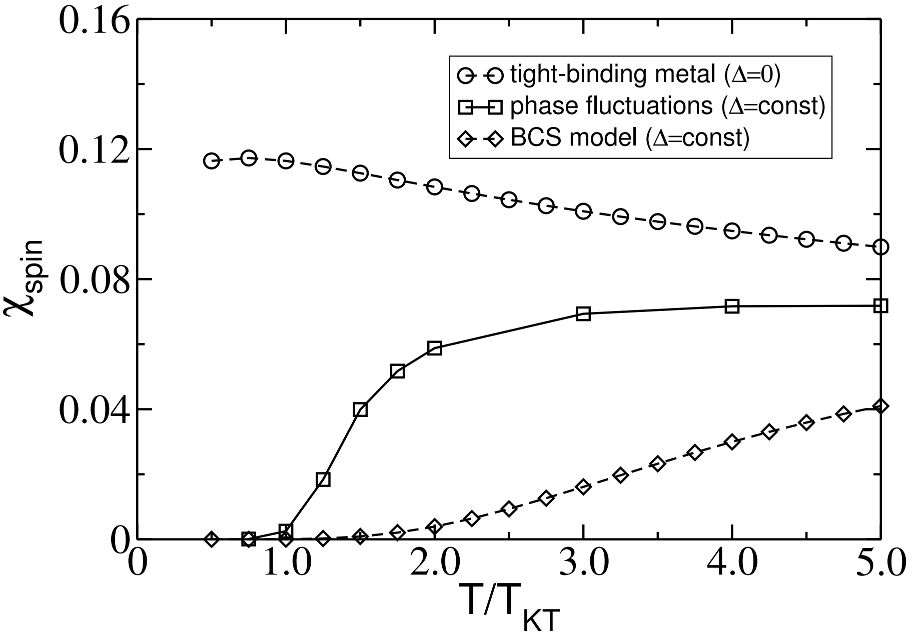

Figure 5.12: Spin susceptibility χ_{spin} in units of $g^2\mu_B^2/t$ ($\hbar = c = a = 1$) as a function of temperature for a constant s-wave gap with phase fluctuations ($\langle n\rangle = 0.9$). For comparison we also show the temperature dependence of the spin susceptibility χ_{spin} for a BCS-superconductor with a constant gap and for the tight-binding model ($\Delta = 0$).

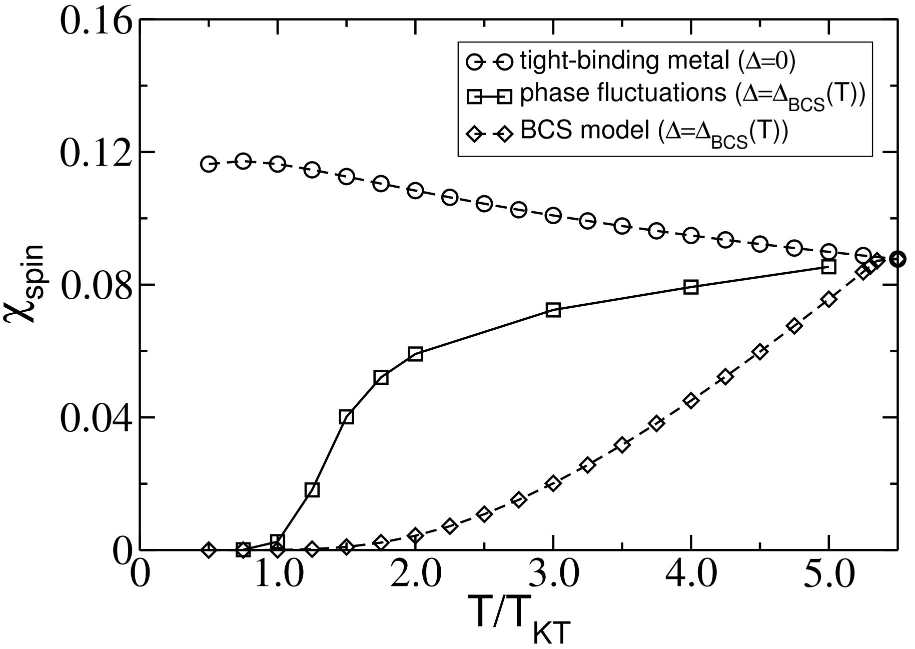

Figure 5.13: Spin susceptibility χ_{spin} in units of $g^2\mu_B^2/t$ ($\hbar = c = a = 1$) as a function of temperature for a BCS-temperature-dependent s-wave gap with phase fluctuations ($\langle n\rangle = 0.9$). For comparison we also show the temperature dependence of the spin susceptibility χ_{spin} for a BCS-superconductor and for the tight-binding model ($\Delta = 0$).

6

Conclusion

In conclusion, we have elaborated the important role that phase fluctuation effects might play in the underdoped cuprates. Our phenomenological model was given by a BCS-like Hamiltonian with a constant local pairing-amplitude and phase fluctuations. The pair-phase fluctuations on the scale of the Cooper-pair size ξ_0 were determined from a classical 2D XY action by means of a Monte Carlo simulation. The quasiparticle tunneling conductance (dI/dV) obtained from this model was able to reproduce characteristic and salient features of recent scanning-tunneling studies of Bi2212 and Bi2201 suggesting that the pseudogap behavior observed in these experiments arises from phase fluctuations of the $d_{x^2-y^2}$-wave pairing gap.

We were further able to show, how phase fluctuations influence the experimentally observed quasiparticle spectra in detail. In particular the disappearance of the BCS-Bogoliubov quasiparticle band at T_c and the change from a more V-like superconducting gap to a rather U-like pseudogap above T_c can be explained in a consistent way by assuming that the low-energy pseudogap in the underdoped cuprates is due to phase fluctuations of a local $d_{x^2-y^2}$-wave pairing gap with fixed magnitude. Furthermore, phase fluctuations can explain why the pseudogap starts closing from the nodal points, whereas it rather fills in along the anti-nodal directions and they can also account for the characteristic temperature dependence of the superconducting $(\pi, 0)$-photoemission-peak.

For an s-wave gap, phase fluctuations lead to an anisotropic pseudogap, which starts closing at $\boldsymbol{k} = (\frac{\pi}{2}, \frac{\pi}{2})$, but remains open at $\boldsymbol{k} = (\pi, 0)$. This gap-asymmetry can be related to the different Fermi velocities and might be of some relevance in electron-doped cuprates, where a possible transition from a s-wave symmetry to an anisotropic s-wave (or $d_{x^2-y^2}$-wave) symmetry of the superconducting order parameter was observed as a function of doping and temperature.

Next, we have shown that the recently observed *violation* of the low-frequency optical sum rule in the SC state of underdoped Bi2212, which is associated with a reduction of kinetic energy, can be related to the role of phase fluctuations. The decrease in kinetic energy is due to the sharpening of the quasiparticle peaks close to the superconducting transition at $T_c \equiv T_{KT}$, where the phase correlation length ξ diverges. We suggest that this sum-rule violation should also appear in other superconductors with low charge carrier density (phase stiffness) such as the organic superconductors.

A detailed analysis of the temperature and frequency dependence of the optical conductivity revealed a superconducting scaling of $\sigma_2(\omega)$, which starts already above T_c, exactly as observed in high-frequency microwave conductivity experiments on Bi2212. On the other hand, our model was only able to account for the characteristic peak, which is observed in $\sigma_1(\omega)$ close to the superconducting transition, after the inclusion of an additional marginal-Fermi-liquid scattering-rate in the optical conductivity formula. This manifests a general shortcoming of our phenomenological model for finite-frequency two-particle properties. It is due to the fact that within our model, quasiparticles are only scattered by phase fluctuations.

Finally, we calculated the static uniform diamagnetic susceptibility. It turned out that the precursor effects of the fluctuating diamagnetism above T_c are very small and limited to temperatures close to T_c in a phase-fluctuation scenario of the pseudogap. Instead, the temperature dependence of the uniform static magnetic susceptibility is dominated by the Pauli spin-susceptibility, which displayed a very characteristic temperature dependence, independent of the details of the gap function used in our model. This temperature dependence is qualitatively very similar to the experimentally observed change of the Knight-shift as a function of temperature in underdoped Bi2212.

Hence, all these results strongly support a phase fluctuation scenario of the pseudogap in the underdoped cuprates. In a next step, however, additional fluctuations of other competing order parameters and especially antiferromagnetic spin-fluctuations have to be included for a more realistic modeling of the cuprates. It will be very interesting to see, whether these additional fluctuations resolve the shortcomings of our simplified model or whether they suppress phase fluctuations and limit them to temperatures close to T_c. Additionally, the parameters used in our phenomenological model have to be derived from the true microscopic Hamiltonian of the cuprates. The phase-fluctuation picture would be further strengthened by the inclusion of quantum phase-fluctuations and the continuation of our calculations below T_c and down to lowest temperatures in the superconducting state.

Summary

In this thesis, a phenomenological phase-fluctuation model for the pseudogap regime of the underdoped cuprates was discussed. The key idea of the phase-fluctuation scenario in the high-T_c superconductors is the notion that the pseudogap observed in a wide variety of experiments arises from phase fluctuations of the superconducting gap. In this scenario, below a mean-field temperature scale T_c^{MF}, a $d_{x^2-y^2}$-wave gap amplitude is assumed to develop. However, the superconducting transition is suppressed to a considerably lower transition temperature T_c by phase fluctuations. In the intermediate temperature regime between T_c^{MF} and T_c, phase fluctuations of the superconducting order parameter give rise to the pseudogap phenomena.

Basically, in order to have condensation into the superconducting state, one needs, in addition to the binding of charge carriers into Cooper pairs, long-range phase coherence among the pairs. Since the underdoped cuprates have a relatively low charge carrier density due to the proximity to the Mott insulating state, they are also characterized by a relatively small phase *stiffness*. This implies a significantly larger role for phase fluctuations, than in conventional superconductors. As a consequence, in these materials the transition to the superconducting state does not display a typical mean-field (BCS) behavior, and phase fluctuations may have a significant influence on low-temperature properties. When coherence is lost due to thermal fluctuations of the phase at and above the transition temperature T_c, pairing remains, together with short-range phase correlations, which can cause the observed pseudogap phenomena in the underdoped cuprates.

The phenomenological phase-fluctuation model discussed in this thesis consists of a two-dimensional BCS-like Hamiltonian where the phase of the pairing-amplitude is free to fluctuate. The fluctuations of the phase were treated by a Monte Carlo simulation of a classical XY model. First, however, we derived an effective quantum phase action from our Hamiltonian by means of a cumulant expansion. This allowed us to identify different terms in the quantum phase action with respect to their physical meaning and in concern of a possible "minus-sign" problem which could arise in a quantum Monte Carlo simulation of the phase degrees of freedom. We then argued, that a classical XY action is sufficient for the temperature range of interest above T_c. All further calculations were then performed by means of a Monte Carlo importance-sampling procedure, in which the probability of a given phase configuration was given by the classical XY model. For each phase configuration, the BCS-like Hamiltonian was diagonalized. Finally, all results were averaged over the different phase configurations.

A severe problem in all calculations are finite-size effects. By means of various numerical optimization techniques and using Wolff's cluster algorithm for the creation of the relevant phase configurations, we were able to reach up to 36×36 lattice sites for single particle properties and up to 16×16 lattice sites for correlation functions. Additionally, we employed a recently proposed technique, consisting of applying a small magnetic field to the lattice Hamiltonian, in order to further reduce size-effects.

First, the density of states was calculated. The quasiparticle tunneling conductance (dI/dV) obtained from our phenomenological phase fluctuation model was able to reproduce characteristic and salient features of recent scanning-tunneling studies of Bi2212 and Bi2201 suggesting that the pseudogap behavior observed in these experiments arises from phase fluctuations of the $d_{x^2-y^2}$-wave pairing gap.

In calculating the single-particle spectral weight, we were further able to show how phase fluctuations influence the experimentally observed quasiparticle spectra in detail. In particular the disappearance of the BCS-Bogoliubov quasiparticle band at T_c and the change from a more V-like superconducting gap to a rather U-like pseudogap above T_c can be explained in a consistent way by assuming that the low-energy pseudogap in the underdoped cuprates is due to phase fluctuations of a local $d_{x^2-y^2}$-wave pairing gap with fixed magnitude. Furthermore, phase fluctuations can explain why the pseudogap starts closing from the nodal points, whereas it rather fills in along the anti-nodal directions and they can also account for the characteristic temperature dependence of the superconducting $(\pi,0)$-photoemission-peak.

For an s-wave gap, phase fluctuations lead to an anisotropic pseudogap, which starts closing at $\boldsymbol{k} = (\frac{\pi}{2}, \frac{\pi}{2})$, but remains open at $\boldsymbol{k} = (\pi, 0)$. This gap-asymmetry can be related to the different Fermi velocities and might be of some relevance in electron-doped cuprates, where a possible transition from a s-wave symmetry to an anisotropic s-wave (or $d_{x^2-y^2}$-wave) symmetry of the superconducting order parameter was observed as a function of doping and temperature.

Motivated by the success of our phenomenological phase fluctuation model, we succeeded in obtaining a high-temperature approximation for the single-particle properties by means of a coherent potential approximation (CPA). The local CPA self-energy yielded qualitatively surprisingly good results in the temperature range, where the phases are completely uncorrelated.

Next, we have shown that the *violation* of the low-frequency optical sum rule recently observed in the SC state of underdoped Bi2212, which is associated with a reduction of kinetic energy, can be related to the role of phase fluctuations. The decrease in kinetic energy is due to the sharpening of the quasiparticle peaks close to the superconducting transition at $T_c \equiv T_{KT}$, where the phase correlation length ξ diverges. We suggest that this sum-rule violation should also appear in other superconductors with low charge carrier density (phase stiffness) such as the organic superconductors.

A detailed analysis of the temperature and frequency dependence of the optical conductivity $\sigma(\omega) = \sigma_1(\omega) + i\sigma_2(\omega)$ revealed a superconducting scaling of $\sigma_2(\omega)$, which starts already above T_c, exactly as observed in high-frequency microwave conductivity experiments on Bi2212. On the other hand, our model was only able to account for the characteristic peak, which is observed in $\sigma_1(\omega)$ close to the superconducting transition, after the inclusion of an additional marginal-Fermi-liquid scattering-rate in the optical conductivity formula. This manifests a general shortcoming of our phenomenological model for finite frequency two-particle properties. It is due to the fact that within our model, quasiparticles are only scattered by phase fluctuations.

Finally, we calculated the static uniform diamagnetic susceptibility. There, we first had to solve the numerically challenging problem of calculating the curvature of the current correlation function in the limit $q_y \to 0$. We found a numerical stable solution for the finite lattice, which qualitatively matched very well the exact solution of the tight-binding model.

It turned out that the precursor effects of the fluctuating diamagnetism above T_c are very small and limited to temperatures close to T_c in a phase-fluctuation scenario of the pseudogap. Instead, the temperature dependence of the uniform static magnetic susceptibility is dominated by the Pauli spin susceptibility, which displayed a very characteristic temperature dependence, independent of the details of the gap function used in our model. This temperature dependence is qualitatively very similar to the experimentally observed change of the Knight-shift as a function of temperature in underdoped Bi2212.

Hence, all these results strongly support a phase-fluctuation scenario of the pseudogap in the underdoped cuprates. In a next step, however, additional fluctuations of other competing order parameters and especially antiferromagnetic spin fluctuations have to be included for a more realistic modeling of the cuprates. It will be very interesting to see, whether these additional fluctuations resolve the shortcomings of our simplified model or whether they suppress phase fluctuations and limit them to temperatures close to T_c.

Bibliography

[1] P. Coleman, Ann. Henri Poincare **4**, S559 (2003).

[2] J. R. Anglin and W. Ketterle, Nature **416**, 211 (2002).

[3] M. Greiner, C. A. Regal, and D. S. Jin, Nature **426**, 537 (2003).

[4] S. Jochim, M. Bartenstein, A. Altmeyer, G. Hendl, S. Riedl, C. Chin, J. Hecker Denschlag, and R. Grimm, Science **302**, 2101 (2003).

[5] M. W. Zwierlein, C. A. Stan, C. H. Schunck, S. M. F. Raupach, S. Gupta, Z. Hadzibabic, and W. Ketterle, Phys. Rev. Lett. **91**, 250401 (2003).

[6] C. A. Regal, M. Greiner, and D. S. Jin, Phys. Rev. Lett. **92**, 040403 (2004).

[7] M. Tinkham, *Introduction to Superconductivity* (McGraw-Hill, New York, 1996).

[8] J. Orenstein and A. J. Millis, Science **288**, 468 (2000).

[9] S.-C. Zhang, Science **275**, 1089 (1997).

[10] S.-C. Zhang, J.-P. Hu, E. Arrigoni, W. Hanke, and A. Auerbach, Phys. Rev. B **60**, 13070 (1999).

[11] S. Sachdev, Science **288**, 475 (2000).

[12] E. Demler, W. Hanke, and S.-C. Zhang, cond-mat/0405038 (Review article to appear in Rev. Mod. Phys.) (unpublished).

[13] E. W. Carlson, V. J. Emery, S. A. Kivelson, and D. Orgad, cond-mat/0206217. Review chapter to appear in 'The Physics of Conventional and Unconventional Superconductors' ed. by K. H. Bennemann and J. B. Ketterson (Springer-Verlag) (unpublished).

[14] J. C. Campuzano, M. R. Norman, and M. Randeria, in *Physics of Conventional and Unconventional Superconductors*, edited by K. H. Bennemann and J. B. Ketterson, Springer-Verlag, Berlin, 2003.

[15] V. M. Loktev, R. M. Quick, and S. G. Sharapov, Physics Reports **349**, 1 (2001).

[16] M. R. Norman and C. Pépin, Rep. Prog. Phys. **66**, 1547 (2003).

[17] A. Damascelli, Z.-X. Shen, and Z. Hussain, Rev. Mod. Phys. **75**, 473 (2002).

[18] A. G. Loeser, Z.-X. Shen, D. S. Dessau, D. S. Marshall, C. H. Park, P. Fournier, and A. Kapitulnik, Science **273**, 325 (1996).

[19] H. Ding, T. Yokoya, J. C. Campuzano, T. Takahashi, M. Randeria, M. R. Norman, T. Mochiku, K. Kadowaki, and J. Giapintzakis, Nature (London) **382**, 51 (1996).

[20] H. Ding, M. R. Norman, T. Yokoya, T. Takeuchi, M. Randeria, J. C. Campuzano, T. Takahashi, T. Mochiku, and K. Kadowaki, Phys. Rev. Lett. **78**, 2628 (1997).

[21] M. Takigawa, A. P. Reyes, P. C. Hammel, J. D. Thompson, R. H. Heffner, Z. Fisk, and K. C. Ott, Phys. Rev. B **43**, 247 (1991).

[22] H. Alloul, A. Mahajan, H. Casalta, and O. Klein, Phys. Rev. Lett. **70**, 1171 (1993).

[23] J. Orenstein, G. A. Thomas, A. J. Millis, S. L. Cooper, D. H. Rapkine, T. Timusk, L. F. Schneemeyer, and J. V. Waszczak, Phys. Rev. B **42**, 6342 (1990).

[24] C. Renner, B. Revaz, J.-Y. Genoud, K. Kadowaki, and Ø. Fischer, Phys. Rev. Lett. **80**, 149 (1998).

[25] N. Miyakawa, J. F. Zasadzinski, L. Ozyuzer, P. Guptasarma, D. G. Hinks, C. Kendziora, and K. E. Gray, Phys. Rev. Lett. **83**, 1018 (1999).

[26] M. Kugler, Ø. Fischer, C. Renner, S. Ono, and Y. Ando, Phys. Rev. Lett. **86**, 4911 (2001).

[27] Y. Wang, N. P. Ong, Z. A. Xu, T. Kakeshita, S. Uchida, D. A. Bonn, R. Liang, and W. N. Hardy, Phys. Rev. Lett. **88**, 257003 (2002).

[28] S. Chakravarty, R. B. Laughlin, D. K. Morr, and C. Nayak, Phys. Rev. B **63**, 094503 (2001).

[29] J. R. Schrieffer and A. P. Kampf, J. Phys. Chem. Solids **56**, 1673 (1995).

[30] D. Pines, Zeit. Phys. B **103**, 129 (1997).

[31] A. V. Chubukov and J. Schmalian, Phys. Rev. B **57**, R11085 (1998).

[32] V. J. Emery and S. A. Kivelson, Nature (London) **374**, 434 (1995).

[33] M. Randeria, N. Trivedi, A. Moreo, and R. T. Scalettar, Phys. Rev. Lett. **69**, 2001 (1992).

[34] M. Franz and A. J. Millis, Phys. Rev. B **58**, 14572 (1998).

[35] H.-J. Kwon and A. T. Dorsey, Phys. Rev. B **59**, 6438 (1999).

[36] B. Kyung, S. Allen, and A.-M. S. Tremblay, Phys. Rev. B **64**, 075116 (2001).

[37] Y. J. Uemura, G. M. Luke, B. J. Sternlieb, J. H. Brewer, J. F. Carolan, W. N. Hardy, R. Kadono, J. R. Kempton, R. F. Kiefl, S. R. Kreitzman, P. Mulhern, T. M. Riseman, D. L. Williams, B. X. Yang, S. Uchida, H. Takagi, J. Gopalakrishnan, A. W. Sleight, M. A. Subramanian, C. L. Chien, M. Z. Cieplak, G. Xiao, V. Y. Lee, B. W. Statt, C. E. Stronach, W. J. Kossler, and X. H. Yu, Phys. Rev. Lett. **62**, 2317 (1989).

[38] R. Preuss, W. Hanke, C. Gröber, and H. G. Evertz, Phys. Rev. Lett. **79**, 1122 (1997).

[39] K. Baberschke, M. Donath, and W. Nolting (Eds.), *Band-Ferromagnetism* (Springer, Berlin, 2001).

[40] J. Corson, R. Mallozzi, J. Orenstein, J. N. Eckstein, and I. Bozovic, Nature **398**, 221 (1999).

[41] D. Feng, D. Lu, K. Shen, C.Kim, H. Eisaki, A. Damascelli, R. Yoshizaki, J. i. Shimoyama, K. Kishio, G. D. Gu, S. Oh, A. Andrus, J. O'Donnell, J. N. Eckstein, and Z.-X. Shen, Science **289**, 277 (2000).

[42] F. Rullier-Albenque, H. Alloul, and R. Tourbot, Phys. Rev. Lett. **91**, 047001 (2003).

[43] M. Sutherland, D. G. Hawthorn, R. W. Hill, F. Ronning, S. Wakimoto, H. Zhang, C. Proust, E. Boaknin, C. Lupien, L. Taillefer, R. Liang, D. A. Bonn, , W. N. Hardy, R. Gagnon, N. E. Hussey, T. Kimura, M. Nohara, and H. Takagi, Phys. Rev. B **67**, 174520 (2003).

[44] M. Franz and Z. Tešanović, Phys. Rev. Lett. **87**, 257003 (2001).

[45] I. F. Herbut, Phys. Rev. Lett. **88**, 047006 (2002).

[46] J. W. Negele and H. Orland, *Quantum Many-Particle Systems* (Addison-Wesley, Redwood City, California, 1988).

[47] J. E. Hirsch, Phys. Rev. B **28**, 4059 (1983).

[48] J. E. Hirsch, Phys. Rev. B **31**, 4403 (1985).

[49] R. M. Fye, Phys. Rev. B **33**, 6271 (1986).

[50] R. Blankenbecler, D. J. Scalapino, and R. L. Sugar, Phys. Rev. D **24**, 2278 (1981).

[51] D. J. Scalapino and R. L. Sugar, Phys. Rev. B **24**, 4295 (1981).

[52] E. Y. Loh Jr. and J. E. Gubernatis, in *Electronic phase transitions*, edited by W. Hanke and Yu. V. Kopaev, North-Holland, Amsterdam, 1992.

[53] C. Gröber, Diplomarbeit, Universität Würzburg, 1996.

[54] S. Yunoki and A. Moreo, Phys. Rev. B **58**, 6403 (1998).

[55] E. Dagotto, S. Yunoki, A. L. Malvezzi, A. Moreo, J. Hu, S. Capponi, D. Poilblanc, and N. Furukawa, Phys. Rev. B **58**, 6414 (1998).

[56] Y. Motome and N. Furukawa, J. Phys. Soc. Japan **68**, 3853 (1999).

[57] N. E. Bickers and D. J. Scalapino, cond-mat/0010480 (unpublished).

[58] P. Monthoux and D. J. Scalapino, Phys. Rev. B **65**, 235104 (2002).

[59] G. D. Mahan, *Many-Particle Physics* (Kluwer, New York, 2000).

[60] A. G. Moreira, S. A. Baeurle, and G. H. Fredrickson, Phys. Rev. Lett. **91**, 150201 (2003).

[61] S. De Palo, C. Castellani, C. Di Castro, and B. K. Chakraverty, Phys. Rev. B **60**, 564 (1999).

[62] A. Paramekanti, M. Randeria, T. V. Ramakrishnan, and S. S. Mandal, Phys. Rev. B **62**, 6786 (2000).

[63] L. Benfatto, S. Caprara, C. Castellani, A. Paramekanti, and M. Randeria, Phys. Rev. B **63**, 174513 (2001).

[64] V. J. Emery and S. A. Kivelson, Phys. Rev. Lett. **74**, 3253 (1995).

[65] S. Kivelson and P. Lee, private communications,
http://forums.its.yale.edu/cuprates/index.jspa.

[66] C. Honerkamp and P. A. Lee, cond-mat/0309469 (unpublished).

[67] B. Lake, G. Aeppli, K. N. Clausen, D. F. McMorrow, K. Lefmann, N. E. Hussey, N. Mangkorntong, M. Nohara, H. Takagi, T. E. Mason, and A. Schröder, Science **291**, 1759 (2001).

[68] V. F. Mitrović, E. E. Sigmund, M. Eschrig, H. N. Bachman, W. P. Halperin, A. P. Reyes, P. Kuhns, and W. G. Moulton, Nature **413**, 501 (2001).

[69] R. I. Miller, R. F. Kiefl, J. H. Brewer, J. E. Sonier, J. Chakhalian, S. Dunsiger, G. D. Morris, A. N. Price, D. A. Bonn, W. H. Hardy, and R. Liang, Phys. Rev. Lett. **88**, 137002 (2002).

[70] K. Kakuyanagi, K. Kumagai, Y. Matsuda, and M. Hasegawa, Phys. Rev. Lett. **90**, 197003 (2003).

[71] V. F. Mitrović, E. E. Sigmund, W. P. Halperin, A. P. Reyes, P. Kuhns, and W. G. Moulton, Phys. Rev. B **67**, 220503 (2003).

[72] J. E. Hoffman, E. W. Hudson, K. M. Lang, V. Madhavan, H. Eisaki, S. Uchida, and J. C. Davis, Science **295**, 466 (2002).

[73] F. F. Assaad, W. Hanke, and D. J. Scalapino, Phys. Rev. B **50**, 12835 (1994).

[74] T. Paiva, R. R. dos Santos, R. T. Scalettar, and P. J. H. Denteneer, Phys. Rev. B **69**, 184501 (2004).

[75] H. Kleinert, Phys. Rev. Lett. **84**, 286 (2000).

[76] K. B. Efetov, Sov. Phys. JETP **51**, 1015 (1980).

[77] J. E. Loh, D. J. Scalapino, and P. M. Grant, Phys. Rev. B **31**, 4712 (1985).

[78] H.-Q. Ding and M. S. Makivić, Phys. Rev. B **42**, 6827 (1990).

[79] K. Harada and N. Kawashima, Phys. Rev. B **55**, R11949 (1997).

[80] G. Schön and A. D. Zaikin, Physics Reports **198**, 237 (1990).

[81] E. Granato and J. M. Kosterlitz, Phys. Rev. Lett. **65**, 1267 (1990).

[82] Y. M. Blanter, G. Schön, and A. D. Zaikin, Phys. Rev. B **55**, 8452 (1997).

[83] E. W. Carlson, S. A. Kivelson, V. J. Emery, and E. Manousakis, Phys. Rev. Lett. **83**, 612 (1999).

[84] J. Tobochnik and G. V. Chester, Phys. Rev. B **20**, 3761 (1979).

[85] J. E. Van Himbergen and S. Chakravarty, Phys. Rev. B **23**, 359 (1981).

[86] J. F. Fernández, M. F. Ferreira, and J. Stankiewicz, Phys. Rev. B **34**, 292 (1986).

[87] R. Gupta, J. DeLapp, G. G. Batrouni, G. C. Fox, C. F. Baillie, and J. Apostolakis, Phys. Rev. Lett. **61**, 1996 (1988).

[88] N. Schultka and E. Manousakis, Phys. Rev. B **49**, 12071 (1994).

[89] G. Franzese, V. Cataudella, S. E. Korshunov, and R. Fazio, Phys. Rev. B **62**, R9287 (2000).

[90] P. Minnhagen and B. J. Kim, Phys. Rev. B **67**, 172509 (2003).

[91] N. D. Mermin and H. Wagner, Phys. Rev. Lett. **17**, 1133 (1966).

[92] P. C. Hohenberg, Phys. Rev. **158**, 383 (1967).

[93] V. L. Berezinskiĭ, Sov. Phys. JETP **32**, 493 (1971).

[94] V. L. Berezinskiĭ, Sov. Phys. JETP **34**, 610 (1972).

[95] J. M. Kosterlitz and D. J. Thouless, J. Phys. C **6**, 1181 (1973).

[96] J. Cardy, *Scaling and Renormalization in Statistical Physics* (Cambridge University Press, Cambridge, 1996).

[97] M. Le Bellac, *Quantum and statistical field theory* (Clarendon Press, Oxford, 1991).

[98] C. Itzykson and J.-M. Drouffe, *Statistical field theory* (Cambridge University Press, Cambridge, 1989).

[99] P. Minnhagen, Rev. Mod. Phys. **59**, 1001 (1987).

[100] D. W. Lynch and C. G. Olson, *Photoemission studies of high temperature superconductors* (Cambridge Univ. Press, Cambridge, 1999).

[101] A. Damascelli, Z. Hussain, and Z.-X. Shen, Rev. Mod. Phys. **75**, 473 (2003).

[102] F. F. Assaad, Phys. Rev. B **65**, 115104 (2002).

[103] O. Jepsen and O. K. Andersen, Solid State Commun. **9**, 1763 (1971).

[104] G. Lehmann and M. Taut, Phys. Stat. Solid. (b) **54**, 469 (1972).

[105] P. E. Blöchl, O. Jepsen, and O. K. Andersen, Phys. Rev. B **49**, 16223 (1994).

[106] C. Gros, Z. Phys. B **86**, 359 (1992).

[107] F. F. Assaad, W. Hanke, and D. J. Scalapino, Phys. Rev. B **49**, 4327 (1994).

[108] T. Eckl, E. Arrigoni, W. Hanke, and D. J. Scalapino, in *High Performance Computing in Science and Engineering ’01*, edited by E. Krause and W. Jäger (Springer Verlag, Berlin, 2002), pp. 210–218.

[109] R. Peierls, Z. Phys. **80**, 763 (1933).

[110] J. J. Sakurai, *Modern Quantum Mechanics* (Addison-Wesley, New York, 1994).

[111] J. Zak, Phys. Rev. **134**, A1602 (1964).

[112] W. Kinzel and G. Reents, *Physik per Computer* (Spektrum Verlag, Heidelberg, Berlin, Oxford, 1996).

[113] R. H. Swendsen and J.-S. Wang, Phys. Rev. Lett. **58**, 86 (1987).

[114] U. Wolff, Phys. Rev. Lett. **62**, 361 (1989).

[115] U. Wolff, Nucl. Phys. B **322**, 759 (1989).

[116] J. M. Thijssen, *Computational physics* (Cambridge Univ. Press, Cambridge, 1999).

[117] W. H. Press, S. A. Teukolsky, W. T. Vetterling, and B. P. Flannery, *Numerical recipes in C* (Cambridge Univ. Press, Cambridge, 1995).

[118] B. Efron and G. Gong, American Statistician **37**, 36 (1983).

[119] K. Dowd and C. Severance, *High Performance Computing* (O’Reilly, Sebastopol, CA, 1998).

[120] C. Howald, P. Fournier, and A. Kapitulnik, Phys. Rev. B **64**, 100504(R) (2001).

[121] S. H. Pan, J. P. O'Neal, R. L. Badzey, C. Chamon, H. Ding, J. R. Engelbrecht, Z. Wang, H. Eisaki, S. Uchida, A. K. Gupta, K.-W. Ng, E. W. Hudson, K. M. Lang, and J. C. Davis, Nature **413**, 282 (2001).

[122] K. M. Lang, V. Madhavan, J. E. Hoffman, E. W. Hudson, H. Eisaki, S. Uchida, and J. C. Davis, Nature **415**, 412 (2002).

[123] J. E. Hoffman, K. McElroy, D. H. Lee, K. M. Lang, H. Eisaki, S. Uchida, and J. C. Davis, Science **297**, 1148 (2002).

[124] K. McElroy, R. W. Simmonds, J. E. Hoffman, D. H. Lee, J. Orenstein, H. Eisaki, S. Uchida, and J. C. Davis, Nature **422**, 592 (2003).

[125] L. Capriotti, D. J. Scalapino, and R. D. Sedgewick, Phys. Rev. B **68**, 014508 (2003).

[126] W. A. Atkinson, P. J. Hirschfeld, and L. Zhu, Phys. Rev. B **68**, 054501 (2003).

[127] T. Cren, D. Roditchev, W. Sacks, J. Klein, J.-B. Moussy, C. Deville-Cavellin, and M. Laguës, Phys. Rev. Lett. **84**, 147 (2000).

[128] G. Kinoda, T. Hasegawa, S. Nakao, T. Hanaguri, K. Kitazawa, K. Shimizu, J. Shimoyama, and K. Kishio, Phys. Rev. B **67**, 224509 (2003).

[129] J. W. Loram, J. L. Tallon, and W. Y. Liang, Phys. Rev. B **69**, 060502(R) (2004).

[130] V. M. Krasnov, A. Yurgens, D. Winkler, P. Delsing, and T. Claeson, Phys. Rev. Lett. **84**, 5860 (2000).

[131] M. Suzuki and T. Watanabe, Phys. Rev. Lett. **85**, 4787 (2000).

[132] A. Yurgens, D. Winkler, T. Claeson, S. Ono, and Y. Ando, Phys. Rev. Lett. **90**, 147005 (2003).

[133] Y. Yamada, K. Anagawa, T. Shibauchi, T. Fujii, T. Watanabe, A. Matsuda, and M. Suzuki, Phys. Rev. B **68**, 054533 (2003).

[134] V. N. Zavaritsky, cond-mat/0306081 (unpublished).

[135] V. N. Zavaritsky, cond-mat/0309429 (unpublished).

[136] A. Yurgens, D. Winkler, T. Claeson, S. Ono, and Y. Ando, cond-mat/0309132 (unpublished).

[137] A. Yurgens, D. Winkler, T. Claeson, S. Ono, and Y. Ando, cond-mat/0309131 (unpublished).

[138] R. M. Dipasupil, M. Oda, N. Momono, and M. Ido, J. Phys. Soc. Jpn. **71**, 1535 (2002).

[139] A. Sharoni, G. Leibovitch, A. Kohen, R. Beck, G. Deutscher, G. Koren, and O. Millo, Europhys. Lett. **62**, 883 (2003).

[140] T. Pereg-Barnea and M. Franz, Phys. Rev. B **68**, 180506(R) (2003).

[141] L. Alff, S. Meyer, S. Kleefisch, U. Schoop, A. Marx, H. Sato, M. Naito, and R. Gross, Phys. Rev. Lett. **83**, 2644 (1999).

[142] A. Biswas, P. Fournier, M. M. Qazilbash, V. N. Smolyaninova, H. Balci, and R. L. Greene, Phys. Rev. Lett. **88**, 207004 (2002).

[143] J. A. Skinta, M.-S. Kim, T. R. Lemberger, T. Greibe, and M. Naito, Phys. Rev. Lett. **88**, 207005 (2002).

[144] C.-T. Chen, P. Seneor, N.-C. Yeh, R. P. Vasquez, L. D. Bell, C. U. Jung, J. Y. Kim, M.-S. Park, H.-J. Kim, and S.-I. Lee, Phys. Rev. Lett. **88**, 227002 (2002).

[145] L. Alff, Y. Krockenberger, B. Welter, M. Schonecke, R. Gross, D. Manske, and M. Naito, Nature **422**, 698 (2003).

[146] M. Lindroos, S. Sahrakorpi, and A. Bansil, Phys. Rev. B **65**, 054514 (2002).

[147] C. Dahnken and R. Eder, Phys. Rev. B **67**, 075107 (2003).

[148] T. Eckl, W. Hanke, S. V. Borisenko, A. A. Kordyuk, T. Kim, A. Koitzsch, M. Knupfer, and J. Fink, cond-mat/0402340 (unpublished).

[149] E. Pavarini, I. Dasgupta, T. Saha-Dasgupta, O. Jepsen, and O. K. Andersen, Phys. Rev. Lett. **87**, 047003 (2001).

[150] A. A. Kordyuk, S. V. Borisenko, T. K. Kim, K. A. Nenkov, M. Knupfer, J. Fink, M. S. Golden, H. Berger, and R. Follath, Phys. Rev. Lett. **89**, 077003 (2002).

[151] S. V. Borisenko, A. A. Kordyuk, T. K. Kim, A. Koitzsch, M. Knupfer, J. Fink, M. S. Golden, M. Eschrig, H. Berger, and R. Follath, Phys. Rev. Lett. **90**, 207001 (2003).

[152] M. R. Norman, H. Ding, M. Randeria, J. C. Campuzano, T. Yokoya, T. Takeuchi, T. Takahashi, T. Mochiku, K. Kadowaki, P. Guptasarma, and D. G. Hinks, Nature **392**, 157 (1998).

[153] M. R. Norman, A. Kaminski, J. Mesot, and J. C. Campuzano, Phys. Rev. B **63**, 140508(R) (2001).

[154] D. L. Feng, A. Damascelli, K. M. Shen, N. Motoyama, D. H. Lu, H. Eisaki, K. Shimizu, J. i. Shimoyama, K. Kishio, N. Kaneko, M. Greven, G. D. Gu, X. J. Zhou, C. Kim, F. Ronning, N. P. Armitage, and Z.-X. Shen, Phys. Rev. Lett. **88**, 107001 (2002).

[155] T. Sato, H. Matsui, S. Nishina, T. Takahashi, T. Fujii, T. Watanabe, and A. Matsuda, Phys. Rev. Lett. **89**, 067005 (2002).

[156] T. Eckl, D. J. Scalapino, E. Arrigoni, and W. Hanke, Phys. Rev. B **66**, 140510(R) (2002).

[157] P. Pieri, L. Pisani, and G. C. Strinati, Phys. Rev. Lett. **92**, 110401 (2004).

[158] C. Honerkamp and P. A. Lee, Phys. Rev. Lett. **90**, 246402 (2003).

[159] H. Matsui, T. Sato, T. Takahashi, S. C. Wang, H. B. Yang, H. Ding, T. Fujii, T. Watanabe, and A. Matsuda, Phys. Rev. Lett. **90**, 217002 (2003).

[160] S. Allen, H. Touchette, S. Moukouri, Y. M. Vilk, and A.-M. S. Tremblay, Phys. Rev. Lett. **83**, 4128 (1999).

[161] S. V. Borisenko, A. A. Kordyuk, T. K. Kim, S. Legner, K. A. Nenkov, M. Knupfer, M. S. Golden, J. Fink, H. Berger, and R. Follath, Phys. Rev. B **66**, 140509(R) (2002).

[162] D. S. Marshall, D. S. Dessau, A. G. Loeser, C.-H. Park, A. Y. Matsuura, J. N. Eckstein, I. Bozovic, P. Fournier, A. Kapitulnik, W. E. Spicer, and Z.-X. Shen, Phys. Rev. Lett. **76**, 4841 (1996).

[163] T. Sato, T. Yokoya, Y. Naitoh, T. Takahashi, K. Yamada, and Y. Endoh, Phys. Rev. Lett. **83**, 2254 (1999).

[164] J. Mesot, M. R. Norman, H. Ding, M. Randeria, J. C. Campuzano, A. Paramekanti, H. M. Fretwell, A. Kaminski, T. Takeuchi, T. Yokoya, T. Sato, T. Takahashi, T. Mochiku, and K. Kadowaki, Phys. Rev. Lett. **83**, 840 (1999).

[165] B. Kyung, Phys. Rev. B **63**, 014502 (2000).

[166] A. A. Kordyuk, S. V. Borisenko, M. Knupfer, and J. Fink, Phys. Rev. B **67**, 064504 (2003).

[167] A. Ino, T. Mizokawa, K. Kobayashi, A. Fujimori, T. Sasagawa, T. Kimura, K. Kishio, K. Tamasaku, H. Eisaki, and S. Uchida, Phys. Rev. Lett. **81**, 2124 (1998).

[168] R. H. He, D. L. Feng, H. Eisaki, J. i. Shimoyama, K. Kishio, and G. D. Gu, cond-mat/0402247 (unpublished).

[169] H. Ding, J. R. Engelbrecht, Z. Wang, J. C. Campuzano, S.-C. Wang, H.-B. Yang, R. Rogan, T. Takahashi, K. Kadowaki, and D. G. Hinks, Phys. Rev. Lett. **87**, 227001 (2001).

[170] R. J. Elliott, J. A. Krumhansl, and P. L. Leath, Rev. Mod. Phys. **46**, 465 (1974).

[171] B. L. Gyorffy, J. B. Staunton, and G. M. Stocks, Phys. Rev. B **44**, 5190 (1991).

[172] A. L. Fetter and J. D. Walecka, *Quantum Theory of Many-Particle Systems* (Mc Graw-Hill, New York, 1971).

[173] I. Paul and G. Kotliar, Phys. Rev. B **67**, 115131 (2003).

[174] D. J. Scalapino, S. R. White, and S. Zhang, Phys. Rev. B **47**, 7995 (1993).

[175] J. R. Schrieffer, *Theory of superconductivity*, Vol. 20 of *Frontiers in physics* (Addison-Wesley, New York, 1993).

[176] H. J. A. Molegraaf, C. Presura, D. van der Marel, P. H. Kes, and M. Li, Science **295**, 2239 (2002).

[177] A. Santander-Syro, R. Lobo, N. Bontemps, Z. Konstantinovic, Z. Li, and H. Raffy, Europhys. Lett. **62**, 568 (2003).

[178] D. N. Basov, E. J. Singley, and S. V. Dordevic, Phys. Rev. B **65**, 054516 (2002).

[179] C. C. Homes, S. V. Dordevic, D. A. Bonn, R. Liang, and W. N. Hardy, Phys. Rev. B **69**, 024514 (2004).

[180] C. Bernhard, private communications (unpublished).

[181] W. Hanke and L. J. Sham, Phys. Rev. B **12**, 4501 (1975).

[182] W. Hanke and L. J. Sham, Phys. Rev. B **21**, 4656 (1980).

[183] Hirsch, Science **295**, 2226 (2002).

[184] M. R. Norman, M. Randeria, B. Jankó, and J. C. Campuzano, Phys. Rev. B **61**, 14742 (2000).

[185] M. R. Norman and C. Pepin, Phys. Rev. B **66**, 100506 (2002).

[186] R. Haslinger and A. V. Chubukov, Phys. Rev. B **67**, 140504 (2003).

[187] T. A. Maier, M. Jarrell, A. Macridin, and C. Slezak, Phys. Rev. Lett. **92**, 027005 (2004).

[188] H. Yokoyama, Y. Tanaka, M. Ogata, and H. Tsuchiura, J. Phys. Soc. Japan **73**, 1119 (2004).

[189] S. Chakravarty, H.-Y. Kee, and E. Abrahams, Phys. Rev. B **67**, 100504(R) (2003).

[190] Z. Gu, T. Li, and Z.-Y. Weng, cond-mat/0402550 (unpublished).

[191] S. Chakravarty, A. Sodbø, P. W. Anderson, and S. Strong, Science **261**, 337 (1993).

[192] P. W. Anderson, Science **268**, 1154 (1995).

[193] P. W. Anderson, Science **279**, 1196 (1998).

[194] S. Chakravarty, H.-Y. Kee, and E. Abrahams, Phys. Rev. Lett. **82**, 2366 (1999).

[195] S. Chakravarty, H.-Y. Kee, and K. Völker, Nature **428**, 53 (2004).

[196] W. Kim and J. P. Carbotte, Phys. Rev. B **62**, 8661 (2000).

[197] D. N. Basov, C. C. Homes, E. J. Singley, M. Strongin, T. Timusk, G. Blumberg, and D. van der Marel, Phys. Rev. B **63**, 134514 (2001).

[198] A. F. Santander-Syro, R. P. S. M. Lobo, N. Bontemps, Z. Konstantinovic, Z. Li, and H. Raffy, Phys. Rev. Lett. **88**, 097005 (2002).

[199] T.-H. Gimm and H.-Y. Choi, cond-mat/0212361 (unpublished).

[200] D. N. Basov, R. Liang, B. Dabrowski, D. A. Bonn, W. N. Hardy, and T. Timusk, Phys. Rev. Lett. **77**, 4090 (1996).

[201] A. V. Puchkov, D. N. Basov, and T. Timusk, J. Phys.: Condens. Matter **8**, 10049 (1996).

[202] T. Timusk, cond-mat/0303383 (APS Frank Isakson Prize paper) (unpublished).

[203] J. Hwang, T. Timusk, and G. D. Gu, Nature **427**, 714 (2004).

[204] J. Corson, J. Orenstein, S. Oh, J. O'Donnell, and J. N. Eckstein, Phys. Rev. Lett. **85**, 2569 (2000).

[205] C. M. Varma, P. B. Littlewood, S. Schmitt-Rink, E. Abrahams, and A. E. Ruckenstein, Phys. Rev. Lett. **63**, 1996 (1989).

[206] P. B. Littlewood and C. M. Varma, Phys. Rev. B **46**, 405 (1992).

[207] R. M. White, *Quantum theory of magnetism* (Springer, Berlin, 1983).

[208] P. Skudlarski and G. Vignale, Phys. Rev. B **43**, 5764 (1991).

[209] C. Torrón, A. Díaz, A. Pomar, J. A. Veira, and F. Vidal, Phys. Rev. B **49**, 13143 (1994).

[210] P. Carretta, A. Lascialfari, A. Rigamonti, A. Rosso, and A. A. Varlamov, Physica B **259**, 536 (1999).

[211] P. Carretta, A. Lascialfari, A. Rigamonti, A. Rosso, and A. Varlamov, Phys. Rev. B **61**, 12420 (2000).

[212] A. Sewer and H. Beck, Phys. Rev. B **64**, 014510 (2001).

[213] A. Lascialfari, A. Rigamonti, L. Romano', P. Tedesco, A. Varlamov, and D. Embriaco, Phys. Rev. B **65**, 144523 (2002).

[214] A. Lascialfari, A. Rigamonti, L. Romano', A. A. Varlamov, and I. Zucca, Phys. Rev. B **68**, 100505(R) (2003).

[215] R. M. White, Phys. Rev. B **10**, 3426 (1974).

[216] I. Iguchi, T. Yamaguchi, and A. Sugimoto, Nature **412**, 420 (2001).

[217] U. Thisted, J. Nyhus, T. Suzuki, J. Hori, and K. Fossheim, Phys. Rev. B **67**, 184510 (2003).

[218] K. Ishida, K. Yoshida, T. Mito, Y. Tokunaga, Y. Kitaoka, K. Asayama, Y. Nakayama, J. Shimoyama, and K. Kishio, Phys. Rev. B **58**, R5960 (1998).

[219] G.-Q. Zheng, W. G. Clark, Y. Kitaoka, K. Asayama, Y. Kodama, P. Kuhns, and W. G. Moulton, Phys. Rev. B **60**, R9947 (1999).

[220] T. Watanabe, T. Fujii, and A. Matsuda, Phys. Rev. Lett. **84**, 5848 (2000).

[221] H. Kotegawa, Y. Tokunaga, K. Ishida, G.-Q. Zheng, Y. Kitaoka, H. Kito, A. Iyo, K. Tokiwa, T. Watanabe, and H. Ihara, Phys. Rev. B **64**, 064515 (2001).

[222] H. Alloul, T. Ohno, and P. Mendel, Phys. Rev. Lett. **63**, 1700 (1989).

[223] J. L. Tallon and J. W. Loram, Physica C **349**, 53 (2001).

[224] J. M. Singer, M. H. Pedersen, T. Schneider, H. Beck, and H.-G. Matuttis, Phys. Rev. B **54**, 1286 (1996).

Zusammenfassung

In der vorliegenden Arbeit wurde ein phänomenologisches Phasenfluktuationsmodell zur Beschreibung der „Pseudolücken“-Phase in den unterdotierten Hochtemperatur-Supraleitern untersucht. Bei den meisten Hochtemperatur-Supraleitern handelt es sich um keramische Verbindungen. Ihr gemeinsames Merkmal sind zweidimensionale Kupferoxidebenen, welche die elektronischen Eigenschaften der Kuprate bestimmen. Im Gegensatz zu konventionellen metallischen BCS-Supraleitern skaliert in den unterdotierten Kupraten die kritische Temperatur, unterhalb derer Supraleitung einsetzt, nicht mit der Größe der supraleitenden Energielücke Δ, und damit der Stärke der Paaranziehung, sondern mit der superfluiden Dichte ρ_s, d. h. der Dichte der supraleitenden Elektronen.

Eine Erklärung hierfür liegt in der Tatsache begründet, dass alle Kuprate dotierte Mott-Isolatoren sind. Für den supraleitenden Zustand ist nun einerseits die Paarung der Elektronen zu Cooper-Paaren notwendig, andererseits aber auch eine globale Phasenkohärenz zwischen den Cooper-Paaren. Die Temperatur unterhalb derer Paarung einsetzt wird durch die konventionelle BCS-Molekularfeldtheorie beschrieben und ist proportional zur supraleitenden Energielücke $T_c^{MF} \sim \Delta$. Auf der anderen Seite entsteht die globale Phasenkohärenz zwischen den Cooper-Paaren erst unterhalb einer Temperatur T_φ, die von der so genannten Phasensteifheit bestimmt wird. Diese ist proportional zur superfluiden Dichte, d. h. $T_\varphi \sim \rho_s$.

In konventionellen Supraleitern und in den überdotierten Kupraten ist $T_\varphi \gg T_c^{MF}$. Somit setzt mit der Paarung auch augenblicklich die Phasenkohärenz ein und die supraleitende Sprungtemperatur wird alleine durch T_c^{MF} bestimmt. Unterdotierte Kuprate liegen im Phasendiagramm jedoch sehr nahe am Mott-isolierenden Zustand und haben daher eine relativ geringe Anzahl an beweglichen Ladungsträgern. Dies hat zur Folge, dass bei einer Temperatur $T^* = T_c^{MF}$ zunächst die Paarung der Ladungsträger einsetzt, diese sich aber erst bei einer sehr viel niedrigeren Temperatur $T_c = T_\varphi$ phasenkohärent bewegen und damit supraleitend werden. Dies ist das so genannte Phasenfluktuationsszenario für die Pseudolücke im Energiespektrum der unterdotierten Kuprate. Die Pseudolücke entwickelt sich oberhalb von T_c kontinuierlich aus der supraleitenden Energielücke heraus und wird bis zu einer Temperatur $T^* \gg T_c$ in verschiedenen Experimenten beobachtet.

Als Ausgangspunkt der vorliegenden Arbeit diente nun ein BCS-artiger Hamiltonoperator mit fester Paarungsamplitude, bei dem jedoch die Phase der lokalen Paare frei fluktuieren konnte. Für diesen Hamiltonoperator wurde zunächst eine effektive Phasenwirkung mittels Kumulantenentwicklung abgeleitet. Dies erlaubte es, verschiedene Terme zu unterscheiden und in Bezug auf ihre physikalischen Eigenschaften und im Hinblick auf ein mögliches Minuszeichenproblem bei einer späteren Monte Carlo Simulation der Phasenfreiheitsgrade zu untersuchen. Es stellte sich dabei heraus, dass eine klassische XY-Wirkung zur Beschreibung der Phasenfluktuationen oberhalb von T_c vollkommen ausreicht. Alle weiteren Rechnungen wurden nun durchgeführt, indem mittels einer Monte Carlo Simulation des klassischen XY-Modells verschiedene Phasenkonfigurationen erzeugt wurden und für jede dieser Phasenkonfigurationen der BCS-artige Hamiltonoperator exakt diagonalisiert wurde. Am Ende fand dann eine Mittelung über sämtliche Phasenkonfigurationen statt.

Wie bei allen Monte Carlo Simulationen, so stellte auch hier die, von der zur Verfügung stehenden Computerleistung begrenzte, relativ kleine Gittergröße das größte Hindernis dar. Mittels numerischer Optimierung und der Verwendung des Wolff-Cluster-Algorithmus zur Erzeugung der Phasenkonfigurationen konnten Systeme mit bis zu 36×36 Gitterplätzen für Einteilchengrößen und 16×16 Gitterplätzen für Korrelationsfunktionen auf dem Hitachi SR-8000 Bundeshöchstleistungsrechner in München berechnet werden. Des weiteren wurde eine kürzlich vorgeschlagene Methode zur Reduzierung von „finite-size“ Effekten, welche auf der Einführung eines „virtuellen“ Magnetfeldes beruht, erfolgreich implementiert und getestet.

Die erste Anwendung dieses phänomenologischen Phasenfluktuationsmodells bestand in der Berechnung von Einteilchen-Tunnelspektren. Hierbei konnte eine ausgezeichnete Übereinstimmung mit den Experimenten, insbesondere was die Temperaturentwicklung der supraleitenden Kohärenzpeaks und das charakteristische auffüllen der Pseudolücke mit ansteigenden Temperaturen betrifft, erzielt werden.

Durch einen detaillierten Vergleich zwischen Theorie und Experiment konnte gezeigt werden, auf welche Weise Phasenfluktuationen das Quasiteilchenspektrum beeinflussen. Insbesondere das Verschwinden der BCS-Bogoliubov Quasiteilchenbänder oberhalb von T_c und die Veränderung der Energielücke, von einer V-artigen supraleitenden Lücke hin zu einer mehr U-artigen Pseudolücke oberhalb von T_c, konnte in konsistenter Weise durch Phasenfluktuationen des supraleitenden Ordnungsparameters erklärt werden. Darüberhinaus war das Phasenfluktuationsmodell in der Lage zu erklären, warum die Pseudolücke von den Knotenpunkten an der Fermifläche her anfängt sich zu schließen, wohingegen sie an den Anti-Knotenpunkten eher aufgefüllt wird. Auch konnte die charakteristische Temperaturentwicklung des so genannten „supraleitenden“ $(\pi, 0)$-Photoemissionspeaks sehr gut durch Phasenfluktuationen beschrieben werden.

Durch den Erfolg des Phasenfluktuationsmodells motiviert, wurde eine Hochtemperatur-Näherung für die Pseudolücke untersucht. Diese so genannte kohärente Potentialnäherung (CPA) beruht auf einem Legierungsanalogon für Unordnungsprobleme. In unserem Fall wurde die Unordnung durch die fluktuierende Phase der lokalen Paare repräsentiert. Es konnte gezeigt werden, dass die lokale CPA Selbstenergie erstaunlich gut die charakteristischen Einteilchen-Eigenschaften bei hohen Temperaturen wiedergeben kann.

Als nächstes wurden Experimente zur Verletzung der optischen Niederfrequenz-Summenregel in unterdotierten Bi2212-Verbindungen untersucht, welche auf eine Reduktion der kinetischen

Energie im supraleitenden Zustand hindeuten. Es konnte gezeigt werden, dass diese Reduktion mit der Rolle von Phasenfluktuationen beim supraleitenden Übergang in Verbindung gebracht werden kann. Die Reduktion der kinetischen Energie erfolgt durch das Entstehen scharfer Quasiteilchenpeaks bei T_c. Dort beginnt die Korrelationslänge der fluktuierenden Phasen zu divergieren, und es stellt sich eine quasi-langreichweitige Ordnung ein.

Eine detailliert Analyse der Frequenz und Temperaturabhängigkeit der optischen Leitfähigkeit ergab eine supraleitende Skalierung des Imaginärteils der optischen Leitfähigkeit schon oberhalb von T_c, genau wie in Mikrowellen-Hochfrequenzleitfähigkeitsexperimenten beobachtet. Das experimentell beobachtete Maximum im Realteil der optischen Leitfähigkeit bei T_c konnte unser phänomenologisches Phasenfluktuationsmodell jedoch nur durch den Einbau einer zusätzlichen marginalen Fermiflüssigkeits-Streurate in die Formel für die optische Leitfähigkeit beschreiben.

Als letztes wurde die homogene statische diamagnetische Suszeptibilität berechnet. Hierbei musste zunächst das anspruchsvolle numerische Problem der Berechnung der Krümmung der Strom-Strom Korrelationsfunktion für den Limes $q_y \to 0$ auf einem 16×16 Gitter gelöst werden. Nachdem eine numerisch stabile Lösung für das endliche Gitter gefunden wurde, die qualitativ gut mit der exakten Lösung des freien Systems übereinstimmt, stellte sich heraus, dass Vorläufereffekte des idealen diamagnetischen Zustands oberhalb von T_c in der statischen diamagnetische Suszeptibilität äußerst gering sind und sich auf Temperaturen in der Nähe von T_c beschränken. Stattdessen wird die Temperaturabhängigkeit der statischen homogenen magnetischen Suszeptibilität von der Pauli-Spinsuszeptibilität bestimmt. Diese zeigt für das Phasenfluktuationsmodell einen charakteristischen Verlauf, der erstaunlich gut mit der Temperaturabhängigkeit des Magnetresonanz Knight-shift in unterdotierten Bi2212-Verbindungen übereinstimmt.

Insgesamt konnte in der vorliegenden Arbeit gezeigt werden, dass das phänomenologische Phasenfluktuationsmodell eine erstaunlich gute und in sich konsistente Beschreibung vieler Erscheinungen in der „Pseudolücken“-Phase der unterdotierten Kuprate liefert. Auf der anderen Seite treten jedoch auch Mängel klar zu Tage, so bei dynamischen Zweiteilchengrößen wie der optischen Leitfähigkeit. Diese müssen, z. B. durch den Einbau von antiferromagnetischen Fluktuationen beseitigt werden, um eine realistischere Beschreibung der unterdotierten Kuprate zu ermöglichen und Phasenfluktuationen als Ursache für die niederenergetische Pseudolücke zu bestätigen.

LEBENSLAUF

Name		Thomas Eckl
Anschrift		Kirchbergstraße 18 97980 Bad Mergentheim Tel. 0171-144-5761 (privat) 0931-888-5872 (dienstlich) Email: eckl@physik.uni-wuerzburg.de
geboren		15. August 1974 in Bad Mergentheim
Familienstand		ledig
Nationalität		deutsch
Schulbildung	Aug. 81–Jul. 85	Grundschule Bad Mergentheim
	Aug. 85–Jun. 94	Deutschorden-Gymnasium Bad Mergentheim
Studium	Okt. 94 –Nov. 99	Studium der Physik an der Universität Würzburg
	Nov. 99	Diplom, Note: 1.0 „mit Auszeichnung“
Promotion	Jan. 00 –Jun. 04	Doktorarbeit zur Theorie der Hochtemperatursupraleiter bei Prof. Dr. W. Hanke am Institut für Theoretische Physik und Astrophysik der Universität Würzburg
	Okt. 01 –Nov. 01	Gastaufenthalt bei Prof. D. J. Scalapino am Physics Department der University of California in Santa Barbara, USA
Anstellungen	Dez. 99–Aug. 04	Wissenschaftlicher Mitarbeiter an der Universität Würzburg

PUBLIKATIONEN

1. T. Eckl, E. Arrigoni, W. Hanke, und F. F. Assaad:
   t-U-W model of a $d_{x^2-y^2}$ *superconductor in the proximity of an antiferromagnetic Mott insulator: Diagrammatic studies versus quantum Monte Carlo simulations,*
   Phys. Rev. B **62**, 12395 (2000).

2. T. Eckl, E. Arrigoni, W. Hanke, und D. J. Scalapino:
   Interplay of Phase Fluctuations and Electronic Excitations in High-Temperature Superconductors - A Monte Carlo Simulation,
   „High Performance Computing in Science and Engineering '01“, p. 210 (Springer, Heidelberg, 2002).

3. T. Eckl, D. J. Scalapino, E. Arrigoni, und W. Hanke:
   Pair Phase Fluctuations and the Pseudogap,
   Phys. Rev. B **66**, 140510(R) (2002).

4. T. Eckl, Z.-B. Huang, W. Hanke, und E. Arrigoni:
   Phase Fluctuations and the Role of Electron Phonon Coupling in High-T_c *Superconductors,*
   „High Performance Computing in Science and Engineering, Munich 2002“, p. 269 (Springer-Verlag, Berlin Heidelberg, 2003).

5. E. Arrigoni, M. G. Zacher, T. Eckl, und W. Hanke:
   Interrelation between antiferromagnetic and superconducting gaps in high-T_c *materials,*
   Ann. Phys. (Leipzig) **12**, 320 (2003).

6. T. Eckl, W. Hanke und E. Arrigoni:
   Phase-fluctuation-induced reduction of the kinetic energy at the superconducting transition,
   Phys. Rev. B **68**, 014505 (2003).

Danksagung

Ich möchte mich bei allen bedanken, die mich bei meiner Arbeit unterstützt haben.

An erster Stelle möchte ich mich bei meinem Doktorvater Herrn Prof. Dr. W. Hanke für die Freiheit und Unterstützung, sowie die zahlreichen — nicht nur physikalischen — Gespräche während der letzten Jahre bedanken. Insbesondere bedanke ich mich dafür, dass er es mir ermöglichte, das Physics Department der University of California in Santa Barbara zu besuchen und dort eine Reihe der führenden Wissenschaftler zu treffen.

Herrn Prof. Dr. E. Arrigoni danke ich für die Vermittlung des physikalischen *Handwerkszeugs*, welches mir seit meiner Diplomarbeit half meine physikalische Denkweise zu verbessern, sowie für das sorgfältige Korrekturlesen der Arbeit.

Herrn Prof. D. J. Scalapino, danke ich für seine Gastfreundschaft während meines Aufenthalts am Physics Department der University of California in Santa Barbara, sowie die zahlreichen aufschlussreichen Gespräche. Ebenfalls möchte ich mich bei Herrn Prof. B. Sugar für die anregende Diskussion über Monte Carlo Simulationen und Monte Carlo Fehler bedanken, sowie bei allen anderen für den angenehmen Aufenthalt in Santa Barbara.

Allen Mitgliedern der Arbeitsgruppe danke ich für die zahlreichen Gespräche und das gute Arbeitsklima.

Meinen Eltern danke ich für die bedingungslose Unterstützung meiner Arbeit und meinen Bruder für die zahlreichen Diskussionen über *alles Mögliche* sowie das „letzte“ Korrekturlesen der Arbeit.